Texas A&M University
Mechanical Engineering Department
Turbomachinery Laboratory
Tribology Group

A Novel Computational Model for Tilting Pad Journal Bearings with Soft Pivot Stiffnesses

Research Progress Report to the TAMU Turbomachinery Research Consortium

TRC-B&C-01-2013

by

Yujiao Tao

Research Assistant

Luis San Andrés

Mast-Childs Tribology Professor
Principal Investigator

May 2013

COMPUTATIONAL MODEL FOR TILTING PAD JOURNAL BEARINGS
TRC Project, TEES # 32513/1519 6B (Year II)

EXECUTIVE SUMMARY

A NOVEL COMPUTATIONAL MODEL FOR TILTING PAD JOURNAL BEARINGS WITH SOFT PIVOT STIFFNESSES

A novel tilting pad journal bearing model including pivot flexibility as well as temporal fluid inertia effects on the thin film fluid flow aims to accurately predict the bearing forced performance. The predictive model also accounts for the thermal energy transport effects in a TPJB. A Fortran program with an Excel GUI models TPJBs and delivers predictions of the bearing static and dynamic forced performance. The calculation algorithm uses a Newton-Raphson procedure for successful iterations on the equilibrium pad radial and transverse displacements and journal center displacements, even for bearings pads with very soft pivots.

The predictive model accounts for the effect of film temperature on the operating bearing and pad clearances by calculating the thermal expansion of the journal and pad surfaces. The pad inlet thermal mixing coefficient (λ) influences moderately the predicted fluid film temperature field.

Pad pivot flexibility decreases significantly and dominates the bearing stiffness and damping coefficients when the pivot stiffness is lower than 10% of the fluid film stiffness coefficients (with rigid pivots). Pivot flexibility has a more pronounced effect on reducing the bearing damping coefficients than the stiffness coefficients. Pad pivot flexibility may still affect the bearing behavior at a light load condition for a bearing with a large pad preload.

Pad pivot flexibility, as well as the fluid inertia and the pads' mass and mass moment of inertia, could influence the bearing impedance coefficients, in particular at high whirl frequencies. The stiffness and damping coefficients of a TPJB increase with a reduction in the operating bearing and pad clearances.

The work delivers a predictive tool benchmarked against a number of experimental results for test bearings available in the recent literature. The static and dynamic forced performance characteristics of actual TPJBs can not be accurately predicted unless their

pad flexibility and pivot flexibility, fluid film temperature, pad inlet thermal mixing coefficient, operating bearing and pad clearances, among others are well known in advance. However, the extensive archival literature showcasing test procedures and experimental results for TPJBs does not report the above parameters. Thus, reasonable assumptions on the magnitude of certain elusive parameters for use in the predictive TPJB model are necessary.

NOMENCLATURE

$C_{XX}, C_{XY}, C_{YX}, C_{YY}$	Bearing damping force coefficients [N.s/m]
C_P	Pad radial clearance [m], $C_P = R_P - R_J$
C_B	Bearing radial clearance [m], $C_B = R_B - R_J$
D	Rotor diameter [m]
e	Journal center displacement [m], $e = \sqrt{e_X^2 + e_Y^2} = \sqrt{e_\xi^2 + e_\eta^2}$
F_X, F_Y	Fluid film forces (X, Y) on a pad [N]
F_s, F_h, F_{in}	Flow rate of supplied cold oil, hot oil and mixing oil[m^3/s]
F_ξ, F_η	Fluid film forces (ξ, η) on a pad [N]
$F_{\xi_{piv}}, F_{\eta_{piv}}$	Pivot reaction forces on a pad [N]
h	Film thickness [m]
$h_X, h_Y, h_\xi, h_\eta, h_\delta$	Perturbed film thickness components due to pad motions
I_p	Pad mass moment of inertia about pivot [kg.m^2], $I_p = I_G + ml^2$
I_G	Pad mass moment of inertia about mass center [kg.m^2]
$K_{XX}, K_{XY}, K_{YX}, K_{YY}$	Bearing stiffness force coefficients [N/m]
K_p	Pivot stiffness [N/m]
$\tilde{K}_s$	Pad pivot structure stiffness matrix
L	Bearing axial length [m]

l	Distance from a pivot point to pad mass center [m],
$l = \sqrt{l_\xi^2 + l_\eta^2}$ M	Fluid film moment on a pad [N.m]
M_{piv}	Pivot reaction moment on a pad [N.m]
m	Pad mass [kg]
m_J	Journal mass [kg]
$\tilde{M}$	Pad generalized inertia matrix
N_{pad}	Numbers of pads on a bearing
O_B	Bearing center
O_P	Pad center
P_a	Ambient pressure [Pa]
P_s	Supply pressure [Pa]
$P_X, P_Y, P_\delta, P_\xi, P_\eta$	Perturbed pressure fields due to pad motions [Pa/m]
R_B	Bearing radius [m]
R_J	Journal radius [m]
R_P	Pad radius [m]
R_d	Distance from a pivot to pad center [m]
r_P	Bearing dimensional preload [m], $r_p = C_P - C_B$
$\bar{r}_P$	Bearing dimensionless preload, $\bar{r}_p = 1 - C_B/C_P$

T_s, T_h, T_{in}	Absolute bulk-temperature of supplied oil, hot oil and mixing flow [$^{\circ}$C]
W	Load on a journal [N], $W = \sqrt{W_X^2 + W_Y^2}$
$Z_{\alpha\beta}$	Fluid film impedance coefficients $\alpha, \beta = X, Y, \delta, \xi, \eta$
$Z_{R\alpha\beta}$	Fluid film reduced impedance coefficients $\alpha, \beta = X, Y$
$\tilde{Z}_{R\alpha\beta}$	Fluid film reduced impedance coefficients $\alpha, \beta = \xi, \eta$
$\tilde{Z}_s$	Pad pivot structure impedance matrix
Z_P, Z_{PJ}, Z_{JP}	Fluid film impedance matrices
δ_p	Pad tilt angle [rad]
ε	Journal center eccentricity ratio, $\varepsilon = e/C_P$
ϕ	Coordinate transformation angle, $\phi = \theta_p + \pi$ [rad]
η_{piv}	Pad transverse displacement [m]
$\bar{\eta}$	Transverse displacement between a journal and a pad [m]
λ	Thermal oil-mixing coefficient
μ_0	Supply lubricant viscosity [Pa.s]
Θ	Pad arc angle [rad]
θ_L	Angular position of a pad trailing edge starting from - X axis [rad]
θ_P	Pivot angular position starting from - X axis [rad]
θ_T	Angular position of a pad leading edge starting from - X axis [rad]

Ω	Journal rotation speed [rad/s]
ω	Excitation frequency [Hz]
ξ_{piv}	Pad radial displacement [m]
$\bar{\xi}$	Radial displacement between a journal and a pad [m]

Subscripts

0	Static
(X,Y)	Journal center global coordinates
(ξ,η)	Pad pivot local coordinates

Superscripts

k	k^{th} pad

TABLE OF CONTENTS

LIST OF FIGURES

LIST OF TABLES

INTRODUCTION

Rotating machinery with larger power output demands rotor bearing systems (RBSs) operate at high speeds. However, a destructive rotordynamic instability, such as oil whirl, may occur in RBSs supported on fixed geometry fluid film bearings when the rotor operates at rotational speeds exceeding twice the system first natural frequency [1].

Tilting pad journal bearings (TPJBs) are superior to fixed geometry fluid film bearings because of their inherent hydrodynamic stability. In a TPJB, pads tilt about their pivots point to form a convergent hydrodynamic fluid film along each pad thus developing small, even negligible, cross-coupling stiffness coefficients which are known to be destabilizing [2]. Accurately predicting the static and dynamic forced performance of TPJBs is vital to the successful design and operation of a RBS.

Figure 1 shows a schematic view of an ideal five-pad tilting pad bearing with a (static) load-on-pad (LOP) configuration. The bearing comprises of a number of pads supported on pivots and a rotating journal spinning at speed Ω. The lubricant film thickness between the pads and shaft (journal) generates a hydrodynamic pressure in reaction to an applied load (W). Upon operation, a pad tilts with angle (δ) about its pivot to form a convergent fluid film wedge.
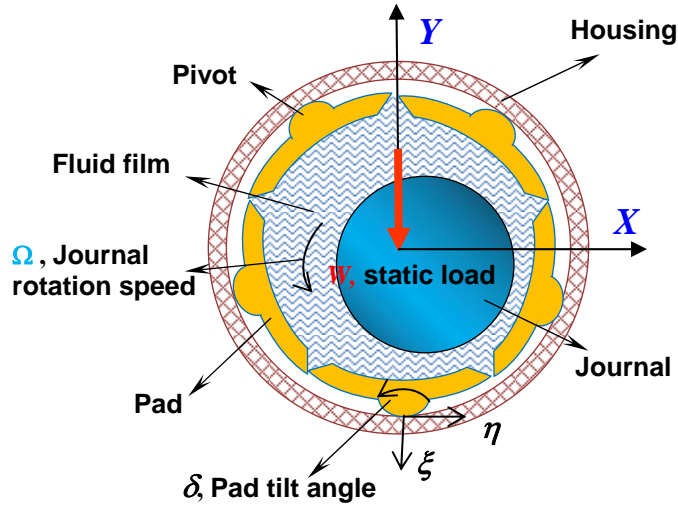
Fig. 1 Schematic view of an ideal five-pad tilting pad bearing.

Lund [3] introduces the "Pad Assembly Method" for predicting TPJB stiffness and damping force coefficients. This method, widely adopted by many researchers, has been improved and extended to model more general TPJBs. Later, Lund [4] develops an elasto-hydrodynamic analysis of a bearing to deliver more accurate predictions of TPJB performance. He demonstrates that pad flexibility and pivot flexibility have a significant effect on the TPJB forced performance. References [5-8] show that pivot flexibility and pad compliance dramatically reduce the TPJB stiffness and damping force coefficients. Also, thermal effects [9], turbulent flow effects [10], and fluid inertia effects [2] are included in analyses to improve the accuracy of TPJB computational models.

Recently, the authors of references [7, 11] repeatedly emphasize that pivot flexibility has a great effect on TPJB force coefficients. This effect is not well accounted for in many analyses [12-14] which typically over-predict TPJB force coefficients. Wilkes [7] claims that pad flexibility and the effect of temperature on bearing clearance also influence significantly the magnitude of TPJB force coefficients.

TASKS

The present work aims to deliver an efficient TPJB predictive model, which considers pivot flexibility and thermal fluid flow energy transport effects, for the accurate prediction of TPJB static and dynamic forced performance. To this end, the tasks to be completed are:

(1) Extend an existing Fortran code coupled to an EXCEL interface to accurately predict the static and dynamic force performance of TPJBs with different types of pivot-housing contact structures, e.g. rocker-back pivot, ball-in-socket pivot and flexure pivot.

(2) Considering fluid flow thermal energy transport effect, obtain the zero-order hydrodynamic pressure field of the fluid film flow governed by the modified Reynolds equation and calculate the static fluid film reaction forces. Develop an advanced and efficient algorithm to find the equilibrium journal displacement, pad tilt angle, pivot radial and transverse displacements using a Newton-Raphson iterative procedure and accounting for pivot flexibility.

(3) Solve the first-order Reynolds equation for the perturbed hydrodynamic pressure fields to obtain the bearing impedance force coefficients. Employ a frequency-reduced (synchronous or non-synchronous frequency) model to obtain the reduced TPJB stiffness and damping force coefficients.

(4) Compare the predictions obtained from the novel model with published experiment data and published predicted results.

LITERATURE REVIEW

Pivot flexibility is known to affect the static performance parameters (journal eccentricity, load capacity, power loss, etc.) and the force coefficients of TPJBs. The literature on the topic is not scant; see Refs. [4-7] for relevant papers that shaped the following review. However, not until recently the issue of pivot flexibility has become important again; in particular for highly loaded TPJBs operating at relatively high speeds, as per the experimental data advanced in Refs. [12-14] where predictions from conventional models, i.e., those that consider a pad pivot as rigid, deliver very poor damping and stiffness force coefficients when compared to the experimental results. Recently, Wilkes [7] also emphasizes the importance to account for pad flexibility to ensure accurate predictions, as was also demonstrated in earlier work conducted by Lund [4] and Kim et al. [15].

In general, the more flexible the pad pivot is, the smaller are the bearing stiffness and damping force since the pivot stiffness acts in series with the fluid film stiffness (and damping). However, such generalization needs caution re-assessment under heavy load operation which also produces an increase in pivot stiffness. That is, the elastic deformation from a pivot is typically nonlinear depending on the load, area of contact, hardness of the materials, and surface conditions.

The load applied on the TPJB causes the journal center in a bearing to displace radially on the X-Y plane. As shown in Fig.1, a pad in a TPJB tilts about its pivot; and if the pivot is flexible, the pad also displaces along the radial (ξ) and transverse (η) directions. Hence, each pad has three degrees of freedom (DOF) and a TPJB with N_{pad} pads has a total of ($3 \times N_{pad}+2$) degrees of freedom.

Lund [4] assumes the pads move at the same frequency as the journal does, say (ω), and produces a most elegant analysis that reduces the full stiffness and damping matrices, ($3N_{pad}+2$)$\times$ ($3N_{pad}+2$) elements, into (2×2) stiffness and damping matrices, both known as frequency reduced force coefficients. Instead of employing TPJB

stiffness and damping coefficients including all DOFs, most rotor-bearing analyses are conducted with a set of four stiffness and four damping coefficients, $(K,C)_{i,j=X,Y}$, both frequency reduced, representing changes in bearing reaction forces due to lateral displacements of the journal center, Δe_X and Δe_Y. Incidentally, when $\omega=\Omega$, i.e., the excitation frequency coincides with the rotor angular speed, the analysis delivers what are known as synchronous frequency (or synchronous speed) force coefficients.

Chen [6] delivers a theoretical analysis for prediction of the dynamic force coefficients of a five pad, LBP TPJB. The rotor diameter (D) is 20.8mm (slenderness ratio $L/D=1$) and the pads dimensionless preload equals to 0.25. Chen accounts for pivot radial stiffness and includes the pad mass and pad mass moment of inertia in the calculation of the reduced impedances matrix for a flexural beam type supported pad. The bearing journal spins at a high speed of 76,500 rpm and supports a unit load (W/LD) equal to 2,057 kPa. Accounting for pivot flexibility, damping coefficients, reduced with a synchronous frequency, decrease by ~8% and the synchronous reduced stiffness coefficients decrease by about ~3% compared against the results for a bearing with rigid pivots. Chen also shows that the stiffness of the elastic support web, if too large, can make unstable a flexure pivot type TPJB.

Kirk and Reedy [16], based on (dry on dry) Hertzian contact stress theory, present the equations for derivation of the structural stiffness in several pivot types. The pivot stiffness is a function of applied load, material type, and contact area and shape as in line contact, sphere into a sphere, and sphere into a cylinder. The authors calculate synchronous reduced TPJBs force coefficients for increasing pivot flexibilities and compare them against those force coefficients assuming a rigid pivot (infinite stiffness). Results show that pivot flexibility can reduce the bearing damping by a considerable amount, 72% for a line contact pivot with small radius, for example.

Dmochowski [11] investigates experimentally and theoretically the frequency dependency of the dynamic force coefficients in two five-pad TPJBs, both with the same pivot stiffnesses determined by a pivot load-deflection function given in Ref. [11]. The

two tilting pad bearings have the same preload (0.3) and with diameters equaling to 99mm and 100mm. The slenderness ratios (*L/D*) are 0.4 and 1 for each bearing, and static unit loads applied on the bearings (W/LD) are 1,031 kPa and 445 kPa, respectively. The load is applied in between pads for the short bearing (*L/D* = 0.4), while the long bearing (*L/D* = 1) has a load-on-pad configuration. The excitation frequency ranges from 0 Hz to 300 Hz with the maximum excitation frequency at twice the operating rotating speed (9,000 rpm=150 Hz). The model, which accounts for pivot flexibility and fluid thermal energy transport, gives good predictions for the bearing stiffness and damping force coefficients. Results show that pivot flexibility significantly affects the long bearing, yet it has a negligible effect on the short bearing. For the short bearing with a unit load (W/LD) of 1,031 kPa, the damping coefficients are independent on the excitation frequency and the stiffness coefficients slightly decrease with the excitation frequency. For the long bearing with a unit load of 445 kPa, stiffness and damping coefficients show a pronounced dependency on the excitation frequency, especially for the damping force coefficients. The damping coefficients decrease with excitation frequency while the stiffness increases with excitation frequency. The reason causing the frequency dependency of the force coefficients in the long TPJB is that due to being lightly loaded thus operating at a small eccentricity so that every pad is loaded and a pivot softens when the load on a pad decreases. The corresponding soft pivot influences the frequency dependency of the TPJB stiffness and damping force coefficients.

Childs and his students [12,13] detail a test rig for identification of hydrodynamic bearing force coefficients and report frequency reduced experimental force coefficients for various types of TPJBs. The authors call for the need to account for pivot stiffness in a predictive model [13] to improve the agreement between experimental and theoretical results. Carter and Childs [12] carry out tests on a five-pad rocker-pivot TPJB with both load-between-pad and load-on-pad configurations. The rotor diameter (*D*) is 101.587mm and the bearing length (*L*) is 60.325m with a nominal radial clearance of 79.2 μm. The authors use the bulk flow model of San Andrés [17], to predict bearing force coefficients

for comparison with the experimental results. The static load is along $-Y$ direction, as in Fig. 1. The stiffness and damping coefficients are synchronous-frequency reduced. The direct stiffness K_{YY} is well predicted at low unit loads ($W/LD<1,000$kPa) but over predicted at higher loads. The other direct stiffness coefficient K_{XX} is well predicted at all loads for tests conducted at rotor speeds of 4,000 rpm and 7,000 rpm cases, and modestly over predicted at higher rotor speeds. The direct damping coefficients (C_{XX} and C_{YY}) show independence of the excitation of frequency. Reasonable predictions of the direct damping coefficients are obtained at the unit load of 345 kPa, but greatly over predicted with increasing loads, especially for the coefficients along the load direction (C_{YY}). One of the reasons causing the over prediction is that the numerical model used in the prediction does not consider pad pivot flexibility.

Childs and Harris [13] obtain experimentally the static performance characteristics and dynamic force coefficients of a four-pad ball-in-socket TPJB. The bearing has a nominal radial clearance of 95.3 μm, axial length $L=101.60$ mm, and $L/D=1$. Note that novel lubrication structures, e.g. spray bar blocker and by-pass lubricant cooling, are features of the test bearing to decrease the oil operating temperature and pad surface temperature. The unit load (W/LD) on the bearing varies from 0 kPa to 1,896 kPa upon the rotor operation speed from 4,000 rpm to 12,000 rpm. The authors use the analysis in Ref. [17] and obtain poor predictions for the bearing force coefficients. Recall that the computational model does not include the effect of pivot flexibility. The bearing stiffness coefficients are significantly over-predicted by the model. At a speed of 12,000 rpm and with a unit load of 1,896 kPa, the predicted stiffness coefficients are about twice the test stiffness coefficients. At the same operating condition, the bearing damping coefficients are over-predicted by 400%. Childs and Harris [13] show that a simple stiffness-in-series correction significantly improves the agreement of predictions against test data. The average difference between the prediction and measurements in direct stiffness coefficients reduces to 2%, however damping coefficients are still over predicted by a factor of 2 and more at low rotor speeds. A pivot radial stiffness (K_p=350 MN/m) obtained from measurements is used in the correction scheme. Note that the

method used in Ref. [13] to measure pad pivot structural stiffness is not accurate; since as demonstrated in Ref. [7], the measured stiffness is smaller than the actual pivot structural stiffness.

Wilkes [7] investigates the effects of several important factors, e.g. pivot flexibility, pad flexibility and reduced hot bearing clearance (experimental), in the predictions on TPJB static and dynamic forced performance. He crafts a model for evaluation (theoretical and experimental) of the transfer functions between rotor motions and pads displacements (radial, transverse and rotational) and applies the model to dynamic load measurements conducted on a LOP, five-pad rocker-pivot TPJB. Wilkes is the first to measure pad translational and pad rotational motions for correlation with rotor displacements. The test bearing length (L) is 55.88mm, rotor diameter (D) is 101.587mm, and with a cold bearing radial clearance of 120.65 μm. The rotor speed ranges from 4,400 rpm to 10,100 rpm, and the static unit load (W/LD) on the bearing is as high as 3,134 kPa. Wilkes measures the bearing radial clearance at different pad temperature for ready use in his predictive model. He notes that the bearing radial clearance significantly decreases as the TPJB operating temperature increases.

When Wilkes' rotor operates at a high speed of 10,200 rpm, the frequency reduction model delivers good predictions when compared to test data; in particular for the damping coefficients at the unit loads of 783 kPa and 3,134 kPa. The stiffness coefficients along the load direction (K_{YY}) are over-predicted by 10%. At a low operating speed of 4,400 rpm, the predictions deviate in accuracy moderately. At a unit load (W/LD) of 783kPa, damping coefficients (C_{XX} and C_{YY}) are over-predicted by 15% and 18%, respectively. The damping coefficients along the load direction (C_{YY}), however, are under-predicted by 14% with a unit load (W/LD) of 3,134 kPa. Wilkes [7] also emphasizes the need to account for pad flexibility as well as pivot flexibility in the prediction model to deliver sound predictions of the measured TPJBs rotor-pad transfer functions and dynamic force coefficients. Note that a good agreement between predictions and test results relies on the a-priori knowledge of certain parameters (pivot

structural stiffness, bearing radial clearance and pad temperatures) that are not readily available to most bearing designers.

Advances in TPJB technology aim to increase bearing load capacity with reduced power losses while keeping the lubricant relatively cool and maintaining the bearing unique dynamic stability characteristics. Novel lubrication methods such as leading edge groove (LEG) injection and spray blockers that directly feed fresh oil into the film land and block upstream hot fluid have become industry standards [13,18,19].

Figure 2 shows schematic views of a leading edge groove (LEG) oil feed arrangement machined at the leading edge of a pad where cold oil is supplied. This structure efficiently reduces the mixing of the cold oil with the hot oil carried over from the upstream pad, consequently decreasing the oil inlet, lubricant film and pad operating temperatures.

Figure 3 shows a schematic view of spray bar blocker, another design innovation applied to TPJBs, that prevents excessive hot oil carry over from the upstream pad [19]. The spray-bar blocker consists of the blocker segment and fluid ejecting conduit, blocking hot oil carried over from the upstream and ejecting fresh oil directly on to the surface of downstream pad. Note that Fig.2 and Fig.3 exaggerate the fluid film thickness between the pads and journal.

(a)Top view

(b) Cross section view
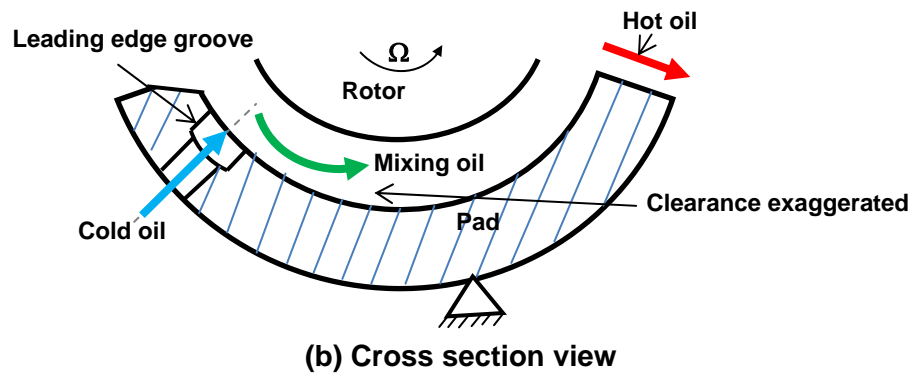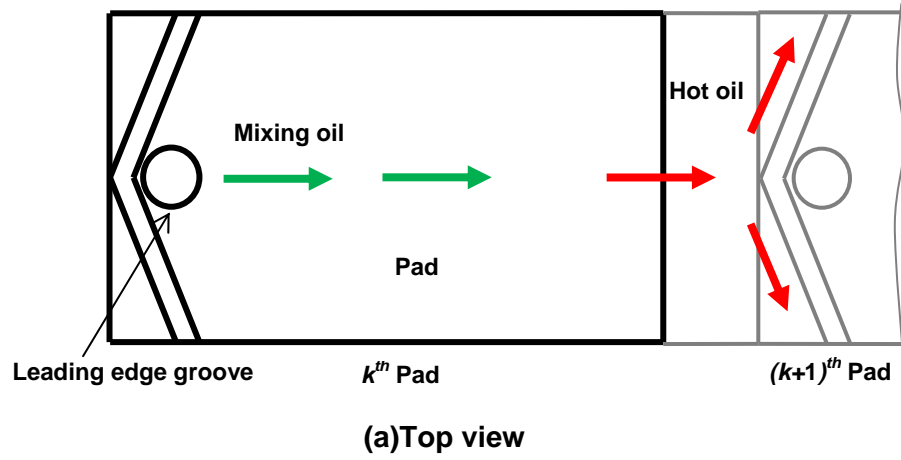
Fig. 2 Schematic views of a leading edge groove oil feed arrangement in a tilting pad.
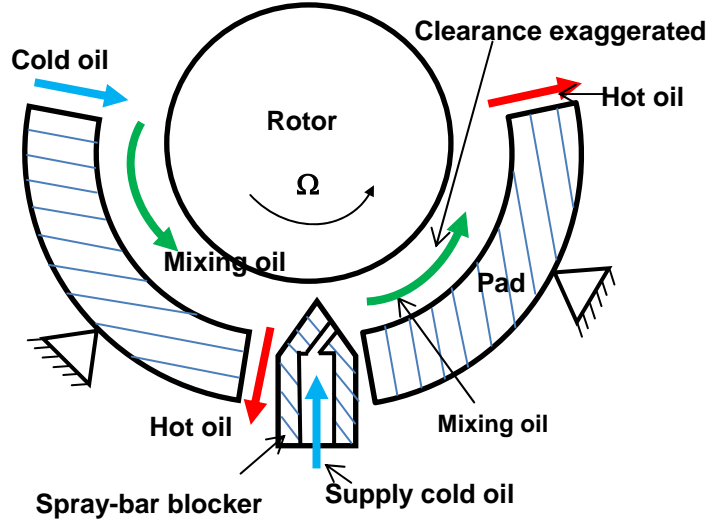
Fig. 3 Schematic view of an oil spray-bar blocker arrangement in a TPJB.

Dmochoswski et al. [20] examine experimentally and analytically the thermal characteristics of a TPJB operating with and without a leading edge groove oil feed arrangement. The test five-pad TPJB has a slenderness ratio L/D=0.387, a bearing radial clearance (C_b) of 0.076mm, and a dimensionless pad preload (r_P) equal to 0.25. The authors employ a thermohydrodynamic model to predict pad temperatures for TPJBs with LEG feeding and operating under LOP or LBP configurations. The unit load (W/LD) applied on the TPJB is 3,013 kPa. For the TPJB in a LBP configuration, the maximum pad temperatures do not change much with rotor speeds below 5,000 rpm. When the rotor operates at a speed of 16,500 rpm, a TPJB with LEG feeding has a maximum pad temperature of 103 ^{o}C, 16.3% lower than a TPJB without a LEG feeding.

As the literature reveals; pivot flexibility and pad flexibility, viscosity variation in the fluid film field, frequency excitation types (synchronous/ non-synchronous speeds) and bearing clearance appear as significant factors in the numerical analysis of TPJBs and the prediction of bearing forced performance, static and dynamic.

11

TILTING PAD JOURNAL BEARING MODEL

Figure 4 shows an ideal TPJB model with its main components and the coordinate systems for analysis. Only one pad is shown in Fig. 4 and the superscript k denoting a kth pad parameter is omitted for simplicity. Figure 4 grossly exaggerates the film thickness *(h)* filling the gap between the bearing pad and the rotating journal. The (X,Y) inertial (fixed) coordinate system has its origin at the bearing center (O_B) and serves to note the static and dynamic displacements of the journal center, $e_{X(t)}$ and $e_{Y(t)}$, rotating with angular speed (Ω). The bearing has radius R_B and the journal has radius R_J, its difference defines the bearing clearance $C_B=R_B-R_J$. The circumferential coordinate (θ) has its origin along the $-X$ axis. A bearing pad of arc length Θ_P has thickness t and inner radius R_P with origin at O_P. The distance (O_P-O_B) is known as the pad preload r_p. The pad machined clearance is known as $C_P=R_P-R_J$; and hence $r_p=C_P-C_B$. The pad pivot is located at angle θ_p, while θ_L and θ_T denote a pad leading edge and trailing edge, respectively. The ratio $(\theta_p - \theta_L)/(\theta_T - \theta_L)$ is known at the pad offset ratio. Inertial coordinate systems (ξ,η) are affixed to the pad at the pivot point P (undeformed condition) to define the pivot translational deflections (ξ_{piv}, η_{piv}) and pad rotation or tilt (δ_p) about the pivot P. The figure also displays the components (W_X, W_Y) of the external load acting on the bearing.
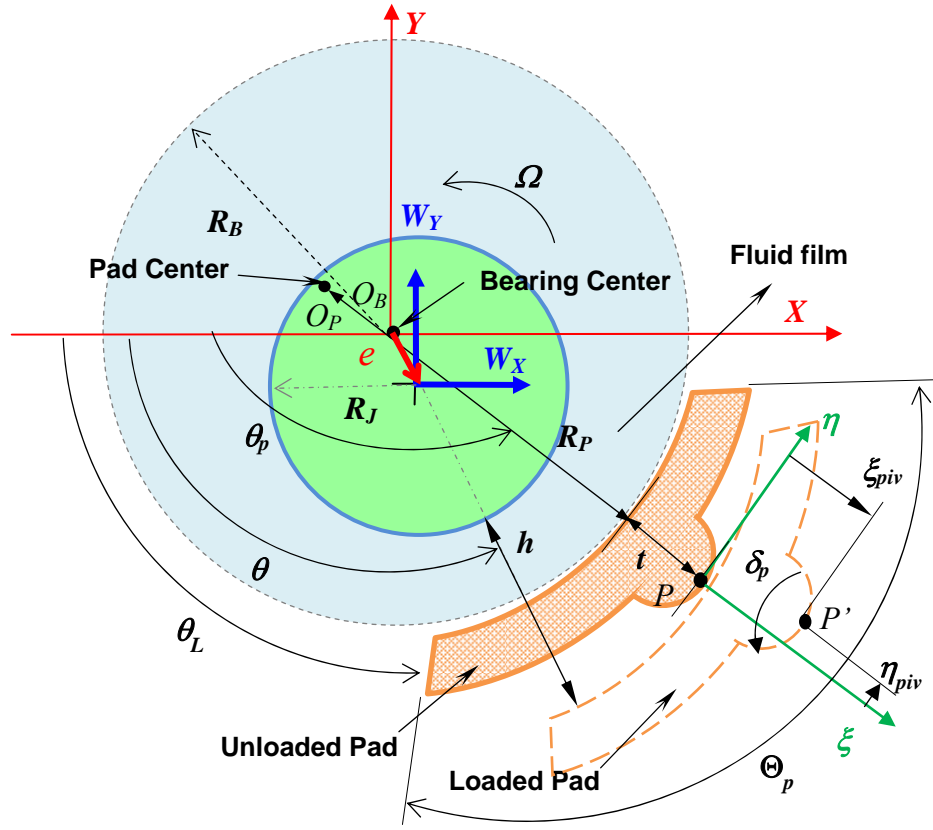
Fig. 4 Schematic view of a tilting pad and journal, coordinate system and nomenclature.

A TPJB with N_{pad} pads has a total of $(3N_{pad}+2)$ DOF since each pad-pivot has three DOF, $(\xi_{piv}, \eta_{piv}, \delta_p)^k$, $k=1\ldots N_{pad}$, and the journal has two DOF (e_X, e_Y). Note that pad pitching motions, i.e., rotations about the Z axis are not accounted for.

On the k- pad, the film thickness h^k at angle θ is [4],

$$h^k = C_P + e_X \cos\theta + e_Y \sin\theta + \left(\xi_{piv}^k - r_P\right)\cos\left(\theta - \theta_p^k\right) + \left(\eta_{piv}^k - R_d\delta_p^k\right)\sin\left(\theta - \theta_p^k\right) \qquad (1)$$

13

Note that r_p is the pad dimensional preload for the k-pad with $r_P = C_P - C_B$, and C_P and C_B are known as the pad machined radial clearance and bearing assembly clearance, respectively. Above $R_d = R_P + t$ is the sum of pad radius and pad thickness at the pivot position. With respect to the pad coordinates $(\xi, \eta)^k$, the film thickness is written as

$$h^k = C_P + \left\{\xi^k_{piv} - r_P - e^k_\xi\right\}\cos\left(\theta - \theta^k_p\right) + \left\{\eta^k_{piv} - R_d\delta^k_p - e^k_\eta\right\}\sin\left(\theta - \theta^k_p\right), \ k = 1,...,N_{pad} \tag{2}$$

with $\begin{bmatrix} e^k_\xi \\ e^k_\eta \end{bmatrix} = \mathbf{A}^{(k)} \begin{bmatrix} e_X \\ e_Y \end{bmatrix}$. The transformation matrix $\mathbf{A}^{(k)}$ converts the components of a vector in the inertial coordinates system (X,Y) to the pad inertial coordinates $(\xi,\eta)^k$,

$$\mathbf{A}^{(k)} = \begin{bmatrix} \cos(\varphi^k) & \sin(\varphi^k) \\ -\sin(\varphi^k) & \cos(\varphi^k) \end{bmatrix}, \ k = 1,...,N_{pad} \tag{3}$$

Above φ^k is the angle between the coordinates $(\xi,\eta)^k$ and coordinates (X,Y), i.e., $\varphi^k = \pi + \theta^k_p$, see Fig.4. Note that the fluid film thickness can also be written as,

$$h^k = C_P + \bar{\xi}^k \cos\left(\theta - \theta^k_p\right) + \bar{\eta}^k \sin\left(\theta - \theta^k_p\right), \ k = 1,...N_{pad} \tag{4}$$

Here, $\bar{\xi}^k$ and $\bar{\eta}^k$ are the displacements between the kth pad and rotor expressed in pad coordinates $(\xi,\eta)^k$, i.e.,

$$\bar{\xi}^k = \xi^k_{piv} - r_P - e^k_\xi, \ \bar{\eta}^k = \eta^k_{piv} - R_d\delta^k_p - e^k_\eta \tag{5}$$

Reynolds equation governs the generation of hydrodynamic pressure (P^k) in the laminar flow region with film thickness h^k, i.e.,

$$\frac{1}{R_J^2}\frac{\partial}{\partial\theta}\left\{\frac{(h^k)^3}{12\mu_{(T)}}\frac{\partial P^k}{\partial\theta}\right\} + \frac{\partial}{\partial z}\left\{\frac{(h^k)^3}{12\mu_{(T)}}\frac{\partial P^k}{\partial z}\right\} = \frac{\partial h^k}{\partial t} + \frac{\Omega}{2}\frac{\partial h^k}{\partial\theta} + \frac{\rho(h^k)^2}{12\mu_{(T)}}\frac{\partial^2 h^k}{\partial t^2}, \ k = 1,...N_{pad} \tag{6}$$

Above (z,θ) correspond to the axial and circumferential coordinates on the plane of the bearing, and $(\rho, \mu_{(T)})$ are the density and viscosity of the lubricant, respectively. Equation (6) includes temporal fluid inertia effects [21].

14

The boundary conditions for the hydrodynamic pressure are

(a) uniform supply pressure (P_s) at the pad leading edge, $P(z, \theta_l^k) = P_s$

(b) ambient pressure (P_a) at both the trailing edge of a pad and its axial ends,

$$P(z, \theta_t^k) = P_a, \; P(z = \pm\tfrac{1}{2}L, \theta^k) = P_a$$

In the analysis, the lubricant viscosity ($\mu_{(T)}$) is a function of the bulk-temperature (T) in the film and determined from solution of the thermal energy transport equations with appropriate boundary conditions. Considering the liquid in the fluid land is incompressible, the bulk flow energy transport equation is [21],

$$C_v \left[\frac{\partial}{R_J \partial\theta}\left(\rho h^k U^k T^k\right) + \frac{\partial}{\partial z}\left(\rho h^k V^k T^k\right) \right] + Q_s = S = \frac{12\mu_{(T)}}{h^k}\left((V^k)^2 + \frac{\Omega^2 R_J^2}{12} + \left[U^k - \frac{\Omega R_J}{2} \right]^2 \right) \quad (7)$$

here $k = 1, \ldots N_{pad}$. $Q_s = \overline{h}_B(T - T_B) + \overline{h}_J(T - T_J)$ is the heat flow into the journal and bearing surfaces. T is the bulk temperature representing an average across the film thickness. V^k and U^k are the axial and circumferential mean flow velocities in the kth pad expressed by,

$$V^k = -\frac{\left(h^k\right)^2}{12\mu_{(T)}}\frac{\partial P^k}{\partial z}; \; U^k = -\frac{\left(h^k\right)^2}{12\mu_{(T)}}\frac{\partial P^k}{R_J\partial\theta} + \frac{\Omega R_J}{2}, \; k = 1, \ldots N_{pad} \quad (8)$$

Lubricant is supplied into the bearing at a known supply temperature (T_s) and mixes with the hot lubricant leaving the upstream pad with temperature T_h. The temperature of the mixing oil at the leading edge of each pad is T_{in}. The above lubricant temperatures satisfy the flow and thermal energy mixing conditions [21],

$$F_{in} = F_s + \lambda F_h \quad (9)$$
$$F_{in}T_{in} = F_s T_s + \lambda F_h T_h \quad (10)$$

Above F_s, F_h and F_{in} are the supply cold oil volumetric flowrate, hot oil flowrate, and flowrate of the mixing oil flowing into the pad, respectively. The lubricant thermal mixing coefficient (λ) is an empirical parameter, depending on the lubrication feed arrangement. $\lambda \sim 0.6$–0.9 for conventional lubricant feed arrangements with deep grooves and wide holes [21].

15

In the computational procedure, implementation of a finite element method solves Reynolds equation for the zero and first order hydrodynamic pressure fields while a control volume method is employed to obtain the temperature field from the energy transport equation [21]. A new developed algorithm employing the Newton-Raphson method to obtain the equilibrium position of the journal and pads in a TPJB model is discussed in the following sections.

STATICS AND DYNAMICS IN A TILTING PAD JOURNAL BEARING

At a static load operating condition, the journal rotates at constant speed (Ω) and an applied constant load $\mathbf{W} = \left(W_{X_0}, W_{Y_0} \right)^T$ acts on the journal[1]. The static load determines the equilibrium position of the journal center $\mathbf{e_0} = \left(e_{X_0}, e_{Y_0} \right)^T$, or $\left(e_{\xi_0}^k, e_{\eta_0}^k \right)^T$ as seen from each kth pad. The kth pad also reaches its equilibrium position with a pad rotation angle $\left(\delta_{P_0}^k \right)$ and pivot displacements $\left(\xi_{piv_0}^k, \eta_{piv_0}^k \right)$. On the kth pad, the film thickness $\left(h_0^k \right)$ generates a static hydrodynamic pressure field $\left(P_0^k \right)$. This pressure fields satisfies the boundary conditions and the steady state form of the Reynolds equation, i.e.,

$$\frac{1}{R_J^2} \frac{\partial}{\partial \theta} \left\{ \frac{\left(h_0^k \right)^3}{12 \mu_{(T)}} \frac{\partial P_0^k}{\partial \theta} \right\} + \frac{\partial}{\partial z} \left\{ \frac{\left(h_0^k \right)^3}{12 \mu_{(T)}} \frac{\partial P_0^k}{\partial z} \right\} = \frac{\Omega}{2} \frac{\partial \left(h_0^k \right)}{\partial \theta} , \quad k = 1, \ldots N_{pad} \tag{11}$$

Note that the film pressures integrated over the journal surface generate a reaction force vector ($\mathbf{F_0}$) that balances the applied load, $\mathbf{F_0} + \mathbf{W_0} = \mathbf{0}$,

$$-\begin{bmatrix} W_{X_0} \\ W_{Y_0} \end{bmatrix} = \begin{bmatrix} F_{X_0} \\ F_{Y_0} \end{bmatrix} = \sum_{k=1}^{N_{pad}} \begin{bmatrix} F_{X_0}^k \\ F_{Y_0}^k \end{bmatrix}; \quad \begin{bmatrix} F_{X_0}^k \\ F_{Y_0}^k \end{bmatrix} = \int_{-L/2}^{L/2} \int_{\theta_l^k}^{\theta_t^k} P_0^k \begin{Bmatrix} \cos\left(\theta_p^k \right) \\ \sin\left(\theta_p^k \right) \end{Bmatrix} R_J \, d\theta dz , \quad k = 1, \ldots N_{pad} \tag{12}$$

At static equilibrium, the moment $\left(M_0^k \right)$ induced by the film on a pad must be either zero (null) for an ideal[2] TPJB or equal to the reaction moment from a flexural web type support, for example. In addition, the pivot must react to the fluid film induced force and moment on the pad; hence

---

[1] Note that this load must also be transmitted to the bearing casing through the pad pivots.
[2] In practice, the pad-pivot surface condition may cause a frictional moment that needs to be properly modeled.

$$
\begin{bmatrix} M^k_{piv_0} \\ F^k_{\xi_{piv0}} \\ F^k_{\eta_{piv0}} \end{bmatrix} + \begin{bmatrix} M^k_0 \\ F^k_{\xi_0} \\ F^k_{\eta_0} \end{bmatrix} = \begin{Bmatrix} 0 \\ 0 \\ 0 \end{Bmatrix}, \quad k = 1, ..., N_{pad} \tag{13}
$$

While keeping the rotor speed (Ω) constant, consider that external dynamic forces ($\Delta \mathbf{F}_{(t)}$) with excitation frequency (ω) act on the journal. The applied loads cause the journal center to displace with small amplitude ($\Delta \mathbf{e}$) and frequency (ω) about the equilibrium position ($\mathbf{e_0}$), i.e., $\mathbf{e}_{(t)} = \mathbf{e}_0 + \Delta \mathbf{e} e^{i\omega t}$. The perturbed journal motion induces changes in the pads' fluid film forces and moment as well as the pad pivot displacements, which move with the same frequency (ω), i.e.,

$$
\begin{Bmatrix} \xi^k_{piv} \\ \eta^k_{piv} \\ \delta^k_p \end{Bmatrix} = \begin{Bmatrix} \xi^k_{piv_0} \\ \eta^k_{piv_0} \\ \delta^k_{p_0} \end{Bmatrix} + \begin{Bmatrix} \Delta \xi^k_{piv} \\ \Delta \eta^k_{piv} \\ \Delta \delta^k_p \end{Bmatrix} e^{i\omega t}, \quad k = 1, ..., N_{pad} \tag{14}
$$

The journal and pad motions also produce changes in the film thickness and pressure fields, hereby written as

$$
h^k_{(t)} = h^k_0 + \left\{ h^k_X \Delta e_X + h^k_Y \Delta e_Y + h^k_\delta \Delta \delta^k_p + h^k_\xi \Delta \xi^k_{piv} + h^k_\eta \Delta \eta^k_{piv} \right\} e^{i\omega t}, \quad k = 1, ..., N_{pad} \tag{15}
$$

$$
P^k_{(t)} = P^k_0 + \left\{ P^k_X \Delta e_X + P^k_Y \Delta e_Y + P^k_\delta \Delta \delta^k_p + P^k_\xi \Delta \xi^k_{piv} + P^k_\eta \Delta \eta^k_{piv} \right\} e^{i\omega t}, \quad k = 1, ..., N_{pad} \tag{16}
$$

with $k=1,2,...,N_{pad}$. Above the first order pressure fields due to the pad tilt angle, pivot radial and transverse displacements are [22],

$$
\begin{aligned}
P^k_\xi &= P^k_X \cos\theta^k_P + P^k_Y \sin\theta^k_P \\
P^k_\eta &= -P^k_X \sin\theta^k_P + P^k_Y \cos\theta^k_P \qquad , \quad k = 1, ..., N_{pad} \\
P^k_\delta &= R_J (P^k_X \sin\theta^k_P - P^k_Y \cos\theta^k_P)
\end{aligned} \tag{17}
$$

Figure 5 depicts the fluid film forces (F^k_X, F^k_Y) acting on the journal and pad as well as the pad moment (M^k) and rotation, and the pivot displacements. The pivot displacements ($\xi^k_{piv}, \eta^k_{piv}$) and tilt angle ($\delta^k_p$) are marked in Fig. 5 with the pivot point

18

moving away from P to P' after being loaded. The dashed outline indicates the undeformed position of the pad. The origin of the inertial coordinates $(\xi,\eta)^k$ locates on the undeformed position of the pivot P.
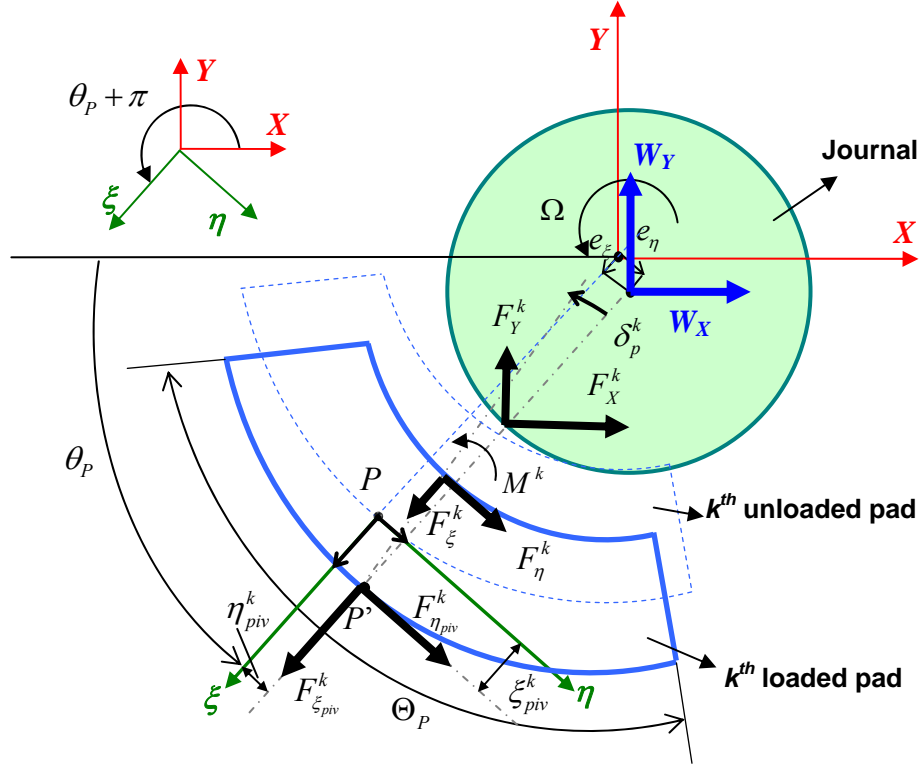
Fig. 5 Free body diagram of kth pad and journal in a tilting pad journal bearing.

The journal's equation of motion is,

$$m_J \begin{bmatrix} \ddot{e}_X \\ \ddot{e}_Y \end{bmatrix} = \begin{bmatrix} F_X \\ F_Y \end{bmatrix} + \begin{bmatrix} W_X \\ W_Y \end{bmatrix} \tag{18}$$

with $\begin{bmatrix} F_X \\ F_Y \end{bmatrix} = \sum_{k=1}^{N_{pad}} \begin{bmatrix} F_X^k \\ F_Y^k \end{bmatrix}$ and m_J as the journal mass.

The fluid film reaction forces acting on the journal consist of static and dynamic parts. For each pad,

$$
\begin{bmatrix} F_X^k \\ F_Y^k \end{bmatrix} = \begin{bmatrix} F_{X_0}^k \\ F_{Y_0}^k \end{bmatrix} - \begin{bmatrix} Z_{XX}^k & Z_{XY}^k & Z_{X\xi}^k & Z_{X\eta}^k & Z_{X\delta}^k \\ Z_{YX}^k & Z_{YY}^k & Z_{Y\xi}^k & Z_{Y\eta}^k & Z_{Y\delta}^k \end{bmatrix} \begin{bmatrix} \Delta e_X \\ \Delta e_Y \\ \Delta \xi_{piv}^k \\ \Delta \eta_{piv}^k \\ \Delta \delta_p^k \end{bmatrix} e^{i\omega t}
\tag{19}
$$

Here $(Z_{X\alpha}^k, Z_{Y\alpha}^k, \alpha = X, Y, \xi, \eta, \delta)$ are the kth pad fluid film impedance coefficients denoting the changes in the lateral fluid film reaction forces due to changes in journal displacements $(\Delta e_X, \Delta e_Y)$, and the kth pad translational displacements $(\Delta \xi_{piv}^k, \Delta \eta_{piv}^k)$ and the tilt angle $(\Delta \delta_p^k)$.

The fluid film forces (F_ξ^k, F_η^k) acting on the kth pad are also decomposed as[3],

$$
\begin{bmatrix} F_\xi^k \\ F_\eta^k \end{bmatrix} = \begin{bmatrix} F_{\xi_0}^k \\ F_{\eta_0}^k \end{bmatrix} - \begin{bmatrix} Z_{\xi\xi}^k & Z_{\xi\eta}^k \\ Z_{\eta\xi}^k & Z_{\eta\eta}^k \end{bmatrix} \begin{bmatrix} \Delta \overline{\xi}^k \\ \Delta \overline{\eta}^k \end{bmatrix} e^{i\omega t}
\tag{20}
$$

with

$$
\Delta \overline{\xi}^k = \Delta \xi_{piv}^k - \Delta e_\xi, \; \Delta \overline{\eta}^k = \Delta \eta_{piv}^k - R_d \Delta \delta_p^k - \Delta e_\eta
$$

The fluid film moment on the kth pad is $M^k = -R_d F_\eta^k$ [2]. Substitution of Eq. (20) into the moment equation renders,

$$
M^k = -R_d F_{\eta_0}^k - (-R_d Z_{\eta\xi}^k \Delta \overline{\xi}^k - R_d Z_{\eta\eta}^k \Delta \overline{\eta}^k) e^{i\omega t}
\tag{21}
$$

Note that the fluid film impedances coefficients $(Z_{\alpha\beta}^k, \alpha, \beta = \xi, \eta)$ in the pad inertial coordinates $(\xi, \eta)^k$ are changes in the kth pad fluid film forces due to the displacements $(\Delta \overline{\xi}^k, \Delta \overline{\eta}^k)$ between the rotor and k^{th} pad.

---

[3] For convenience, the pad local coordinates $(\xi, \eta)^k$ are used to define these forces, and $\begin{bmatrix} F_X^k \\ F_Y^k \end{bmatrix} = (\mathbf{A}^k)^{\mathrm{T}} \begin{bmatrix} F_\xi^k \\ F_\eta^k \end{bmatrix}$.

Consider the pad as a rigid body[4], i.e., without structure flexibility. For general pivot types, the kth pad equations of motion are,

$$\tilde{\mathbf{M}}^k \begin{bmatrix} \ddot{\delta}_p^k \\ \ddot{\xi}_{piv}^k \\ \ddot{\eta}_{piv}^k \end{bmatrix} = \begin{bmatrix} M^k \\ F_\xi^k \\ F_\eta^k \end{bmatrix} + \begin{bmatrix} M_{piv}^k \\ F_{\xi_{piv}}^k \\ F_{\eta_{piv}}^k \end{bmatrix}, \quad k = 1,..N_{pad} \tag{22}$$

here $\tilde{\mathbf{M}}^k = \begin{bmatrix} I_p^k & m^k l_\eta^k & -m^k l_\xi^k \\ m^k l_\eta^k & m^k & 0 \\ -m^k l_\xi^k & 0 & m^k \end{bmatrix}$ is the kth pad generalized inertia matrix [2]. m^k and

I_p^k are the kth pad mass and pad moment of inertia about the pivot; and l_ξ^k and l_η^k are the radial and transverse components of the displacement vector from pivot P to the pad mass center.

The pivot reaction forces and moment on the kth pad are,

$$\begin{bmatrix} M_{piv}^k \\ F_{\xi_{piv}}^k \\ F_{\eta_{piv}}^k \end{bmatrix} = \begin{bmatrix} M_{piv_0}^k \\ F_{\xi_{piv_0}}^k \\ F_{\eta_{piv_0}}^k \end{bmatrix} - \begin{bmatrix} Z_{s\delta\delta}^k & Z_{s\delta\xi}^k & Z_{s\delta\eta}^k \\ Z_{s\xi\delta}^k & Z_{s\xi\xi}^k & Z_{s\xi\eta}^k \\ Z_{s\eta\delta}^k & Z_{s\eta\xi}^k & Z_{s\eta\eta}^k \end{bmatrix} \begin{bmatrix} \Delta\delta_p^k \\ \Delta\xi_{piv}^k \\ \Delta\eta_{piv}^k \end{bmatrix} e^{i\omega t} \tag{23}$$

Above $\tilde{\mathbf{Z}}_s^k = \begin{bmatrix} Z_{s\delta\delta}^k & Z_{s\delta\xi}^k & Z_{s\delta\eta}^k \\ Z_{s\xi\delta}^k & Z_{s\xi\xi}^k & Z_{s\xi\eta}^k \\ Z_{s\eta\delta}^k & Z_{s\eta\xi}^k & Z_{s\eta\eta}^k \end{bmatrix}$ is the kth pad structural impedance matrix, determined

by the geometry and materials of the pad pivot contact structure which are known a-priori. The kth pad structural stiffness and damping coefficients make the real and imaginary parts of the pad structural impedance, i.e., $Z_{s\alpha\beta}^k = K_{s\alpha\beta}^k + i\omega C_{s\alpha\beta}^k$, $\alpha,\beta=X,Y$.

Equations (18, 20) show that there are 5 equations of motion for the kth pad and the journal, including 25 impedance coefficients ($Z_{\alpha\beta}^k$, $\alpha,\beta=X,Y,\xi,\eta,\delta$).

---

[4] In practice, pad flexibility is also important in the analysis of heavily loaded TPJBs [7].

REDUCED FORCE IMPEDANCE COEFFICIENTS

Since the TPJB has a total of $(3N_{pad}+2)$ DOFs, there are $(3N_{pad}+2)^2$ impedance coefficients. The 25 impedances of the kth pad due to the journal center displacements (e_X, e_Y), pivot displacements $(\xi_{piv}^k, \eta_{piv}^k)$ and pad rotation (δ_p^k) are calculated from integration of the first order pressure fields,

$$Z_{\alpha\beta}^k = \int_{-L/2}^{L/2} \int_{\theta_l^k}^{\theta_t^k} P_\beta^k h_\alpha^k R_J d\theta^k dz, \quad \alpha, \beta = X, Y, \xi, \eta, \delta \tag{24}$$

where $\begin{bmatrix} h_X^k \\ h_Y^k \end{bmatrix} = \begin{bmatrix} \cos\theta \\ \sin\theta \end{bmatrix}, \begin{bmatrix} h_\xi^k \\ h_\eta^k \end{bmatrix} = \begin{bmatrix} \cos(\theta-\theta_p) \\ \sin(\theta-\theta_p) \end{bmatrix}, h_\delta^k = -R_d h_\eta^k$.

The 25 impedance coefficients reduce to 4 frequency reduced impedance $(Z_{XX}^k, Z_{XY}^k, Z_{YX}^k, Z_{YY}^k)$, representing changes in bearing reaction forces (F_X, F_Y) due to journal center translational displacements (e_X, e_Y). The real parts and imaginary parts of these 4 reduced impedance coefficients correspond to the stiffness and damping coefficients for the kth pad, i.e., $Z_{\alpha\beta}^k = K_{\alpha\beta}^k + i\omega C_{\alpha\beta}^k$, $\alpha, \beta = X, Y$.

Substitution of Eq. (13), (14), (20), (21) and (23) into Eq. (22) gives,

$$\left(\tilde{\mathbf{Z}}_s^k - \omega^2 \tilde{\mathbf{M}}^k + \tilde{\mathbf{Z}}_P^k\right)\tilde{\mathbf{d}}_P^k = \tilde{\mathbf{Z}}_{PJ}^k \tilde{\mathbf{d}}_J^k \tag{25}$$

where $\tilde{\mathbf{Z}}_P^k = \begin{bmatrix} Z_{\eta\eta}^k R_d^2 & -Z_{\eta\xi}^k R_d & -Z_{\eta\eta}^k R_d \\ -Z_{\xi\eta}^k R_d & Z_{\xi\xi}^k & Z_{\xi\eta}^k \\ -Z_{\eta\eta}^k R_d & Z_{\eta\xi}^k & Z_{\eta\eta}^k \end{bmatrix}, \tilde{\mathbf{Z}}_{PJ}^k = \begin{bmatrix} -Z_{\eta\xi}^k R_d & -Z_{\eta\eta}^k R_d \\ Z_{\xi\xi}^k & Z_{\xi\eta}^k \\ Z_{\eta\xi}^k & Z_{\eta\eta}^k \end{bmatrix}$.

$\tilde{\mathbf{d}}_J^k = \begin{bmatrix} \Delta e_\xi \\ \Delta e_\eta \end{bmatrix}$ and $\tilde{\mathbf{d}}_P^k = \begin{bmatrix} \Delta \delta_p^k \\ \Delta \xi_{piv}^k \\ \Delta \eta_{piv}^k \end{bmatrix}$ correspond to the displacement vectors of the journal and

pad pivot. From Eq. (25), the displacement vector of the pad pivot is,

$$\tilde{\mathbf{d}}_P^k = \left[\tilde{\mathbf{Z}}_s^k - \omega^2 \tilde{\mathbf{M}}^k + \tilde{\mathbf{Z}}_P^k \right]^{-1} \tilde{\mathbf{Z}}_{PJ}^k \tilde{\mathbf{d}}_J^k \tag{26}$$

Next, substitute Eq.(26) into Eq.(20) to obtain,

$$\tilde{\mathbf{F}}^k = \left(\tilde{\mathbf{Z}}^k - \tilde{\mathbf{Z}}_{JP}^k \left[\tilde{\mathbf{Z}}_s^k - \omega^2 \tilde{\mathbf{M}}^k + \tilde{\mathbf{Z}}_P^k \right]^{-1} \tilde{\mathbf{Z}}_{PJ}^k \right) \tilde{\mathbf{d}}_J^k \tag{27}$$

with $\tilde{\mathbf{Z}}^k = \begin{bmatrix} Z_{\xi\xi}^k & Z_{\xi\eta}^k \\ Z_{\eta\xi}^k & Z_{\eta\eta}^k \end{bmatrix}$, $\tilde{\mathbf{Z}}_{JP}^k = \begin{bmatrix} -Z_{\xi\eta}^k R_d & Z_{\xi\xi}^k & Z_{\xi\eta}^k \\ -Z_{\eta\eta}^k R_d & Z_{\eta\xi}^k & Z_{\eta\eta}^k \end{bmatrix}$.

Hence, the reduced impedance coefficients are,

$$\tilde{\mathbf{Z}}_R^k = \tilde{\mathbf{Z}}^k - \tilde{\mathbf{Z}}_{JP}^k \left[\tilde{\mathbf{Z}}_s^k - \omega^2 \tilde{\mathbf{M}}^k + \tilde{\mathbf{Z}}_P^k \right]^{-1} \tilde{\mathbf{Z}}_{PJ}^k \tag{28}$$

Note that, this reduce impedance coefficient matrix refers to the inertial coordinates $(\xi, \eta)^k$. Recall that $\mathbf{A}^{(k)}$ is a coordinate transformation matrix. Thus, the reduced impedance matrix for the kth pad in the inertial coordinates (X, Y) follows the transformation,

$$\mathbf{Z}_R^k = \left[\mathbf{A}^k \right]^{\mathrm{T}} \tilde{\mathbf{Z}}_R^k \mathbf{A}^k \tag{29}$$

AN ALGORITHM TO FIND THE EQUILIBRIUM POSITION OF THE PADS AND JOURNAL

Ref. [2] details an algorithm to find the equilibrium position of the pads and journal in a TPJB. In the procedure, the fluid film forces and moment balance of each pad are simultaneously satisfied by devising a Newton-Raphson iterative procedure. Iterations on the kth pad tilt angle ($\delta_{p_0}^k$), pivot radial and transverse displacements ($\xi_{piv_0}^k, \eta_{piv_0}^k$) are carried out to balance the kth pad fluid film forces and moment, as shown in Eq.(13), with an invariant journal static position (e_{X_0}, e_{Y_0}). Next, a second Newton-Raphson method is employed to obtain the journal equilibrium position (e_{X_0}, e_{Y_0}) to balance the static load on the journal, i.e., **F$_0$+W$_0$=0**.

However, for a TPJB with soft pivots, the Netwon-Raphson procedure has difficulties in convergence when iterating simultaneously on the pad tilt angle, the radial and transverse displacements, as well as the journal center displacements. Frequently, when a pivot is very soft, a too large pad updated radial displacement and tilt angle cause the failure in convergence during an iteration.

Hence, a novel algorithm employing the Newton-Raphson iterative procedure is introduced to correct this shortcoming. Figure 6 shows the flow chart to find the pad and journal equilibrium position for a TPJB with pivot flexibility.

$k=1, 2,\ldots,N_{pad}$

$\delta_{p_0}^k$

Consider TPJB with rigid pivots

Step A

e_{X_0} e_{Y_0}

$k=1, 2,\ldots,N_{pad}$

$\xi_{piv_0}^k$

Step B

Step C

$k=1, 2,\ldots,N_{pad}$

$\xi_{piv_0}^k$ $\eta_{piv_0}^k$

Tilt angle ($\delta_{p_0}^k$) remains invariant

$k=1, 2,\ldots,N_{pad}$

$\delta_{p_0}^k$

Pad radial and transverse displacements ($\xi_{piv_0}^k,\eta_{piv_0}^k$) remain invariant

e_{X_0} e_{Y_0}

Step D

$k=1, 2,\ldots,N_{pad}$

$\delta_{p_0}^k$ $\xi_{piv_0}^k$ $\eta_{piv_0}^k$

End of procedure
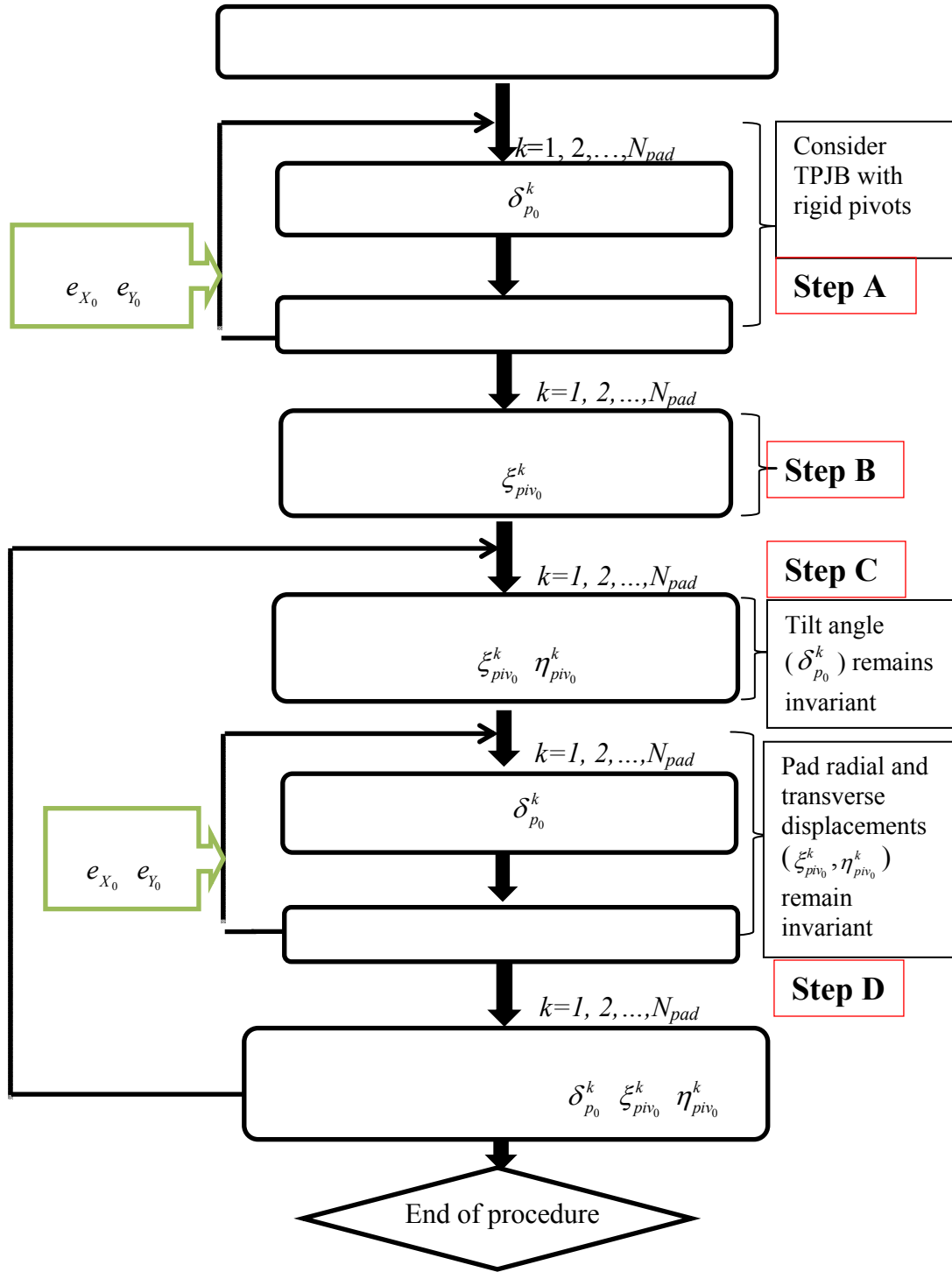
Fig. 6 Flow chart of an algorithm to find the equilibrium position of the pads and journal in a TPJB.

This algorithm always leads to convergence in the Newton-Raphson iterative procedure, even for a TPJB with very soft pivots. The flow chart in Fig.6 consists of four steps (**A-D**), executed in the following sequence,

Step A assumes a TPJB with rigid pivots and determines the kth pad static tilt angle $(\delta_{p_0}^k)$ and static journal center displacement (e_{X_0}, e_{Y_0}) by using a Newton-Raphson iterative procedure. The kth pad tilt angle is incremented during the iteration to balance the moment on the kth pad, $M_{p_0}^k + M_0^k \rightarrow 0$. An estimation of the equilibrium tilt angle $(\delta_{p_0}^k)$ at the $(n+1)^{th}$ iteration is,

$$\left[\delta_{p_0}^k\right]_{n+1} = \left[\delta_{p_0}^k\right]_n + \left[M_{p_0}^k + M_0^k\right]_n / (K_{\delta\delta}^k + K_{s_{\delta\delta}}^k) \tag{30}$$

Here, $K_{\delta\delta}^k$ and $K_{s_{\delta\delta}}^k$ are the fluid film rotational stiffness and pad pivot structural rotational stiffness, respectively.

Next, using a similar Newton-Raphson procedure to balance the static load on the journal, i.e., $\mathbf{F_0} + \mathbf{W_0} \rightarrow \mathbf{0}$, the updated journal center displacements are,

$$\mathbf{e}_{n+1} = \mathbf{e}_n + \mathbf{K}_R^{-1} \left[\mathbf{F_0} + \mathbf{W_0}\right]_n \tag{31}$$

Above $\mathbf{K}_R$ is the reduced fluid film static stiffness matrix evaluated at zero frequency.

Step B accounts for pad pivot flexibility and estimates the radial displacement $(\xi_{piv_0}^k)$ for the kth pad and adjusts the journal center displacements (e_{X_0}, e_{X_0}). In general, the pivot radial displacement $(\xi_{piv_0}^k)$ is a nonlinear function of the static load acting on the kth pad $(F_{piv_0}^k)$, i.e.,

$$\xi_{piv_0}^k = f(F_{piv_0}^k) \tag{32}$$

Different pad pivot contact structures yield different functional forces in Eq.(32), and which are determined by the geometry and material of the pad pivot contact structure. **Appendix A** presents pivot deflection-load functions (*f*) for three typical types of pad

26

pivot contact structures. The estimation of the journal displacements (e_{X_0}, e_{X_0}) depends on the estimated pad radial displacement ($\xi_{piv_0}^k$) and the load configuration (LOP or LBP).

Step C determines the radial and transverse displacements ($\xi_{piv_0}^k$, $\eta_{piv_0}^k$) for the kth pad by iterating the displacements ($\bar{\xi}_0^k$, $\bar{\eta}_0^k$) between the rotor and k^{th} pad; recall from Eq.(5) that $\bar{\xi}_0^k = \xi_{piv_0}^k - e_{\xi_0} - r_P^k$, $\bar{\eta}_0^k = \eta_{piv_0}^k - R_d \delta_{p_0}^k - e_{\eta_0}$. In this iteration procedure, the pad tilt angle ($\delta_{p_0}^k$) and journal center displacements (e_{X_0}, e_{X_0}) remain invariant. The displacements ($\bar{\xi}_0^k$, $\bar{\eta}_0^k$) are iterated until the force balance equation for each pad is satisfied, $\mathbf{F}_0 + \mathbf{F}_{piv_0} \to \mathbf{0}$,

$$\begin{bmatrix} \bar{\xi}_0^k \\ \bar{\eta}_0^k \end{bmatrix}_{n+1} = \begin{bmatrix} \bar{\xi}_0^k \\ \bar{\eta}_0^k \end{bmatrix}_n + \begin{bmatrix} K_{\xi\xi}^k & K_{\xi\eta}^k \\ K_{\eta\xi}^k & K_{\eta\eta}^k \end{bmatrix}^{-1} \begin{bmatrix} F_{\xi_0}^k + F_{\xi_{piv0}}^k \\ F_{\eta_0}^k + F_{\eta_{piv0}}^k \end{bmatrix}_n \tag{33}$$

Here, ($K_{\alpha\beta}^k$, $\alpha,\beta=X,Y$) is the kth pad static fluid film stiffness in the coordinates $(\xi,\eta)^k$ evaluated at zero frequency.

Note that the success of the iterations on the displacements ($\bar{\xi}_0^k$, $\bar{\eta}_0^k$) between the rotor and k^{th} pad can be attributed to the reasonably estimated journal center displacements (e_{X_0}, e_{X_0}), pad tilt angle ($\delta_{p_0}^k$) and pivot radial displacement ($\xi_{E_{piv_0}}^k$) obtained from **Step B**.

Step D determines the kth pad equilibrium pad tilt angle ($\delta_{p_0}^k$) and journal center displacements (e_{X_0}, e_{X_0}) by using a similar Newton-Raphson iterative procedure in Step A, as shown in Eqs. (30,31). In **Step D**, the kth pad radial and transverse displacements ($\xi_{piv_0}^k$, $\eta_{piv_0}^k$) remain constant.

The procedure to find the equilibrium positions of the journal and pads is completed when all the iterations in step **C** and **D** converge to satisfy the balance equations for the pad and journal.

27

Implementation of a leading-edge-groove (LEG) oil feed arrangement in a TPJB is nowadays a desirable practice. The LEG feature reduces the operating lubricant temperature and the drag loss in a TPJB [20]. This novel lubrication structure is included in the TPJB model. Figure 7 shows schematic views of tilting pads with and without a LEG oil feed arrangement.

(a) Tilting pad without a leading-edge-groove feed   (b) Tilting pad with a leading-edge-groove feed
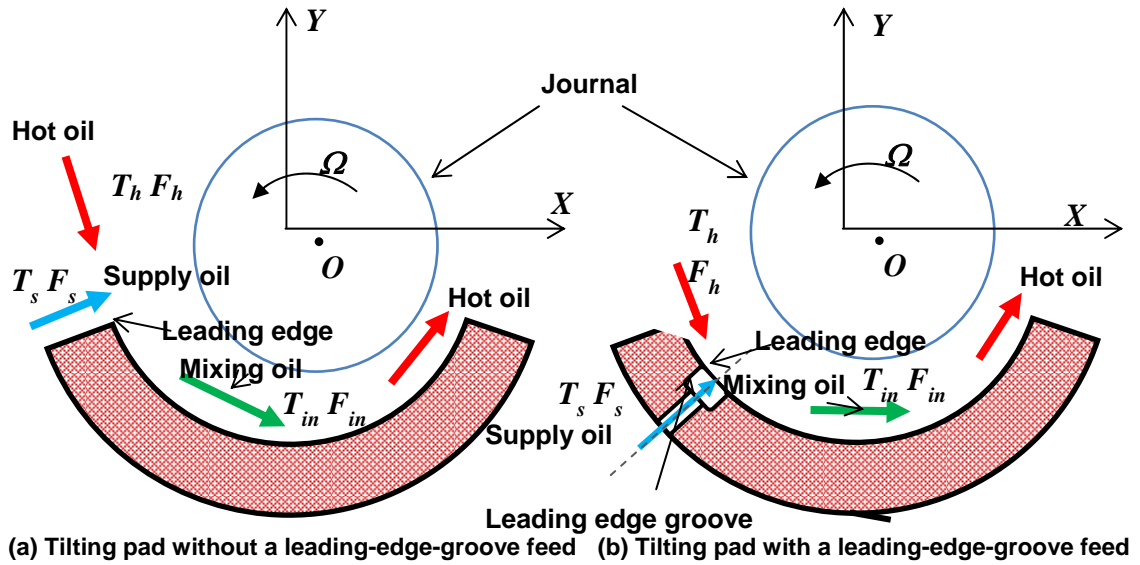
Fig. 7 Schematic views of tilting pads with and without a leading-edge-groove feed arrangement.

Note that for a tilting pad with a leading-edge-groove feed, the oil is supplied at the leading edge of the pad, as seen in Fig.7(b), differing from that of a tilting pad with no LEG feeding arrangements, as shown in Fig.7(a). The oil flowrates and the corresponding temperatures satisfy the flow and thermal energy mixing conditions in Eq.(9) and (10). Note that the TPJB with a novel lubrication method such as the leading

edge groove usually has a lower thermal mixing coefficient, e.g. $\lambda\sim0.5$ [13], than the conventional lubrication arrangements.

COMPARISON OF PREDICTIONS WITH PUBLISHED RESULTS

A modified Fortran code named "TPJB" to model TPJBs with the effect of pad pivot flexibility delivers predictions for comparison against measured TPJB characteristics reported in the open literature, Refs. [7,13,23,24,25]. The predicted TPJBs forced performance characteristics include the static journal eccentricity, film mean temperature and drag power loss, and dynamic force coefficients, e.g. stiffness, damping, and virtual mass coefficients. After assessing the agreement between predictions and test data, recommendations provide a better understanding of the TPJB behavior and aid to further improve TPJB modeling.

Childs and his students [7,13,23] have conducted plentiful experiments with various TPJBs and under various operating conditions. A previous computational model, which considers a pad pivot as rigid, overpredicts the stiffness and damping coefficients of the test TPJBs, as shown in Refs. [13,23]. The model hereby introduced delivers improved predictions of the static and dynamic forced performance for various tested TPJBs.

The results section discusses the predicted performances of various test TPJBs given in Refs. [7,13,23,24,25]. Table 1 lists the major differences between the test TPJBs, including the bearing geometry and operating condition. Note Delgado et.al conduct tests for different bearings on the same test rig, [24,25].

Table 1 Important parameters of various test TPJBs in the published literature.

No.	Pad number	Load configuration[*]	Pivot type	Lubrication method	Authors, reference
1	4	LBP	Ball-in-socket	Spray-bar blockers, by-pass cooling	Childs and Harris [13]
2	5	LOP	Rocker-back	N/A	Wilkes [7]
3	5	LBP	Rocker-back	Leading edge groove	Kulhanek and Childs [23]
4	4 & 5	LOP & LBP	Rocker-back	Direct lubrication	Delgado et. al [24]
5	5	LOP	Rocker-back	Direct lubrication	Delgado et. al [25]

[*]LBP: Load between pad, LOP: Load on pad

Example 1-Predicted Forced Performance for a Ball-in-Socket LBP TPJB [13]

Childs and Harris [13] measure the static and dynamic forced performance a four-pad TPJB with ball-in-socket pivots. This section compares the predicted and experimental static and dynamic forced performance parameters of the test bearing in Ref. [13] and investigates the effect of pivot flexibility on bearing behavior. Table 2 shows the nominal geometry of the test TPJB, the lubricant type and feed method[5]. Figure 8 shows a picture of a test TPJB in Ref. [13,14].

Table 2 Parameters of the test ball-in-socket TPJB in Ref. [13,14].

Number of pads, N_{pad}	4
Configuration	LBP
Rotor diameter, D	101.6 mm
Pad axial length, L	101.6 mm
Pad arc angle, Θ_P	73°
Pivot offset	65%
Dimensionless preload of loaded pads, $\overline{r}_P$	Pad#1, #2 : 0.37[6]
Dimensionless preload of unloaded pads, $\overline{r}_P$	Pad#3, #4 : 0.58
Nominal bearing clearance, C_B	95.3 μm
Measured bearing clearance, C_B	54.6 μm, 99.6 μm
Pad clearance[7], C_P	Pad#1: 86.7μm, Pad#2: 158.1μm Pad#3: 130μm, Pad#4: 237.1μm
Pad mass, m_P	1.2 kg
Pad moment of inertia, I_P	7.91×10^{-4} kg.m^2
Pivot type	Ball-in-Socket
Pivot material	Ball: Steel, Socket: Bronze
Measured pivot radial stiffness, K_{piv}	350 MN/m

---

[5] The published bearing geometry data in Ref. [13] is not enough to conduct meaningful and accurate predictions.
[6] Reference [14] reports a different pad preload for the loaded and unloaded pads.
[7] Pad clearances are obtained from the cold measured bearing clearance and pad preloads, i.e. $C_P=C_B/(1-\overline{r}_P)$.

Table 2 Continued

Estimated pivot radial stiffness, $\bar{K}_{piv}$	443 MN/m (6 krpm), 548 MN/m (10 krpm)
Oil inlet temperature	~40 $^\text{o}$C
Lubricant type	ISO VG32, DTE 797
Lubrication method	Spray bar blocker, by pass cooling
Lubricant density	856.2 kg/m^3
Oil supply viscosity at 40 $^\text{o}$C, μ_0	0.0275 Pa.s
Oil viscosity at 60 $^\text{o}$C, 67 $^\text{o}$C	0.0151 Pa.s, 0.0125 Pa.s
Temperature viscosity coefficient, α	0.029 1/K
Specific load, W/LD	0 kPa-1,896 kPa
Journal speed, Ω	4,000 rpm-12,000 rpm

Predicted results for the test TPJB operating at rotor speeds equaling 6 krpm and 10 krpm are compared with the measured data in Ref. [13], which incidentally does not report the pad mass. Presently, the pad mass is set at 1.2 kg, following prior experience.

Childs and Harris [13] report maximum pad subsurface temperatures equal to ~60 $^\text{o}$C for operation at 6 krpm and 67 $^\text{o}$C at 10 krpm for tests with the largest static specific load equaling 1,896 kPa (W=19.6kN). The VG32 oil viscosity at 60 $^\text{o}$C and 67 $^\text{o}$C is 0.0151 Pa.s and 0.0125 Pa.s, respectively. Hence, the maximum shear flow Reynolds number (Re=$\rho\Omega RC_B/\mu$) at rotor speeds of 6 krpm and 10 krpm are 172 and 347, respectively. As the shear flow Reynolds numbers are much smaller than 1,000, the thin film flow is laminar.

The predictive model assumes that the lubricant carries away all the heat generated in the bearing, i.e., an adiabatic flow process. Note that the test TPJB uses a spray-bar blocker and by-pass cooling arrangements to lower the overall oil operating temperature. Hence, the lubricant thermal mixing coefficient (λ) for this test TPJB is smaller than the typical value (λ~0.6–0.9 [21]) of a conventional lubricated TPJB. Presently λ=0.5 is

selected due to the effect of the spray-bar blocker arrangement which reduces the amount of hot oil mixing with the supply cold oil. The adequacy of this selection will be discussed later.

Spray Bar Blocker
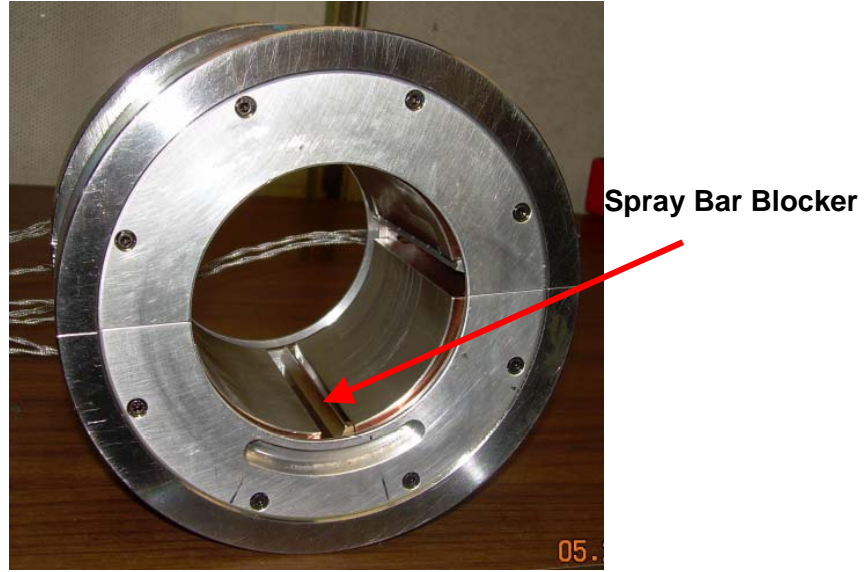
Fig. 8 Photograph of a four-pad TPJB in Ref. [13].

Figure 9 shows the load configuration and angular position of each pad in the test TPJB. Note that Harris measured unequal bearing clearances, pad preloads and pad radial clearances for each pad, as noted in Ref. [14]. The model used in Refs. [13,14] only accepts equal bearing clearances and pad preloads for the bearing. Hence, Childs and Harris [13] used an average bearing radial clearance (C_B=77.1 μm).

In Ref. [14], the effective pad preloads are calculated with the formula,

$$\bar{r}_P = \frac{1}{2}\left[\left(1+\frac{e_Y}{C_{y'}}\right)\bar{r}_{P,\text{bottom}} + \left(1-\frac{e_Y}{C_{y'}}\right)\bar{r}_{P,\text{upper}}\right] \tag{34}$$

Here $C_{y'}$ is the bearing clearance about the y' axis, as shown in Fig.9. $\bar{r}_{P,\text{bottom}} = 0.37$ and $\bar{r}_{P,\text{upper}} = 0.58$ are the preloads of the bottom and upper pads, respectively. According to

Eq. (34), the effective pad preload varies from 0.38 to 0.46 based on different measured journal eccentricities (e_Y) corresponding to various operating conditions.

The current model allows for different bearing clearances, pad preloads and pad radial clearances. Note that the measured bearing radial clearance along the x' axis is 29% smaller than the average bearing radial clearance (C_B=77.1 μm), while the measured bearing radial clearance along the y' axis is 29% larger than the average bearing radial clearance.
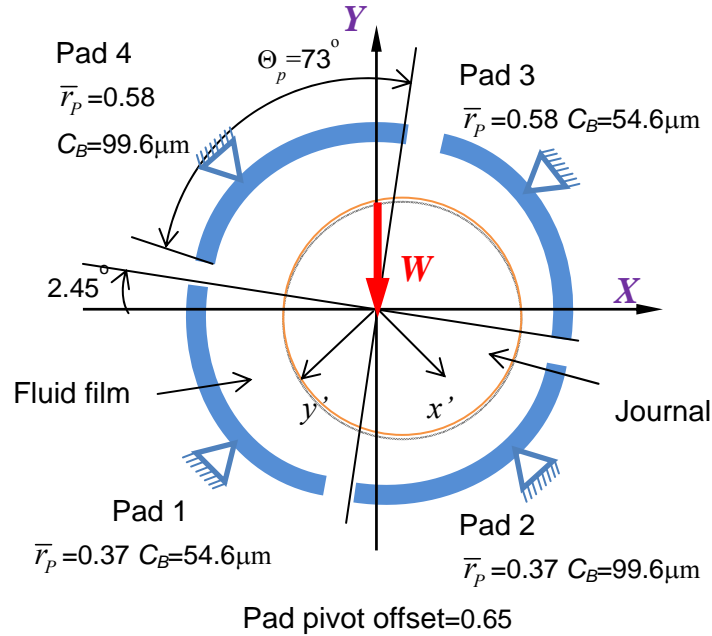
Fig. 9 Load configuration and pad arrangements of a test four-pad tilting pad journal bearing in Ref. [13]. Nominal bearing clearance C_B=95.3 μm, nominal pad preload $\bar{r}_P$ =0.37 (loaded pads) and 0.58 (unloaded pads).

Pivot flexibility Childs and Harris [13] used a measured "pad-support structure stiffness", K_{piv}=350 MN/m, to calculate the bearing equivalent stiffness and damping coefficients. Wilkes [7] demonstrates that the method used in Ref. [13] to measure the

pivot stiffness will produce in actuality a support structure stiffness which is softer than the actual pivot stiffness[8]

The current model employs a modified constant pivot radial stiffness. The pivot stiffnesses of the bearing (K_{pX}, K_{pY}) along the X and Y direction are estimated using the formulas,

$$\frac{1}{K_{pX}} = \frac{1}{K_{mX}} - \frac{1}{K_{rX}} \quad , \quad \frac{1}{K_{pY}} = \frac{1}{K_{mY}} - \frac{1}{K_{rY}} \tag{35}$$

here (K_{pX}, K_{pY}) are the estimated pivot stiffnesses, (K_{mX}, K_{mY}) are the experimental bearing static stiffness coefficient, and (K_{rX}, K_{rY}) are the predicted bearing stiffness coefficients (rigid pivot). Thus, (K_{rX}, K_{rY}) are the fluid film stiffness only. Note the predicted stiffness coefficients of the test bearing with a LBP configuration along X and Y direction are identical, while the test data show orthotropic stiffness coefficient ($K_{rX} \neq K_{rY}$) for the bearing, in particular at heavy loads. Table 3 lists the estimated pivot stiffness (K_{pX}, K_{pY}), the measured static stiffness coefficient (K_{mX}, K_{mY}) for the bearing, and the predicted film stiffness coefficient (K_{rX}, K_{rY}) versus specific load. Note that the pivot stiffness varies with not only the rotor speed but also the specific load. For the test bearing in Ref. [14], the bearing stiffness and damping coefficients do not change a lot with the static load, in particular at a high speed of 10 rpm. Thus, the predictive model employs a constant pivot stiffness for operations at all static loads.

---

[8] Reference [7] does not provide the actual measured pivot stiffness for the loaded pad of the test bearing in Ref. [13].

Table 3 Fluid film stiffness, measured TPJB stiffness and estimated pivot stiffness, [14]

Rotor speed (Ω)	Specific load (kPa)	Predicted bearing stiffness (rigid pivot) K_r (MN/m)		Measured bearing static stiffness K_m (MN/m) [14]		Estimated pivot stiffness K_p (MN/m)	
		K_{rX}	K_{rY}	K_{mX}	K_{mY}	K_{pX}	K_{pY}
6,000	0	1,140	1,140	309	260	423	337
	687	1,170	1,170	309	287	419	379
	1,376	1,250	1,250	340	315	467	420
	1,905	1,350	1,350	382	398	532	565
	Average estimated pivot stiffness for Pad#2					K_{piv}=443 MN/m	
		K_{rX}	K_{rY}	K_{mX}	K_{mY}	K_{pX}	K_{pY}
10,000	0	1,350	1,350	416	342	602	459
	687	1,380	1,380	383	329	530	432
	1,376	1,450	1,450	399	351	550	462
	1,905	1,540	1,540	436	394	608	529
	Average estimated pivot stiffness for Pad#2					K_{piv}=548 MN/m	

For simplicity, the pivot stiffness is obtained by averaging the estimated pivot stiffnesses along *X* and *Y* direction for operations at all static loads (0-1,905 kPa) and the pivot stiffnesses of each pad are equal. The pivot stiffnesses for operation at 6 krpm and 10 krpm are 443 MN/m and 548 MN/m, which are 27% and 57% larger than the experimental "pad-support structure stiffness" (350 MN/m) in Ref. [13], respectively.

Journal displacement and attitude angle Figure 10 depicts the comparison between the measured and predicted journal center displacements (e_X, e_Y) versus increasing specific load (*W/LD*) at two rotor speeds, 6 krpm and 10 krpm. The journal center displacements are under predicted by a maximum of 30%, which may be attributed to the over prediction of the pivot stiffness. At a low rotor speed of 6,000 rpm, the journal displacement (e_Y) along the loaded (*Y*) direction exceeds measured bearing clearance (C_B=54.6 μm) for the loaded pad#1 when the specific load equals to 1,905 kPa, denoting large radial deflections of the pivot. Both the predictions and measurements show that the journal displacements increase nearly linearly with the static load applied on the bearing. Thus, the TPJB static fluid film stiffnesses do not vary

much the static load. Note that both the predictions and measurements show sizeable journal displacements along the unloaded direction (-*X*), thus indicating that cross-coupling stiffness coefficients may be significant.

(a) rotor speed Ω=6,000 rpm
Pivot stiffness K_{piv}=443 MN/m

(b) rotor speed Ω=10,000 rpm
Pivot stiffness K_{piv}=548 MN/m
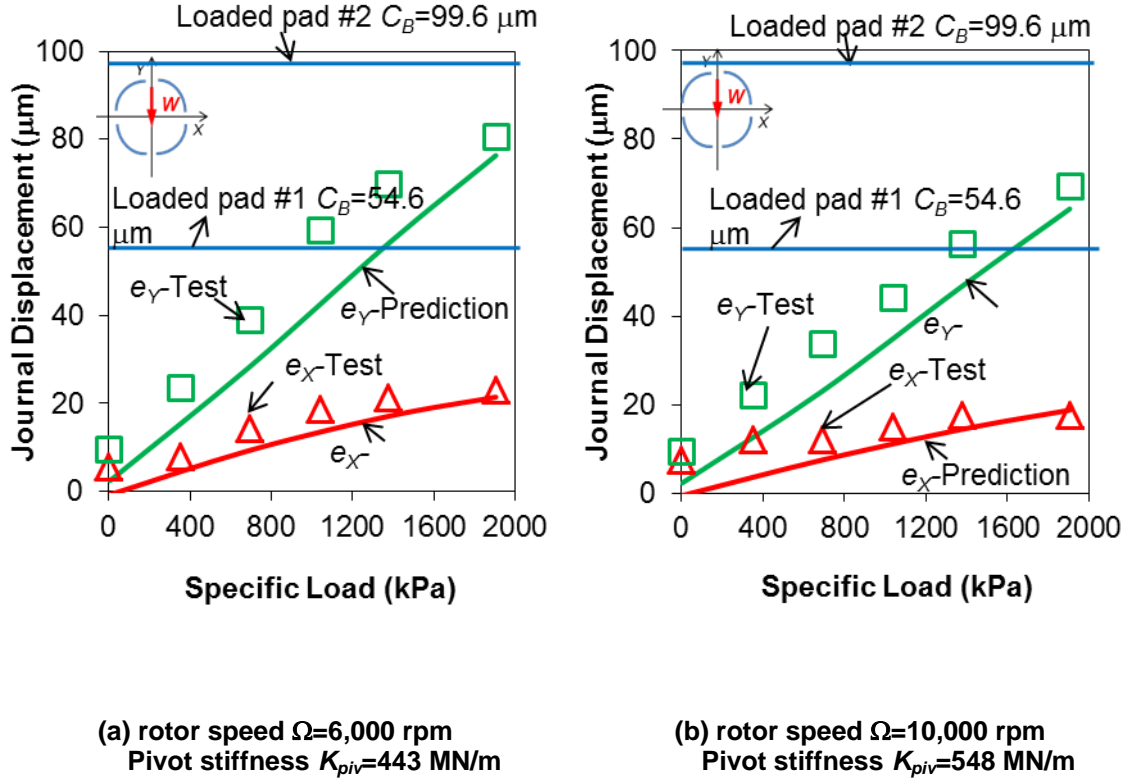
Fig. 10 Journal displacement (e_X, e_Y) versus specific load (*W/LD*). Predictions and measurements in Ref. [13] for two rotor speeds.

Figure 11 shows the journal attitude angle (ϕ) versus increasing operating specific load (*W/LD*). The journal attitude angle (ϕ) for the test bearing with the load applied in –*Y* direction is,

$$\tan(\phi) = \frac{e_X}{e_Y} \tag{36}$$

The predicted attitude angle (ϕ) is in a good agreement with measurements at the large specific load (*W/LD*) of 1,904 kPa. At specific loads (*W/LD*) from 686 kPa to 1,904 kPa, the predicted journal attitude angle correlates well with the measurement. Note that the measured attitude angle of the journal at small specific loads (*W/LD* ≤ 345 kPa) is about

64% larger than the predicted value at a large specific load. The measured e_X, e_Y are very small at the small load condition, and hence the attitude angle shows a large deviation. However, it is not clear why the measured data shows such large attitude angle at low loads.
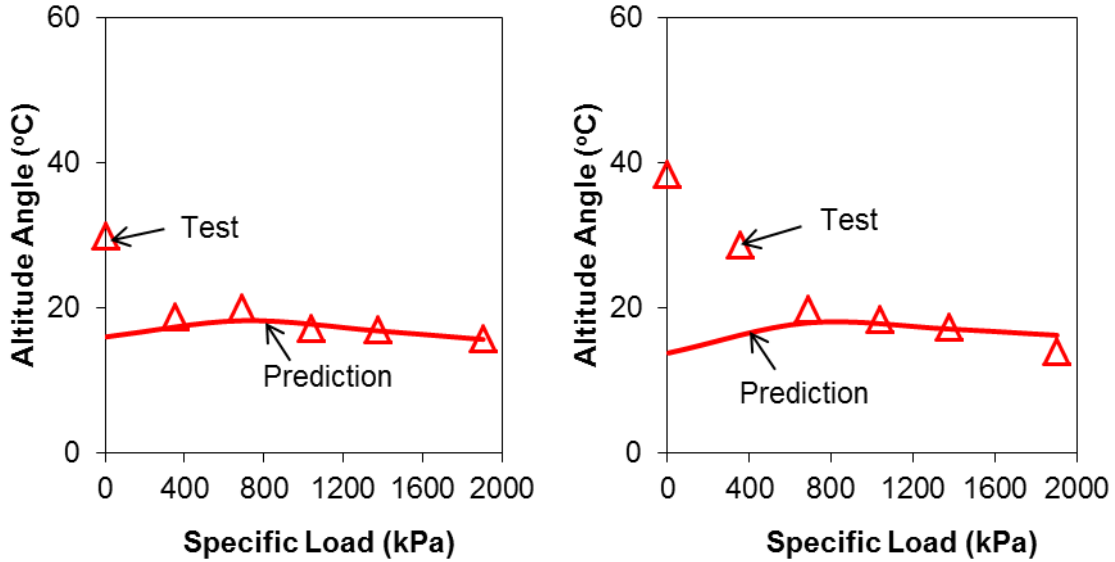
(a) rotor speed Ω=6,000 rpm   (b) rotor speed Ω=10,000 rpm
Fig. 11 Journal attitude angle (ϕ) versus specific load (*W/LD*). Predictions and measurements in Ref. [13] for two rotor speeds.

TPJB power loss and pad trailing edge temperature In a TPJB, the mechanical shear dissipation energy balances the thermal energy transport due to advection by the fluid flow and convection into the bearing and journal surfaces [21]. In the current model, the heat conduction into the bearing and journal surface equals to zero which yields an adiabatic surface thermal condition. According to Ref. [13], the experimental TPJB drag power loss is estimated from,

$$P_l = Q\rho C_v (T_{out} - T_{in}) \tag{37}$$

where Q is the volumetric flow rate measured upstream of the bearing supply inlet. In the predictive model, the drag power loss is obtained by integrating the shear dissipation power over the whole flow domain.

Figure 12 shows the predicted and measured power loss versus the specific load applied on the bearing. Predictions correlate well with the measured power loss. The power loss does not vary much with the load applied on the TPJB; however, it increases significantly with rotor speed.
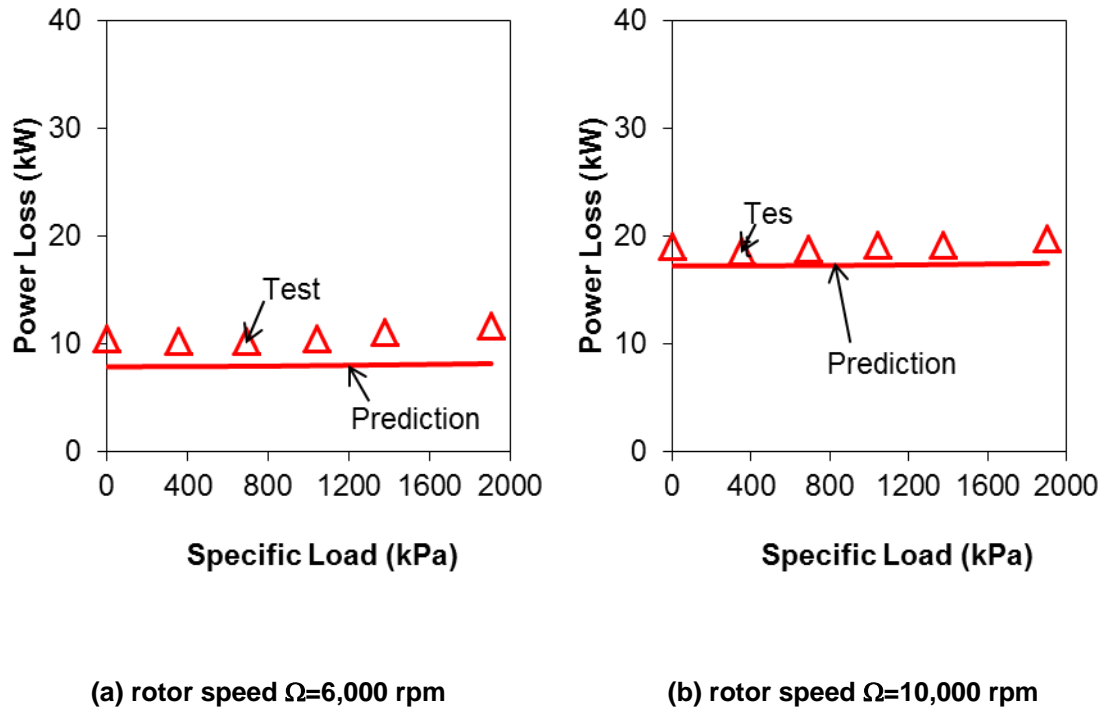
(a) rotor speed Ω=6,000 rpm   (b) rotor speed Ω=10,000 rpm
Fig. 12 TPJB power loss versus specific load (*W/LD*). Predictions and measurements in Ref. [13] for two rotor speeds.

Childs and Harris [13] also measure the pads' temperatures at the trailing edge and at a depth of 2.8 mm from the pad surface[9]. Figures 13 and 14 show the measured pad sub-surface temperature rise at the trailing edge relative to the oil supply temperature and the predicted fluid film temperature rise at the trailing edge of each pad. Note that both the

----

[9] Reference [13] does not provide the pad thickness.

measured pad sub-surface temperature and predicted fluid film temperature along Pad 1 and Pad 2 increase with an increasing specific load. However, the pads #3 and #4 measured and predicted temperatures decrease with increasing specific load. The film thickness along the loaded pads 1 and 2 decreases with increasing specific load along the *Y* direction, thus increasing the fluid film and sub-surface temperatures on each pad. As the film thickness along the unload pads #3 and #4 increases with specific load, the film temperature and the pad sub-surface temperature of pads #3 and #4 decrease. At the zero load condition, the experimental pad sub-surface temperature at trailing edge is sizable due to the large preload. The film temperature rise is
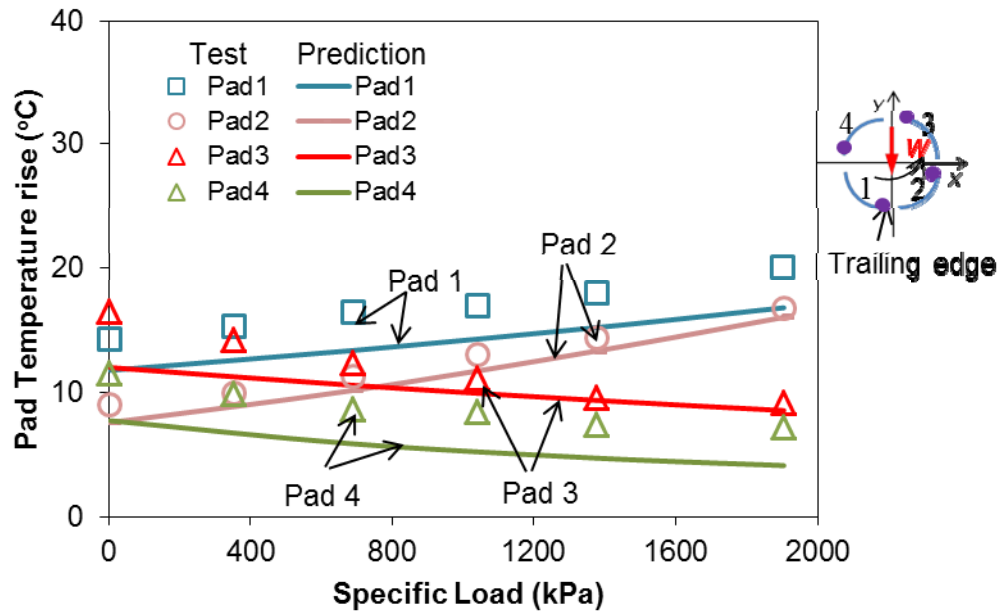
Fig. 13 Measured temperature rise at pad sub-surface trailing edge and predicted trailing edge film temperature rise versus specific load (*W/LD*). Rotor speed Ω=6,000 rpm. Pad inlet thermal mixing coefficient *λ* =0.5. Measurements in Ref. [13] and predictions.
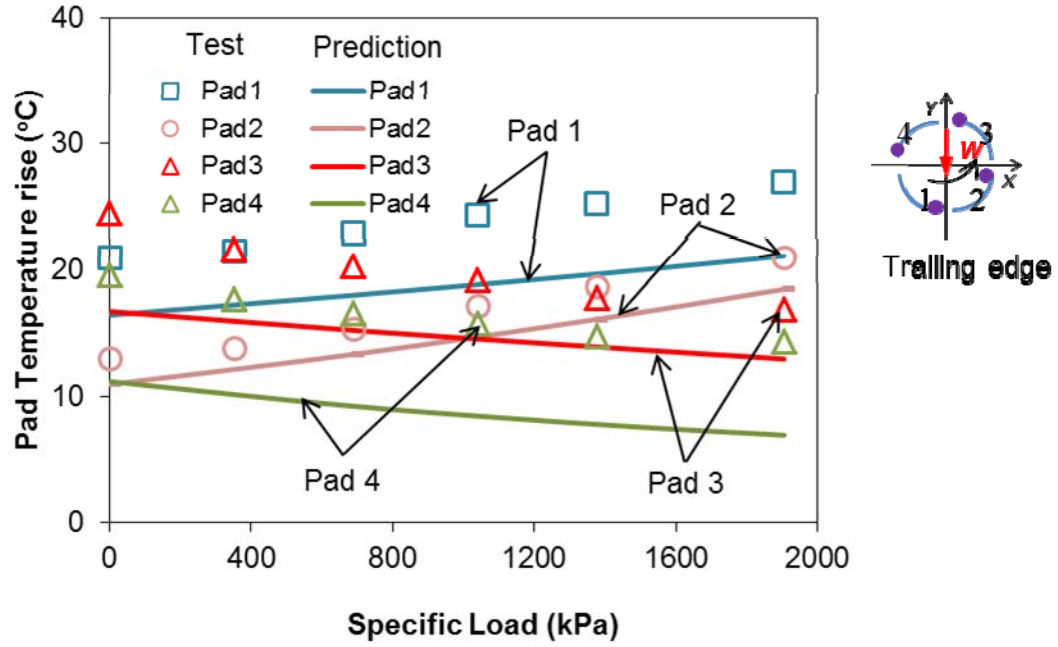
Fig. 14 Measured temperature rise at pad sub-surface trailing edge and predicted trailing edge film temperature rise versus specific load (*W/LD*). Rotor speed Ω=10,000 rpm. Inlet thermal mixing coefficient λ =0.5. Measurements in Ref. [13] and predictions.

Note that when the rotor operates at the high speed of 10,000 rpm, all pad sub-surface trailing edge temperatures are under predicted; as shown in Fig. 14. The predicted film temperatures are about 7 ^{o}C lower than the measured metal temperatures which indicates that the inlet thermal mixing coefficient λ=0.5 is too small when the bearing operates at a high rotor speed. Hence, a larger thermal mixing coefficient (λ=0.95) is used in the model with a high rotor speed and the following predictions show better correlations with the measurements of pad sub-surface temperatures.

Figure 15 shows the predicted film temperature versus the measured pad sub-surface temperatures at a high rotor speed of 10,000 rpm. When the pad inlet thermal mixing coefficient λ =0.95, the predicted film trailing edge temperatures for pads #1 and #3 are a little lower than the measured pad trailing edge temperatures. As Figs. 14 and 15 show,

41

at a high journal speed of 10 krpm, enlarging the thermal mixing coefficient λ $(0.5 \to 0.95)$ leads to an increase in the predicted trailing edge film temperatures, and improves the prediction on the pad trailing edge temperatures.
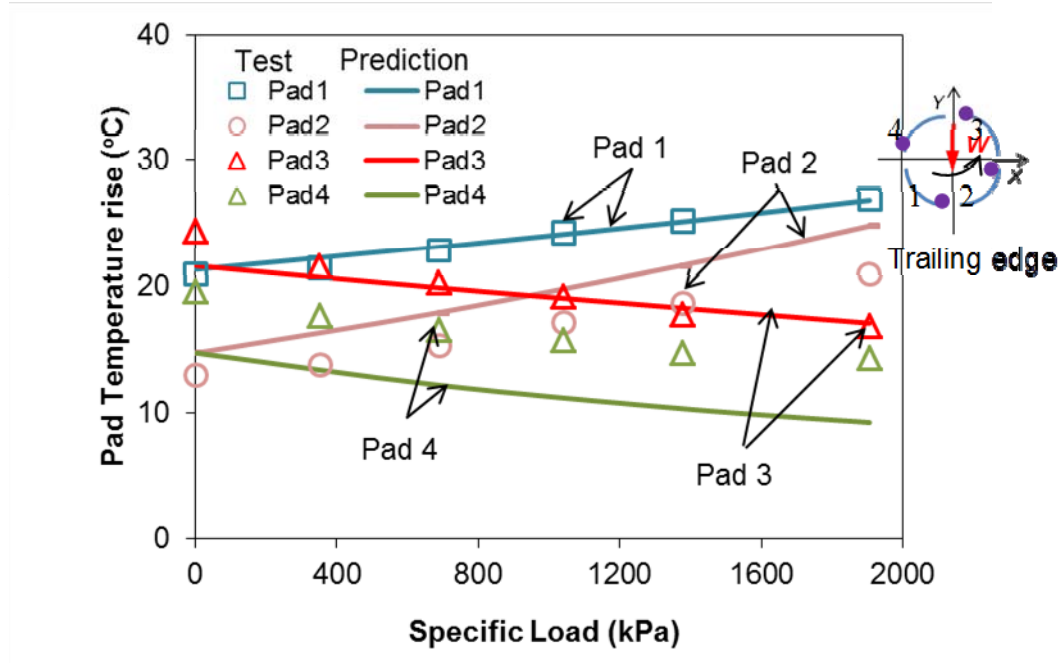
Fig. 15 Measured temperature rise at pad sub-surface trailing edge and improved predicted trailing edge film temperature rise versus specific load (*W/LD*). Rotor speed Ω=10,000 rpm. Inlet thermal mixing coefficient λ=0.95. Measurements in Ref. [13] and predictions.

Hence, the rotor speed, as well as the oil feed arrangement; determine the magnitude of the inlet thermal mixing coefficient (λ). Even with a spray bar blocker machined between two adjacent pads, at a high rotor speed, results obtained from the predictive model indicates that a large amount of hot oil is carried over from the upstream pad, enters the downstream pad, and mixes with the cold inlet oil at the pad leading edge. In other words, when the rotor operates at a high rotor speed, the resistance to the inlet flow

42

increases, thus the spray bar blocker arrangement is less effective on reducing the fraction of hot oil carried over from the upstream pad.

Impedance coefficients In Ref. [13], Childs and Harris employ a frequency-independent [*K-C-M*] model to extract the bearing static stiffness (*K*), damping (*C*), and virtual mass coefficients (*M*) from curve fits to the real and imaginary parts of the experimentally derived impedance coefficients (*Z*). The formulas are:

$$\text{Re}(Z) \rightarrow K - M\omega^2, \quad \text{Im}(Z) \rightarrow C\omega \tag{38}$$

Thus, the TPJB stiffness coefficients in Ref. [13] are static coefficients at zero excitation frequency. The bearing static stiffness and the viscous damping coefficients delivered by the [*K-C-M*] fit model are hereby reported for the predictive model impedances and compared with those from the test data.

The following figures compare the impedances (*Z*) obtained from the current predictions and the experiments [13]. The bearing operates with a specific load (*W/LD*) equaling 1,376 kPa and at two rotor speeds, 6 krpm and 10 krpm. The graphs also include the constructed real and imaginary parts of the impedances based on the [*K,C,M*] coefficients.

Figures 16 and 17 show the real part of the bearing impedances, Re(*Z*), versus excitation frequency. Note that the predictions show identical impedances along the *X* and *Y* directions, i.e., Re(Z_{XX}) = Re(Z_{YY}). At the low rotor speed, the static stiffness *K* derived from the experimental impedances is ~9% higher than the predicted stiffness. For operation at 10,000 rpm, the [*K-C-M*] model adequately captures the real part of the bearing impedances, i.e., the curve fits constructed with the [*K-C-M*] model coefficients reproduce well the predicted impedances. The experimental impedances are fairly constant, thus yielding a zero virtual mass coefficient (*M*~0). On the other hand, the predicted Re(*Z*) increase slightly with increasing excitation frequency. Thus, predictions display a negative virtual mass coefficient, revealing a "stiffening" effect on the bearing stiffness coefficients over the test frequency range.
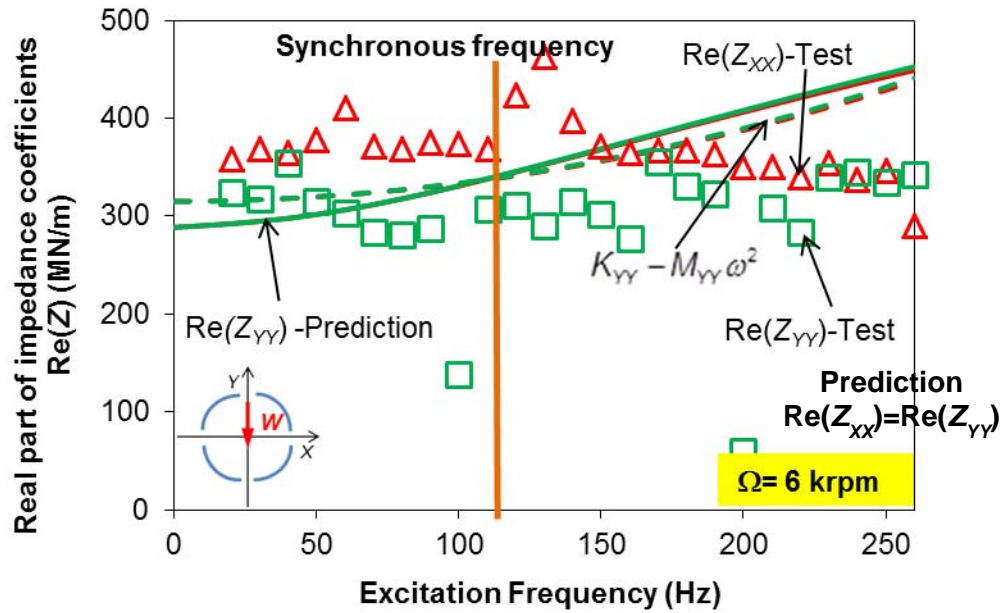
Fig. 16 Real part of TPJB impedance coefficients, Re(*Z*), versus excitation frequency. Rotor speed Ω = 6,000 rpm and specific load (*W/LD*) = 1,376 kPa. Pivot stiffness K_{piv} =443 MN/m. Pad inlet thermal mixing coefficient λ = 0.5. Measurements in Ref. [13], predicted Re(*Z*) and constructed K-$\omega^2 M$ curves.
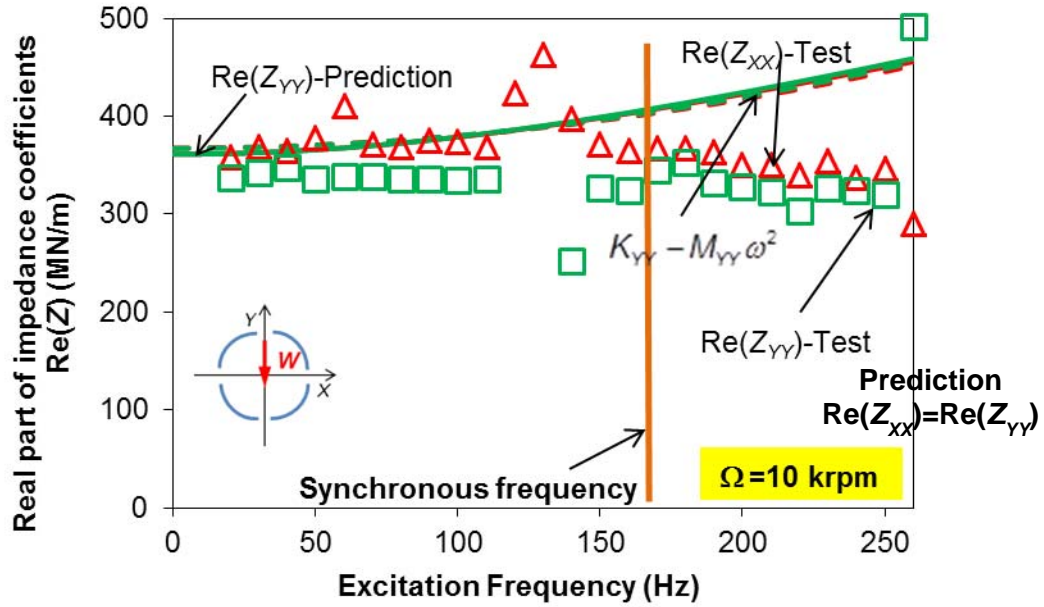
Fig. 17 Real part of TPJB impedance coefficients, Re(Z), versus excitation frequency. Rotor speed Ω=10,000 rpm and specific load (W/LD) =1,376 kPa. Pivot stiffness K_{piv}=548 MN/m. Pad inlet thermal mixing coefficient λ=0.95. Measurements in Ref. [13], predicted Re(Z) and constructed $K\text{-}\omega^2 M$ curves.

Figures 18 and 19 display the imaginary part of the bearing impedances when the specific load equals to 1,376 kPa for operations at 6 krpm and 10 krpm. The slope of the imaginary part of impedance gives the viscous damping coefficient. The decreasing slope of the impedance (imaginary) at speed 6,000 rpm denotes that the damping coefficients are frequency dependent. Measured damping coefficients decrease slightly with increasing whirl frequency when the frequency is higher than the synchronous speed frequency (ω>Ω). The predicted imaginary part of impedance is a little smaller than the measured ones.

45
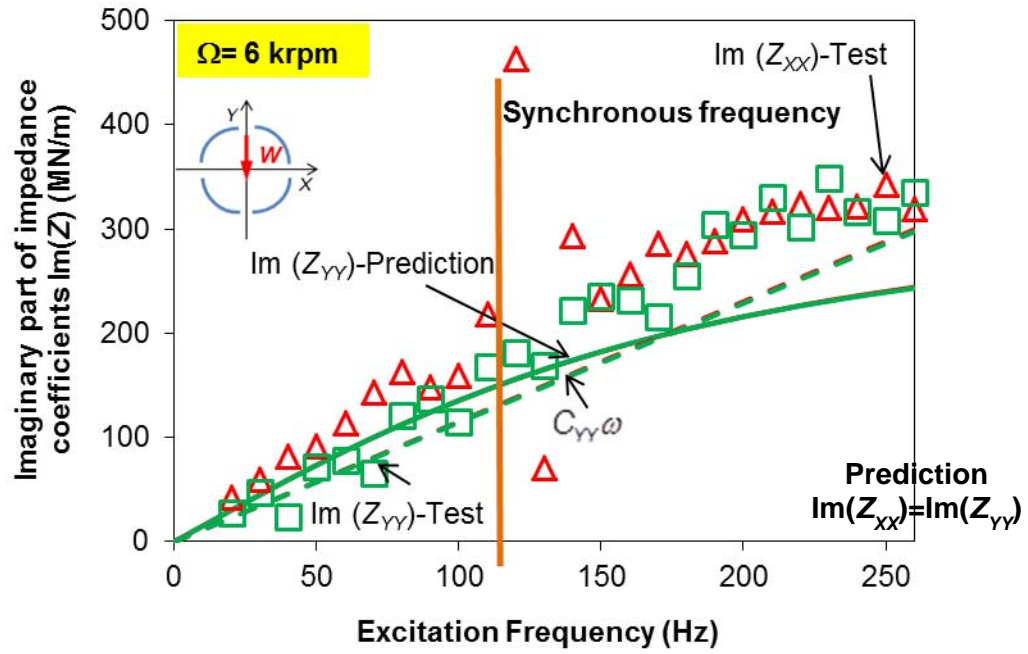
Fig. 18 Imaginary part of TPJB impedance coefficients, Im(*Z*), versus excitation frequency. Rotor speed Ω=6,000 rpm and specific load (*W/LD*) =1,376 kPa. Pivot stiffness *K_{piv}*=443 MN/m. Pad inlet thermal mixing coefficient λ=0.5. Measurements in Ref. [13], predicted Re(*Z*) and constructed C*ω* curves.
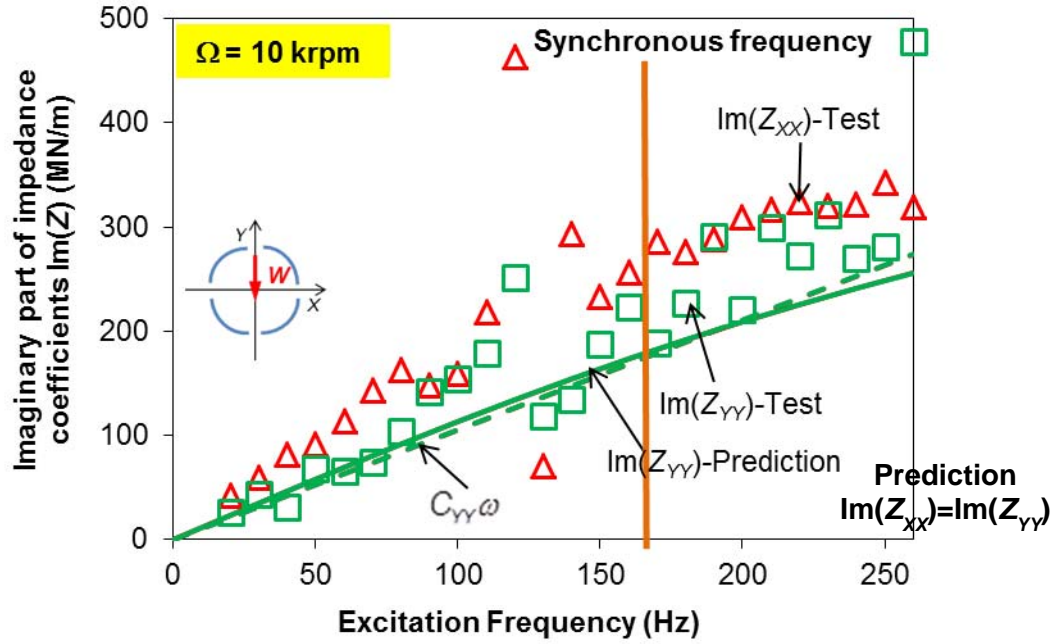
Fig. 19 Imaginary part of TPJB impedance coefficients, Im(*Z*), versus excitation frequency. Rotor speed Ω=10,000 rpm and specific load (*W/LD*) =1,376 kPa. Pivot stiffness K_{piv}=548 MN/m. Pad inlet thermal mixing coefficient λ=0.95. Measurements in Ref. [13], predicted Re(*Z*) and constructed Cω curves.

A correlation coefficient (*r*) represents the goodness of fit between the built curves $K-\omega^2 M$ to Re (*Z*) and $C\omega$ to Im(*Z*), predicted or experimental. This coefficient equals

$$r^2 = \frac{\sum (x-\overline{x})(y-\overline{y})}{\sqrt{\sum (x-\overline{x})^2 \sum (y-\overline{y})^2}}$$

(39)

$$\begin{cases} x = \mathrm{Re}(Z) \\ y = K - M\omega^2 \end{cases}, \text{ and } \begin{cases} x = \mathrm{Im}(Z) \\ y = C\omega \end{cases}$$

Table 4 gives r^2 of the model curve fits to the impedances from predictions and test data at each operating condition. As the correlation coefficient $r^2 \to 1$, the [*K-C-M*] model accurately represents the bearing impedances. At the high rotor speed of 10 krpm,

47

the damping coefficients (*C*) show frequency independency over the frequency test range (0-260 Hz) while the damping at speed 6 krpm is slightly frequency dependent. Note that for operation at speed 6 krpm, Ref. [13] did not use the [*K-C-M*] model to extract the stiffness and damping coefficients from the test data since Re(*Z*) is nearly constant over the test frequency range.

Table 4 Correlation coefficients of the curve fits to the impedances from predictions and test data at various operating conditions for a TPJB in Ref. [13]. Excitation frequency varies from 0 to 260 Hz.

Rotor speed		Prediction				Measurement [13]			
	Specific load (kPa)	0	687	1,375	1,905	0	687	1,375	1,905
6 krpm	$K_{sXX} - M_{XX}\omega^2 \rightarrow \text{Re}(Z_{XX})$	0.99	0.98	0.98	0.97	-	-	-	-
	$K_{sYY} - M_{YY}\omega^2 \rightarrow \text{Re}(Z_{YY})$	0.99	0.98	0.98	0.97	0.22	-	-	-
10 krpm	$K_{sXX} - M_{XX}\omega^2 \rightarrow \text{Re}(Z_{XX})$	1.00	1.00	1.00	0.99	0.80	0.24	0.17	0.52
	$K_{sYY} - M_{YY}\omega^2 \rightarrow \text{Re}(Z_{YY})$	1.00	1.00	1.00	0.99	0.38	0.32	0.12	0.14
6 krpm	$C_{XX}\omega \rightarrow \text{Im}(Z_{XX})$	0.98	0.97	0.97	0.97	0.74	0.87	0.81	0.87
	$C_{YY}\omega \rightarrow \text{Im}(Z_{YY})$	0.97	0.97	0.96	0.96	0.92	0.97	0.92	0.97
10 krpm	$C_{XX}\omega \rightarrow \text{Im}(Z_{XX})$	1.00	1.00	1.00	0.99	0.96	0.85	0.89	0.76
	$C_{YY}\omega \rightarrow \text{Im}(Z_{YY})$	1.00	1.00	0.99	0.99	0.78	0.76	0.80	0.83

TPJB stiffness, damping and virtual mass coefficients Figure 20 depicts the experimental and predicted static direct stiffness coefficients versus increasing specific load at rotor speeds, 6 krpm and 10 krpm. Note that the predicted stiffness coefficients (*K_XX* and *K_YY*) from the model in Ref. [17], which considers the TPJB with rigid pivots, are about 200%-300% larger than the experimental values (600 MN/m~900 MN/m). Hence, the pivot flexibility of the test bearing pads reduces significantly the bearing stiffness coefficients. Recall the material of the test TPJB pivot is Bronze. The pad inlet thermal mixing coefficient (*λ*) for operation at rotor speeds, 6,000 rpm and 10,000 rpm are assumed as 0.5 and 0.95, respectively.

Figure 20 shows that the current model under predicts the TPJB stiffness (K_{YY}) by up to 17% at the journal speed of 6,000 rpm. At the high journal speed of 10,000 rpm, the difference between the stiffness coefficients (K_{YY}) derived from the experimental and predicted impedances varies from 1% to 7%. The predicted stiffness coefficients (K_{XX}) are ~10% smaller than those obtained from the test data. Note the experimental results show orthotropic stiffness ($K_{XX} \neq K_{YY}$), conflicting with the commonly held view that a LBP bearing has identical stiffness coefficients ($K_{XX} = K_{YY}$).
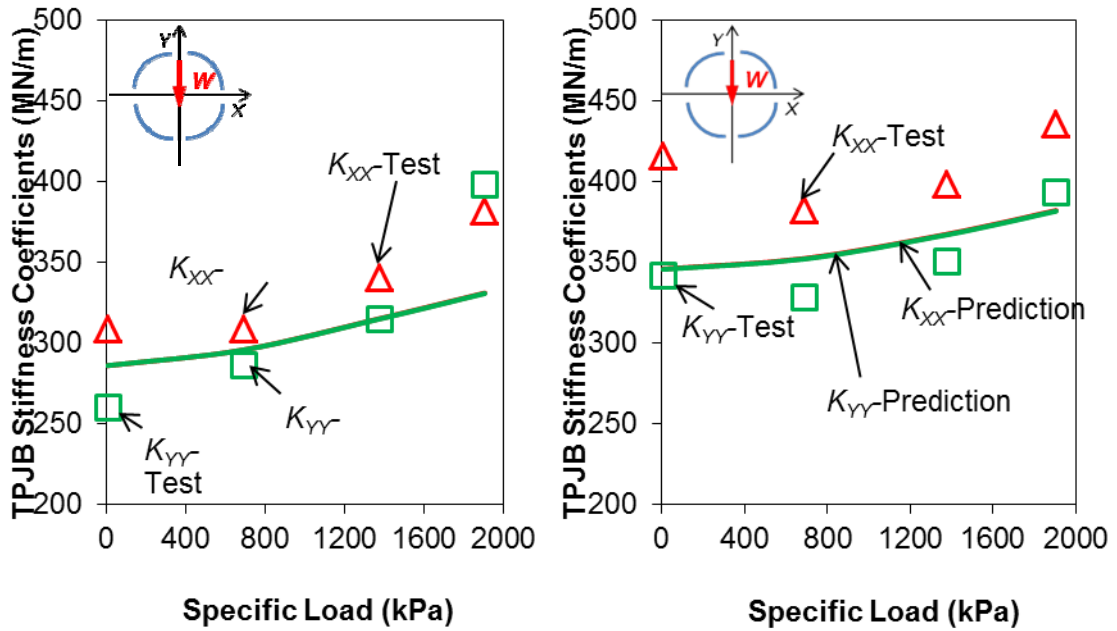
(a) rotor speed Ω=6,000 rpm
Pivot stiffness K_{piv}=443 MN/m
Inlet thermal mixing coefficient λ=0.5

(b) rotor speed Ω=10,000 rpm
Pivot stiffness K_{piv}=548 MN/m
Inlet thermal mixing coefficient λ=0.95

Fig. 20 TPJB static stiffness coefficients (*K*) versus specific load (*W/LD*). Two pivot stiffnesses. Current predictions and measurements in Ref. [13] for two rotor speeds.

Figure 21 shows the predicted damping coefficients derived from the impedances (imaginary part) using a [*K-C-M*] model with the TPJB loaded to 19 kN. The TPJB model with rigid pivot in Ref. [17] overpredicts the bearing damping coefficients by

350%-450% (700 kN.s/m to 950 kN.s/m). For the current model, results show a good agreement between the predictions and the measured damping coefficients at a rotor speed of 10 krpm. Damping coefficients are underpredicted by 7%~20% by the current model at the low rotor speed of 6 krpm. Note the bearing damping coefficients decrease with increasing journal speed, as shown in Fig. 21.

(a) rotor speed Ω=6,000 rpm
Pivot stiffness K_{piv}=443 MN/m
Inlet thermal mixing coefficient λ=0.5

(b) rotor speed Ω=10,000 rpm
Pivot stiffness K_{piv}=548 MN/m
Inlet thermal mixing coefficient λ=0.95
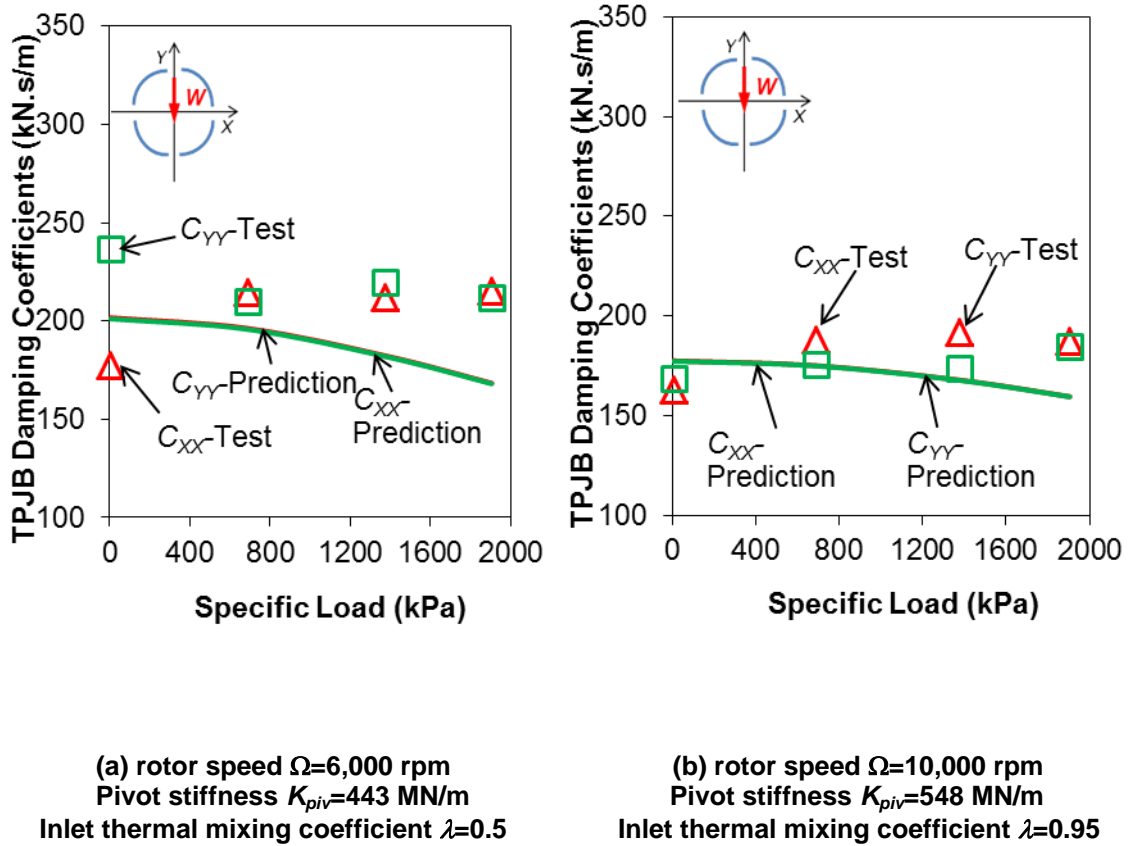
Fig. 21 TPJB damping coefficients (*C*) versus specific load (*W/LD*). Two pivot stiffnesses. Current predictions and measurements in Ref. [13] for two rotor speeds.

Figure 22 shows the TPJB virtual mass (*M*) force coefficients. Recall these coefficients are determined from curve fitting Re(*Z*) to a quadratic function of the excitation frequency, as stated in Eq.(39). At the zero load condition, a negative virtual mass coefficient (M_{YY}) curve fitted to the test impedances shows the bearing dynamic

stiffness coefficient (K-$M\omega^2$) to increase with excitation frequency. The predicted virtual mass coefficients are large in magnitude as a result of a strongly frequency dependent Re(Z). Note that the reported uncertainties of the experimental mass coefficients are 9.5 kg or less for all operating conditions [13].

(a) rotor speed Ω=6,000 rpm
Pivot stiffness K_{piv}=443 MN/m
Inlet thermal mixing coefficient λ=0.5

(b) rotor speed Ω=10,000 rpm
Pivot stiffness K_{piv}=548 MN/m
Inlet thermal mixing coefficient λ=0.95
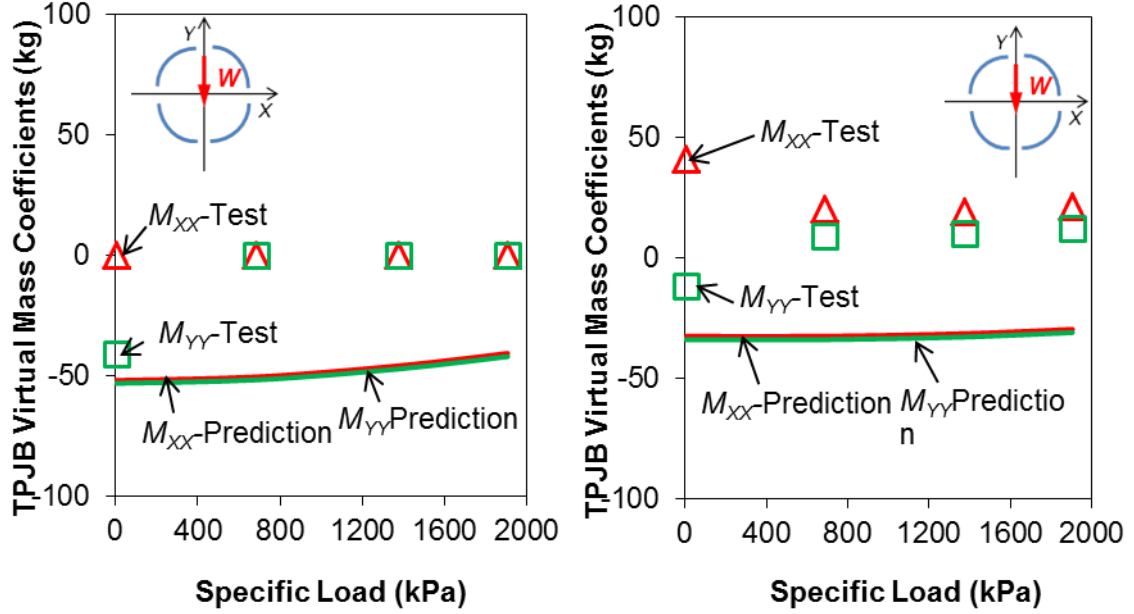
Fig. 22 TPJB virtual mass coefficients (M) versus specific load (W/LD). Two pivot stiffnesses. Current predictions and measurements in Ref. [13] for two rotor speeds.

Effect of pivot flexibility on the bearing static forced performance and dynamic force coefficients Comparison between the test data and predictions for the bearing in Ref. [13] illustrates a great effect of the pivot flexibility on the bearing static stiffness (ω=0) and damping coefficients with an estimated soft pivot stiffness (K_{piv} = 443MN/m, 548 MN/m). Appendix B aims to further highlight the effect of pivot stiffness on the static characteristics (journal eccentricity) and dynamic forced performance (stiffness,

damping, virtual mass coefficients and impedance coefficients) for the test bearing in Ref. [13].

The analysis results in Appendix B show that pad pivot flexibility produces a significant increase in the journal eccentricity along the loaded direction (*Y*), in particular at a heavy load condition. For a TPJB with considerably soft pivots, the journal displacement can be much larger than the nominal bearing clearance, thus also revealing large pivot radial deflections.

Pivot stiffness also affects the bearing impedances (real and imaginary part) at high excitation frequencies. A bearing with rigid pivots reveals always a "softening" effect of the dynamic stiffness coefficients, i.e., the real part of the direct impedances decreases with increasing excitation frequency. However, the pivot flexibility "stiffens" the bearing dynamic stiffness coefficients as the excitation frequency increases, though reducing the bearing static stiffness coefficients. Hence, the frequency dependency of the bearing dynamic stiffness coefficients is prone to be influenced by pivot stiffness.

For a pad pivot stiffness 10 times larger than the fluid film stiffness (bearing stiffness with rigid pivots), pivot flexibility has little effect on the bearing force coefficients. This pivot stiffness determines a constant force coefficient for various operating static loads and rotor speeds, as the pivot stiffness is only 10% of the fluid film stiffness coefficients. Note that the bearing static stiffness coefficients (ω=0) can be obtained by using a simple equation based on the pivot stiffness and fluid film stiffness. Incidentally, pivot flexibility has a more pronounced effect in reducing the bearing damping coefficients than the stiffness coefficients.

Closure A predictive model [17], which considers the pivot as rigid, over predicts the bearing stiffness and damping coefficients in Ref. [13]. Pad pivot flexibility reduces significantly the bearing stiffness and damping coefficients, even for operation with small specific loads.

The current model delivers better predictions for the bearing stiffness and damping coefficients by employing estimated pivot stiffnesses. For operation at rotor speeds of 6

krpm and 10 krpm, the estimated pivot stiffness equals to 443 MN/m and 538 MN/m, 27% and 57% higher than the measured "pad-support structure stiffness" reported in Ref. [13], respectively. The differences between the predicted and measured static stiffness coefficients (K_{YY}) are within 17% and 10% at speeds 6 krpm and 10 krpm.

In the current model, the pad inlet thermal mixing coefficient λ, which determines the fraction of hot oil entering the downstream pad, influences greatly the prediction of the film temperatures in a TPJB. A pad inlet thermal mixing coefficient λ=0.5 is first used in the model since the bearing has spray bar blockers and by-pass cooling arrangements to reduce the fraction of hot oil flowing onto the downstream pad. However, results show that pad trailing edge film temperatures are underpredicted, in particular at the highest rotor speed. Predictions using a larger thermal mixing coefficients λ=0.95 show an improvement on the pad trailing edge film temperatures at a high rotor speed of 10 krpm. The results illustrate that there may be a large amount of hot oil mixing with fresh oil at a pad leading edge. Hence, the implementation of spray bar blockers and by-pass cooling arrangements does not guarantee the reduction in the oil operating temperature for this TPJB model, in particular at a high rotor speed. Test results for a tilting pad thrust bearing in Ref. [26] support this conclusion.

For predictions of bearing stiffness and damping coefficients, λ is selected as 0.5 and 0.95 for the TPJB model with a rotor speed of 6 krpm and 10 krpm, respectively. The [K-C-M] model captures adequately the bearing impedances at a high rotor speed of 10 krpm. The measurements evidence small virtual mass coefficients, thus denoting that the bearing stiffness coefficients are frequency independent. However, the model predicts negative virtual mass coefficients of large magnitude. Thus, the predicted dynamic stiffness coefficients (K-$\omega^2 M$) will steadily increase with frequency (ω).

Example 2-Predicted Forced Performance for a Rocker-Back LOP TPJB [7]

Wilkes [7] carries out comprehensive experiments on a five-pad TPJB with rocker-back pivots. Table 5 lists the parameters of the test TPJB geometry, lubricant type and inlet temperature, and material properties. This section correlates more to the experimental bearing force coefficients in Ref. [7]. The analysis uses a measured pivot load-deflection function and takes into account the operating bearing clearances.

Table 5 Parameters for test TPJB in Ref. [7].

Number of pads, N_{pad}	5
Configuration	LOP
Pad arc angle, Θ_P	58.9^o
Pivot offset	50%
Rotor diameter, D	101.6 mm
Pad axial length, L	55.9 mm
Cold bearing clearance, C_B	68 μm
Cold pad clearance, C_P	121.4 μm
Cold pad preload, $\bar{r}_P$	0.44
Pad mass, m	0.385 kg
Pad Inertia about pivot, I_P	1.807×10^{-4} kg.m^2
Pivot type	Rocker back
Pad thickness, t	13.68 mm
Lubricant type	DTE 797, ISO VG32
Oil inlet temperature	~36.7^{o}C
Oil density, ρ	856.2 kg/m^3
Oil supply viscosity at 36.7^{o}C, μ_0	0.0285 Pa.s
Oil viscosity at 78 ^{o}C, 125 ^{o}C	0.0090 Pa.s, 0.0023
Temperature viscosity	0.0291/K
Specific load, W/LD	0 kPa-3,132 kPa
Journal speed, Ω	4,400 rpm-13,100 rpm

Wilkes [7] reports a maximum pad surface temperature equal to 78 $^{\circ}$C for operations at 4,400 rpm, and 125 $^{\circ}$C at 13,100 rpm for tests with the largest static specific load equaling 3,132 kPa (W=17.8kN). The viscosity of ISO VG32 oil at 78 $^{\circ}$C and 125 $^{\circ}$C is 0.0090 Pa.s and 0.0023 Pa.s. The maximum shear flow Reynolds numbers (Re=$\rho\Omega R C_B/\mu$) at rotor speeds of 4,400 rpm and 13,100 rpm are 316 and 1,243, respectively. Hence, the thin film flow in the test TPJB is laminar at all operating conditions except for operation at a speed of 13,100 rpm and under a specific load of 3,132 kPa[10].

Figure 23 shows the load configuration of the test TPJB. The specific load (W/LD) acting on the TPJB ranges from 0 kPa to 3,132 kPa and the rotor speed varies from 4,400 to 13,100 rpm. The predictive model assumes the fluid flow carries away all the heat in a TPJB, i.e., an adiabatic surfaces condition is selected for simplicity. The inlet thermal mixing coefficient λ=0.9 for operation at rotor speed of 13,100 rpm, and λ=0.8 when the rotor spins at 4,400 rpm. The λ magnitudes selected produce film temperature fields agreeing with the overall shape and peak temperature values observed in the experiments.

---

[10] The predictive model at this time does not account for the effect of flow turbulence.
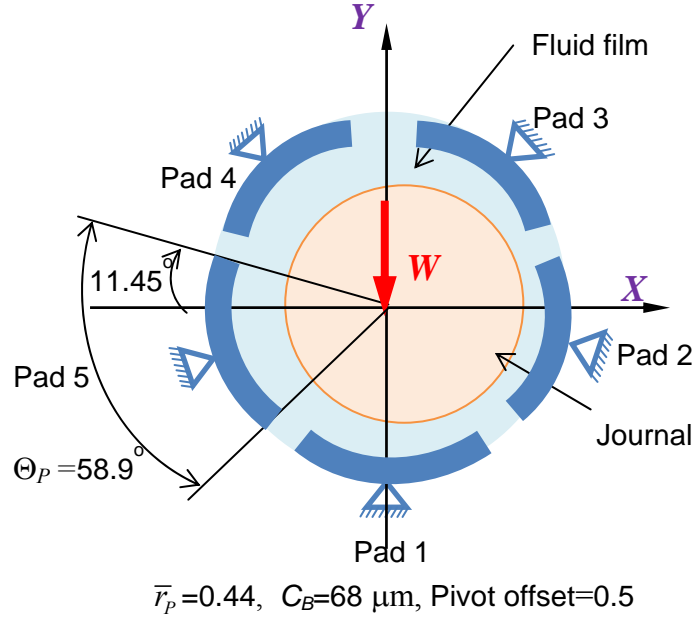
Fig. 23 Load configuration and pad arrangements of a test tilting pad journal bearing in Ref. [7].

The effect of temperature on the operating pad clearances and bearing clearances Wilkes [7] finds that the bearing radial clearance reduces with increases in pad temperature. He figures out that the reduction of the bearing clearance is proportional to the increase of the average pad temperature (at the pivot position) [7], which represents the average temperature along each pad surface, i.e.,

$$c_b = c_{b,ref} - \alpha_{c_b}(T_{avg} - T_{ref})$$

(40)

Here α_{c_b} is an ad-hoc thermal expansion coefficient (m/^{o}C) specific to the test rig and bearing. For the test TPJB in Ref. [7], α_{c_b} equals to 0.396 μm/^{o}C. Here, a simple model is used to estimate the relationship between the material thermal expansion coefficient α_T (1/^{o}C) and the coefficient α_{c_b} (m/^{o}C). As the thermal expansions of both the journal

and the pad surface contribute to the reduction of the bearing clearance, the change of the bearing clearance is,

$$c_{b,ref} - c_b = \alpha_{c_b} \Delta T = \alpha_T (R - \gamma t) \Delta T \tag{41}$$

Both the journal and the pads are assumed to expand radially outwards for the test TPJB in Ref. [7]. $\alpha_T = 1.3 \times 10^{-5} /{}^{\circ}C$ is the linear thermal expansion coefficient of steel, material for the rotor and pads. R and t are the rotor radius and pad thickness, respectively. The predictive model assumes the journal and pad surface have the same temperature rise ΔT relative to the oil supply temperature (ambient temperature). Note that a Babbitt layer with a thickness of 1.78mm is machined on the surface of the pad. As the Babbitt has a higher thermal expansion coefficient ($\alpha_T = 1.94 \times 10^{-5} - 2.4 \times 10^{-5} /{}^{\circ}C$) than steel, a coefficient $\gamma = 1.85$ is included in Eq. (41) to account for the thermal expansion of the Babbitt surface.

In the current model, the hot bearing clearance is estimated by using the average measured pad sub-surface temperature rise at the pivot location, which represents the average temperature rise in a TPJB, as demonstrated in Ref. [7]. The average temperature rise is obtained from the measured pad surface temperatures given in Ref. [7].

Note that bearing clearance ($C_B = R_B - R_J$) and pad clearance ($C_P = R_P - R_J$) both decrease due to the thermal expansion of the rotor (rotor radius R_J increases). Presently, assume the linear thermal expansion of the pad surface reduces the pad clearance the same amount as with the bearing clearance, thus the dimensional pad preload ($r_P = C_P - C_B$) remains invariant. However, the dimensionless pad preload ($\bar{r}_P = 1 - C_B / C_P$) varies.

Table 6 shows the hot bearing and pad clearances, dimensionless pad preload and the average pad temperature in a TPJB. The test data is taken from Ref. [7].

Table 6 Hot bearing clearances, pad clearances, pad preload and measured pad sub-surface average temperatures. Data from Ref. [7].

Rotor speed Ω (rpm)	Specific load W/LD (kPa)	Bearing clearance C_B (μm)	Pad clearance C_P (μm)	Dimensionless Pad preload $\bar{r}_P$	Measured average temperature T_{avg} (°C)
d 4,400	0	58.5	111.3	0.474	49.8
	783	58.2	111.0	0.476	50.7
	1,566	57.9	110.7	0.477	51.5
	2,350	58.2	111.0	0.476	50.7
	3,132	56.6	109.4	0.483	54.7
13,100	0	51.2	104.0	0.508	68.3
	783	50.9	103.7	0.509	69.2
	1,566	50.0	102.8	0.513	71.3
	2,350	49.1	101.9	0.518	73.7
	3,132	48.6	101.4	0.520	74.8

Nominal bearing clearance C_B= 68 mm, nominal pad clearance C_P= 121 mm nominal pad preload $\bar{r}_P$ =0.44

Note that the minimum pad clearance for operation at 13,100 rpm with the largest specific load is 16.5% smaller than the nominal pad clearance. The difference between the cold bearing clearance and the operating hot bearing clearance varies from 14% to 28%. For predictions, the model has a large nominal pad dimensionless preload i.e., $\bar{r}_p = 0.44$, resulting in a large difference between the pad and bearing clearances. The dimensionless pad preload increases as the temperature in the fluid film increases due to the heavy static load applied on the bearing and the high rotor speed.

Pivot flexibility In Ref. [7], Wilkes obtains experimentally a pivot load (F_{piv})-versus-deflection (ξ_{piv}) curve for his test bearing, $F_{piv}=f(\xi_{piv})$, fitted as a fourth-order polynomial, and from which the pivot stiffness is extracted.

$$F_{piv} = -64.44 + 1.773 \times 10^8 \, \xi_{piv} + 3.339 \times 10^{13} \, \xi_{piv}^2 - 6.653 \times 10^{17} \, \xi_{piv}^3 + 7.321 \times 10^{21} \, \xi_{piv}^4 \text{ [N]} \qquad (42)$$

Here F_{piv} is the load on a pivot and ξ_{piv} is the pivot radial deflection. The physical unit of the load (F_{piv}) is Newton and the unit of pivot deflection (ξ_{piv}) is meter. The slope of the pivot load-versus-deflection curve gives the pivot stiffness as,

$$K_{piv} = 1.773 \times 10^8 + 6.678 \times 10^{13}\xi_{piv} - 1.996 \times 10^{18}\xi_{piv}^2 + 2.928 \times 10^{22}\xi_{piv}^3 \qquad \text{[N/m]} \qquad (43)$$

Pad flexibility Lund [4] demonstrates that the pad flexibility, as well as the pivot flexibility, reduce the stiffness and damping coefficients of a TPJB. For the test bearing, the predictions in Ref. [7] also include the effect of pad flexibility on TPJB forced performance. The current TPJB model accounts for the effect of pad flexibility by calculating an equivalent pad-pivot radial stiffness which is determined from the pivot radial stiffness and pad bending stiffness. The equivalent pad-pivot radial stiffness (K_{eq}) is,

$$\frac{1}{K_{eq}} = \frac{1}{K_{piv}} + \frac{l^2}{K_{pad}} \qquad (44)$$

here l is half of the pad length, . K_{piv} and K_{pad} are the pivot radial stiffness and pad bending stiffness, respectively. The pad bending stiffness is a function of the pad bending moment [7],

$$K_{pad} = 5.4644 \times 10^4 M_p + 1.1559 \times 10^5 \quad \text{(N.m/rad)} \qquad (45)$$

Integration of the hydrodynamic force (F_ξ) on the fluid flow domain gives the pad bending moment M_p, as stated in Ref. [7]. Note the above method to include the pad flexibility is not as accurate as that in Ref. [7] which obtains the pad mechanical deformation based on the experimental results.

Journal displacement Table 7 shows the journal center displacement (e_Y), test data and predictions, at different operating conditions. Both the experimental and predictive results show very small journal displacements in the direction (X) [7], orthogonal to the load direction. Figure 24 depicts the predicted and measured journal center displacement

along the direction (Y) when the TPJB operates at increasing specific loads and rotor speeds.

Table 7 Journal center displacement and pad radial clearance. Current predictions and measurements in Ref. [7].

Rotor speed Ω (rpm)	Specific load W/LD (kPa)	Pad clearance C_P (μm)	Journal displacement e_Y (μm)		Difference between test and prediction
			Test	Prediction	
	0	104.5	1.6	0.0	N/A
	783	103.9	31.4	27.3	-16.6%
4,400	1,566	103.3	49.3	43.0	-12.2%
	2,350	103.9	60.3	53.8	-12.4%
	3,132	101.1	68.7	60.3	-13.6%
	0	91.5	1.2	0.0	N/A
	783	90.8	14.7	18.3	40.8%
13,100	1,566	89.3	24.7	33.0	38.6%
	2,350	87.6	34.0	44.9	36.0%
	3,132	86.9	42.0	52.2	25.4%

At the journal speed of 13,100 rpm, the measured journal displacement is ~50% smaller than that at a low rotational speed of 4,400 rpm. At the large specific load of 3,132 kPa and 4.4 krpm, the predictive model under predicts the journal center displacement by 13.6%. At the high speed of 13,100 rpm, the journal eccentricity is over predicted by a maximum of 40.8%. Test data shows that the journal eccentricity exceeds the operating bearing clearance for operation at a highest static load of 3,132 kPa and speed 4,400 rpm. A very soft pivot stiffness results in a large pivot radial deflection, allowing for a large journal eccentricity at the highest static load.
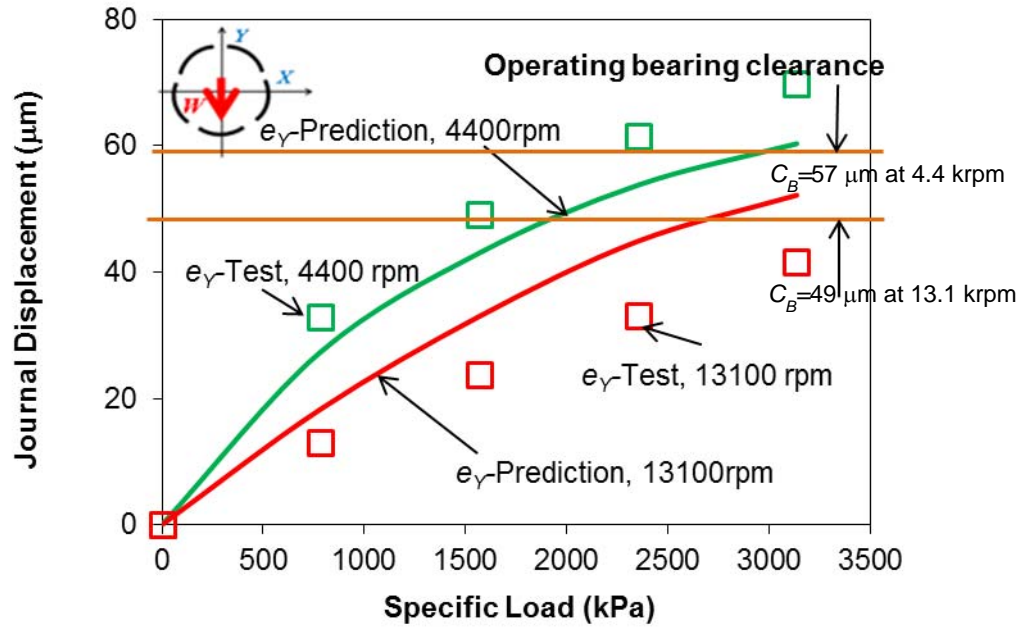
Fig. 24 TPJB Journal center displacement (e_Y) versus specific load (W/LD). Predictions and measurements in Ref. [7] for two rotor speeds.

Predicted film and measured pad temperatures Figure 25 shows the circumferential locations for measurement of pad temperatures in the test TPJB. Reference [7] presents recorded pad temperatures measured at depths of 3.2 mm and 11.2 mm from the pad surface, as shown in Fig.25. Hence, the measured pad sub-surface temperatures should be lower than the pad surface temperature (exposed to the lubricant) and the fluid film temperature.

61
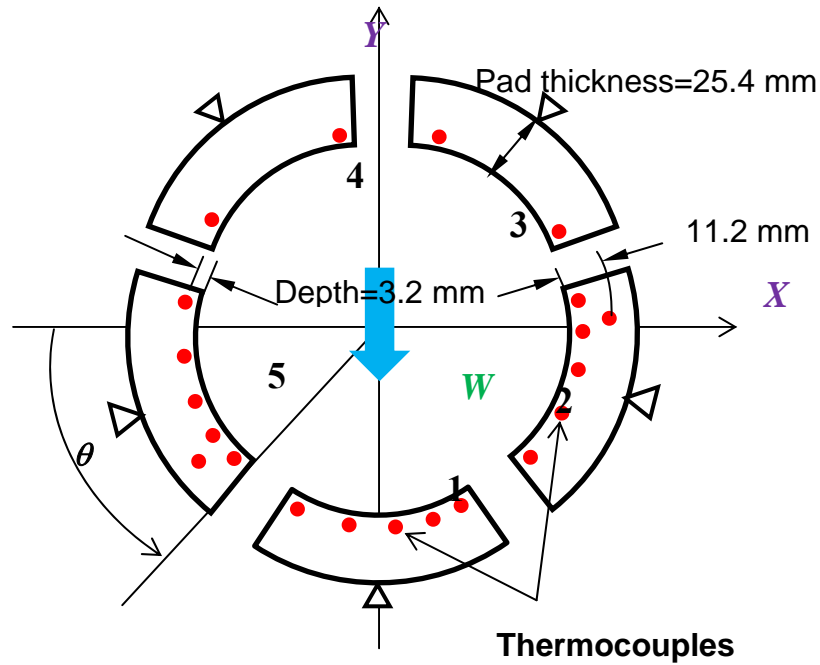
Fig. 25 Angular locations for measurement of pad temperature in a bearing, Ref.[7].

The predicted film temperature is a bulk-flow temperature which should also be a little higher than the measured pads sub-surface temperature. Figures 26 and 27 show the measured pad sub-surface temperatures and the predicted film temperatures versus specific load at two rotor speeds. The predicted film temperatures are higher than the measured pad sub-surface temperatures on the loaded pad (#1), in particular at a large specific load of 3,132 kPa. Note that the measured pad temperature decreases at the pad trailing edge while the predicted temperature does not. Oil cavitation occurs in the fluid film region near the pad trailing edge; and the hot lubricant leaving the pad cools because of heat conduction into the shaft. For operation at a rotor speed of 13 krpm when the specific load applied on the bearing equals to 3,132 kPa, the predicted maximum film temperature increases dramatically to ~160°C. A high temperature at the

loaded pad trailing edge indicates that the lubricant viscosity and bearing clearance decrease dramatically and the flow may become turbulent.
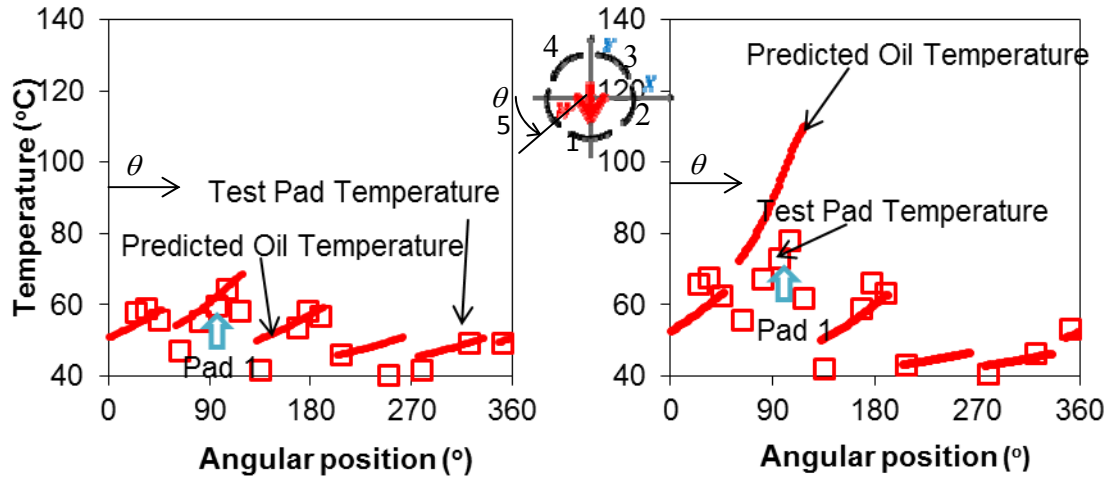
(a) Specific Load W/LD=783 kPa   (b) Specific Load W/LD =3,132 kPa
Inlet thermal mixing coefficient λ=0.8   Inlet thermal mixing coefficient λ=0.9
Fig. 26 TPJB film temperature and pad sub-surface (3.2 mm below) temperature. Rotor speed Ω=4,400 rpm. Oil inlet temperature T_{in}=35.6^{o}C. Predictions and measurements in Ref. [7] for two specific loads.
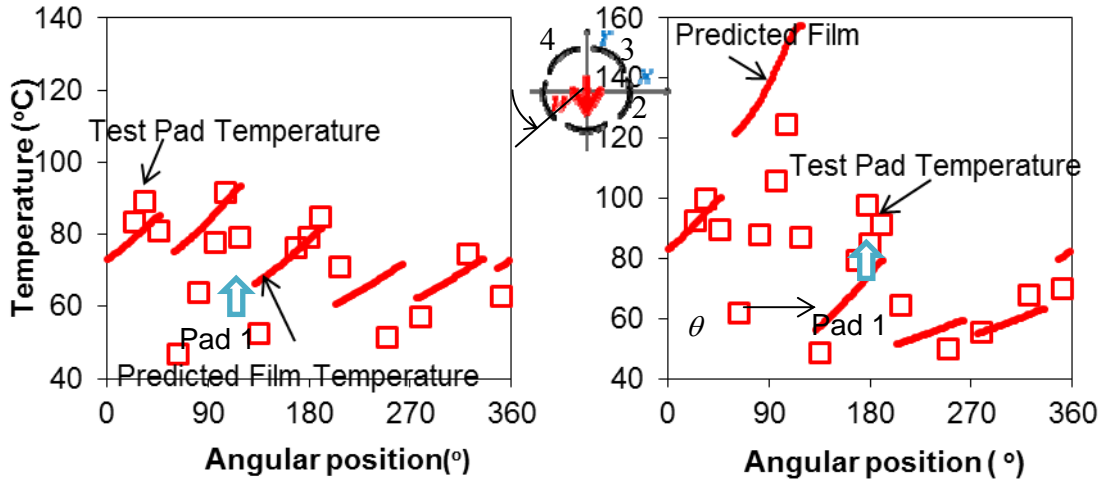
(a) Specific Load *W/LD*=783 kPa   **(b) Specific Load *W/LD* =3,132 kPa**
Inlet thermal mixing coefficient *λ*=0.8   **Inlet thermal mixing coefficient *λ*=0.9**
Fig. 27 TPJB film temperature and pad sub-surface (3.2 mm below) temperature. Rotor speed *Ω*=13,100rpm. Oil inlet temperature *T*$_{in}$=35.6^{o}C. Predictions and measurements in Ref. [7] for two specific loads.

TPJB impedance force coefficients Figure 28 shows the predicted and measured Re(*Z*) for a specific load of 1,566 kPa applied on the bearing and with the journal operating at a low speed of 4,400 rpm. The predicted Re(*Z*) shows a stronger frequency dependency than the measured (and predicted) data in Ref. [7]; in particular at high excitation frequencies (larger than twice the rotor speed synchronous frequency, at ~147 Hz).

The current model does account for the effects of temporal fluid inertia and pad mass and mass moment of inertia, which influence the bearing impedance coefficients at high excitation frequencies. The pivot stiffness also affects the frequency dependency of the impedances. A further study for the effects of fluid inertia, pad inertia, pad mass and pivot stiffness on the bearing impedances (real part and imaginary parts) appears in the following section.

64
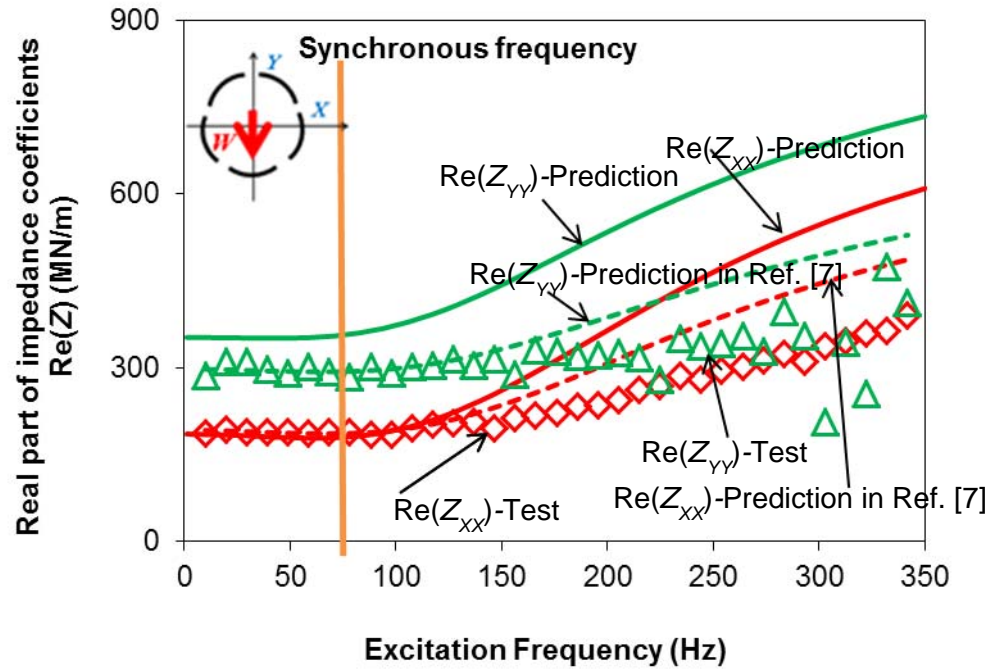
Fig. 28 Real part of TPJB impedance coefficients, Re(*Z*), versus excitation frequency. Rotor speed Ω=4,400 rpm and specific load (*W/LD*) =1,566 kPa. Current predictions, measurements and predictions in Ref. [7].

Figure 29 depicts the comparison of the predicted and experimental real part of the bearing impedances (*Z*) for operation at a high journal speed of 13,100 rpm. The measured and predicted impedances in Ref. [7] are frequency independent. The frequency independency of the impedance real parts results from a small range of the excitation frequency. Note that at a high rotor speed of 13,100 rpm, the maximum excitation frequency (350 Hz) is still lower than twice the synchronous speed frequency (437 Hz).
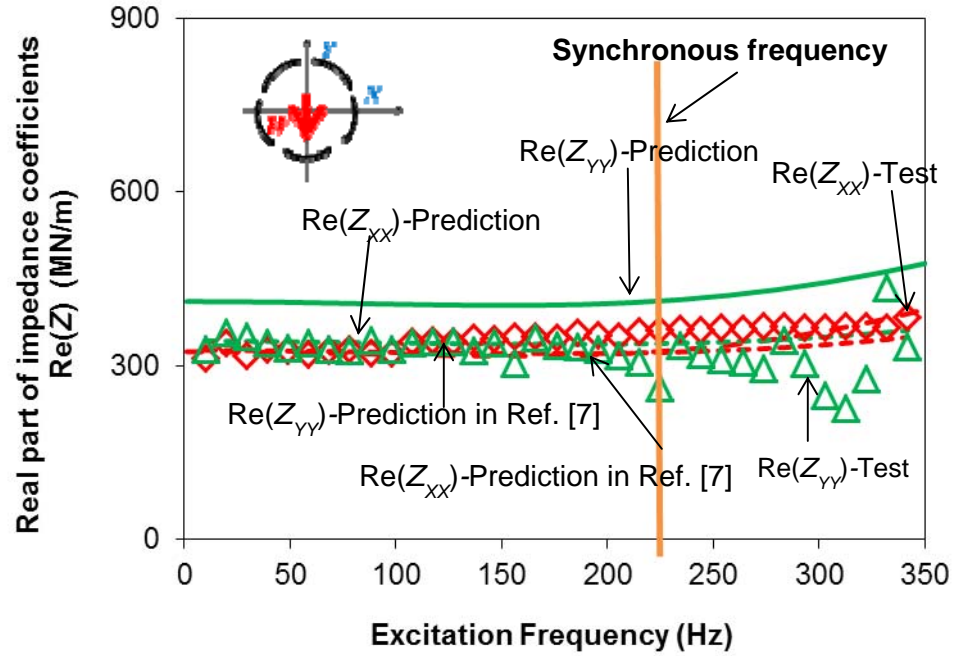
Fig. 29 Real part of TPJB impedance coefficients, Re(*Z*), versus excitation frequency. Rotor speed Ω=13,100 rpm and specific load (*W/LD*) =1,566 kPa. Current predictions, measurements and predictions in Ref. [7].

Figures 30 and 31 show the imaginary part of the bearing impedances, Im(*Z*), versus excitation frequency. The predicted Im(*Z*) are larger than the test data. At a low rotor speed of 4,400 rpm, the impedances in Fig. 30 show that the predicted damping coefficients are strongly frequency dependent at frequencies larger than twice the synchronous speed frequency. Also the bearing damping coefficients first increase and then dramatically decrease with increasing excitation frequency. The predicted Im(*Z*) in Ref. [7] show a similar trend with the current predictions. However, the test data shows a minimal frequency dependency, leading to a constant damping coefficient. At the high journal speed of 13,100 rpm, the slopes of both measured and predicted imaginary part of the bearing impedances increase slightly with excitation frequency, as shown in Fig. 31.
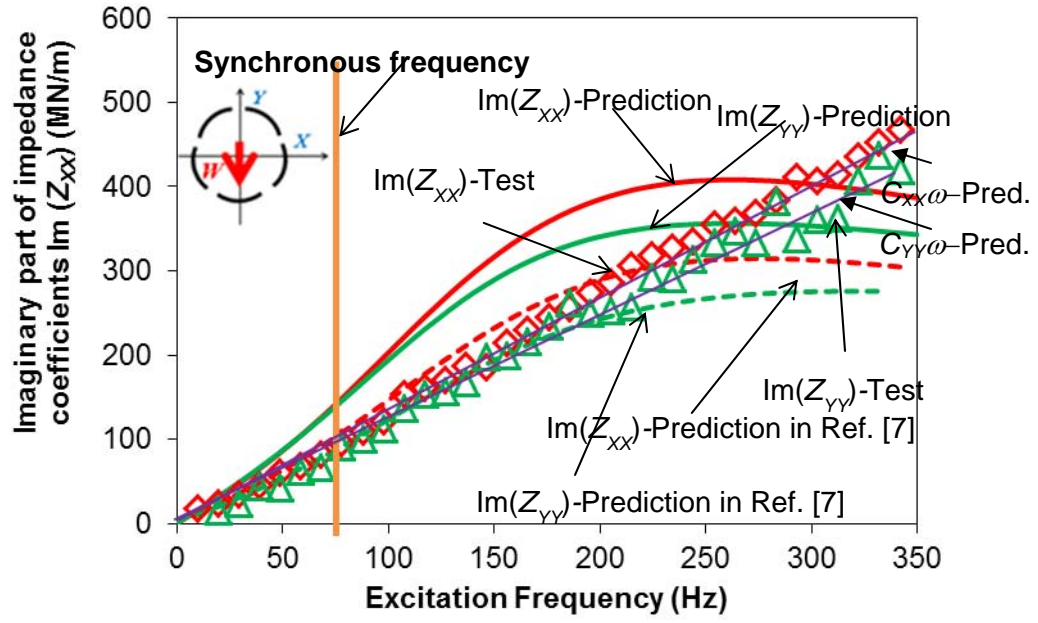
Fig. 30 Imaginary part of TPJB impedance coefficients, Im(*Z*), versus excitation frequency. Rotor speed Ω=4,400 rpm and specific load (*W/LD*) =1,566 kPa. Current predictions, measurements and predictions in Ref. [7].
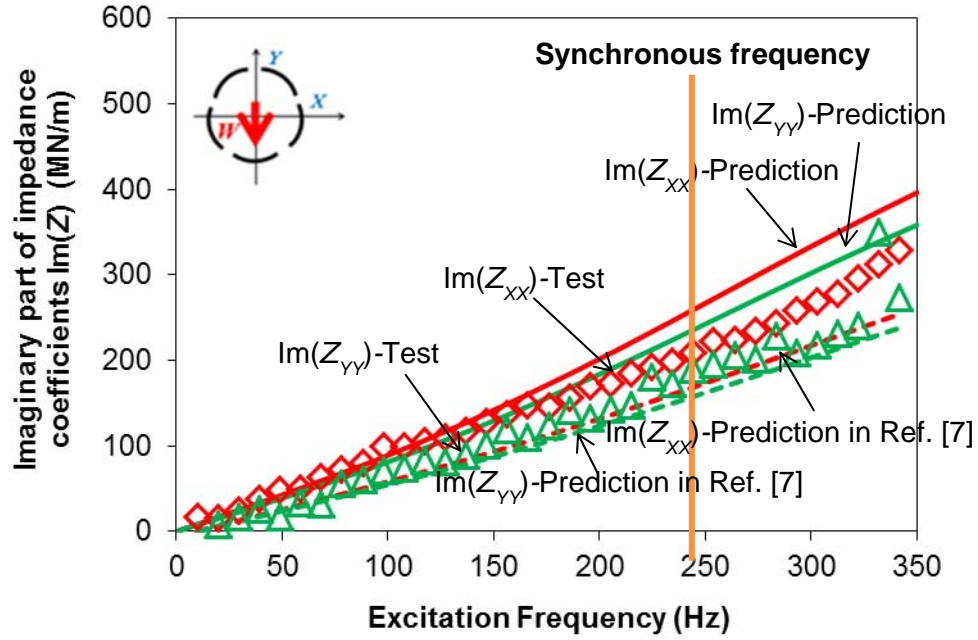
Fig. 31 Imaginary part of TPJB impedance coefficients, Im(Z), versus excitation frequency. Rotor speed Ω=13,100 rpm and specific load (W/LD) =1,566 kPa. Current predictions, measurements and predictions in Ref. [7].

Table 8 lists the correlation coefficient of the [*K-C-M*] curve fit parameters to the bearing predicted impedances (*Z*). The correlation coefficient of curve fit parameters to the predicted real part of the bearing impedance at speed 13.1 krpm is smaller than that for operation at speed 4.4 krpm, illustrating that a [*K-C-M*] model cannot adequately capture the bearing dynamic stiffness ($K-M\omega^2$) over the test frequency range (0-350 Hz) for operating at the high rotor speed (13.1 krpm) due to the frequency independency. Also a small correlation coefficient of the curve fit damping coefficient to the impedances (imaginary) part at a low rotor speed of 4.4 krpm reveals that the predicted damping coefficients are frequency dependent.

Table 8 Correlation coefficients of curve fit parameters to the predicted impedances at various operating conditions for a TPJB in Ref. [7]. Excitation frequency varies from 0 to 350 Hz.

Rotor speed	Specific load (kPa)	0	783	1,566	2,350	3,132
4.4 krpm	$K_{sXX} - M_{XX}\omega^2 \rightarrow \mathrm{Re}(Z_{XX})$	0.99	0.99	0.99	0.98	0.98
	$K_{sYY} - M_{YY}\omega^2 \rightarrow \mathrm{Re}(Z_{YY})$	0.99	0.99	0.98	0.98	0.98
13.1 krpm	$K_{sXX} - M_{XX}\omega^2 \rightarrow \mathrm{Re}(Z_{XX})$	0.83	0.85	0.89	0.93	0.95
	$K_{sYY} - M_{YY}\omega^2 \rightarrow \mathrm{Re}(Z_{YY})$	0.83	0.86	0.90	0.89	0.82
4.4 krpm	$C_{XX}\omega \rightarrow \mathrm{Im}(Z_{XX})$	0.26	0.44	0.54	0.61	0.69
	$C_{YY}\omega \rightarrow \mathrm{Im}(Z_{YY})$	0.26	0.60	0.76	0.79	0.77
13.1 krpm	$C_{XX}\omega \rightarrow \mathrm{Im}(Z_{XX})$	0.99	0.99	0.99	0.99	0.98
	$C_{YY}\omega \rightarrow \mathrm{Im}(Z_{YY})$	0.99	0.99	0.99	0.99	0.99

TPJB stiffness and damping coefficients for increasing specific loads Figures 32 and 33 show the predicted static stiffness coefficients, the measurements and predictions in Ref. [7]. Results show that the current model over predicts the bearing static stiffness coefficients. When the rotor operates at a speed of 4,400 rpm, the stiffness coefficient K_{YY} along the loaded direction (-Y), is over predicted by 27% at a specific load (W/LD) of 3,132 kPa. The predicted stiffness (K_{XX}) correlates well with test data at a low rotor speed of 4,400 rpm. Figures 32 and 33 show that the model in Ref. [7] delivers good predictions for the bearing stiffness coefficients because it includes pad flexibility. Wilkes notes the maximum pad static bending stiffness is just ~4.5 MN/m [7] (0.5%~1.5% of pivot stiffness) which shows that the pads themselves are flexible.
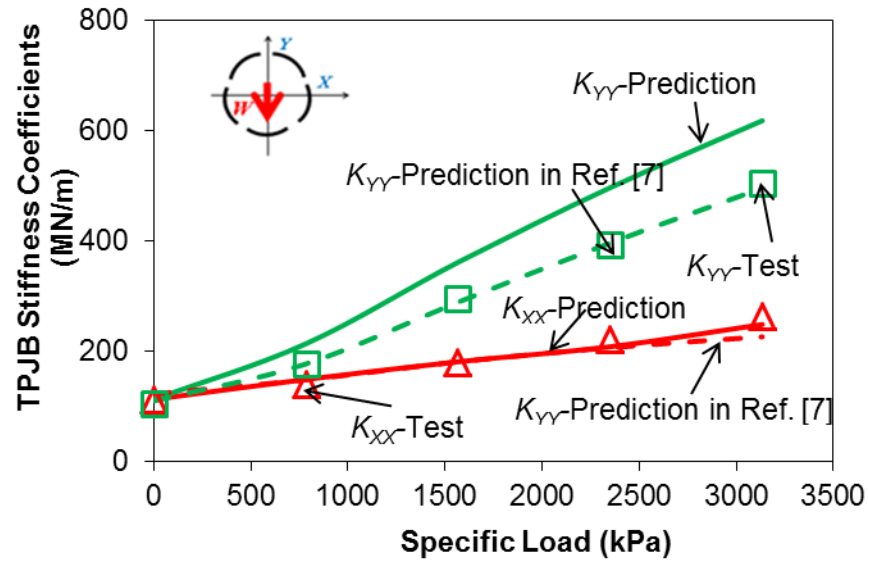
Fig. 32 TPJB static stiffness coefficients (*K*) versus specific load (*W/LD*). Rotor speed Ω=4,400 rpm. Current predictions, measurements and predictions in Ref. [7].
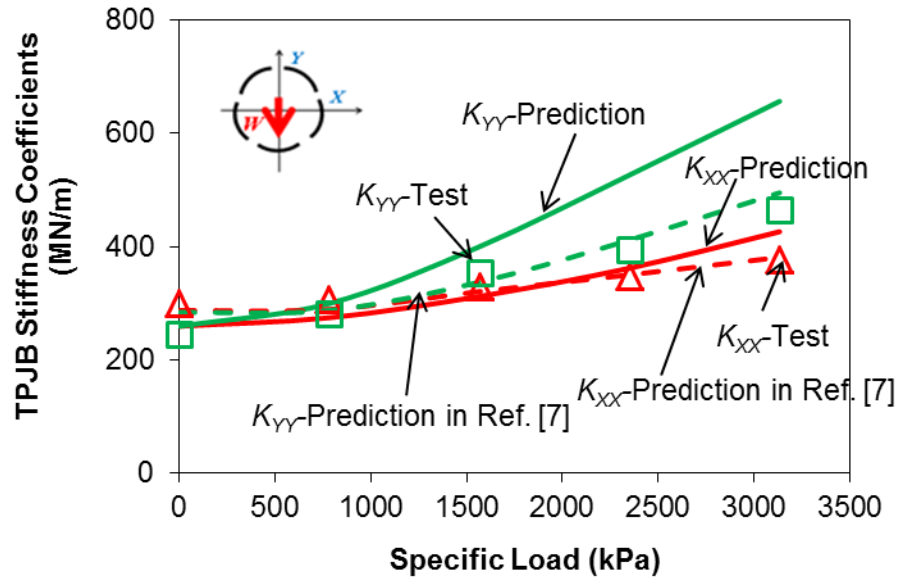
Fig. 33 TPJB static stiffness coefficients (*K*) versus specific load (*W/LD*). Rotor speed Ω=13,100 rpm. Current predictions, measurements and predictions in Ref. [7].

Figures 34 and 35 show the bearing damping coefficients versus specific load for two rotor speeds. The damping coefficients are derived from the bearing impedances (imaginary) using the [*K-C-M*] model. At a rotor speed of 4,400 rpm, the damping coefficient (C_{YY}) is overpredicted by 24% at the specific load of 3,132 kPa. At low specific loads (*WL/D* < 1,000 kPa), the predicted damping coefficients are still 46% larger than the measurements.

Note also that the test bearing has a large preload for each pad ($\bar{r}_p$=0.44). At a low specific load, the current model still predicts large reaction loads for all pads in the bearing, including the upper pads[11]. For example, the fluid film radial force acting on the upper pads at the zero load condition is sizeable and equals to about 2,000 N. In addition, pivot and pad flexibility have a more pronounced effect in reducing the

---

[11] Predictions of the loads acting on each pad are given in the following section.

71

damping coefficients than the stiffness coefficients. Consequently, pad flexibility does affect the bearing damping coefficients at low specific loads. The predicted damping coefficients in Ref. [7] are lower than the measurements, in particular at heavy loads, as shown in Figs. 34 and 35.
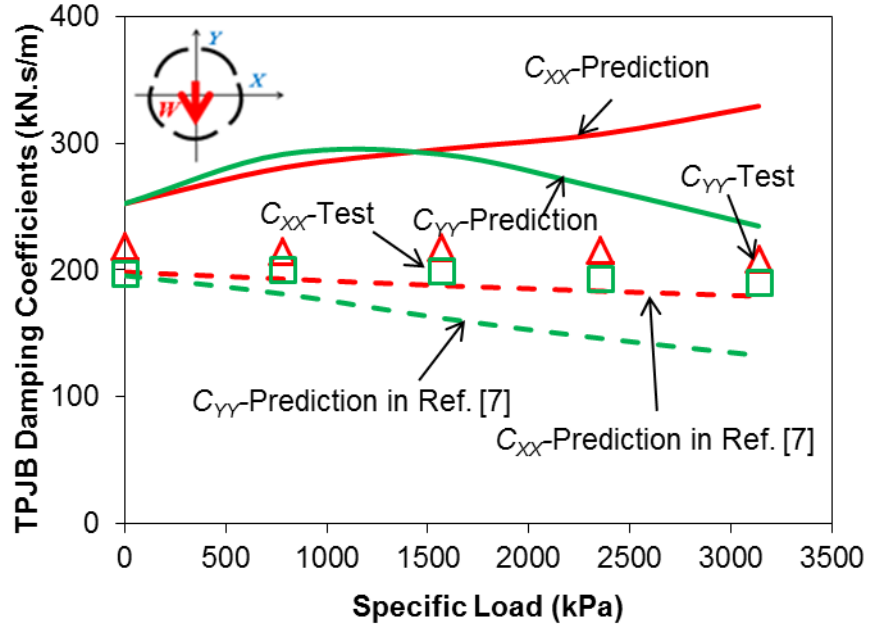
Fig. 34 TPJB damping coefficients (*C*) versus specific load (*W/LD*). Rotor speed Ω=4,400 rpm. Current predictions, measurements and predictions in Ref. [7].
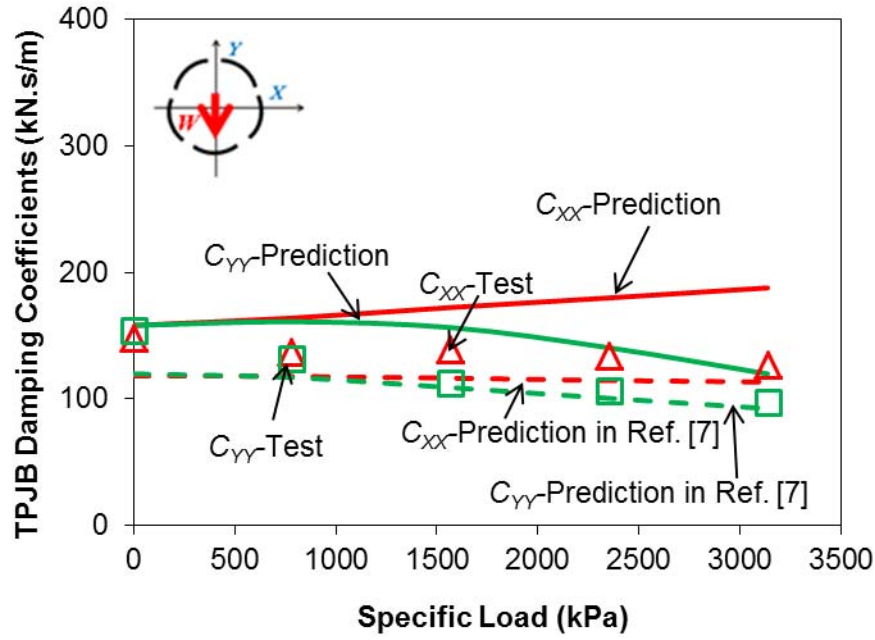
Fig. 35 TPJB damping coefficients (*C*) versus specific load (*W/LD*). Rotor speed Ω=13,100 rpm. Current predictions, measurements and predictions in Ref. [7].

Figures 36 and 37 depict the bearing virtual mass coefficients (*M*) versus increasing specific loads for operation at two rotor speeds, 4.4 krpm and 13.1 krpm. Test data (Fig. 28) show that the bearing dynamic stiffness coefficient ($K=K_s-M\omega^2$) is frequency dependent at the low rotor speed over the frequency range of testing (0-350Hz). At the low rotor speed (4.4 krpm), both current predictions and predictions in Ref. [7] show negative virtual mass coefficients and with a magnitude larger than the test data, indicating a stronger "stiffening" effect in the bearing real part of the bearing impedances at high frequency excitation. For the bearing operates at a high speed of 13.1 krpm, the virtual mass coefficients are nearly zero, denoting frequency independent dynamic stiffness coefficients.

73
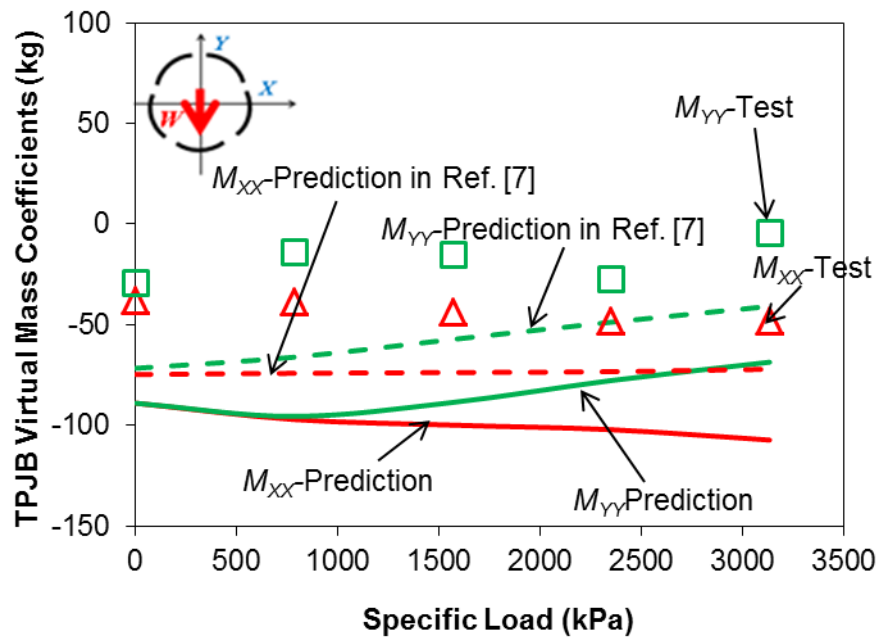
Fig. 36 TPJB virtual mass coefficients (*M*) versus specific load (*W/LD*). Rotor speed Ω=4,400 rpm. Current predictions, measurements and predictions in Ref. [7].
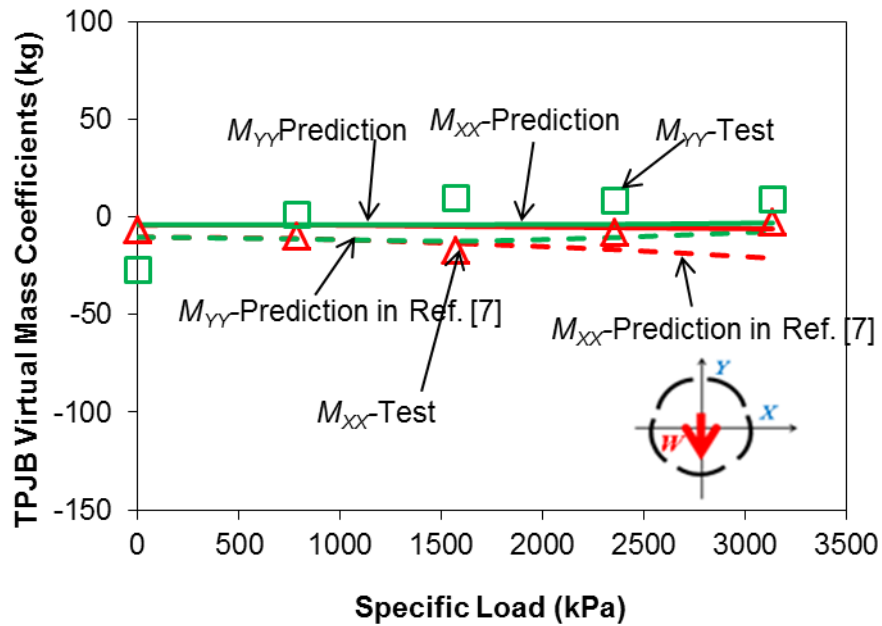
Fig. 37 TPJB virtual mass coefficients (*M*) versus specific load (*W/LD*). Rotor speed Ω=13,100 rpm. Current predictions, measurements and predictions in Ref. [7].

Predicted film thickness, fluid film forces and pivot flexibility Figures 38 and 39 depict the predicted film thickness for various operating conditions. Note that even the upper pads show a converging film thickness. Hence, predictions show that all pads in the test bearing are loaded. The film thickness does not vary much with rotor speed, in particular for the bottom loaded pads due to the heavy preload.
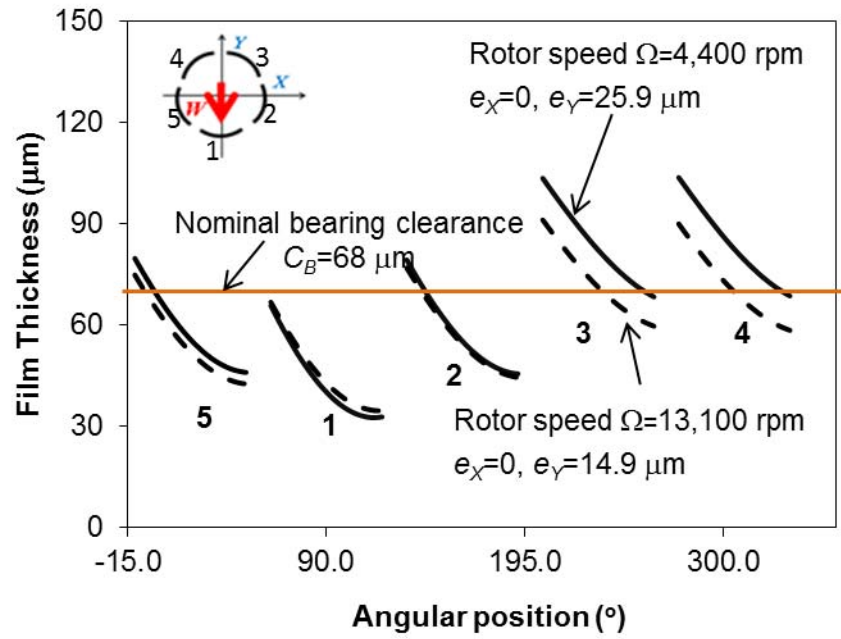
Fig. 38 TPJB predicted film thickness distribution for the bearing in Ref. [7] at two rotor speeds. Specific load (*W/LD*)=783 kPa. Nominal bearing clearance C_B=68 μm. Pad preload $\bar{r}_P$ =0.44.
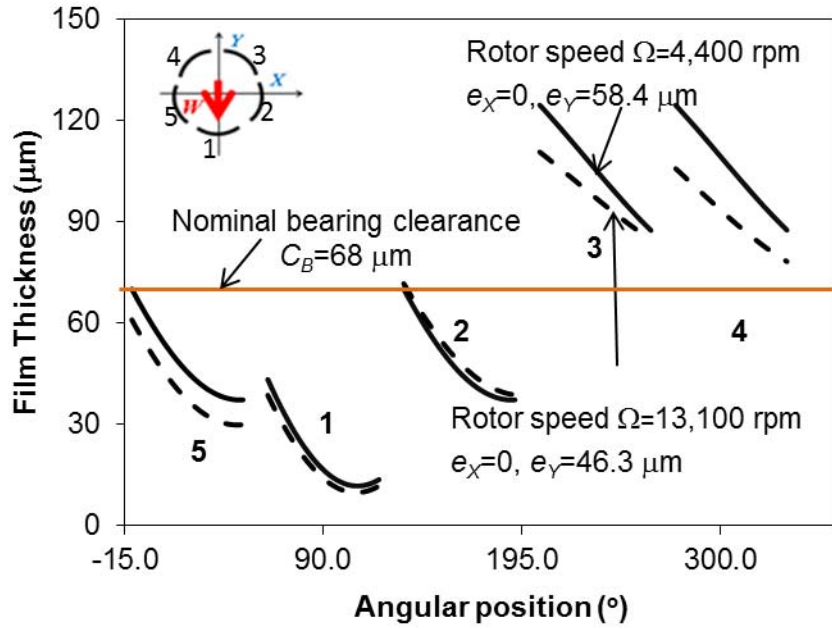
Fig. 39 TPJB predicted film thickness distribution for the bearing in Ref. [7] at two rotor speeds. Specific load (*W/LD*)=3,132 kPa. Nominal bearing clearance *C_B*=68 μm. Pad preload $\bar{r}_P$ =0.44.

Figure 40 shows the predicted fluid film specific load (F_ξ/LD) acting on each pad versus the specific load (*W/LD*) applied on the bearing. Note the pivot pad reaction force balances the fluid film force acting on each pad. Results show that the fluid film force on the bottom pad (#1) increases significantly with the applied load and dominates the static load applied on the bearing ($F_\xi \approx W$) for specific static loads (*W/LD*) > 1,000 kPa. The fluid film forces on Pad #2 and Pad #5 also increase slightly, while those on the upper pads (# 3 and # 4) decrease with increasing specific load. Note that at the zero load condition, the upper pads (Pads #3 and #4) support sizable loads because of the large pad preload ($\bar{r}_P \geq 0.44$). This effect is more pronounced for operation at a high rotor speed, as shown in Fig. 40.

(a) rotor speed Ω=4,400 rpm   **(b) rotor speed Ω=13,100 rpm**
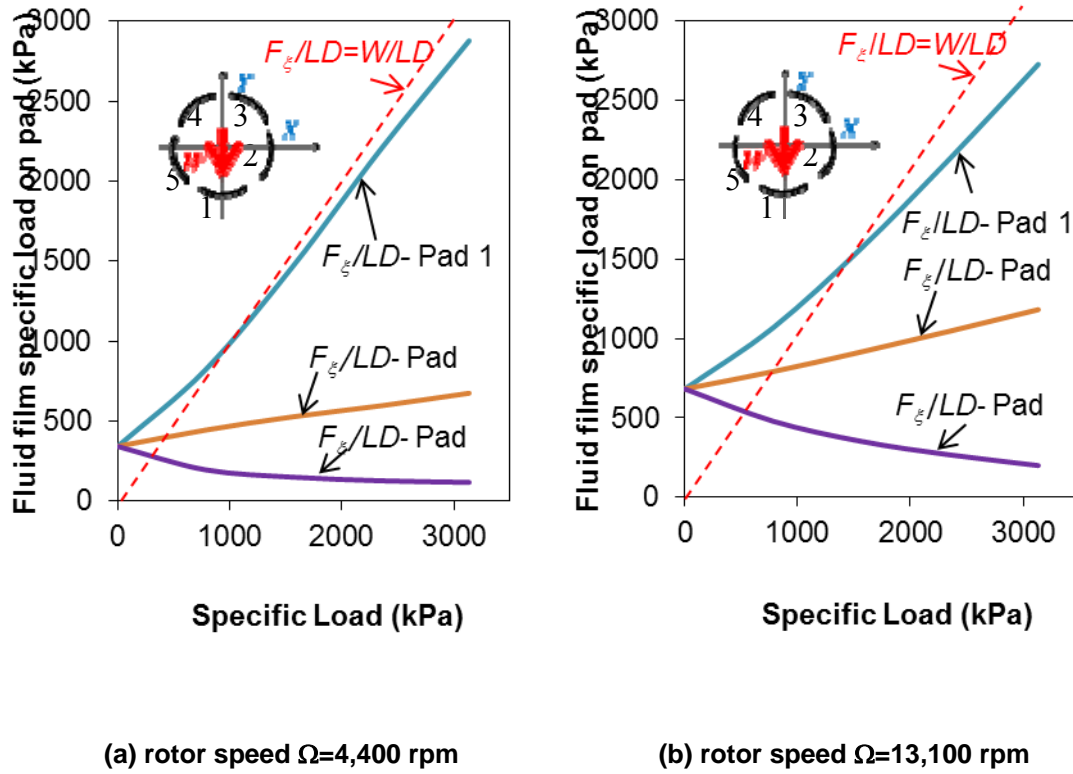
Fig. 40 Fluid film specific load on each pad (F_ξ/LD) versus specific load (W/LD). Predictions for the bearing in Ref. [7] at two rotor speeds.

Figures 41 shows the predicted pivot radial stiffness for each pad of the bearing as it operates at speeds of 4,400 rpm and 13,100 rpm versus increasing static load. Note that the pivot stiffness is a function of the force on the pivot (pad). Hence, the pivot stiffness increases with increasing specific load applied on the bearing as the fluid film force on each pad also raises. The fluid film forces on the pads at a high journal speed of 13,100 rpm are larger than those at the low journal speed of 4,400 rpm, see Fig. 41(b). Thus, each of the load-dependent pivot stiffness increases with increasing journal speed, in particular at a low specific load.

Figure 42 depicts the predicted pivot radial deflections for each pad in the test bearing versus various specific loads. According to Eq. (42), the pivot radial deflection increases with the fluid film force on the load pads (#1), as well as the pivot radial stiffness. Note that for the zero load condition, the pivot of each pad has a radial

78

deflection of ~4 μm at the rotor speed of 4,400 rpm. At a high rotor speed of 13,100 rpm, the pivot radial deflection of the loaded pad is 17.4 μm, which is nearly 25% of the nominal bearing clearance.

(a) rotor speed Ω=4,400 rpm   (b) rotor speed Ω=13,100 rpm
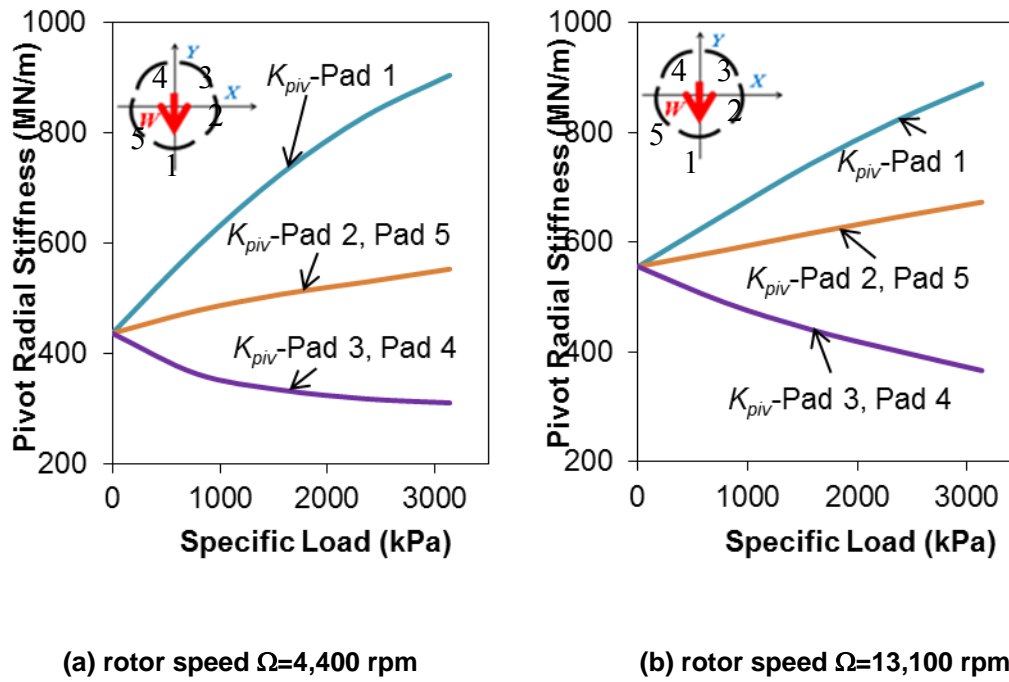
Fig. 41 Pad pivot stiffness (K_{piv}) versus specific load (*W/LD*). Predictions for the bearing in Ref. [7] at two rotor speeds.

(a) rotor speed Ω=4,400 rpm   (b) rotor speed Ω=13,100 rpm
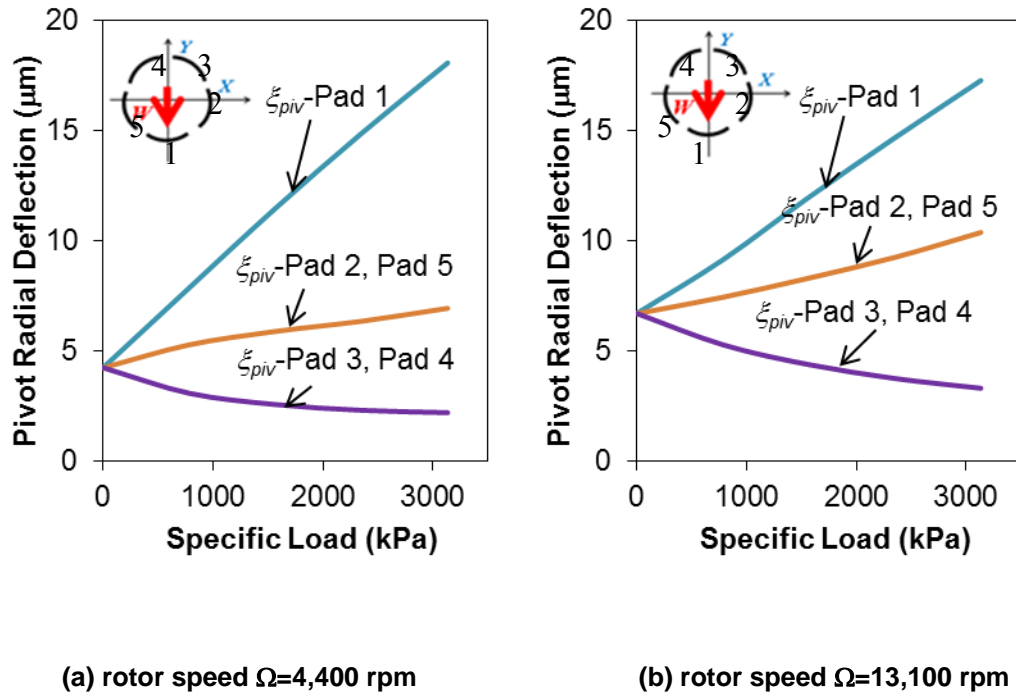
Fig. 42 Pivot radial deflection (ξ_{piv}) versus specific load (*W/LD*). Predictions for the bearing in Ref. [7] at two rotor speeds.

Closure The current model accounts for the effect of pivot flexibility and uses the pivot load-deflection function reported in Ref. [7]. Hot bearing clearances and pad clearances are estimated using an equation based on the average measured temperature rise, as stated in Ref.[7]. The predictive model delivers reasonable predictions on TPJB stiffness force coefficients at low specific loads (*W/LD* < 1,000 kPa). The predicted stiffness coefficients at high specific loads (*W/LD* > 1,000 kPa) and along the loaded direction are about 30% higher than measurements. The damping coefficients are overpredicted at specific loads (*W/LD*) < 3,132 kPa. Wilkes [7] demonstrates that pad flexibility, which is also accounted for in the current predictive model, increases significantly the pad clearances and consequently reduces the TPJB stiffness and damping coefficients for operation with large static loads.

The predicted impedances for the bearing render frequency dependent dynamic stiffness and damping coefficients for the bearing at a low speed of 4.4 krpm.

Incidentally, frequency-independent impedances (real and imaginary part) are apparent when the bearing operates at a high speed of 13.1 krpm. The experimental impedances (real and imaginary part) are always frequency independent for the bearing operating at speeds equaling 4.4 krpm and 13.1 krpm.

The pivot radial stiffness, as well as a pivot radial deflection, increase with an increasing fluid film force acting on a pad. Predictions show that all pads still support sizable loads at the zero load condition due to the large pad preload, in particular at the high rotor speed.

The pad and its pivot in the test bearing are two separate components. Each pad has a small bending stiffness due to a small gap behind the pad, in the section where the rocker-back pivot contacts the bearing housing [7]. The current model accounts for the pad flexibility with an equivalent pad-pivot stiffness. The model delivers bearing stiffness and damping coefficients that over predict slightly the experimental force coefficients.

Example 3-Predicted Forced Performance for a Rocker Back LBP TPJB [23]

Kulhanek and Childs [23,27] investigate experimentally the static and dynamic forced performance of a five-pad TPJB in a load-between-pad configuration. This section presents predictions for the test bearing in Refs. [23,27] by using an estimated pivot stiffness and operating bearing clearances. Figure 43 shows photographs of the test TPJB with a leading edge groove arrangement and 50% offset pivots. Figure 44 shows a schematic view of the test five-pad TPJB with load-between-pad configuration.

Test bearing with oil exit ports and end seals

OIL EXIT PORTS   END SEALS

Front view of a tilting pad with 50% pivot offset and leading edge groove

Top view of a tilting pad with leading edge groove (LEG)

ROTATION

OIL INLET PORT   LEG
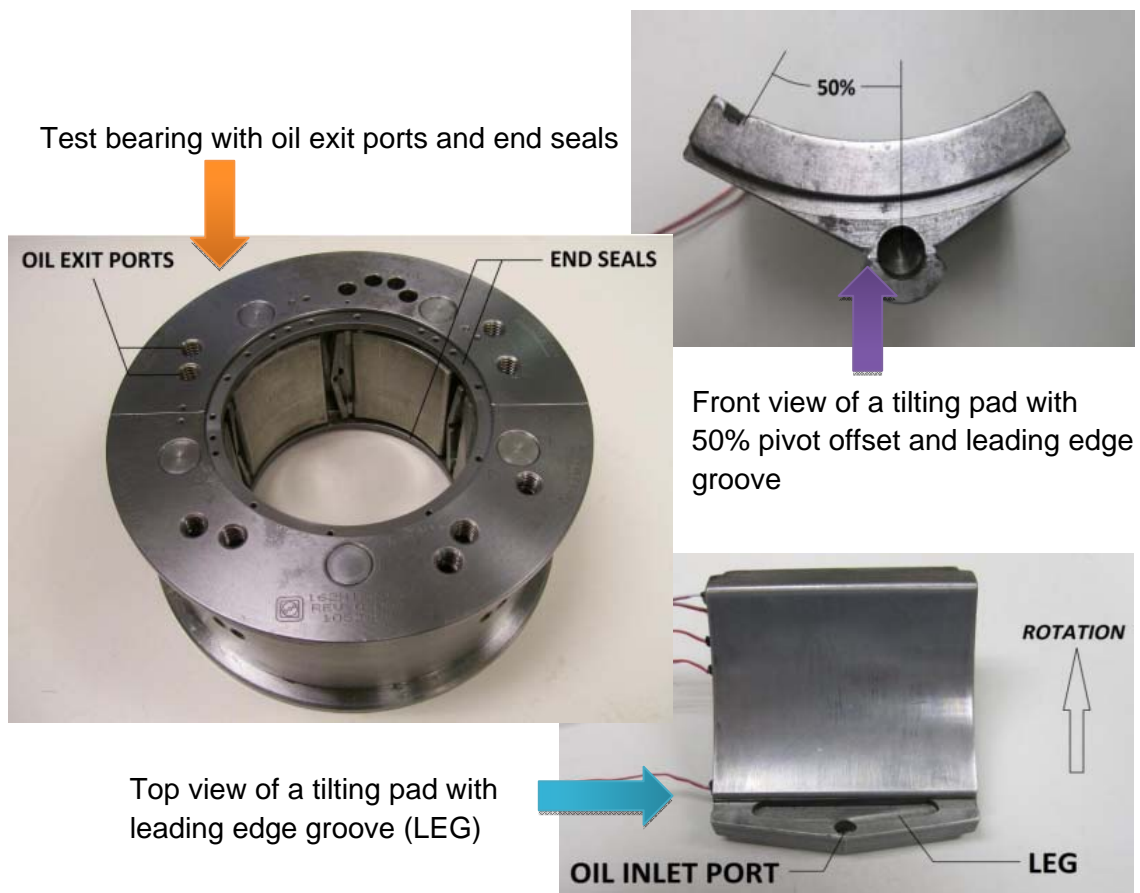
Fig. 43 Photographs of a test TPJB with leading-edge-groove pads in Ref. [23].
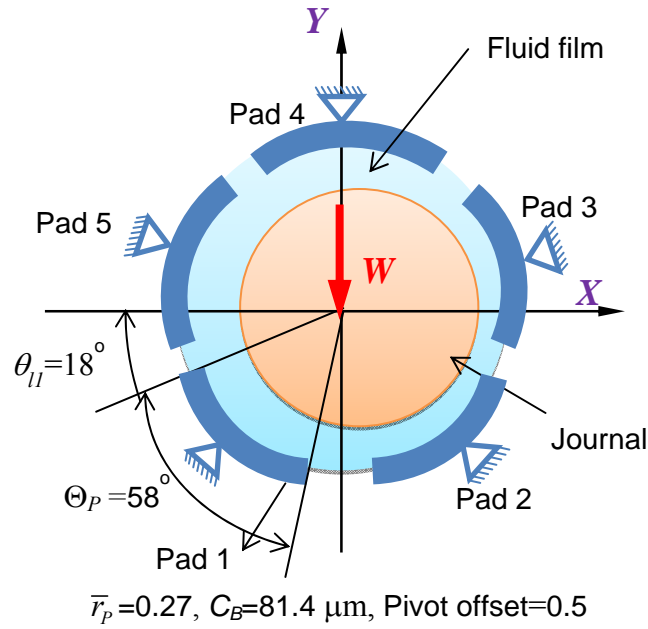
Fig. 44 Load configuration and pad arrangements of the test tilting pad journal bearing in Ref. [23].

Table 9 lists the geometry parameters of the test TPJB and the operating condition as given in Ref. [23,27].

Table 9 Parameters of the test TPJB and operating condition in Refs. [23,27].

Number of pads	5
Configuration	LBP
Pad arc angle	57.87°
Rotor diameter, D	101.6 mm
Pad axial length, L	60.3 mm
Pivot offset	50%
Pad preload, $\bar{r}_P$	0.27
Cold bearing clearance, C_B	81.4 μm
Cold pad clearance, C_P	112 μm

Pivot type	Rocker back
Pad mass, m_P	0.44 kg
Pad inertia about pivot, I_P	2.49×10^{-4} kg.m^2
Lubricant type	ISO VG32
Oil supply temperature	43.6 $^{\circ}$C
Oil density, ρ	856.2 kg/m^3
Oil viscosity at 43.6 $^{\circ}$C	0.0228 Pa.s
Temperature viscosity coefficient, α	0.0291/K
Journal speed, Ω	7,000 rpm-16,000 rpm
Static specific load, *W/LD*	0-3,101 kPa
Inlet thermal mixing coefficient, λ	0.65, 0.75, 0.90

In the predictive model, the rotor speeds are 7 krpm and 16 krpm, the minimum and maximum speeds in Kulhanek's measurements [23]. The maximum shear flow Reynolds numbers (Re=$\rho\Omega RC_B/\mu$) at the rotor speed of 7 krpm and 16 krpm are 357 and 649, respectively. As the shear flow Reynolds numbers are smaller than 1,000, the thin film flow is laminar.

According to the analyses for the bearings [7,13] in the previous sections, a large thermal mixing coefficient (λ>0.7) is necessary for the accurate prediction of the pad maximum temperature at the pad trailing edge when the bearing operates at a high rotor speed (>10,000 rpm) or at a small specific load (~0 kPa). Thus λ=0.9 is selected for tests at the zero load condition, and λ=0.75 for operation at a rotor speed of 16,000 rpm. When the rotor spins at a speed of 7,000 rpm, the inlet thermal mixing coefficient is taken as λ=0.65. Assume that the lubricant carries away all the heat generated in the TPJB, thus the thermal condition is chosen as adiabatic.

Effect of fluid film temperature on the operating bearing and pad clearances
According to the analysis in Ref. [7], a reduction in the bearing and pad clearances upon

operations greatly influences the forced performance of a test TPJB. The current predictive model includes the change of bearing clearance due to fluid film temperature changes. An average pad temperature at the pivot location, reported in Ref. [27], is used to determine the hot bearing clearances under different operating conditions. The average temperature raise used to calculate the operating bearing and pad clearances for this TPJB model is obtained by averaging the predicted fluid film temperature in the TPJB model. Table 10 lists the estimated bearing and pad clearances, dimensionless pad preloads and average pad temperature rises.

The operating bearing clearance for the TPJB is estimated by using the thermal expansion coefficient suggested by Wilkes, α_{c_b} =0.396 μm/°C [7], since Refs. [23] and [7] report bearing dynamic load measurements conducted in the same test rig. The estimated hot bearing clearance equals to $(C_B - \alpha_{c_b} \Delta T_{avg})$. As the bearing clearance $(C_B = R_B - R_J)$ decreases due to the thermal expansion of the rotor and pad surfaces, the pad clearance $(C_P = R_P - R_J)$ decreases as well and the change of pad clearance equals to $\alpha_{c_b} \Delta T_{avg}$. Hence, the dimensional pad preload remains constant while the dimensionless pad preload $(\bar{r}_P = 1 - C_B / C_P)$ varies at different operating conditions. At the journal speed of 16 krpm, the bearing radial clearance (C_B) decreases by 21% from its nominal value for a temperature rise of 42°C and a specific load of 3,101 kPa.

Table 10 Predicted hot bearing and pad radial clearances and measured pad average temperature rise in Ref. [27].

Rotor speed Ω (rpm)	Specific load W/LD (kPa)	Bearing clearance C_B (μm)	Pad clearance C_P (μm)	Pad dimensionless preload $\bar{r}_P$	Average temperature rise ΔT (°C)
	0	73.9	104.0	0.289	18.9
	345	73.7	103.8	0.290	19.5
7,000	1,034	72.9	103.0	0.292	21.4
	1,732	72.3	102.4	0.294	23.1
	2,412	71.6	101.7	0.296	24.7
	3,101	71.1	101.2	0.297	25.9

Table 10 Continued

Rotor speed Ω (rpm)	Specific load *W/LD* (kPa)	Bearing clearance C_B (μm)	Pad clearance C_P (μm)	Pad dimensionless preload $\bar{r}_P$	Average temperature rise ΔT (°C)
	0	67.2	97.3	0.309	35.8
	345	67.1	97.2	0.310	36.1
16,000	1,034	66.9	97.0	0.311	36.7
	1,732	66.1	96.2	0.313	38.7
	2,412	65.4	95.5	0.315	40.5
	3,101	64.7	94.8	0.318	42.3
Nominal bearing clearance C_B= 81.4 mm, Nominal pad clearance C_P= 112 mm					

Pivot flexibility In Refs. [23,27], the predictive model [17] used by Kulhanek and Childs greatly overpredicts the bearing static and dynamic forced performance characteristics, since it does not account for the effect of pivot flexibility.

A load-dependent pivot stiffness is difficult to determine for this test bearing since there is little information known about the pivot-pad structure. Hence, a constant pivot stiffness is estimated and used in the predictive model for simplicity. The pivot stiffness (K_{pY}) along the load direction (-*Y*) is estimated using the formula,

$$\frac{1}{K_{pY}} = \frac{1}{K_{mY}} - \frac{1}{K_{rY}}$$

(46)

Above, K_{mY} is the experimental bearing static stiffness coefficient along the load direction (-*Y*) at a rotor speed of 7,000 rpm, and K_{rY} is the predicted film stiffness coefficient (rigid pivot) using a hot bearing clearance at the same operating condition. Thus, K_{rY} is the fluid film stiffness only. The pivot stiffness obtained from the stiffness K_{mY} and K_{rY} for operation at a high rotor speed of 16 krpm is nearly the same with that at a speed of 7 krpm. Note that the stiffness coefficients in Eq.(46) are applicable to displacements along the load direction (-*Y*). Table 11 lists the estimated pivot stiffness K_{pY}, the measured static stiffness coefficient K_{mY} for the bearing, and the predicted stiffness coefficient K_{rY} versus specific load.

Table 11 Fluid film stiffness, measured TPJB stiffness and estimated pivot stiffness for the bearing in Ref. [27].

Specific Load (kPa)	Predicted TPJB Stiffness (rigid pivot) K_{rY} (MN/m)	Measured TPJB static stiffness K_{mY} (MN/m) [23]	Estimated Pivot Stiffness K_{pY} (MN/m)
345	167.1	148	1,298
1,034	335.2	240	844.0
1,732	584.1	358	926.1
2,412	878.5	471	1,013
3,101	1,234	583	1,106
Average estimated pivot stiffness for the bearing along Y direction			1,037

The simple model gives an average pivot stiffness K_{pY} =1,037 MN/m. Note the estimated pivot stiffness (K_{pY}) varies with the static load applied on the bearing. The static load is applied along the $-Y$ direction and the fluid film reaction forces on the journal are mainly from the bottom two pads. Figure 45 shows a geometrical representation between the deduced pivot stiffness (K_{pY}) and the pivot stiffness of each bottom pad.
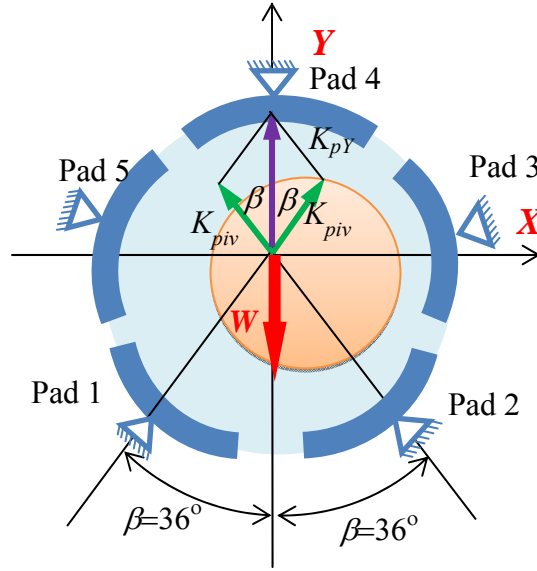
Fig. 45 Geometrical relationship between the bearing pivot stiffness and pad pivot stiffness for the bearing in Ref. [23].

Hence, the pivot stiffness for each pad used in the predictive model is

$$K_{piv} = \frac{K_{pY}}{2\cos\beta} = 641 \text{ MN/m}, \ \beta=36° \tag{47}$$

Note that the process to estimate the pivot stiffness is based on the predicted (rigid pivot) bearing stiffness coefficients calculated by using the operating bearing clearance. Thus, the pivot stiffness is sensitive to the assumption on the operating bearing clearance. An overprediction on the operating bearing clearance will cause an underprediction of the pivot stiffness. Also, in the above procedure to estimate the pivot stiffness, pads #3, #4 and #5 are assumed to be unloaded so that the pivot stiffness of those pads does not influence the bearing stiffness. This assumption is not accurate at a small specific load since the upper pad has a preload $(\bar{r}_P)$ ~0.27.

Journal center displacements Table 12 lists the predicted journal center displacement (e_Y) and operating pad clearance at various operating conditions. The

88

journal center displacement (e_Y) is underpredicted greatly at the highest rotor speed of 16 krpm.

Table 12 Predicted pad clearance (C_P) and journal center displacement (e_Y) for the bearing in Ref. [23,27].

Rotor speed Ω (rpm)	Specific load W/LD (kPa)	Pad clearance C_P (μm)	Journal displacement e_Y (μm)		Difference (%)	Journal displacement e_X (μm)	
			Test	Prediction		Test	Prediction
	0	101.2	0.0	0.09	-	0.0	0.0
	345	101.0	9.8	17.3	25.3%	0.8	0.3
7,000	1,034	99.9	27.7	40.8	22.1%	1.6	0.7
	1,732	99.0	41.5	55.1	20.8%	1.6	1.0
	2,412	98.1	51.3	66.1	24.9%	2.4	1.2
	3,101	97.4	59.4	75.1	24.7%	5.7	1.4
	0	92.1	0.0	0.05	-	0.0	0.0
	345	91.9	6.5	10.0	53.9%	1.6	0.6
16,000	1,034	91.6	16.3	28.2	57.2%	3.3	2.1
	1,732	90.5	26.0	42.8	54.5%	4.9	3.6
	2,412	89.6	35.0	54.8	52.9%	6.5	0.2
	3,101	88.6	43.1	64.8	53.2%	6.5	2.8

Figure 46 shows the predicted and measured journal displacement versus increasing specific load. The journal displacement (e_Y) along the load direction (-Y) is overpredicted by a maximum of 25% and 57% at speeds 7 krpm and 16 krpm, as shown in Table 12 and Fig. 46. The overprediction of the journal displacement is attributed to a too soft pivot stiffness or a too large operating bearing clearance used in the predictive model.
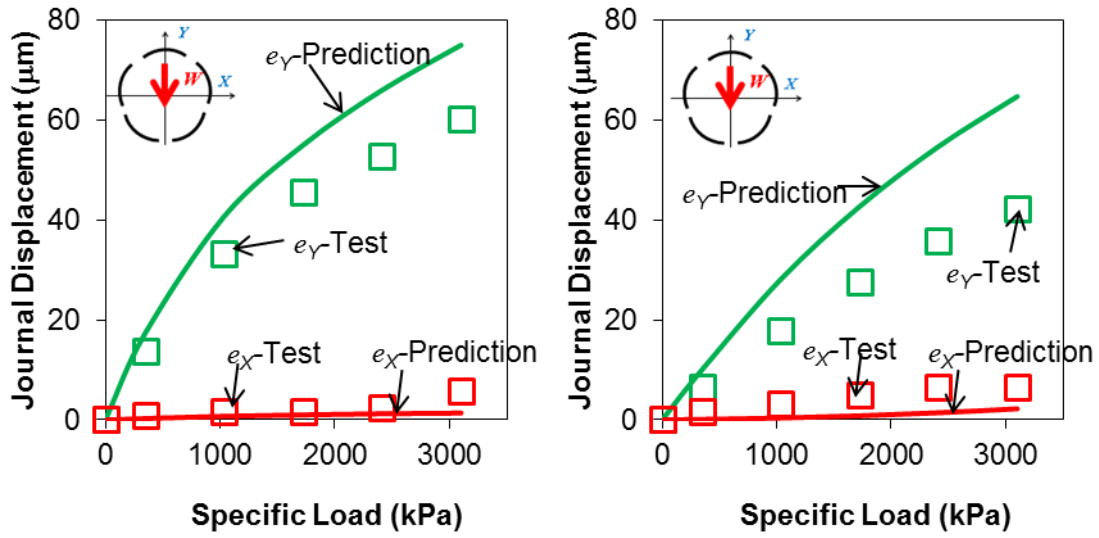
(a) rotor speed Ω=7,000 rpm   **(b) rotor speed Ω=16,000 rpm**
**Fig. 46 TPJB Journal center displacements (*e*) versus specific load (*W/LD*).
Predictions and measurements in Ref. [27] for two rotor speeds.**

Predicted film temperature and measured pad sub-surface temperatures
Figures 47-50 depict the predicted oil film temperature and the recorded pad sub-surface
temperatures along each pad for operation at 7 krpm and 16 krpm and upon various
specific loads. Reference [27] reports the pad sub-surface temperatures measured just
below the Babbitt surface.

Figure 47 shows the predicted and measured temperatures at the zero load operating
condition (*W/LD*=0 kPa). Predicted film temperatures correlate well with the measured
pad sub-surface temperatures at the pad trailing edge. Predictions show that the leading
edge groove oil feed is not advantageous at small specific loads since the large thermal
mixing coefficient (*λ*=0.9) indicates a large amount of hot oil mixes with the fresh oil at
a pad leading edge. The reason is that at the zero load condition, there is no axial
pressure gradient pushing the hot fluid out (to the sides), hence the hot fluid resides more
time inside the bearing and thus increases its operating temperature. Note that in
opposition to the temperatures reported in Ref. [7] for another TPJB, at the zero load

90

condition, the pad sub-surface temperature in Ref. [27] does not experience a drop at the pad trailing edge since there is no oil cavitation in this region.
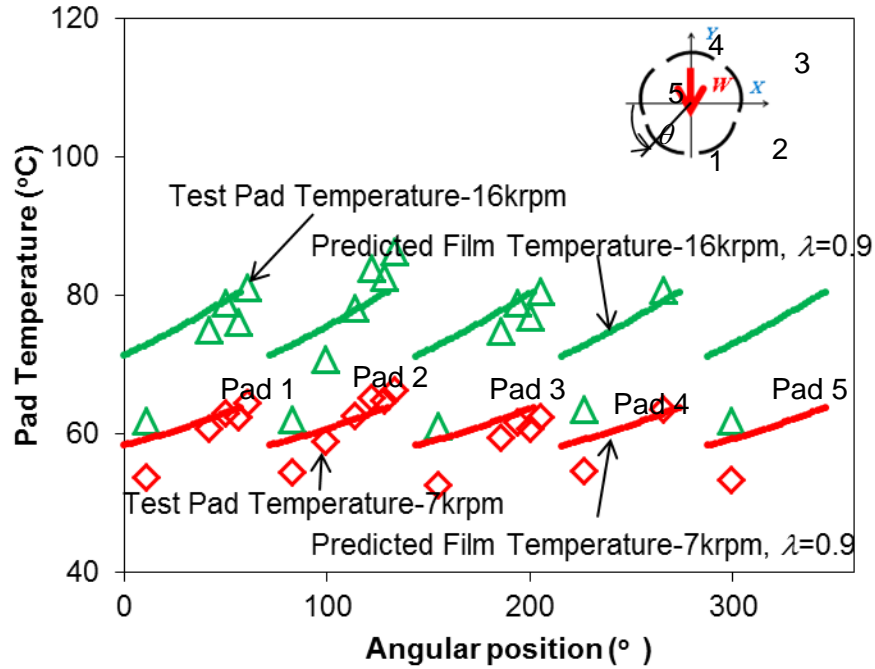
Fig. 47 TPJB predicted oil film temperatures and measured pad sub-surface temperatures in Ref. [27]. Specific load (*W/LD*)= 0 kPa. Rotor speed Ω=7,000 rpm and 16,000 rpm. Pad inlet thermal mixing coefficient λ=0.9.

Figures 48 and 49 show the predicted film temperatures and measured pads sub-surface temperatures in the test TPJB operating with the specific loads equaling to 1,732 kPa and 3,101 kPa and two rotor speeds. At a rotor speed of 7 krpm, the predicted film temperature shows a good correlation with the measured pad temperatures under a specific load equaling 3,101 kPa. The predicted film temperatures are lower than the measured pads sub-surface temperatures, in particular for operations at the rotor speed of 16 krpm, which indicates that a larger thermal mixing coefficient (λ>0.7) is required for a high speed operating condition. Note that when the specific load equals to 1,732 kPa

and 3,101 kPa, the pad sub-surface temperature exhibits a drop at the trailing edge of the loaded pads due to cavitation.
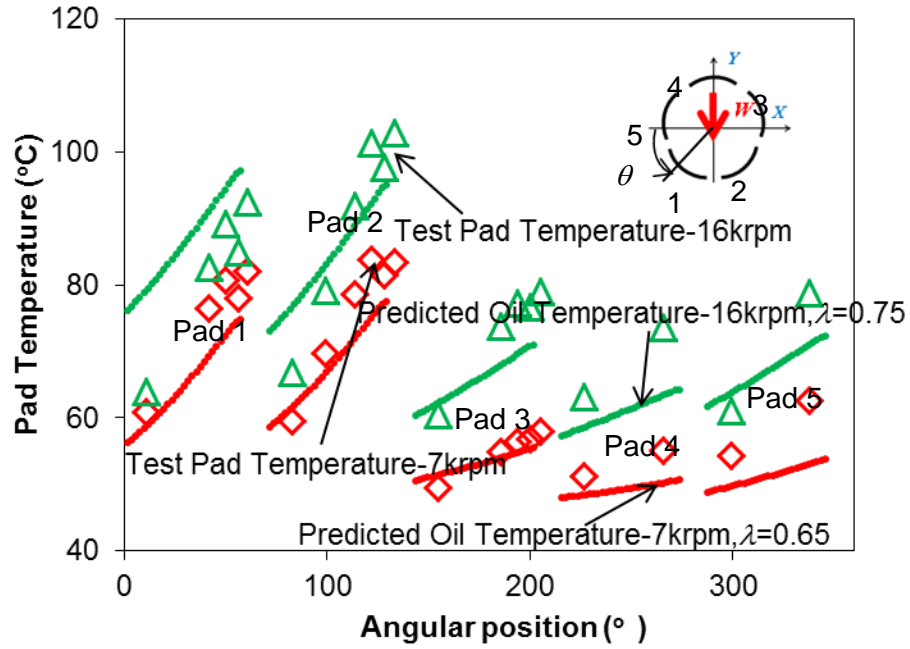
Fig. 48 TPJB predicted oil film temperatures and measured pad sub-surface temperatures in Ref. [27]. Specific load (*W/LD*)= 1,732 kPa. Rotor speed Ω=7,000 rpm and 16,000 rpm. Pad inlet thermal mixing coefficient λ=0.65 and 0.75.
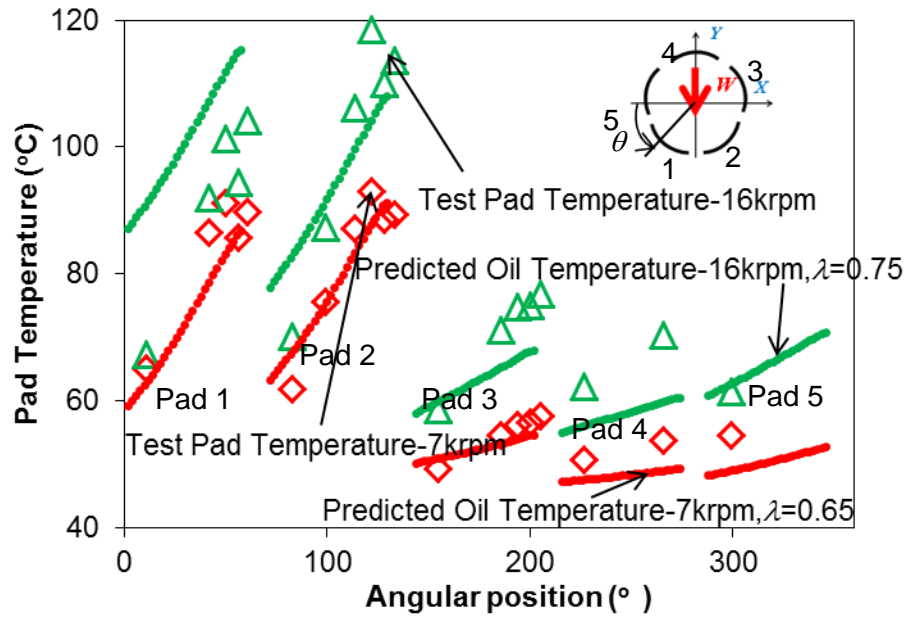
Fig. 49 TPJB predicted oil film temperatures and measured pad sub-surface temperatures in Ref. [27]. Specific load (*W/LD*)= 3,101 kPa. Rotor speed Ω=7,000 rpm and 16,000 rpm. Pad inlet thermal mixing coefficient λ=0.65 and 0.75.

Impedance coefficients for bearing Figures 50 and 51 show the real part of the bearing impedances (*Z*) coefficients versus increasing excitation frequency for operation with a specific load of 1,723 kPa and two rotor speeds. At a low rotor speed of 7 krpm (117 Hz), the predicted real part of *Z* correlates well with test data at subsynchronous excitation frequencies (ω< 117 Hz). When the frequency is larger than about twice the synchronous frequency (234 Hz), the predicted real part of the impedance increases with frequency while the experimental impedance is frequency independent. The frequency dependency of the predicted real part of *Z* gives a negative virtual mass coefficients (*M*) of large magnitude. Note at a high rotor speed of 16 krpm, measurements of the bearing impedances were conducted to a maximum frequency of 244 Hz (14,640 rpm), which is lower than the synchronous frequency (266.7 Hz). Hence, at the high rotor speed, both the predicted and measured real part of the impedances appears frequency independent.

93
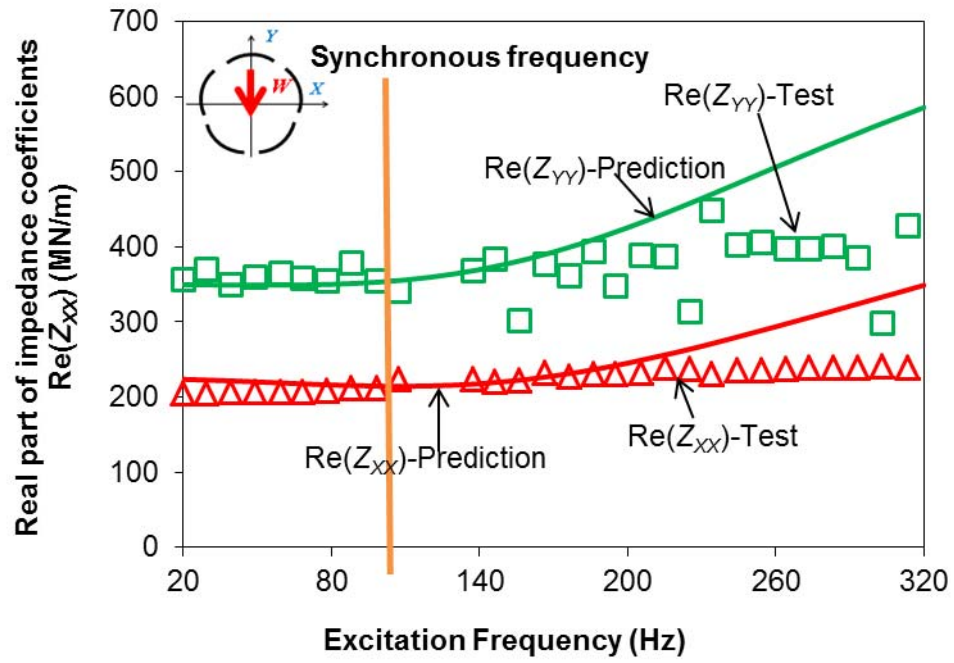
Fig. 50 Real part of TPJB impedance coefficients, Re(*Z*), versus excitation frequency. Rotor speed Ω =7 krpm and specific load (*W/LD*) =1,723 kPa. Current predictions and measurements in Ref. [27].
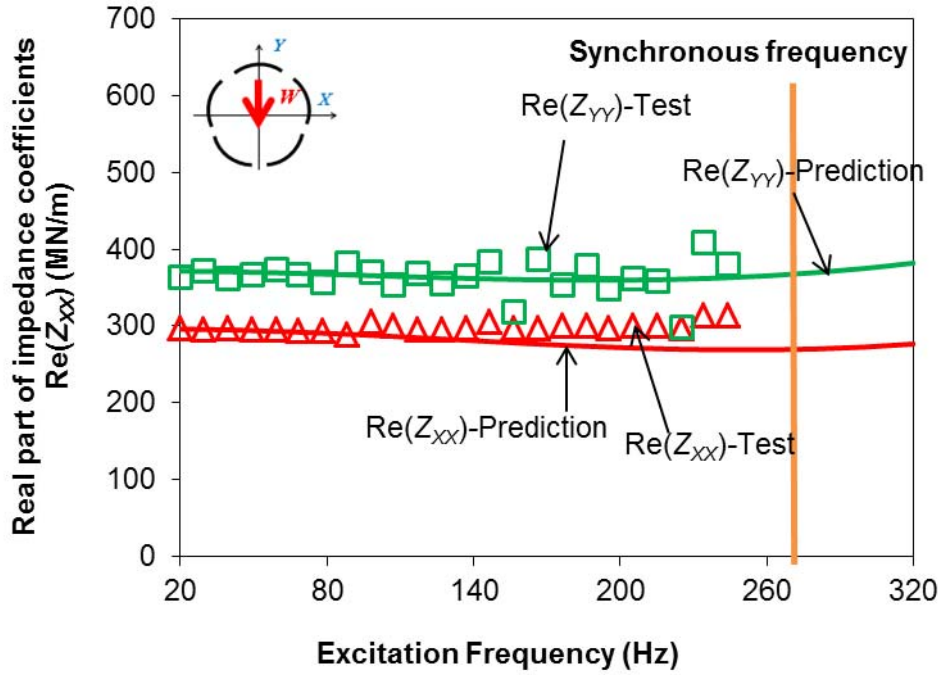
Fig. 51 Real part of TPJB impedance coefficients, Re(*Z*), versus excitation frequency. Rotor speed Ω =16 krpm and specific load (*W/LD*) =1,723 kPa. Current predictions and measurements in Ref. [27].

Figures 52 and 53 display the imaginary part of the bearing impedances, Im(*Z*), versus increasing excitation frequency for operation at two rotor speeds. At the low rotor speed of 7 krpm, the predicted and measured Im(*Z*) agree well, except at the highest end of excitation frequency (ω > 260Hz). The slope of Im(*Z*) shows that at the low rotor speed of 7 krpm, the predicted damping coefficients would be mildly frequency dependent while the measurements show little frequency dependency. When the rotor operates at a speed of 16 krpm, both the predicted and measured damping coefficients show little frequency dependency.
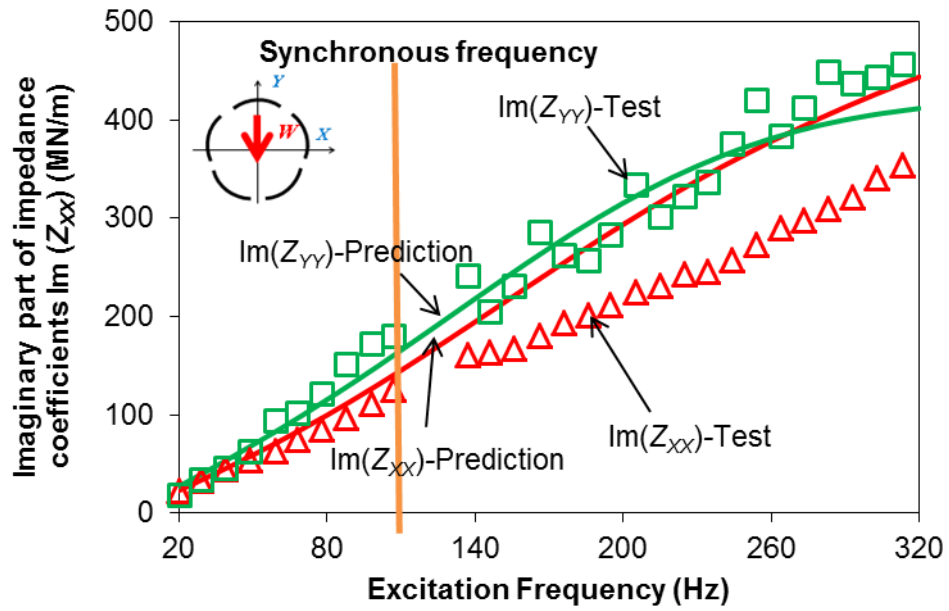
Fig. 52 Imaginary part of TPJB impedance coefficients, Im(*Z*), versus excitation frequency. Rotor speed Ω=7 krpm and specific load (*W/LD*) =1,723 kPa. Predictions and measurements in Ref. [27].
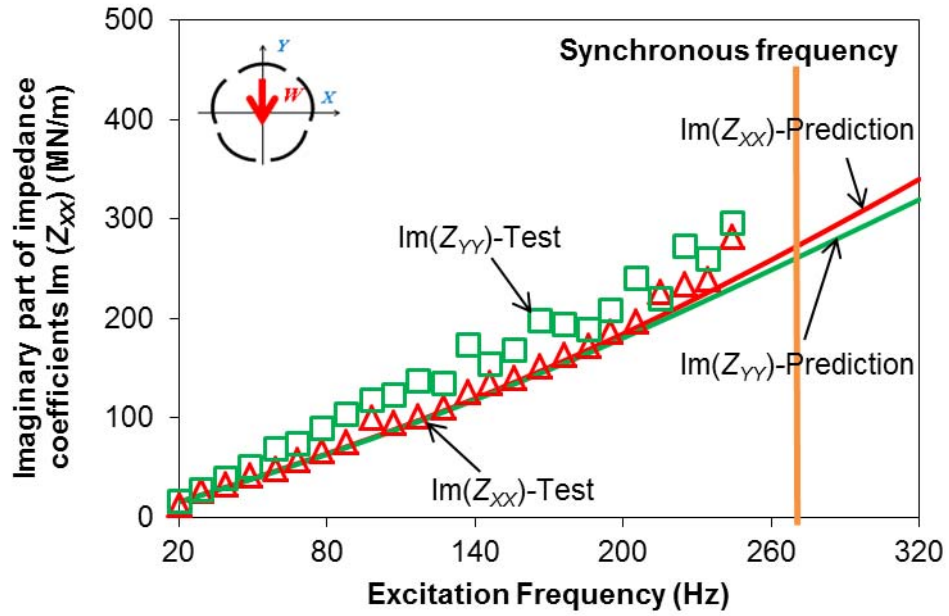
Fig. 53 Imaginary part of TPJB impedance coefficients, Im(*Z*), versus excitation frequency. Rotor speed Ω=16 krpm and specific load (*W/LD*) =1,723 kPa. Predictions and measurements in Ref. [27].

TPJB static stiffness, damping and virtual mass coefficients Table 13 lists the correlation coefficient of the force coefficients curve fitted from the predicted bearing impedances using the [*K-C-M*] model. A large correlation coefficient of the curve fit parameters to the bearing impedance (imaginary part) ($r^2 \to 1$) illustrates that the predicted damping coefficient is frequency independent over the frequency range of analysis (20Hz-320Hz).

Table 13 Correlation coefficients of the curve fit parameters to the predicted impedances at various operating conditions for a TPJB in Ref. [27]. Excitation frequency varies from 20 Hz to 320 Hz.

	Rotor	Specific load (kPa)	0	345	1,034	1,723	2,412	3,101
Prediction	7 krpm	$K_{sXX} - M_{XX}\omega^2 \rightarrow \mathrm{Re}(Z_{XX})$	0.48	0.77	0.93	0.97	0.98	0.99
		$K_{sYY} - M_{YY}\omega^2 \rightarrow \mathrm{Re}(Z_{YY})$	0.48	0.85	0.98	0.99	1.00	1.00
	16 krpm	$K_{sXX} - M_{XX}\omega^2 \rightarrow \mathrm{Re}(Z_{XX})$	0.98	0.90	0.96	0.79	0.75	0.75
		$K_{sYY} - M_{YY}\omega^2 \rightarrow \mathrm{Re}(Z_{YY})$	0.98	0.89	0.64	0.39	0.82	0.92
	7 krpm	$C_{XX}\omega \rightarrow \mathrm{Im}(Z_{XX})$	1.00	1.00	1.00	1.00	1.00	1.00
		$C_{YY}\omega \rightarrow \mathrm{Im}(Z_{YY})$	1.00	1.00	1.00	0.99	0.98	0.98
	16 krpm	$C_{XX}\omega \rightarrow \mathrm{Im}(Z_{XX})$	0.99	0.99	1.00	1.00	1.00	1.00
		$C_{YY}\omega \rightarrow \mathrm{Im}(Z_{YY})$	0.99	0.99	1.00	1.00	1.00	1.00
	Rotor	Specific load (kPa)	0	345	1,034	1,723	2,412	3,101
Test data	7 krpm	$K_{sXX} - M_{XX}\omega^2 \rightarrow \mathrm{Re}(Z_{XX})$	0.50	0.16	0.90	0.90	0.89	0.96
		$K_{sYY} - M_{YY}\omega^2 \rightarrow \mathrm{Re}(Z_{YY})$	0.15	0.29	0.10	0.36	0.64	0.46
	16 krpm	$K_{sXX} - M_{XX}\omega^2 \rightarrow \mathrm{Re}(Z_{XX})$	0.16	0.20	0.38	0.64	0.79	0.95
		$K_{sYY} - M_{YY}\omega^2 \rightarrow \mathrm{Re}(Z_{YY})$	0.55	0.73	0.50	0.07	0.15	0.27
	7 krpm	$C_{XX}\omega \rightarrow \mathrm{Im}(Z_{XX})$	0.99	1.00	1.00	1.00	1.00	0.91
		$C_{YY}\omega \rightarrow \mathrm{Im}(Z_{YY})$	1.00	0.98	0.99	0.99	0.99	0.91
	16 krpm	$C_{XX}\omega \rightarrow \mathrm{Im}(Z_{XX})$	0.99	0.94	0.98	0.99	1.00	1.00
		$C_{YY}\omega \rightarrow \mathrm{Im}(Z_{YY})$	0.99	1.00	1.00	0.99	0.99	0.98

Figure 54 shows the predicted and measured TPJB static stiffness coefficients versus specific load and two speeds. Results show a good agreement between the predictions and measurements. The TPJB stiffness coefficient (K_{YY}) along the loaded direction is underpredicted by 8.6% at a specific load of 3,101 kPa when the rotor operates at 7 krpm. At 16 krpm, the model underpredicts the test stiffness coefficients by 8% at the highest specific load of 3,101 kPa.
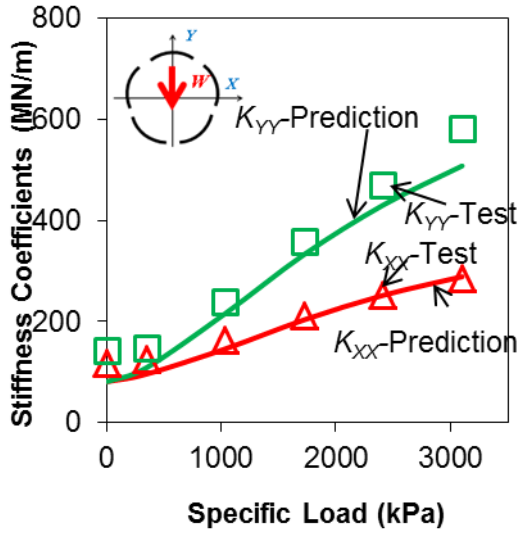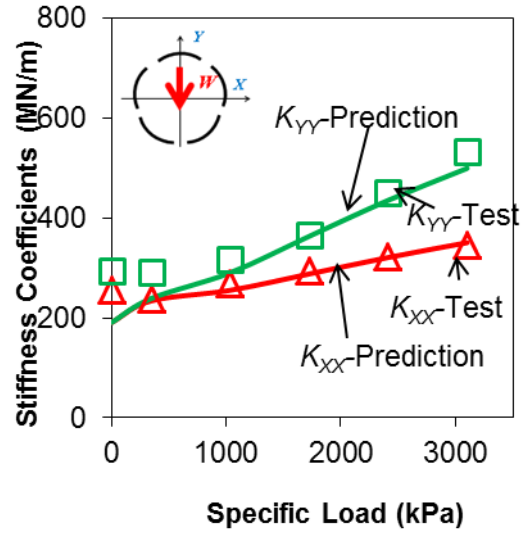
(a) rotor speed Ω=7,000 rpm   (b) rotor speed Ω=16,000 rpm

Fig. 54 TPJB static stiffness coefficients (*K*) versus specific load (*W/LD*). Current predictions and measurements in Ref. [23]. Rotor speed Ω=7,000 rpm and 16,000 rpm. Pad inlet thermal mixing coefficient *λ*=0.65 and 0.75.

Figure 55 depicts the extracted TPJB damping coefficients and experimental results estimated from the imaginary part of the impedances using the [*K-C-M*] model at rotor speeds equaling to 7,000 rpm and 16,000 rpm. At a specific load of 3,101 kPa, the damping coefficient along the load direction (C_{YY}) is underpredicted by 24% and 38% at the load and high speeds, respectively.
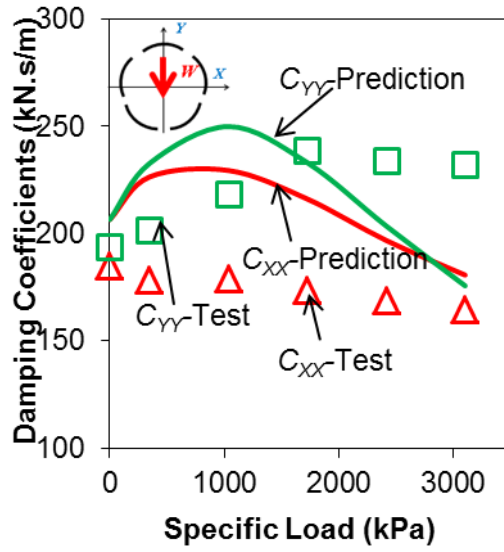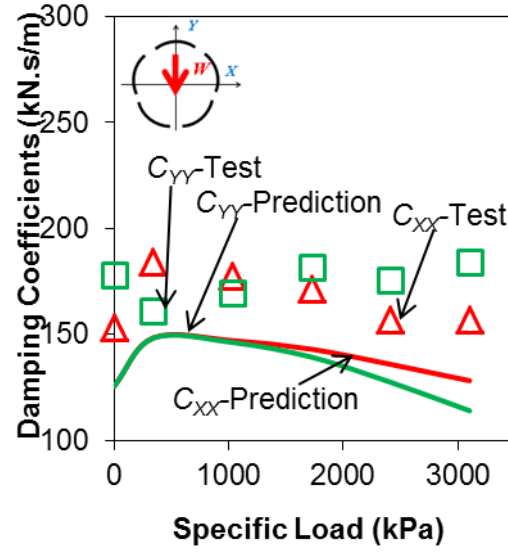
(a) rotor speed Ω=7,000 rpm   (b) rotor speed Ω=16,000 rpm

Fig. 55 TPJB damping coefficients (*C*) versus specific load (*W/LD*). Current predictions and measurements in Ref. [23]. Rotor speed Ω=7,000 rpm and 16,000 rpm. Pad inlet thermal mixing coefficient λ=0.65 and 0.75.

Figure 56 depicts the virtual mass coefficients (*M*) derived from the measured and predicted Re(*Z*). The mass coefficients from the measured impedances are small. Recall that the predicted virtual mass coefficients can not adequately capture the bearing dynamic stiffness (real part of impedance), as shown in Table 13. Hence, it is more relevant to compare the real part of the bearing impedances than the virtual mass coefficients.
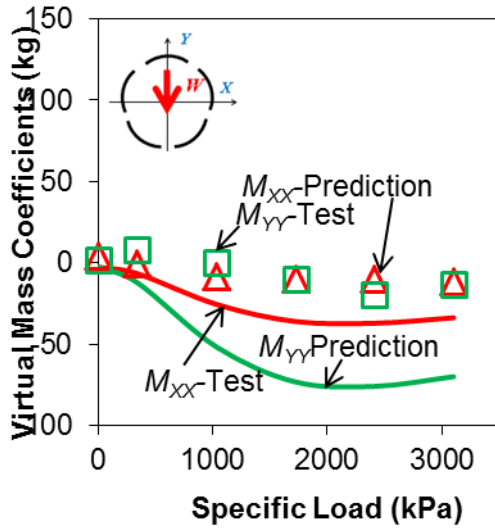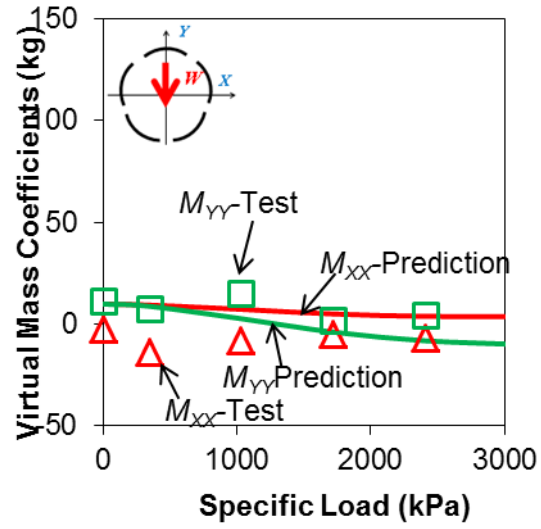
(a) rotor speed Ω=7,000 rpm   (b) rotor speed Ω=16,000 rpm

Fig. 56 TPJB virtual mass coefficients (*M*) versus specific load (*W/LD*). Current predictions and measurements in Ref. [23]. Rotor speed Ω=7,000 rpm and 16,000 rpm. Pad inlet thermal mixing coefficient λ=0.65 and 0.75.

Effect of pivot flexibility on the forced performance of TPJBs with different geometry parameters Appendix C studies the effect of pivot flexibility on the forced performance of bearings with various geometries, such as load configurations and pad preloads. A five-pad bearing in Ref. [27] is selected as an example for analysis.

Results show that the pivot flexibility has a more pronounced effect in reducing the stiffness and damping coefficients of a LBP bearing with a large pad preload (0.5) than a zero-preload bearing since the bearing with a large pad preload exhibits a large fluid film force (pivot reaction force) on each pad. For the bearing with a zero preload, a decreasing pivot stiffness acts to decrease greatly the bearing stiffness and damping coefficients only at large static loads; while pivot flexibility reduces the stiffness and damping coefficients of a $\bar{r}_P$=0.5 bearing over the whole load range. A decrease on the pivot stiffness also "stiffens" the bearing dynamic stiffness coefficients (real part of the impedances) at high frequencies.

101

The comparison between the effects of pivot flexibility on the forced performance of LBP and LOP bearings reveals that the pivot stiffness has the same effect in reducing the stiffness, damping and virtual mass coefficients.

Closure For the test TPJB with rocker back pivots in Refs. [23,27], the current model includes the effect of film temperature on the operating bearing and pad clearances and estimates the operating bearing and pad clearances by employing the ad-hoc thermal expansion coefficient in Ref. [7]. Then, a constant pivot stiffness is estimated based on the predicted and measured bearing stiffness coefficients along the loaded direction (K_{YY}).

Results show that the pad inlet thermal mixing coefficient (λ) employed in the predictive model has a great effect on the predicted film temperatures. At the high rotor speed or no load condition, choosing a large the thermal mixing coefficient ($\lambda \rightarrow 1$) improves the predictions on the pad trailing edge temperature.

Both the experimental results and predictions show that at a high rotor speed of 16 krpm, the bearing dynamic stiffness and damping coefficients are frequency independent. However, at a low rotor speed of 7 krpm, the predicted real part of the bearing impedances increases significantly when the excitation frequency is larger than twice the synchronous frequency ($\omega > 2\Omega$). Thus, for this bearing the predicted negative fluid virtual mass coefficients (M) are of large magnitude when the maximum frequency of analysis exceeds twice the synchronous frequency.

The current model delivers good predictions on the bearing static stiffness and damping force coefficients, thus demonstrating that reasonably estimated hot bearing clearances and pivot stiffnesses for the predictive model are essential to accurately predict the example bearing dynamic forced performance.

Example 4-Predicted Forced Performance for Rocker Back TPJBs [24]

Delgado et.al [24,28] measure the dynamic force coefficients of four TPJBs under two load configurations (LBP/LOP), with pivot offsets (0.5 and 0.6), and number of pads equaling 4 and 5. This section predicts the static and dynamic forced performance of the test TPJBs in Ref. [24] and discusses the frequency dependency of the bearing parameters. The bearing has nearly rigid pivots and operates with a light static load ($W/LD < 300$ kPa).

Table 14 lists the geometry parameters that the four bearings share in common and the operating conditions in Ref. [24]. Table 15 details the unique geometry parameters characteristics for each bearing.

Table 14 Test TPJBs geometry parameters and operating conditions in Refs. [24,28] [12] .

Pad arc angle	60°
Rotor diameter, D	110 mm
Pad axial length, L	44 mm
Pad mass, m_p	0.5 kg
Pad thickness, t	15.4 mm
Pad moment of inertia, I_P	2.5×10^{-4}kg.m^2
Pivot type	Rocker back
Lubricant type	ISO VG32
Oil supply temperature, T_s	43.5 $^{\circ}$C
Oil density, ρ	856.2 kg/m^3
Oil viscosity at 43.5 $^{\circ}$C	0.027 Pa.s
Temperature viscosity coefficient, α	0.0291/K

---

[12] References [24, 28] do not provide enough information on the bearing geometry for the model to predict accurately.
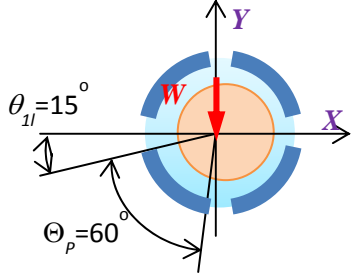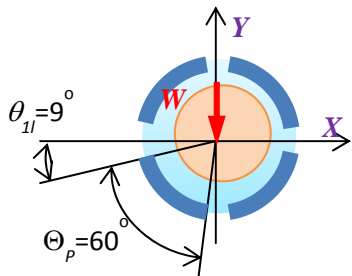
| Static specific load, *W/LD* | 300 kPa |
| Journal speed, Ω | 7.5 krpm, 10 krpm, 15 krpm |

Table 14 Continued

Inlet thermal mixing coefficient, λ	0.9[13]
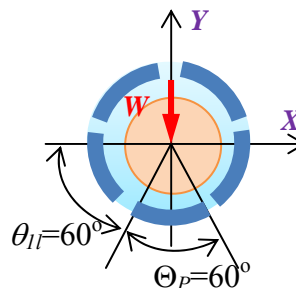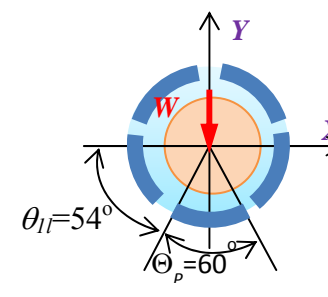
Presently, the model uses a pad mass = 0.5 kg, pad thickness = 15.4 mm and pad mass moment of inertia = 2.5×10^{-4}kg.m^2, since Refs. [24, 28] do not report these three parameters. These magnitudes seem adequate for the size of the test bearings.

Table 15 Detailed geometry parameters of the four test TPJBs in Ref. [24].

Bearing A		
Number of pads	4	
Load configuration	LBP	
Pivot offset	0.5	
Nominal pad preload	0.32	
Cold bearing radial clearance	99 μm	
Cold pad radial clearance	145.6 μm	
Bearing B		
Number of pads	4	
Load configuration	LBP	
Pivot offset	0.6	
Nominal pad preload	0.30	
Cold bearing radial clearance	102 μm	
Cold pad radial clearance	145.7 μm	

---

[13] Parameter not listed in Ref. [24,28]. Presently, $\lambda = 0.9$ is selected because *W/LD* = 300 kPa is low and the operating rotor speeds are high (10 krpm and 15 krpm).

Table 15 Continued

Bearing C		
Number of pads	5	
Load configuration	LOP	
Pivot offset	0.5	
Nominal pad preload	0.16	
Cold bearing radial clearance	101 μm	
Cold pad radial clearance	120 μm	
Bearing D		
Number of pads	5	
Load configuration	LOP	
Pivot offset	0.6	
Nominal pad preload	0.16	
Cold bearing radial clearance	101 μm	
Cold pad radial clearance	120 μm	

The TPJBs in Ref. [24] implement a direct lubrication method with cold oil ejecting from nozzles between the pads and flowing onto the leading edge of each pad. Here assume that the oil carries away all the heat generated in the bearing, i.e. no heat transfers between the oil and the journal and bearing surfaces. Thus an adiabatic surface condition is selected for convenience. The fluid flow in the bearing is laminar since the Reynolds number is much lower than 1,000.

The journal speed varies from 7.5 krpm to 15 krpm and the specific load applied on the test bearing is just 300 kPa (W = 1,452 N). The pad-pivot contact structure is

cylinder on a cylinder (line contact). Appendix A gives the formula to estimate the pivot radial stiffness of this structure, i.e.,

$$\xi_{piv}^k = \frac{2F_{piv}^k(1-\upsilon^2)}{\pi LE}\left(\frac{2}{3} + \ln\frac{4LED_PD_H(D_H-D_P)}{2.15^2 F_{piv}^k}\right) \tag{48}$$

Above, L=44 mm is the pad-pivot contact length. E=212 GPa and ν=0.29 are the elastic modulus and Poisson's ratio of steel, material for the pivot and housing. D_H and D_P are the diameters of the pivot and pad contact curvatures, i.e., D_H=144.4 mm and D_P=141.1 mm. Note that this formula determines a load-dependent pivot stiffness.

Effect of fluid film temperature on operating bearing and pad clearances In the current model, operating hot bearing and pad radial clearances are calculated by using the estimated pad average temperature raise in a TPJB. Recall that the formula to calculate the operating bearing clearance is,

$$C_{B,ref} - C_B = \alpha_{c_b}\Delta T = \alpha_T(R-\gamma t)\Delta T \tag{49}$$

Above, pad thickness equals to 15.4 mm and γ= 1.0. α_T, the linear thermal expansion coefficient for steel, equals to 1.3×10^{-5} m/^{o}C. Note that the temperature raise ΔT refers to the estimated average temperature raise in the bearing. The cold pad clearance and cold bearing clearance are measured at a temperature of 25°C. Thus the thermal expansion coefficient of the bearing clearance α_{c_b} is 0.5148 µm/^{o}C. The decrease of the pad clearance can also be calculated by using Eq. (49) ($\Delta C_P = \alpha_{c_b}\Delta T$) since the thermal expansion of the journal radius influences the pad clearance, as well as the bearing clearance. Table 16 lists the operating bearing clearance, pad clearance and pad preload versus various estimated temperature raises. At the rotor speed of 15,000 rpm, the operating bearing clearances of bearings A-D are 15%, 12%, 19% and 15% smaller than the corresponding nominal bearing clearances, respectively.

Table 16 Predicted hot bearing clearance, pad clearance, pad preload and estimated pad average temperature raise in Ref. [24].

Bearing type	Rotor speed Ω (rpm)	Bearing clearance C_B (µm)	Pad clearance C_P (µm)	Pad preload $\bar{r}_P$	Average temperature raise ΔT (°C)
Bearing A	Nominal	99.0	145.6	0.32	-
4-Pad	7,500	82.3	129.0	0.36	32.2
LBP	10,000	80.5	127.1	0.37	35.9
50% offset	15,000	77.4	124.0	0.38	42.0
Bearing B	Nominal	102.0	145.7	0.30	-
4-Pad	7,500	88.3	132.0	0.33	26.6
LBP	10,000	87.1	130.8	0.33	28.9
60% offset	15,000	85.0	128.7	0.34	33.0
Bearing C	Nominal	101.0	120.2	0.16	-
5-Pad	7,500	83.6	102.8	0.19	33.8
LOP	10,000	81.6	100.8	0.19	37.7
50% offset	15,000	78.1	97.3	0.20	44.4
Bearing D	Nominal	101.0	120.2	0.16	-
5-Pad	7,500	86.8	106.0	0.18	27.6
LOP	10,000	85.6	104.8	0.18	29.9
60% offset	15,000	83.3	102.5	0.19	34.4

Bearing impedance coefficients Figures 57 to 59 show the real part of the bearing impedances, Re(Z), for two four-pad LBP bearings with pad pivot offsets equaling 0.5 and 0.6 and operating at three rotor speeds (7.5 krpm, 10 krpm and 15 krpm). Results show that the measured Re(Z) decrease slightly with increasing excitation frequency for the 0.5-offset pad bearing while the predicted impedances decrease considerably with excitation frequency.

Figure 57 depicts that for the bearing with 60% pivot offset, the measured and predicted impedances (real part) are frequency independent. As the rotor speed increases, experimental results exhibit orthotropic impedances, i.e., $\text{Re}(Z_{XX}) \neq \text{Re}(Z_{YY})$, for the 0.6-offset bearing. However, predictions show identical impedances in the orthogonal directions, $\text{Re}(Z_{XX}) = \text{Re}(Z_{YY})$.

(a) Pad pivot offset =0.50   (b) Pad pivot offset =0.60

Fig. 57 TPJB real part of impedances, Re(Z), versus excitation frequency. Specific load (W/LD) = 300 kPa. Rotor speed (Ω) = 7.5 krpm. Measurements in Ref. [24] and predictions for two four-pad LBP TPJBs with pad pivot offsets equaling 0.5 and 0.6.

(a) Pad pivot offset =0.50   (b) Pad pivot offset =0.60

Fig. 58 TPJB real part of impedances , Re(Z), versus excitation frequency.
Specific load (W/LD) = 300 kPa. Rotor speed (Ω) =10 krpm. Measurements in Ref.
[24] and predictions for two four-pad LBP TPJBs with pad pivot offsets equaling
0.5 and 0.6.

(a) Pad pivot offset =0.50   (b) Pad pivot offset =0.60
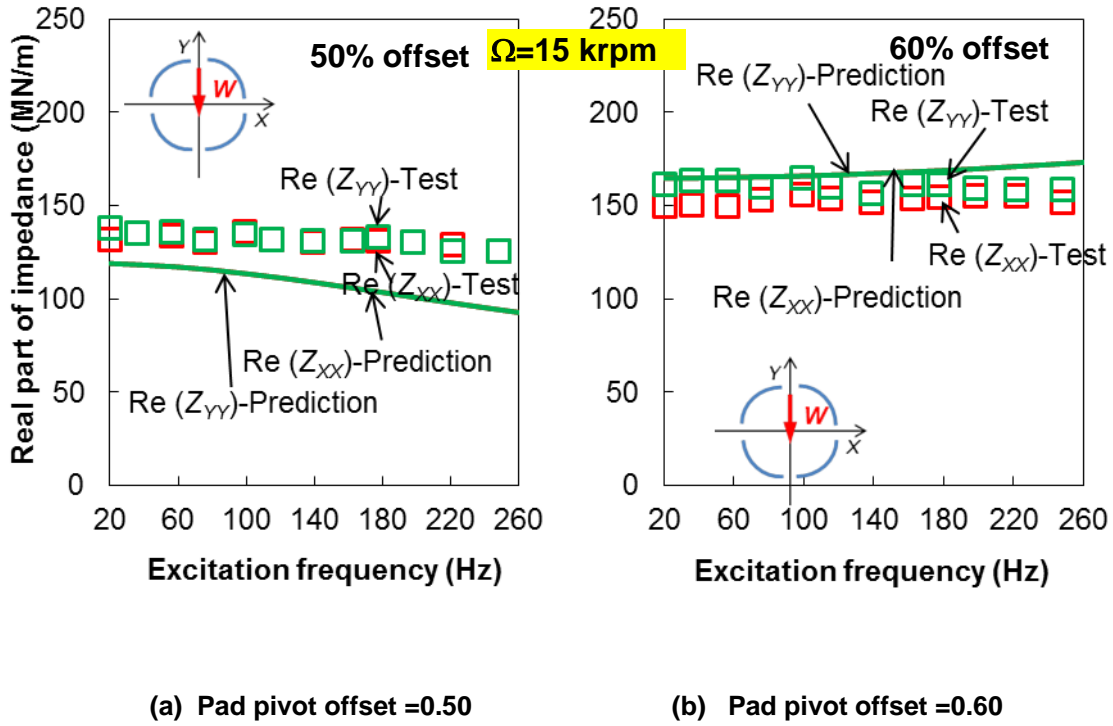
Fig. 59 TPJB real part of impedances, Re(Z), versus excitation frequency. Specific load (W/LD) = 300 kPa. Rotor speed (Ω)=15 krpm. Measurements in Ref. [24] and predictions for two four-pad LBP TPJBs with pad pivot offsets equaling 0.5 and 0.6.

Figures 60 to 62 depict the real part of impedances for two five-pad LOP bearings with 0.5 and 0.6 pivot offsets for operations with rotor speeds equaling to 7.5 krpm, 10 krpm and 15 krpm. The real part of the predicted impedances at a low excitation frequency (~20 Hz) shows good agreement with the test data. For the bearing with 50% pivot offset, the real part of the predicted impedances, Re(Z), decreases with frequency for the three rotor speeds. Note the frequency dependency of the experimental impedances changes with increasing rotor speed.

(a) Pad pivot offset =0.50   (b) Pad pivot offset =0.60
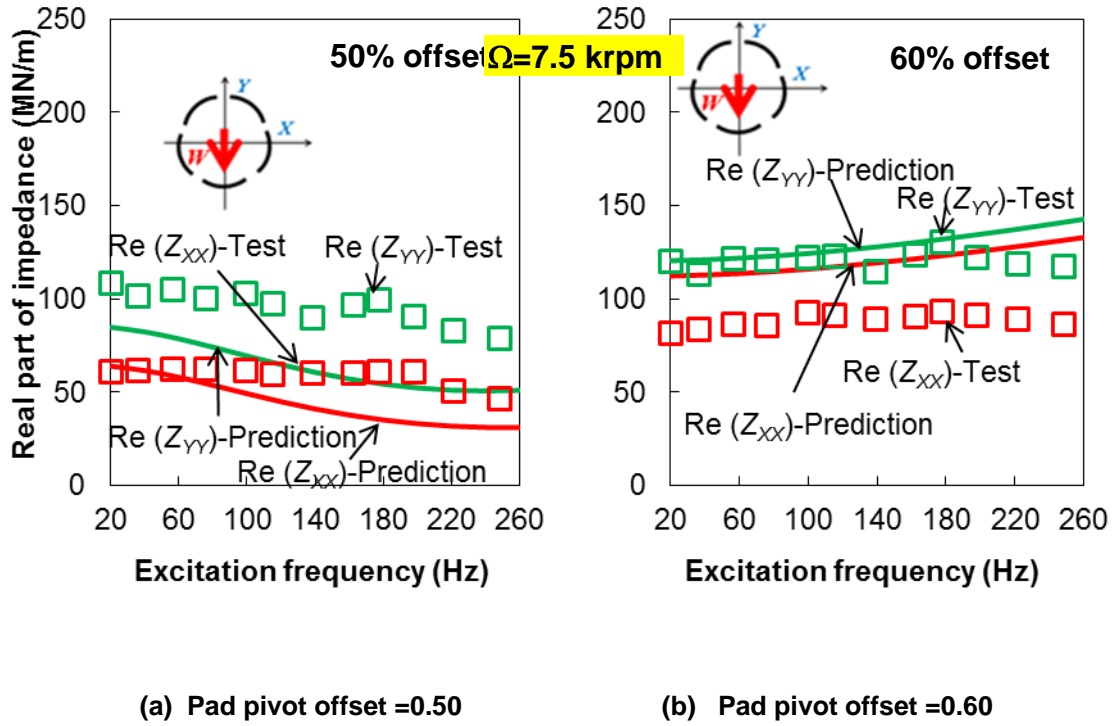
Fig. 60 TPJB real part of impedances, Re(*Z*), versus excitation frequency. Specific load (*W/LD*) = 300 kPa. Rotor speed (Ω)=7.5 krpm. Measurements in Ref. [24] and predictions for two five-pad LOP TPJBs with pad pivot offsets equaling 0.5 and 0.6.
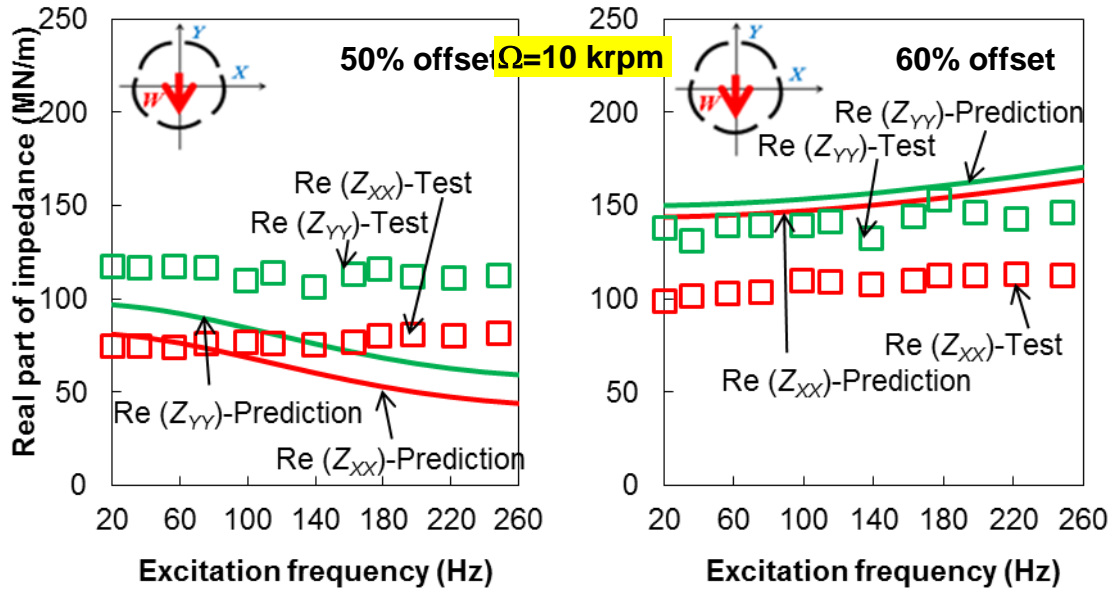
(a) Pad pivot offset =0.50   (b) Pad pivot offset =0.60

Fig. 61 TPJB real part of impedances, Re(Z), versus excitation frequency. Specific load (W/LD) = 300 kPa. Rotor speed (Ω)=10 krpm. Measurements in Ref. [24] and predictions for two five-pad LOP TPJBs with pad pivot offsets equaling 0.5 and 0.6.

112

(a) Pad pivot offset =0.50   (b) Pad pivot offset =0.60
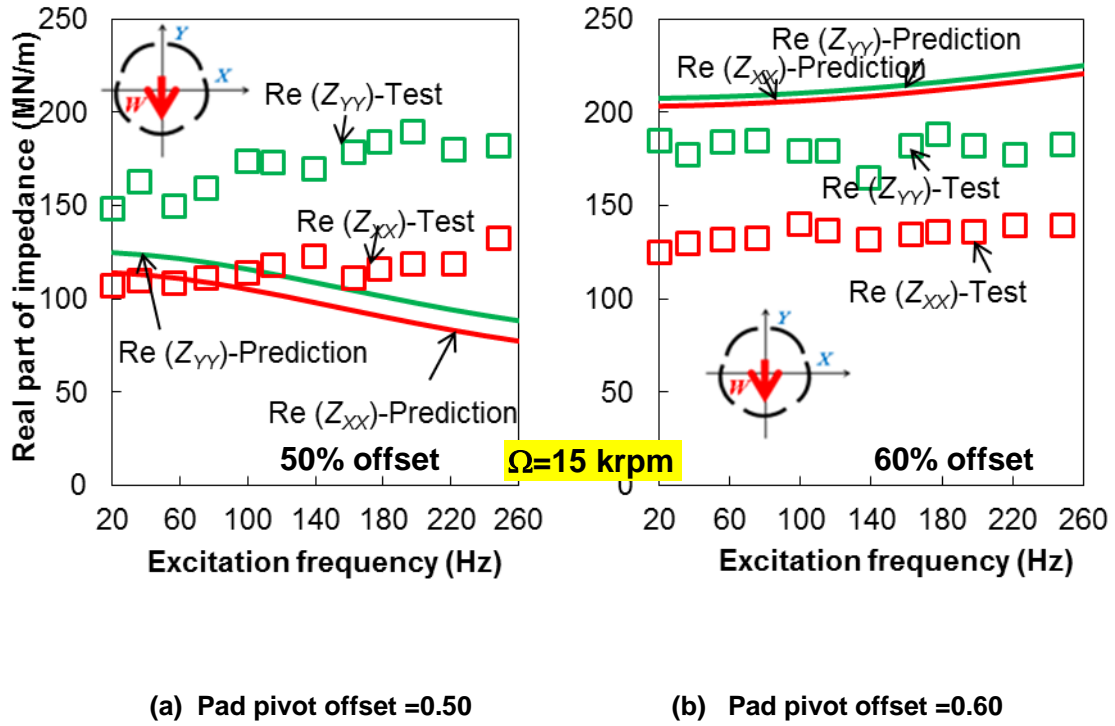
Fig. 62 TPJB real part of impedances, Re(*Z*), versus excitation frequency. Specific load (*W/LD*) = 300 kPa. Rotor speed (Ω)=15 krpm. Measurements in Ref. [24] and predictions for two five-pad LOP TPJBs with pad pivot offsets equaling 0.5 and 0.6.

Figures 63 to 65 display Im(*Z*) for two four-pad LBP bearings with pad pivot offsets equaling 0.5 and 0.6 and operating at three rotor speeds. Note the experimental Im(*Z*) are linear with excitation frequency at rotor speeds equaling to 7.5 krpm, 10 krpm and 15 krpm; thus denoting frequency-independent damping coefficients. The predicted and measured damping coefficients are in good agreement, both are independent on the excitation frequency.

Figures 66 to 68 show the Im(*Z*) for two five-pad LOP bearings with two pivot offsets, 0.5 and 0.6. Results show that the Im(*Z*) are different along the directions *X* and *Y*, i.e., Im(*Z*$_{XX}$)≠Im(*Z*$_{YY}$). Hence, for the bearing with 0.6 pivot offset, the damping coefficients will appear constant with excitation frequency. Note that the predicted Im(*Z*) correlates well with the experimental results, except for the five-pad LOP bearing with a 50% pivot offset for operation at the highest rotor speed of 15 krpm.

113
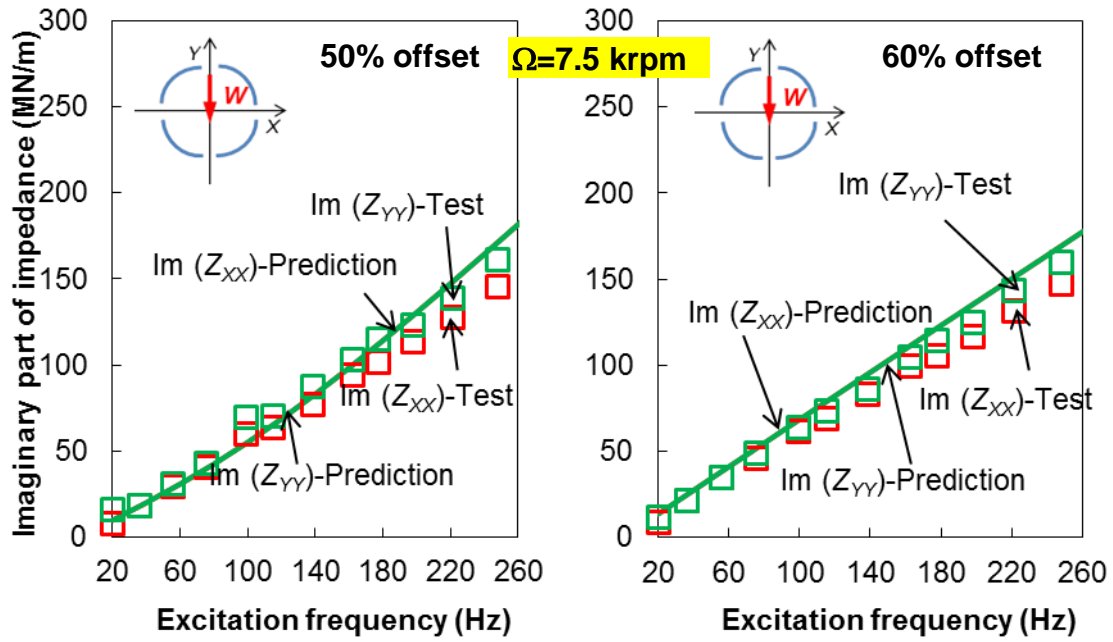
(a) Pad pivot offset =0.50   (b) Pad pivot offset =0.60

Fig. 63 TPJB imaginary part of impedances, Im(Z), versus excitation frequency. Specific load (W/LD) = 300kPa. Rotor speed (Ω) = 7.5 krpm. Measurements in Ref. [24] and predictions for four-pad LBP TPJBs with pad pivot offsets equaling 0.5 and 0.6.
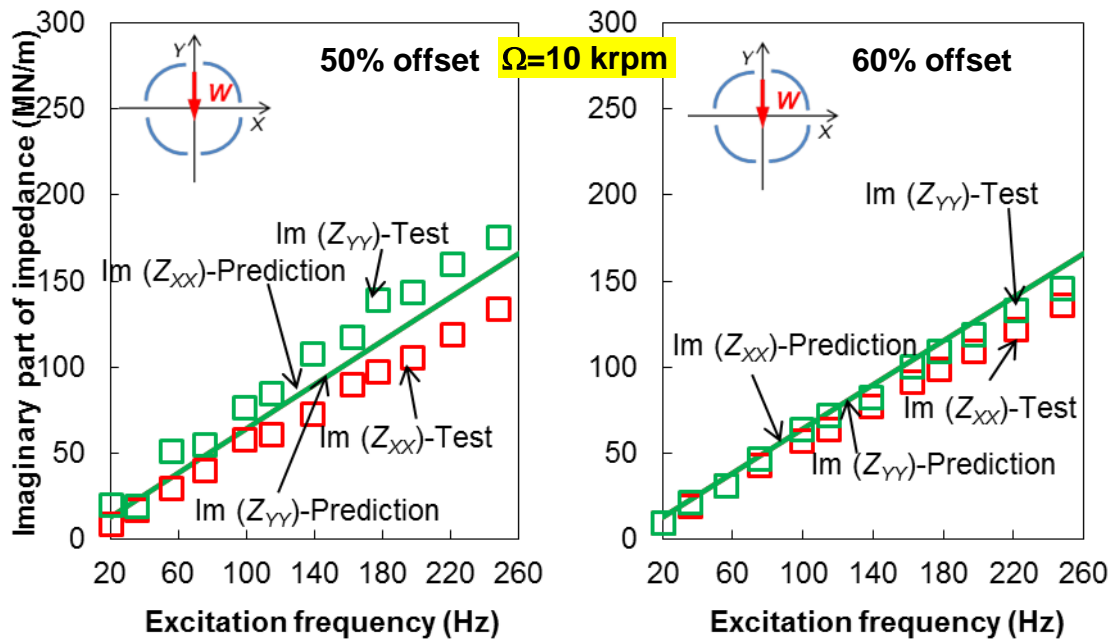
(a) Pad pivot offset =0.50   (b) Pad pivot offset =0.60

Fig. 64 TPJB imaginary part of impedances, Im(*Z*), versus excitation frequency. Specific load (*W/LD*) = 300kPa. Rotor speed (Ω) = 10 krpm. Measurements in Ref. [24] and predictions for four-pad LBP TPJBs with pad pivot offsets equaling 0.5 and 0.6.
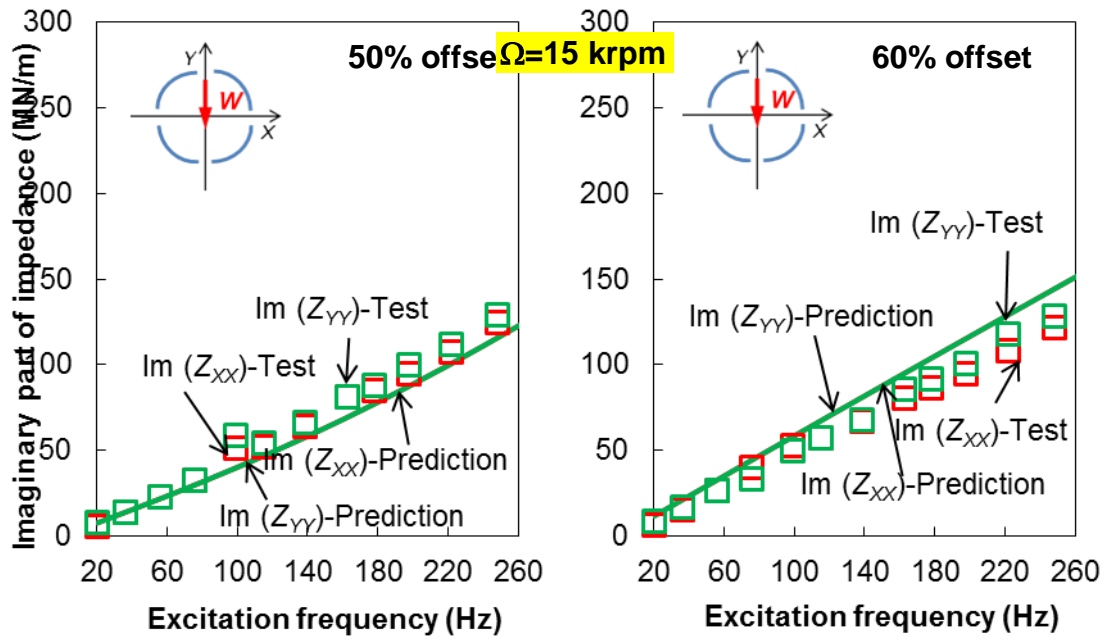
(a) Pad pivot offset =0.50   (b) Pad pivot offset =0.60

Fig. 65 TPJB imaginary part of impedances, Im(Z), versus excitation frequency. Specific load (W/LD) = 300kPa. Rotor speed (Ω) = 15 krpm. Measurements in Ref. [24] and predictions for four-pad LBP TPJBs with pad pivot offsets equaling 0.5 and 0.6.

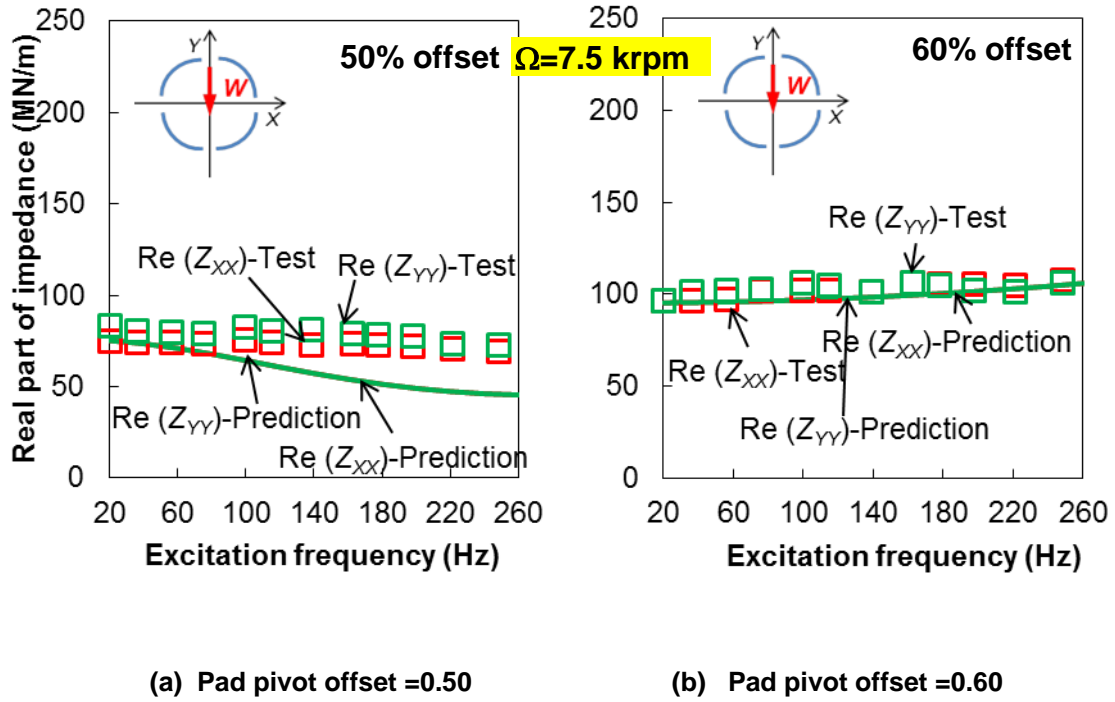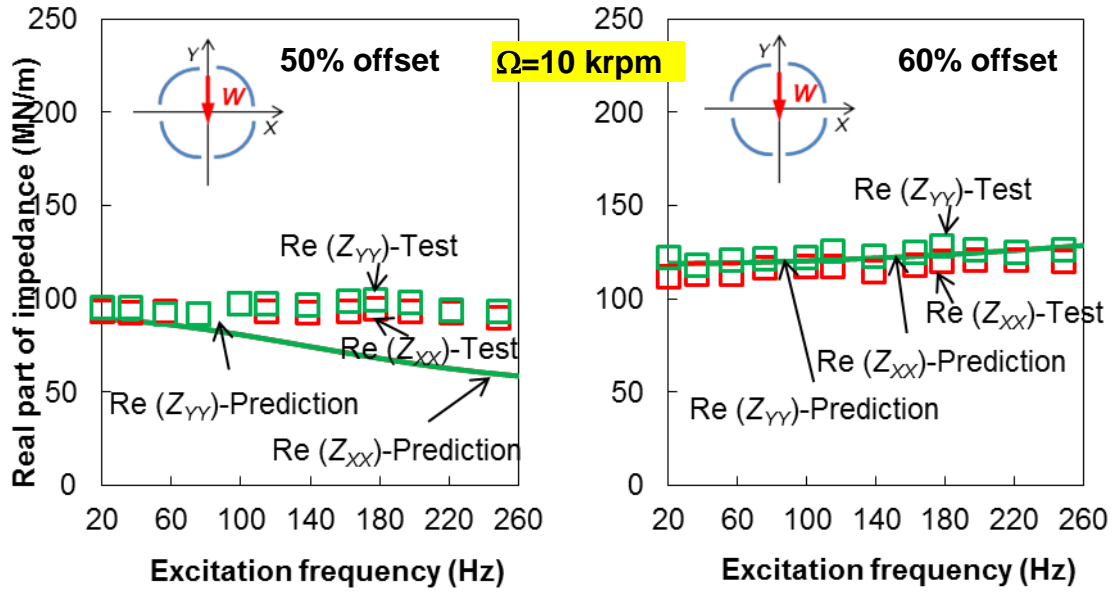**(a) Pad pivot offset =0.50** **(b) Pad pivot offset =0.60**

Fig. 66 TPJB imaginary part of impedances, Im(*Z*), versus excitation frequency. Specific load (*W/LD*) = 300 kPa. Rotor speed (Ω)=7.5 krpm. Measurements in Ref. [24] and predictions for five-pad LOP TPJBs with pad pivot offsets equaling 0.5 and 0.6.

(a) Pad pivot offset =0.50   (b) Pad pivot offset =0.60

Fig. 67 TPJB imaginary part of impedances, Im(Z), versus excitation frequency. Specific load (W/LD) = 300 kPa. Rotor speed (Ω)=10 krpm. Measurements in Ref. [24] and predictions for five-pad LOP TPJBs with pad pivot offsets equaling 0.5 and 0.6.

(a) Pad pivot offset =0.50   (b) Pad pivot offset =0.60

Fig. 68 TPJB imaginary part of impedances, Im(Z), versus excitation frequency. Specific load (W/LD) = 300 kPa. Rotor speed (Ω)=15 krpm. Measurements in Ref. [24] and predictions for five-pad LOP TPJBs with pad pivot offsets equaling 0.5 and 0.6.

Bearing stiffness and damping force coefficients A [K-C-M] model is selected to estimate the bearing static stiffness, damping and virtual mass coefficients. Table 17 lists the correlation coefficients of the curve fit parameters from the [K-C-M] model for the predicted impedances. Note that the [K-C-M] model adequately captures Im(Z) since r-$^2 \rightarrow 1$, thus showing the damping coefficients are frequency independent.

Table 17 Correlation coefficients of the curve fit parameters for the [*K-C-M*] model at various operating conditions for a TPJB in Ref. [24].

Rotor speed	Load configuration	LBP		LOP	
	Pivot offset	0.5	0.6	0.5	0.6
7.5 krpm	$K_{sXX} - M_{XX}\omega^2 \rightarrow \mathrm{Re}(Z_{XX})$	0.83	1.00	0.76	1.00
	$K_{sYY} - M_{YY}\omega^2 \rightarrow \mathrm{Re}(Z_{YY})$	0.83	1.00	0.69	1.00
	$C_{XX}\omega \rightarrow \mathrm{Im}(Z_{XX})$	1.00	1.00	1.00	1.00
	$C_{YY}\omega \rightarrow \mathrm{Im}(Z_{YY})$	1.00	1.00	1.00	1.00
10 krpm	$K_{sXX} - M_{XX}\omega^2 \rightarrow \mathrm{Re}(Z_{XX})$	0.93	1.00	0.89	1.00
	$K_{sYY} - M_{YY}\omega^2 \rightarrow \mathrm{Re}(Z_{YY})$	0.93	1.00	0.88	1.00
	$C_{XX}\omega \rightarrow \mathrm{Im}(Z_{XX})$	1.00	1.00	1.00	1.00
	$C_{YY}\omega \rightarrow \mathrm{Im}(Z_{YY})$	1.00	1.00	1.00	1.00
15 krpm	$K_{sXX} - M_{XX}\omega^2 \rightarrow \mathrm{Re}(Z_{XX})$	0.98	1.00	0.98	1.00
	$K_{sYY} - M_{YY}\omega^2 \rightarrow \mathrm{Re}(Z_{YY})$	0.98	1.00	0.98	1.00
	$C_{XX}\omega \rightarrow \mathrm{Im}(Z_{XX})$	1.00	1.00	1.00	1.00
	$C_{YY}\omega \rightarrow \mathrm{Im}(Z_{YY})$	1.00	1.00	1.00	1.00

Figure 69 shows the static stiffness coefficients ($\omega = 0$) of two four-pad LBP bearings versus increasing journal speeds. The predicted K_{XX} and K_{YY}, identified at zero frequency, correlate well with the experimental parameters. Figure 70 depicts the static stiffness coefficients of two five-pad LOP bearings, one with pad pivot offset 0.5 and the other with 0.6. The predicted stiffness coefficients are identical in the orthogonal directions ($K_{XX} = K_{YY}$) while the measurements show orthotropic stiffness coefficients ($K_{XX} \neq K_{YY}$). For the LOP and LBP bearings, an increase in the pivot offset determines a considerable increase in the bearing stiffness coefficients.

The pad pivot radial stiffness obtained from Eq. (48) for this bearing varies from 1,630 MN/m to 1,900 MN/m. These magnitudes are about 10 times larger than the actual bearing stiffness coefficients. The pivot stiffness (1,630 MN/m~1,900 MN/m) has little effects on reducing the bearing stiffness and damping coefficients; however, it

influences the bearing dynamic stiffness at a high frequency, and thus, the virtual mass coefficients.

Selecting the four bearings in Ref. [24] as examples, Appendix D discusses the effects of pad mass and mass moment of inertia and pivot flexibility on the bearing impedances (real and imaginary parts) over a certain excitation frequency range. Since Re(Z) is always underpredicted at high frequencies ($\omega > 200$Hz), the predictive model does not include the influence of fluid inertia, which will "soften" more the bearing impedances (real) at high excitation frequencies. The effects of pad mass and pad mass moment of inertia, which also "soften" the bearing dynamic stiffness and increase Im(Z) at large frequencies, are included in the model. The current model also includes the effect of pivot stiffness (1,630 MN/m ~1,900 MN/m), which reduces slightly the bearing static stiffness ($\omega = 0$) and damping coefficients. For the test bearings, pivot stiffness "stiffens" the bearing dynamic stiffness, Re(Z), at high frequencies.

(a) Pad pivot offset =0.50   (b) Pad pivot offset =0.60

Fig. 69 TPJB stiffness coefficients versus journal speed (Ω). Specific load (*W/LD*) = 300 kPa. Predictions and measurements [24] for two four-pad LBP TPJBs with pad pivot offsets equaling 0.5 and 0.6.

121

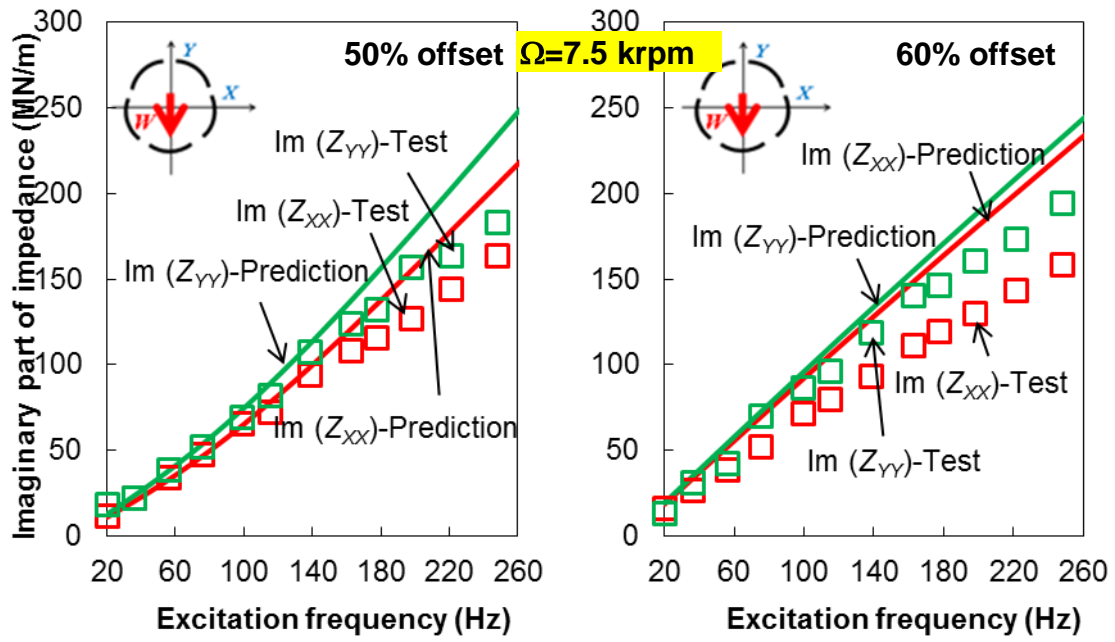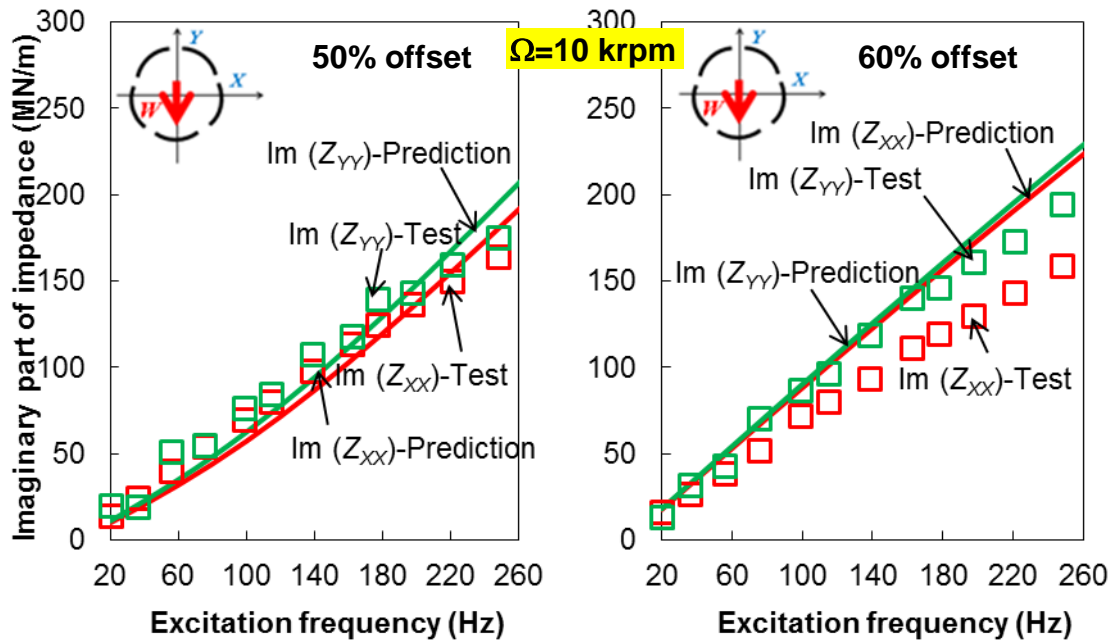(a) Pad pivot offset =0.50   (b) Pad pivot offset =0.60

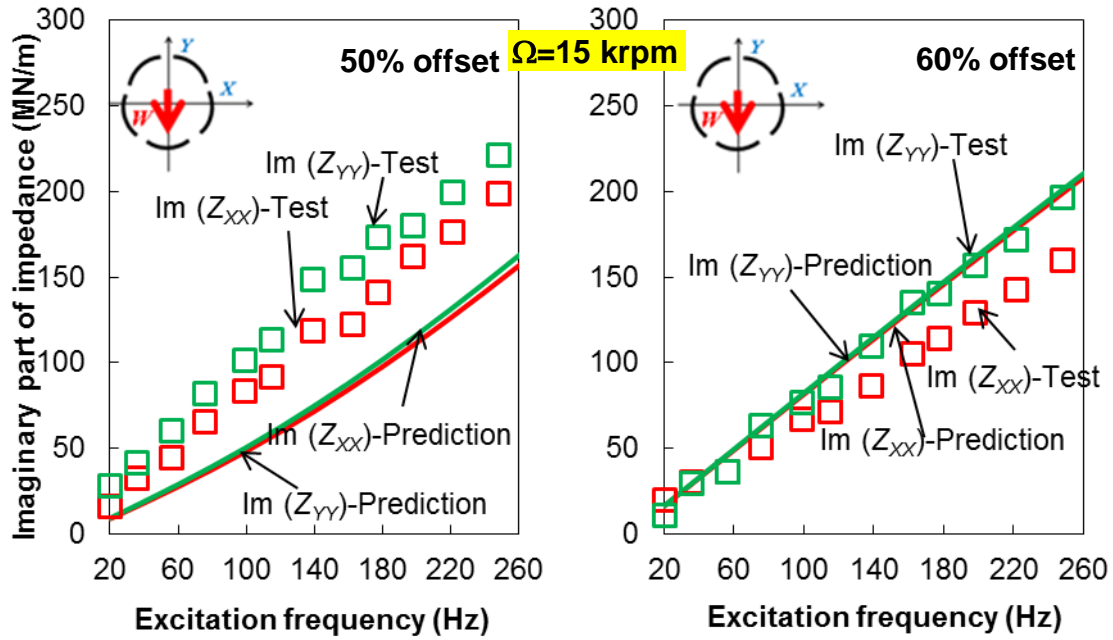**Fig. 70 TPJB stiffness coefficients versus journal speed (Ω). Specific load (W/LD) = 300 kPa. Predictions and measurements [24] for two five-pad LOP TPJBs with pad pivot offsets equaling 0.5 and 0.6.**

Figure 71 shows the predicted damping coefficients of two four-pad (LBP) bearings, derived from the Im(Z), against the experimental results. The damping coefficients along the loaded direction (C_{YY}) are under predicted by a maximum of 11% and 17% for the test bearing with pivot offset equaling 0.5 and 0.6, respectively.

(a) Pad pivot offset =0.50   (b) Pad pivot offset =0.60
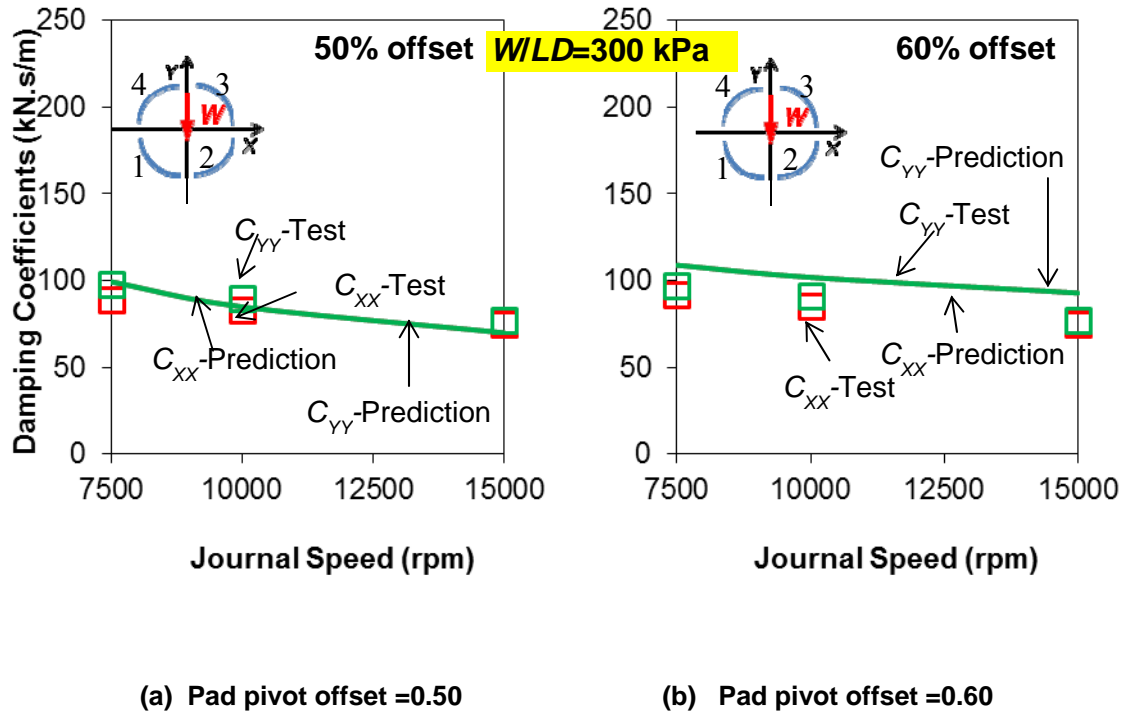
Fig. 71 TPJB damping coefficients versus journal speed (Ω).Specific load (*W/LD*) = 300 kPa. Predictions and measurements [24] for two four-pad LBP TPJBs with pad pivot offsets equaling 0.5 and 0.6.

Figure 72 depicts the damping coefficients versus rotor speed for two five-pad (LOP) bearings with pivot offsets equaling 0.5 and 0.6. Results show that the predicted and measured damping coefficients increase with pivot offset and decrease with rotor speed, except for the five-pad LOP bearing with 0.5 pivot offset. Note the experimental damping coefficients increase with rotor speed for the five-pad LOP bearing with the pivot offset equaling 0.5; however, the predictions show the opposite behavior.
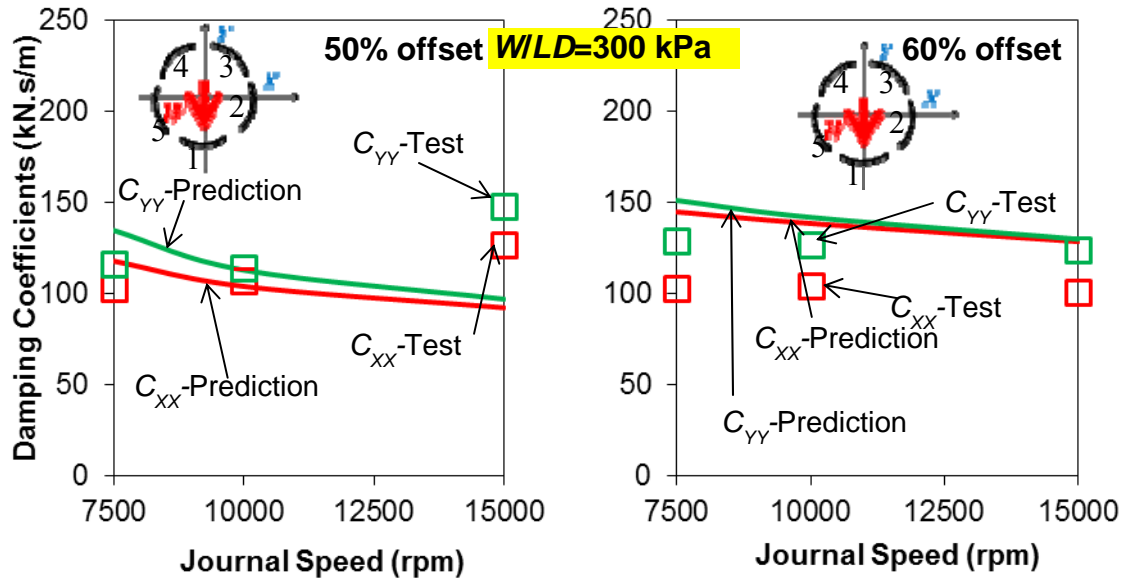
(a) Pad pivot offset =0.50   (b) Pad pivot offset =0.60

Fig. 72 TPJB damping coefficients versus journal speed (Ω).Specific load (*W/LD*) = 300 kPa. Predictions and measurements [24] for two five-pad LOP TPJBs with pad pivot offsets equaling 0.5 and 0.6.

Figure 73 shows the virtual mass coefficients for two four-pad LBP bearings as derived from curve fits to the measured and predicted impedances. The maximum excitation frequency for curve fitting the predicted impedance coefficients at all rotor speeds is 320 Hz, which is 150% larger than the minimum rotor speed (125 Hz) and 28% larger than the maximum rotor speed (250 Hz). Note that the virtual mass coefficients remain constant with rotor speed for the four-pad LBP TPJBs.

The predictions and test data show that the bearing with 0.5 pivot offset has positive virtual mass coefficients while negative virtual mass coefficients are associated with the 0.6 pivot offset bearing. Hence, there is a "softening" effect on the dynamic stiffness coefficients (real part of impedances) for the 0.5 pivot offset bearing and a "stiffening" effect for the 0.6 pivot offset bearing. Note the bearing experimental virtual mass

124

coefficients are orthotropic ($M_{XX} \neq M_{YY}$), however, the predictions are identical in orthogonal directions ($M_{XX} = M_{YY}$).

(a) Pad pivot offset =0.50   (b) Pad pivot offset =0.60
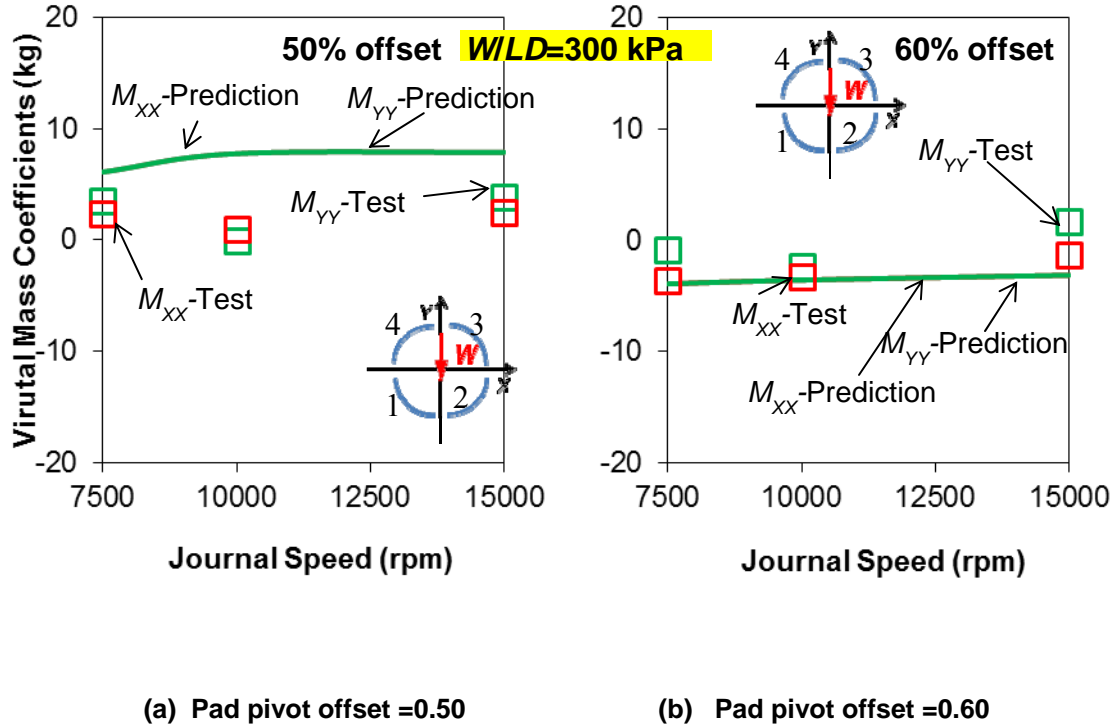
Fig. 73 TPJB virtual mass coefficients versus journal speed (Ω).Specific load (*W/LD*) = 300 kPa. Predictions and measurements [24] for two four-pad LBP TPJBs with pad pivot offsets equaling 0.5 and 0.6.

Figure 74 depicts the virtual mass coefficients for the two five-pad LOP bearings with pivot offsets equaling to 0.5 and 0.6. The virtual mass coefficients for the 50% offset bearing derived from the measured Re(*Z*) decrease significantly with rotor speed; however, the predictions show an increase in the virtual mass coefficient. For the bearing operating at the highest speed of 15 krpm, a predicted Re(Z_{YY})=K-$M\omega^2$ at the synchronous speed frequency (ω=250Hz) is ~27% smaller than that at the zero frequency (K); while the experimental value is ~22% larger than that identified at the zero frequency. Note for the bearing with 60% pad pivot offset, the virtual mass

coefficients derived from the experimental impedances are zero, indicating the bearing dynamic stiffness coefficients (K) are frequency independent, see Figs. 60-62.
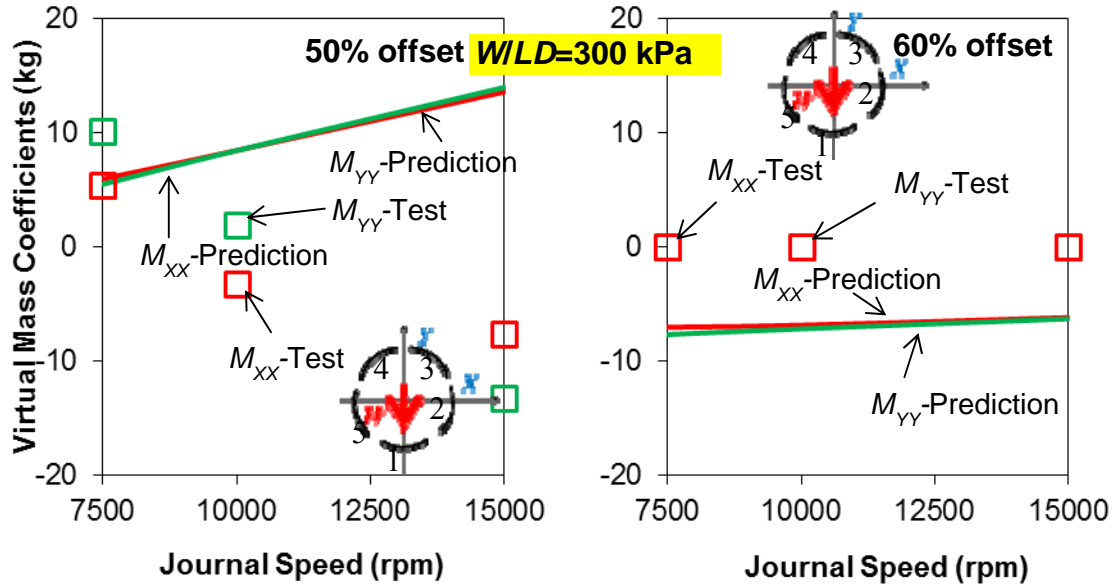
(a) Pad pivot offset =0.50   (b) Pad pivot offset =0.60

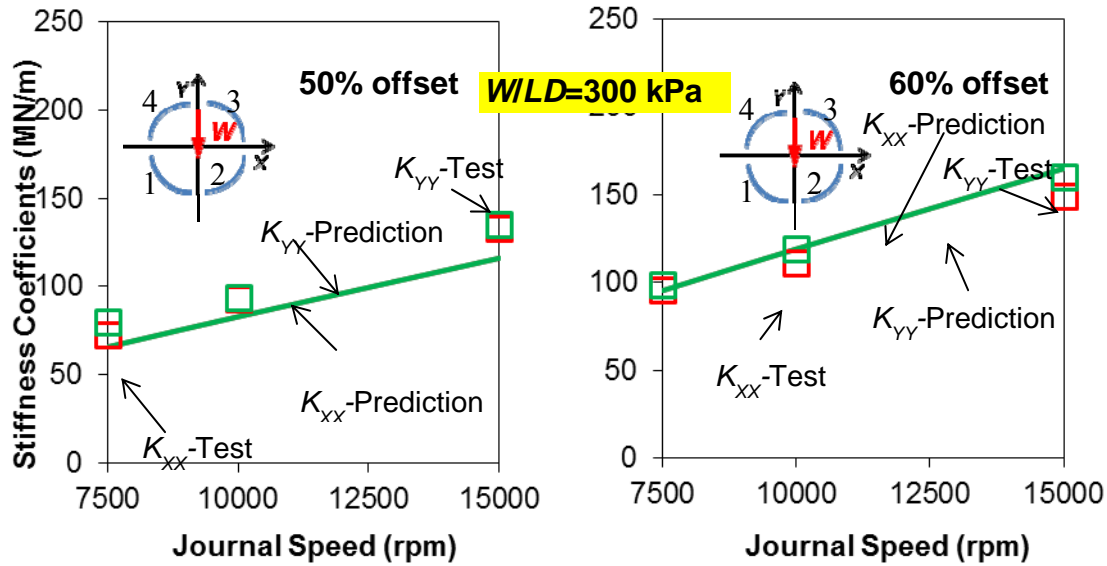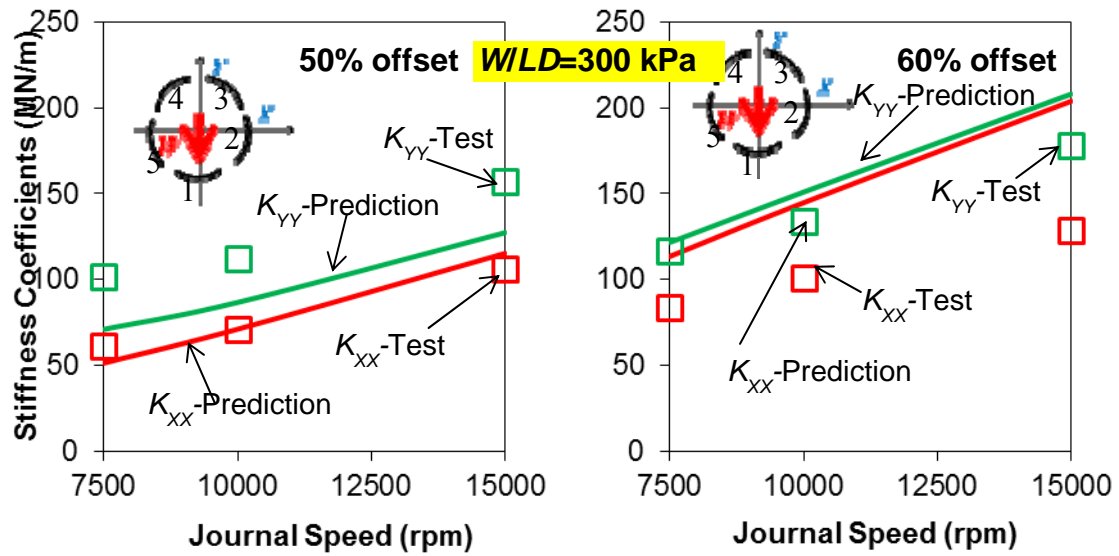**Fig. 74 TPJB virtual mass coefficients versus journal speed (Ω).Specific load (*W/LD*) = 300 kPa. Predictions and measurements [24] for two five-pad LOP TPJBs with pad pivot offsets equaling 0.5 and 0.6.**

Predicted film temperature and measured pad sub-surface temperatures at the pad trailing edge Figure 75 shows the predicted film temperatures and the measured pads' sub-surface temperatures at the trailing edges versus increasing journal speed for two four-pad LBP bearings with pad pivot offset equaling 0.5 and 0.6. The pad temperatures are measured below the surface of the pad[14], as explained in Ref. [24]. Note Fig. 75 only shows the predicted film temperature on pad (#3) since Ref. [24] does not present the test data on pad (#3).

---

[14] References [24, 28] do not provide the depth of the temperature measurements in the pad subsurface.

126

For the four-pad LBP TPJB with pivot offset equaling 0.5, the measured trailing edge temperature on Pad#1 is about 20°C higher than the other bottom pad (#2). However, predictions show a smaller difference between the film temperatures of the bottom two pads (pad #1 and #2). Delgado et.al [24] recognize that the pad sub-surface temperatures were not measured at a thermal steady state; thus they have a large uncertainty.

For the bearing with pad pivot offset equaling 0.6, the predicted film temperature correlates well with measured pad subsurface temperature at its trailing edge. Figure 60 also displays that an increase in pivot offset lowers the pad sub-surface temperatures in a four-pad LBP TPJB, in particular for the loaded pads (#1 and #2).

(a) Pivot offset =0.5   (b)   Pivot offset =0.6
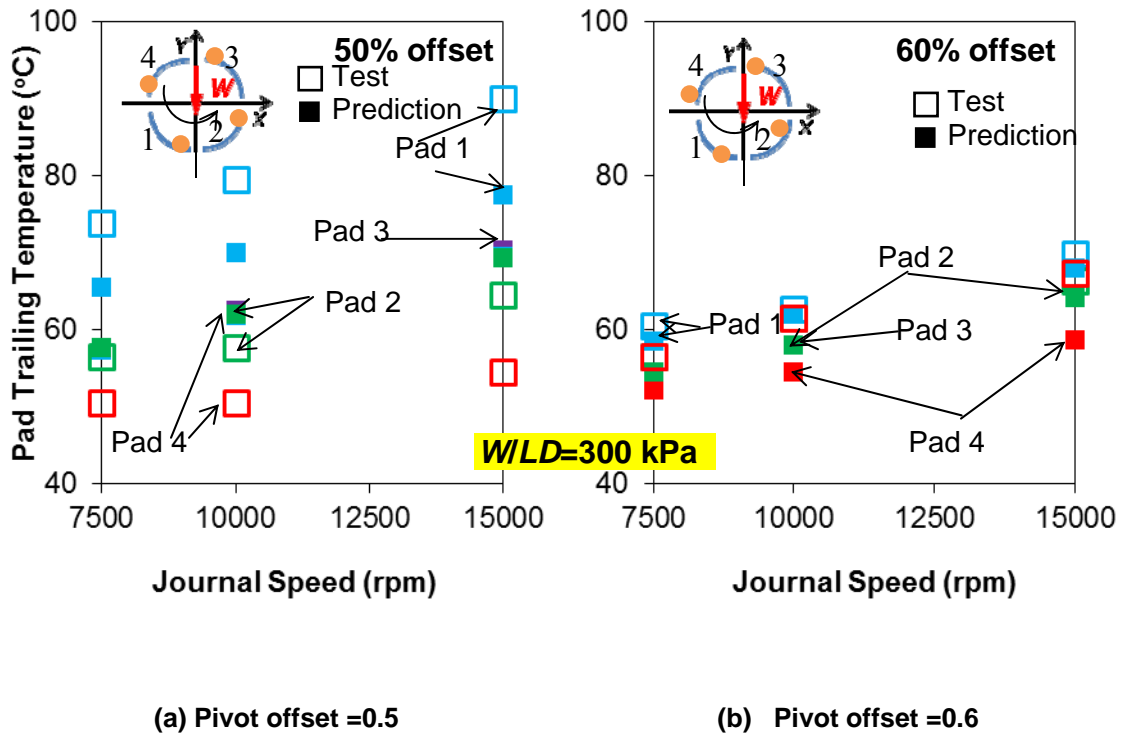
Fig. 75 Film temperature and pad subsurface temperature at pad trailing edge versus journal speed (Ω). Specific load (*W/LD*) = 300 kPa. Predictions and measurements of four-pad LBP TPJBs with different pivot offsets in Ref. [24].

Figure 76 depicts the predictions and measurements on the film and pad sub-surface temperatures at each pad trailing edge in two five-pad LOP TPJBs. Both the predicted and measured results show that the pad temperatures decrease with increasing pad pivot offset for a LOP bearing.

(a) Pivot offset =0.5   (b)   Pivot offset =0.6
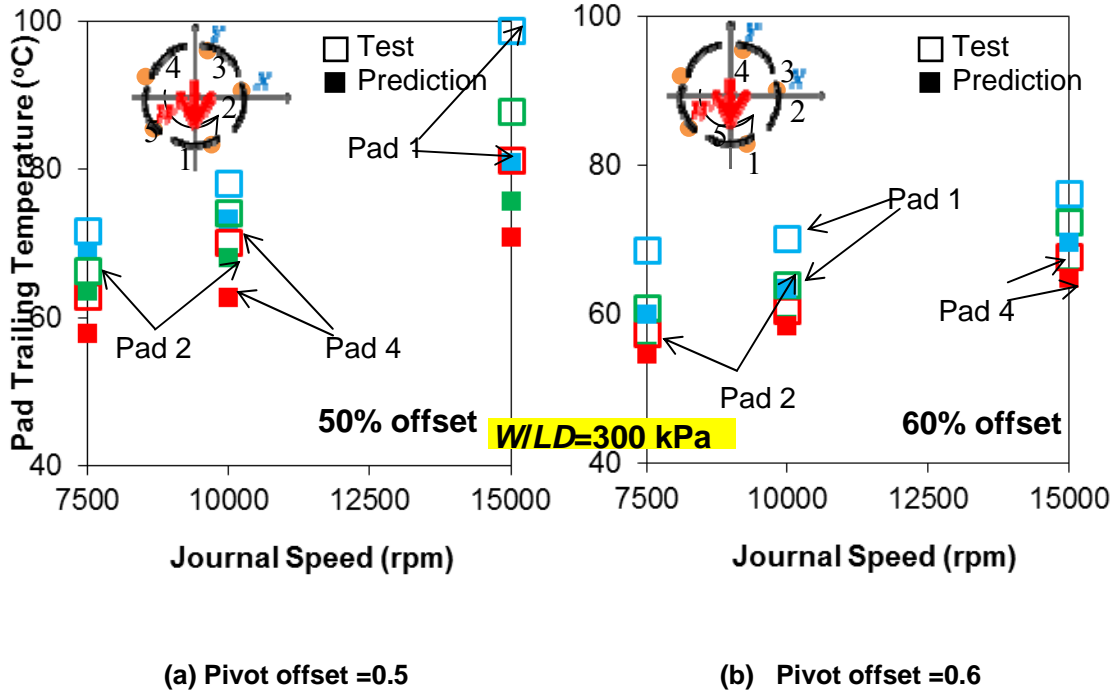
Fig. 76 Film temperature and pad subsurface temperature at pad trailing edge versus journal speed (Ω). Specific load (*W/LD*) = 300 kPa. Predictions and measurements of five-pad LOP TPJBs with different pivot offsets in Ref. [24].

Closure For the model replicating the bearing tested by Delgado et.al [24], a large pad inlet thermal mixing coefficient is selected (λ=0.9); however, pad trailing edge temperatures are still underpredicted for the bearings with a pad pivot offset equaling 0.5. For the bearings with LOP and LBP configurations, an increase in pivot offset causes the pad temperatures to decrease. Hence, those bearings with a larger pivot offset operate cooler.

The predictive model uses a formula, given in Ref. [16], to obtain the pivot radial stiffness considering a cylinder-on-cylinder curvature for the pad pivot contact structure.

The estimated pivot radial stiffness of each pad is ~10 times larger than the bearing static stiffness for operation at all speeds and static loads. Hence, presently, the pivot stiffness has little effects on the bearing static stiffness coefficients and damping coefficients. However, in the model, pivot stiffness increases the bearing dynamic stiffness (real part of the mechanical impedances) and decreases the imaginary part of the impedances at high frequencies.

The experimental bearing impedances show that the bearing dynamic stiffness coefficients are frequency independent and damping coefficients remain invariant. The predictions show that the real part of the bearing impedances decreases with excitation frequency, in particular for the LOP bearing. As seen in Fig.D.1, note the effects of fluid inertia which softens the bearing dynamic stiffness at high excitation frequencies. Hence the model neglects the effects of fluid inertia to correlate the Re(Z) at high excitation frequencies. Pad mass and pad moment of inertia also affect to reduce Re(Z) and to increase Im(Z) at a large excitation frequency. Presently, however, these effects appear not to be dominant.

Example 5-Predicted Forced Performance of a Rocker-Back LOP TPJB [25]

Delgado et.al [25] measure the dynamic forced performance of a TPJB, using the test rig in Ref. [24]. The test bearings are two five-pad LOP TPJBs with pivot offsets equaling 0.5 and 0.6. This section compares the predictions with test data of these two bearings in Ref. [25] utilizing several empirical parameters, such as the pivot stiffness and hot bearing clearances, as stated in Ref. [25].

Table 18 lists the geometry parameters of the test TPJB and operating conditions. Note this bearing is different from the prior example in Ref. [24]. Figure 77 shows a schematic view of the test TPJB. The estimated maximum temperature in the TPJB for operations at a high rotor speed of 15 krpm with the static specific load equaling 0.8 MPa is 89 $^{\circ}$C, and the corresponding Reynolds number ($\mathrm{Re} = \rho \Omega R C_B / \mu$) is 653. Note here C_B is the estimated operating bearing clearance, i.e., $C_B = 58.6$ μm. Hence the flow is laminar in the TPJB.

Table 18 Test TPJBs geometry parameters and operating conditions in Refs. [25].

Number of pads	5	
Rotor diameter, D	110 mm	
Load configuration	LOP	
Cold pad clearance, C_P	135 μm	123 μm
Cold bearing clearance, C_B	99 μm	99 μm
Cold pad preload, $\bar{r}_P$	0.264	0.195
Pad pivot offset	0.5	0.6
Pad arc angle	60°	
Pad axial length, L	44 mm	
Pivot type	Rocker back	
Lubricant type	ISO VG32	
Oil supply temperature, T_s	~40 $^{\circ}$C	
Oil density, ρ	856.2 kg/m^3	
Oil viscosity at 40 $^{\circ}$C	0.0275 Pa.s	

Table 18 Continued

Oil viscosity at 89 $^{\circ}$C	0.00661Pa.s
Temperature viscosity coefficient, α	0.029 1/K
Static specific load, *W/LD*	400 kPa, 800 kPa
Journal speed, Ω	2.5 krpm-15 krpm
Inlet thermal mixing coefficient, λ	0.85

$\bar{r}_P$ =0.264, C_B=99 μm, Pivot offset=0.5

$\bar{r}_P$ =0.195, C_B=99 μm, Pivot offset=0.6
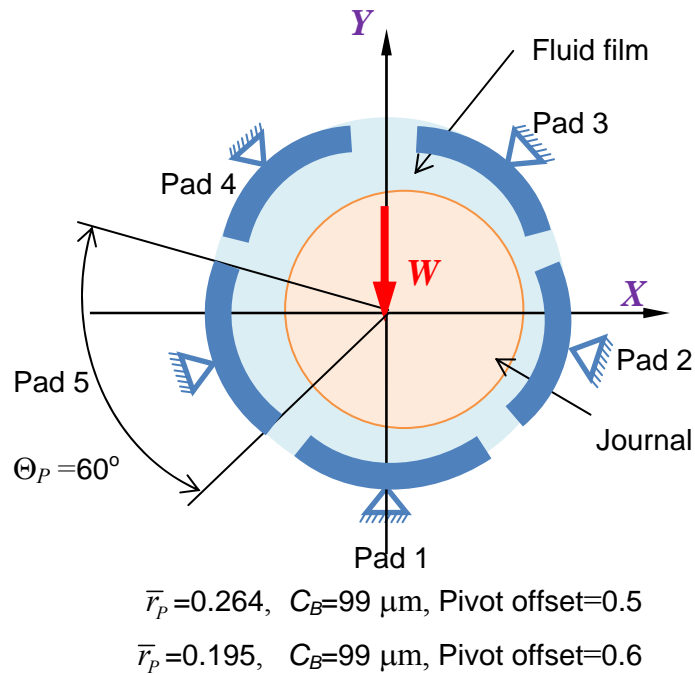
Fig. 77 Schematic view of the test TPJBs in Ref. [25].

Here assume the flow carries away all the heat in the TPJB, i.e. an adiabatic surface condition is selected. Reference [25] reports that the pad thermal mixing coefficient (λ) equals to 0.85. Thus $\lambda = 0.85$ is selected for the predictive model.

Effect of fluid film temperature on operating bearing and pad clearances Delgado et. al measured two bearing radial clearances at 25 $^{\circ}$C and 40 $^{\circ}$C [25]. Recall

131

from Eq. (41) that the formula to calculate the ad-hoc thermal expansion coefficient α_{c_b} is,

$$\alpha_{c_b} = (C_{B,ref} - C_B)/\Delta T \qquad (50)$$

Thus the coefficient α_{c_b} is 0.1651 μm/°C, and α_{c_b} is about 68% smaller than the coefficient estimated for the bearing in Ref. [24], which utilizes the same test rig. The operating bearing and pad clearances are estimated based on the average temperature rise in the TPJB using Eq. (49). Table 19 lists the operating bearing clearances, pad preloads and pad clearances at each operating condition. Note that the hot bearing and pad clearances do not decrease significantly with a great temperature raise in the test TPJB, which is attributed to a small thermal expansion coefficient ($\alpha_{c_b} = 0.1651$ μm/°C) specific to the rotor and bearing. The smallest hot bearing clearance is about 6.7% lower than the nominal value.

Table 19 Estimated operating bearing clearances, pad clearances, pad preload and measured average temperatures raise [25].

Specific load W/LD (kPa)	Rotor speed Ω (rpm)	Bearing clearance C_B (μm)	Pad clearance C_P (μm)	Dimensionless Pad preload $\bar{r}_P$	Measured average temperature raise ΔT_{avg}(°C)
Pivot offset=0.5	Nominal	99.0	134.5	0.264	-
	2,500	95.5	131.0	0.271	21.1
	4,100	95.0	130.5	0.272	24.3
	5,100	94.7	130.2	0.273	26.2
	7,300	94.1	129.6	0.274	29.8
400	9,000	93.7	129.2	0.275	32.2
	11,000	93.3	128.8	0.276	34.8
	13,000	92.9	128.4	0.277	37.0
	15,000	92.6	128.1	0.278	39.1

Table 19 Continued

Specific load *W/LD* (kPa)	Rotor speed Ω (rpm)	Bearing clearance C_B (μm)	Pad clearance C_P (μm)	Dimensionless Pad preload $\bar{r}_P$	Measured average temperature raise ΔT_{avg} (°C)
800	2,500	95.3	130.8	0.271	22.2
	4,100	94.8	130.3	0.272	25.5
	5,100	94.5	130.0	0.273	27.4
	7,300	93.9	129.4	0.274	31.0
	9,000	93.5	129.0	0.275	33.3
	11,000	93.1	128.6	0.276	35.9
	13,000	92.7	128.2	0.277	38.1
	15,000	92.4	127.9	0.278	40.2
Pivot offset=0.5	Nominal	99.0	123.0	0.195	-
400	2,500	95.5	131.0	0.271	21.1
	4,100	95.0	130.5	0.272	24.3
	5,100	94.7	130.2	0.273	26.2
	7,300	94.1	129.6	0.274	29.8
	9,000	93.7	129.2	0.275	32.2
	11,000	93.3	128.8	0.276	34.8
	13,000	92.9	128.4	0.277	37.0
	15,000	92.6	128.1	0.278	39.1
800	2,500	95.3	130.8	0.271	22.2
	4,100	94.8	130.3	0.272	25.5
	5,100	94.5	130.0	0.273	27.4
	7,300	93.9	129.4	0.274	31.0
	9,000	93.5	129.0	0.275	33.3
	11,000	93.1	128.6	0.276	35.9
	13,000	92.7	128.2	0.277	38.1
	15,000	92.4	127.9	0.278	40.2

Pivot flexibility Delgado et. al [25] provide the pivot radial stiffness for operations under two specific loads. The pivot radial stiffness equals to 516 MN/m and 540 MN/m when the specific loads are 400 kPa and 800 kPa, respectively.

TPJB impedance coefficients Figures 78 to 80 show the real part of the TPJB impedance coefficients versus excitation frequency for two test TPJBs, one with pivot offset=0.5 and the other with offset=0.6. The two bearings rotate at speeds 7.3 krpm, 11

krpm and 15 krpm with a specific load equaling to 400 kPa. The bearing dynamic stiffness coefficients slightly decrease with excitation frequency for the 0.5-offset bearing while the 0.6-offset bearing dynamic stiffness slightly increases.
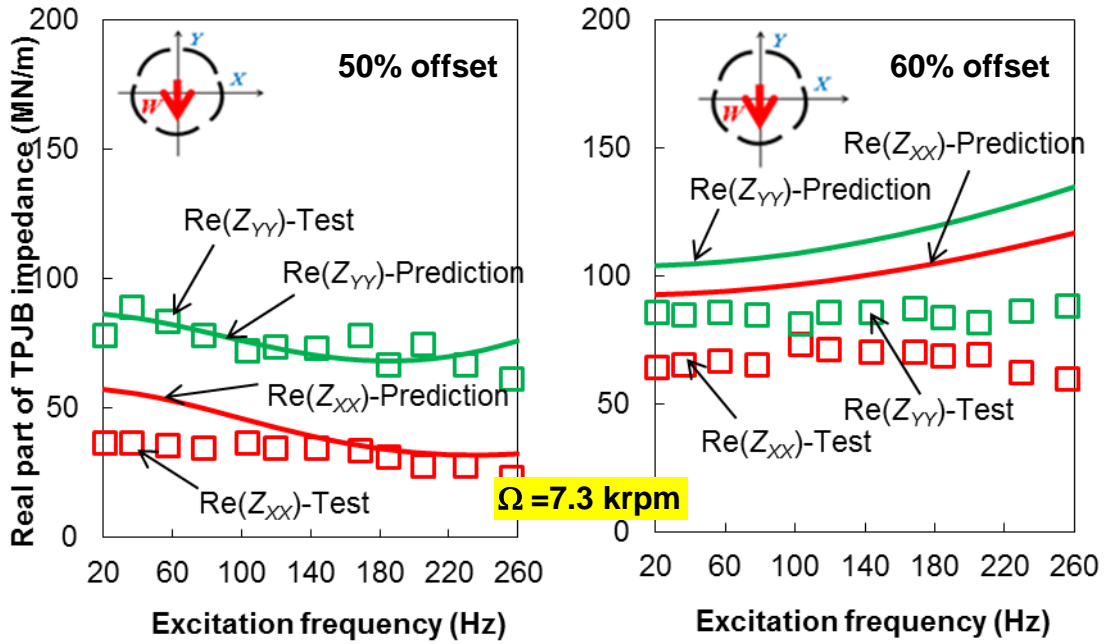
(a) Pad pivot offset =0.50   (b) Pad pivot offset =0.60

Fig. 78 TPJB real part of impedances, Re(Z), versus excitation frequency (Hz). Specific load (W/LD) = 400 kPa. Rotor speed (Ω)=7,300 rpm. Current predictions and measurements in Ref. [25] for two five-pad LOP TPJBs with pad pivot offsets equaling 0.5 and 0.6.
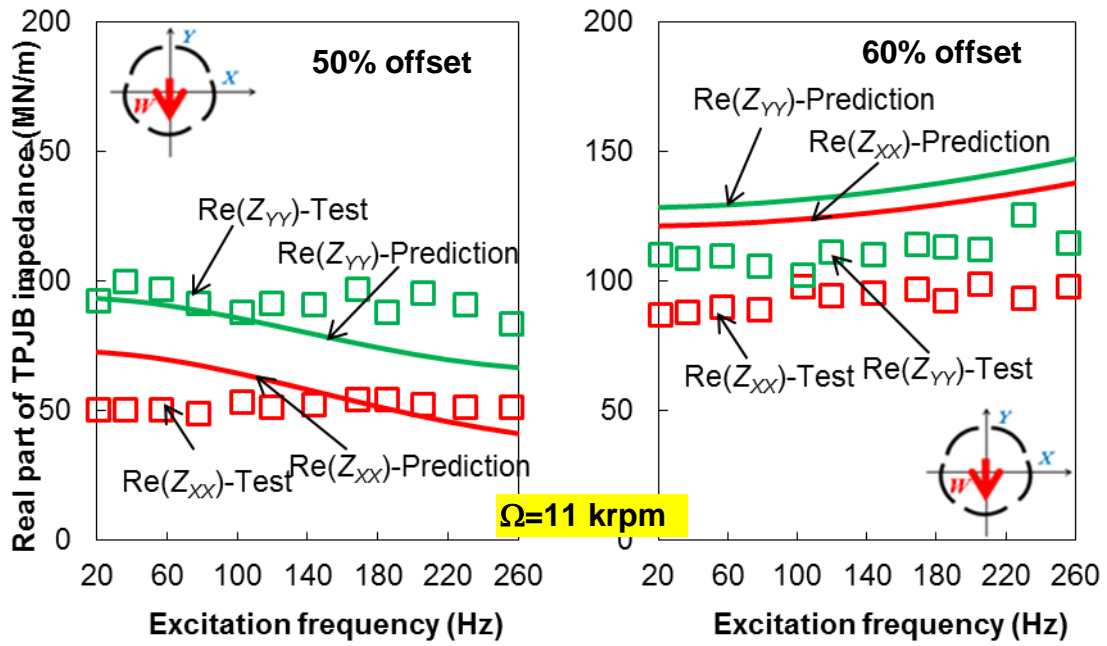
(a) Pad pivot offset =0.50   (b) Pad pivot offset =0.60

Fig. 79 TPJB real part of impedances, Re(*Z*), versus excitation frequency (Hz). Specific load (*W/LD*) = 400 kPa. Rotor speed (Ω)=11,000 rpm. Current predictions and measurements in Ref. [25] for two five-pad LOP TPJBs with pad pivot offsets equaling 0.5 and 0.6.

(a) Pad pivot offset =0.50   (b) Pad pivot offset =0.60

Fig. 80 TPJB real part of impedances, Re(*Z*), versus excitation frequency (Hz). Specific load (*W/LD*) = 400 kPa. Rotor speed (Ω)=15,000 rpm. Current predictions and measurements in Ref. [25] for two five-pad LOP TPJBs with pad pivot offsets equaling 0.5 and 0.6.

Figures 81 to 83 illustrate the imaginary part of the impedances for two LOP bearings operating at speeds equaling to 7.3 krpm, 11 krpm and 15 krpm. The pads have pivot offsets equaling to 0.5 and 0.6. The experimental impedances are linear with the excitation frequency, yielding frequency-independent damping coefficients. The predicted damping coefficients of the 0.5 pivot offset bearing show a minor frequency dependency.
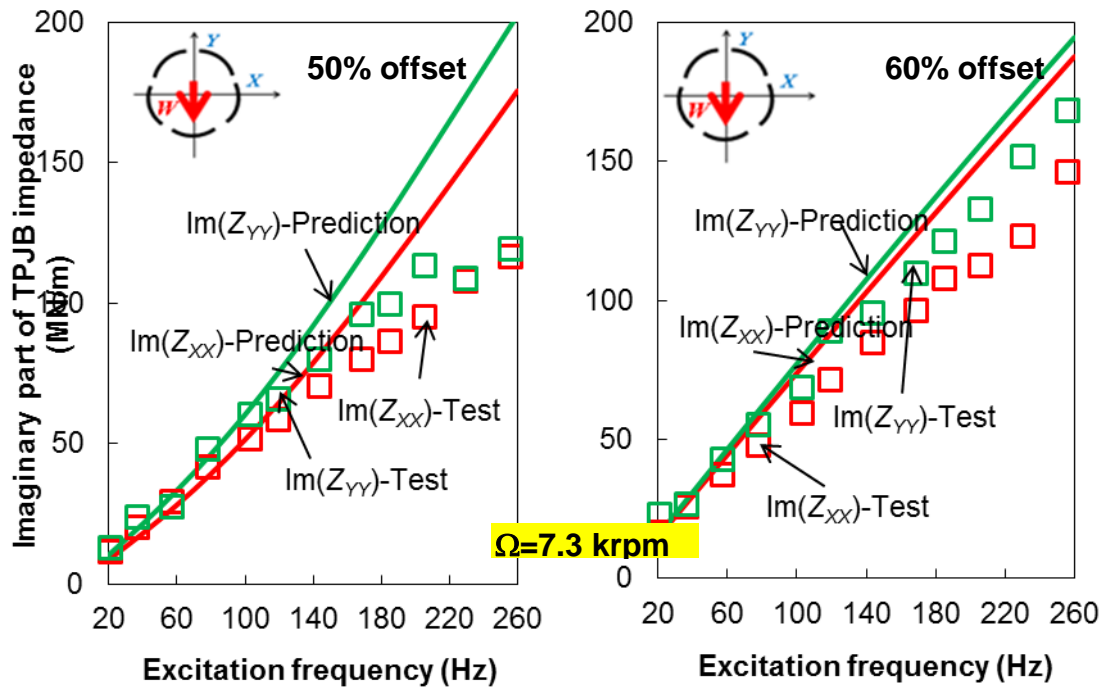
(a) Pad pivot offset =0.50   (b) Pad pivot offset =0.60

Fig. 81 TPJB imaginary part of impedances, Im(*Z*), versus excitation frequency (Hz). Specific load (*W/LD*) = 400 kPa. Rotor speed (Ω)=7,300 rpm. Current predictions and measurements in Ref. [25] for two five-pad LOP TPJBs with pad pivot offsets equaling 0.5 and 0.6.

(a) Pad pivot offset =0.50   (b) Pad pivot offset =0.60

Fig. 82 TPJB imaginary part of impedances, Im(Z), versus excitation frequency (Hz). Specific load (W/LD) = 400 kPa. Rotor speed (Ω)=11,000 rpm. Current predictions and measurements in Ref. [25] for two five-pad LOP TPJBs with pad pivot offsets equaling 0.5 and 0.6.
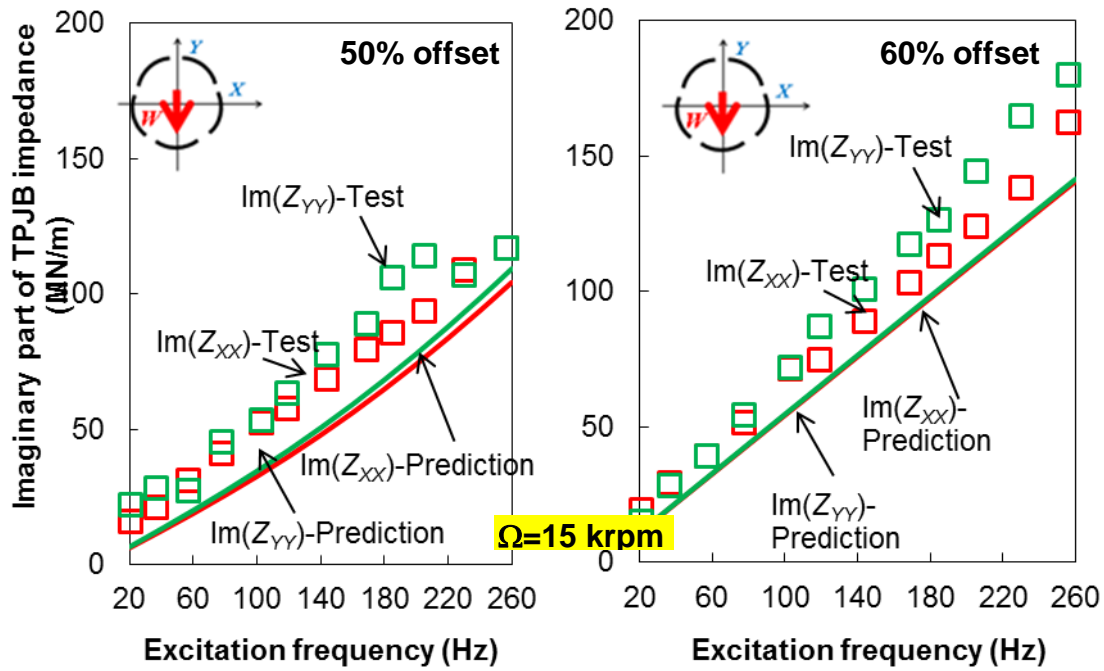
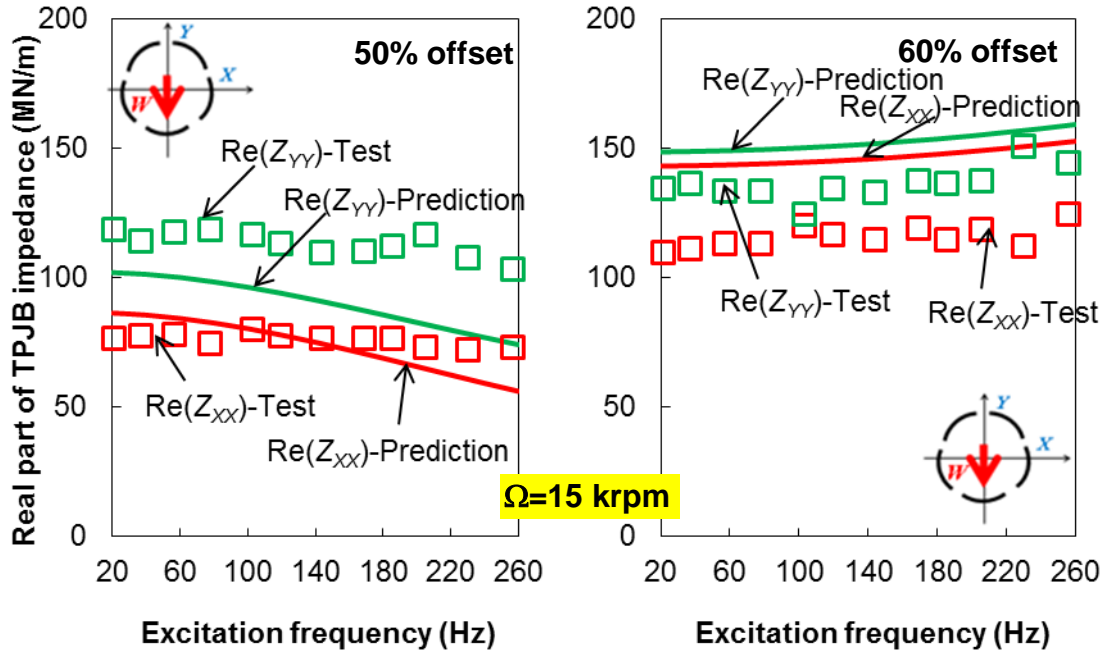**(a) Pad pivot offset =0.50**   **(b) Pad pivot offset =0.60**

Fig. 83 TPJB imaginary part of impedances, Im(*Z*), versus excitation frequency (Hz). Specific load (*W/LD*) = 400 kPa. Rotor speed (Ω)=15,000 rpm. Current predictions and measurements in Ref. [25] for two five-pad LOP TPJBs with pad pivot offsets equaling 0.5 and 0.6.

TPJB stiffness, damping and virtual mass coefficients Figures 84 and 85 show the predicted static stiffness coefficients ($\omega = 0$) and measurements in Ref. [25] for two test TPJBs, one with pivot offset=0.5 and the other with offset=0.6 and for specific loads equaling 400 kPa and 800 kPa. For operation at a specific load of 400 kPa, the predicted stiffness coefficients (K_{YY}) for the 50% and 60% pivot offset bearings are about 10% lower and 20% higher than the measured values, respectively. An increase in pad pivot offset, from 50% to 60%, results in a smaller difference between the direct stiffness coefficients K_{XX} and K_{YY}.

For the five-pad LOP bearings operating at a specific load of 400 kPa and speed 2,500 rpm, $K_{YY} > K_{XX}$; note that K_{YY} shows a peculiar dip at the lowest rotor speeds.

According to Ref. [25], the pivot stiffness remains invariant with the rotor speed (516 MN/m when *W/LD*=400kPa). However, the pivot stiffness may drop significantly for operating at a very low rotor speed (2.5 krpm) and a light load of 400 kPa, since the actual pivot stiffness depends on the pivot reaction load. Hence, the bearings stiffness is overpredicted significantly at that specific condition.

(a) Pad pivot offset =0.50   (b) Pad pivot offset =0.60

Fig. 84 TPJB static stiffness coefficients, *K*, versus journal speed (Ω).Specific load (*W/LD*) = 400 kPa. Current predictions and measurements in Ref. [25] for two five-pad LOP TPJBs with pad pivot offsets equaling 0.5 and 0.6.

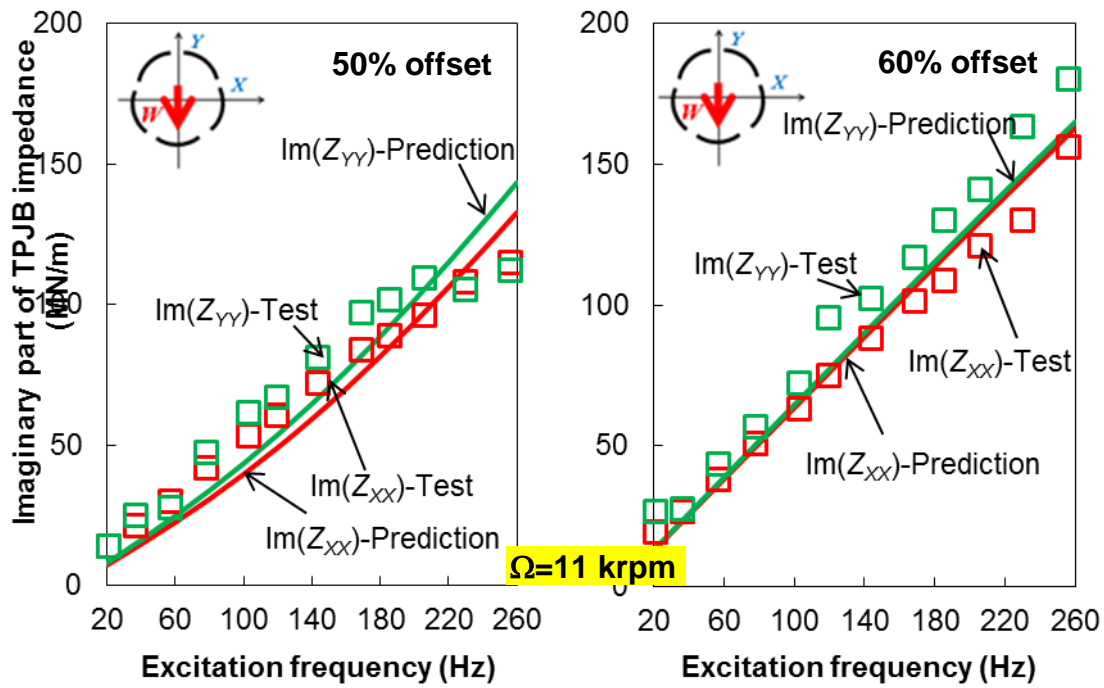(a) Pad pivot offset =0.50   (b) Pad pivot offset =0.60
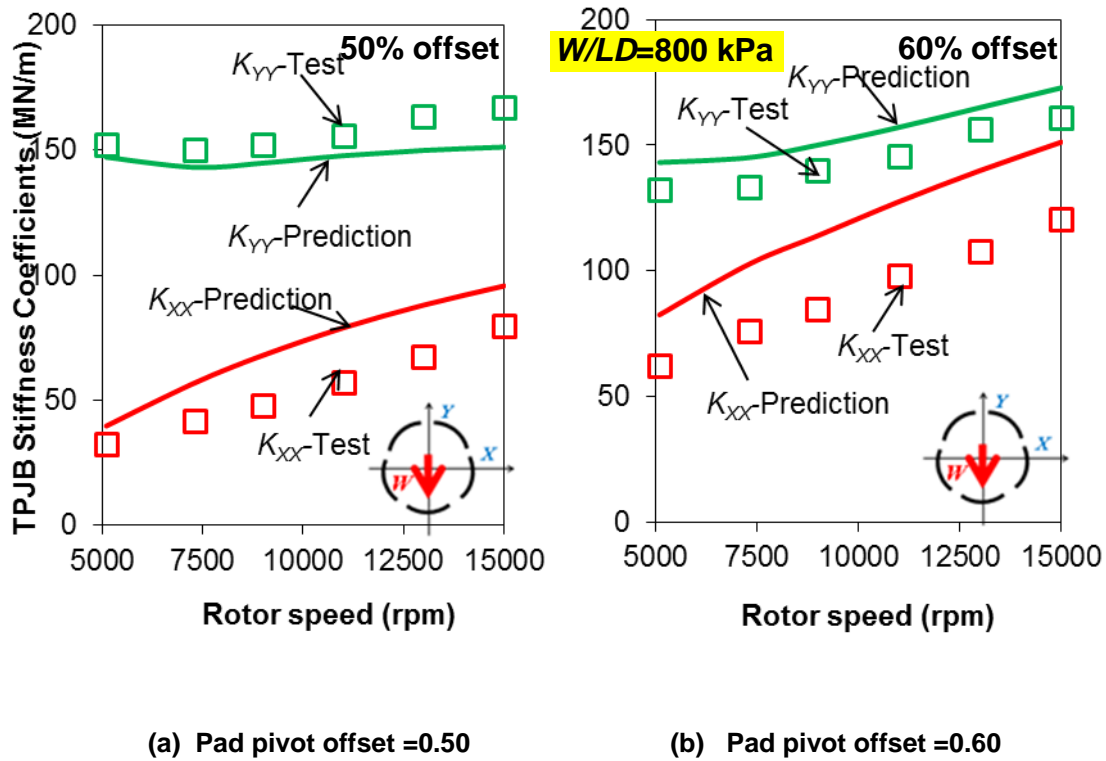
Fig. 85 TPJB static stiffness coefficients, *K*, versus journal speed (Ω).Specific load (*W/LD*) = 800 kPa. Current predictions and measurements in Ref. [25] for two five-pad LOP TPJBs with pad pivot offsets equaling 0.5 and 0.6.

Figures 86 and 87 depict the damping coefficients, *C*, versus journal speed for the two test TPJBs. The damping coefficients are over predicted at low rotor speeds, while under predicted for operation at a high rotor speed. Test data show that the damping coefficients of the two five-pad LOP bearings decrease by ~53% when the rotor speed increases from 2,500 rpm to 15,000 rpm. The predicted damping coefficients experience an even larger decrease (~73%). Note this does not happen to the prior bearing examples in Refs. [7,13,23,24]. The significant over prediction of the bearing damping coefficients at the lowest speed of 2,500 rpm may be due to an over prediction of the pivot stiffness.

(a) Pad pivot offset =0.50   (b) Pad pivot offset =0.60

Fig. 86 TPJB damping coefficients, *C*, versus journal speed (Ω).Specific load (*W/LD*) = 400 kPa. Current predictions and measurements in Ref. [25] for two five-pad LOP TPJBs with pad pivot offsets equaling 0.5 and 0.6.

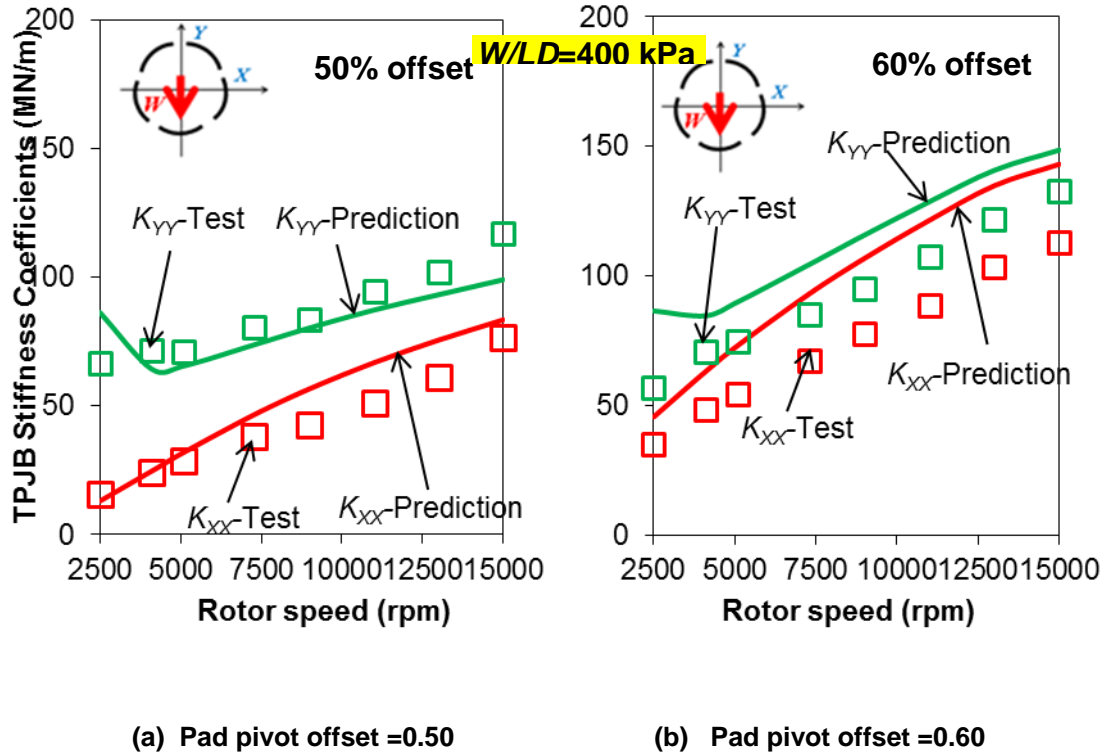(a) Pad pivot offset =0.50   (b) Pad pivot offset =0.60

Fig. 87 TPJB damping coefficients, *C*, versus journal speed (Ω).Specific load (*W/LD*) = 800 kPa. Current predictions and measurements in Ref. [25] for two five-pad LOP TPJBs with pad pivot offsets equaling 0.5 and 0.6.

Figures 88 and 89 display the predicted and measured virtual mass coefficients for the 0.5 and 0.6 pivot offset TPJBs operating at various rotor speeds and two specific loads. Note that the predictions correlate well with the test data and both are nearly zero at rotor speeds higher than 9,000 rpm.

When the operating speed is higher than 9,000 rpm, the virtual mass coefficients are small which reveals the frequency independency of the TPJB dynamic stiffness coefficients over the test frequency range (20 Hz-260 Hz). At the lowest rotor speed of 2,500 rpm, the predicted and measured virtual mass coefficients are negative and large in magnitude, in particular for the predictions. Note that the maximum frequency used to excite the test bearing is 260 Hz, which is about 6.5 times higher than the synchronous speed frequency for operations at the rotor speed of 2,500 rpm. Thus the frequency range

for analysis is presumably large since Re(Z) increases substantially at a high frequency of 260 Hz. At a rotor speed of 2,500 rpm, the real part of the impedance for the LOP bearing with the 50% pivot offset, Re(Z_{YY})=K-$M\omega^2$, at the synchronous speed frequency (42 Hz) equals to 150 MN/m which is only ~2% larger than the stiffness coefficients extracted from the predicted impedance and ~1% smaller than that from the experimental impedance. Hence, though the predicted virtual mass coefficients show a large discrepancy at the lowest journal speed (2,500 rpm), their effect on Re(Z) is small even at a high excitation frequency (ω~6Ω).
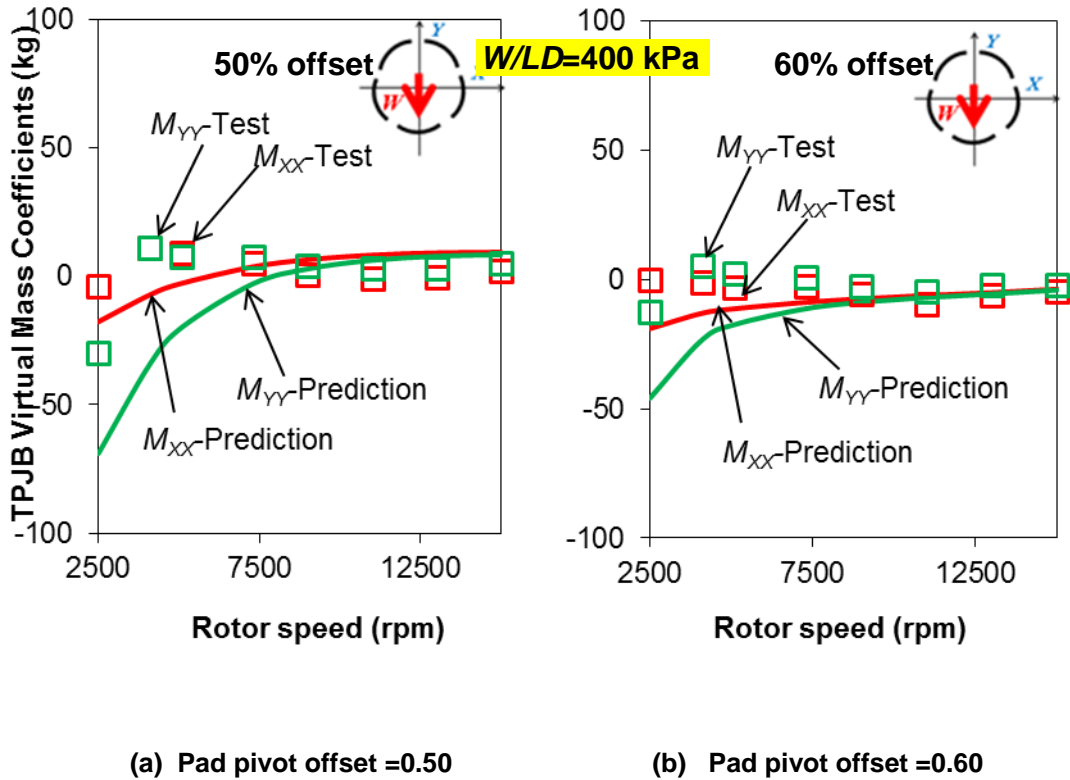
(a) Pad pivot offset =0.50   (b) Pad pivot offset =0.60

Fig. 88 TPJB virtual mass coefficients, *M*, versus journal speed (Ω).Specific load (*W/LD*) = 400 kPa. Current predictions and measurements in Ref. [25] for two five-pad LOP TPJBs with pad pivot offsets equaling 0.5 and 0.6.
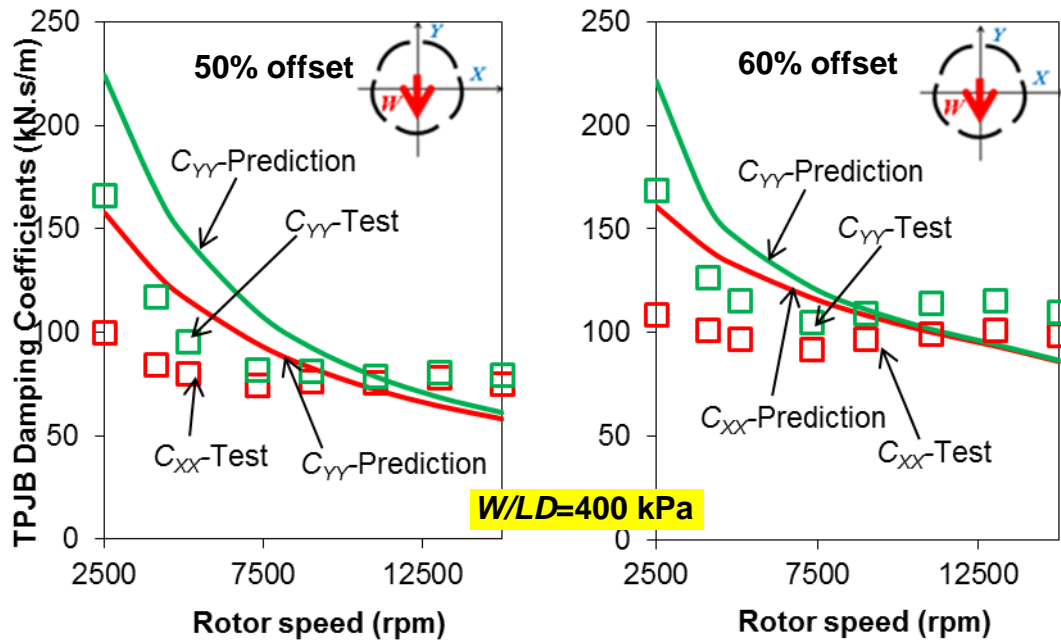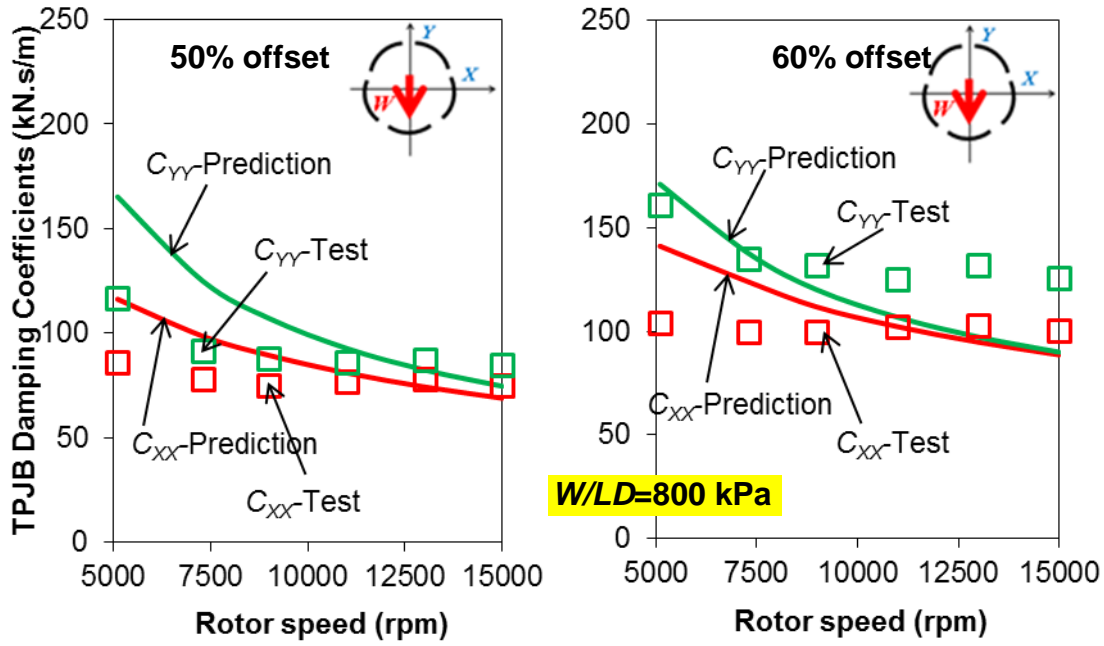
(a) Pad pivot offset =0.50   (b) Pad pivot offset =0.60
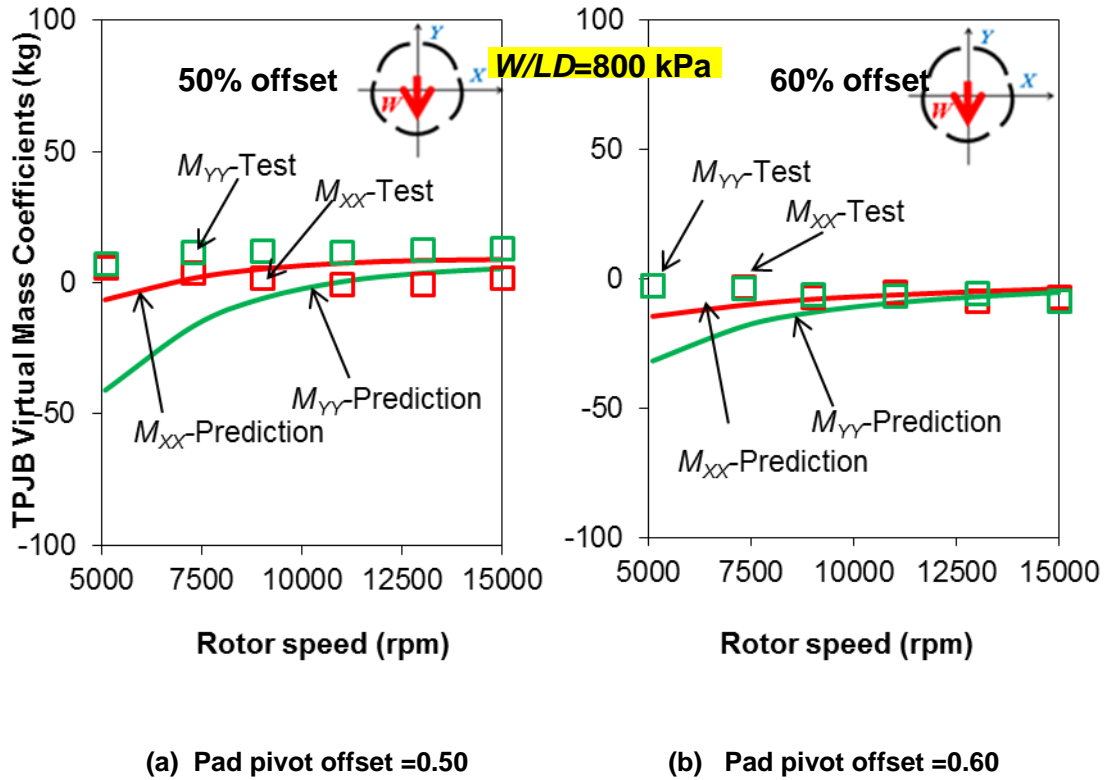
Fig. 89 TPJB virtual mass coefficients, *M*, versus journal speed (Ω).Specific load (*W/LD*) = 800 kPa. Current predictions and measurements in Ref. [25] for two five-pad LOP TPJBs with pad pivot offsets equaling 0.5 and 0.6.

Closure Reference [25] reports that the specific static loads applied on the test TPJB with rocker-back pivots are 400 kPa and 800 kPa and the pivot radial stiffnesses are 516 MN/m and 540 MN/m, respectively. Experimental results show that the TPJB static stiffness coefficient reaches to a maximum of 167 MN/m, which is about 70% smaller than the pivot stiffness. Hence the pivot stiffness does not reduce greatly the TPJB static stiffness and damping coefficients except for operating a very low rotor speed of 2,500 rpm.

According to the measured cold and hot bearing clearances, the temperature in the test TPJB does not decrease significantly the bearing clearance, as compared with other TPJBs studied in the prior sections. The bearing and pad clearances vary by just ~7% at the highest operating temperature (~80°C).

145

For the test TPJBs, the predicted and test static stiffness and virtual mass coefficients are in good agreement for operation at moderate and high rotor speeds ($\Omega \geq 5{,}000$ rpm). For the five-pad LOP bearings at the lowest rotor speed of 2,500 rpm, the static stiffness and virtual mass coefficients deviate significantly from the test results.

CONCLUSIONS

A tilting pad journal bearing model including pads' pivot flexibility, and thermal energy transport and temporal fluid inertia effects is advanced to accurately predict the bearing forced performance. A FORTRAN program with an Excel GUI model TPJBs and deliver predictions of bearing static and dynamic forced performance. The algorithm uses a Newton-Raphson iterative procedure for successful iterations on the equilibrium pad radial and transverse displacements and journal center displacements, even for bearings with very soft pivots. Equations derived from Hertzian contact theory [16] determine the load-dependent pivot radial stiffnesses for various pad-pivot contact structures. Implementation of a frequency-reduction model renders the bearing reduced frequency complex impedance coefficients (Z_{XX}, Z_{XY}, Z_{YX}, Z_{YY}).

The predictive model accounts for the effect of film temperature on the operating bearing and pad clearances for the bearings in Refs. [7,23,24,25] by calculating the thermal expansion of the journal and pad surfaces. Variation of the pad thermal mixing coefficient influences moderately the predicted fluid film temperature. A large thermal mixing coefficient is required to reach good agreement between the predicted and experimental temperatures for operation at either a small load or a high rotor speed or both.

Investigation on the effect of pivot stiffness on the predicted static and dynamic forced performance illustrates that pad pivot flexibility decreases significantly and dominates the bearing stiffness and damping coefficients when the pivot stiffness is smaller than 10% of the fluid film stiffness coefficients (with rigid pivots). The bearing static stiffness coefficient ($\omega=0$) can be obtained by using a simple equation, i.e., $1/K_{YY} = 1/K_{YY,rigid} + 1/K_{piv}$. Pivot flexibility has a more pronounced effect on reducing the bearing damping coefficients than the stiffness coefficients. Since, in general, the pivot radial stiffness depends on the force acting on each pad, pad pivot flexibility does

affect the bearing behavior at a light load condition for a bearing with large pad preloads, such as with the test bearing in Ref. [7].

Pad pivot flexibility influences the bearing impedance coefficients, in particular at high whirl frequencies, thus affecting the frequency dependency of the bearing dynamic stiffness and damping coefficients. Decreasing the pivot stiffness "stiffens" the bearing dynamic stiffness coefficients at high whirl frequencies and "softens" the bearing imaginary part of impedances, causing a frequency dependent damping coefficient.

The pad mass and pad mass moment of inertia also impact the bearing impedance coefficients (real and imaginary parts) for dynamic load operation at high frequencies. The fluid or mass inertia terms set to decrease the bearing dynamic stiffness coefficients. The bearing damping coefficients exhibit frequency dependency when the effects of fluid inertia, pad mass and mass moment of inertia are significant.

The analysis for various TPJBs indicates that neglecting the effect of operating temperature on the actual bearing and pad clearances can cause great discrepancies between the predictions and measurements of the bearing performance characteristics, such as in the test bearings in Refs. [7,23,24]. Since the rotor and pads in a TPJB expand due to the temperature raise of the fluid film and adjacent solids, the operating bearing and pad clearances do change dramatically. Hence, the bearing forced performance varies as well. The stiffness and damping coefficients of a TPJB, as expected, vary with changes in the operating bearing and pad clearances. A simple formula, based on the linear thermal expansion of the material for pads and journal, is used to estimate the operating hot bearing and pad clearances to give a good agreement between the predictions on the TPJB forced performance with experiments.

The pad inlet thermal mixing coefficient (λ) plays an important role in predicting the fluid film temperatures in a TPJB. This empirical parameter varies with the operating conditions. For a TPJB operating at a high rotor speed or a near zero load condition, the pad inlet thermal mixing coefficient λ is large, indicating that a large amount of hot oil

carries over from the upstream pad and mixed with the fresh cold oil entering the downstream pad.

The static and dynamic forced performance characteristics of a TPJB can not be accurately predicted unless the pad pivot flexibility, fluid film thermal energy transport and temperatures, pad inlet thermal mixing coefficient, operating bearing and pad clearances are well known. However, most of the existing published literature [11,23,24,25] does not report the above parameters or flow conditions which are vital to predict successfully the dynamic forced behavior of tilting pad journal bearings. Thus, reasonable assumptions for these parameters to use judiciously in the predictive model are crucial.

Future work shall focus on the accurate prediction of the thermo-mechanical deformations of the journal and pad surfaces by employing a 3-D finite element (FE) model to render the actual bearing and pad clearances. The model shall also include the oil feed arrangements in the 3-D FE model, such as leading edge groove and spray bar blockers, and enhance the thermal energy transport model to correlate better with the experimental pad temperature.

REFERENCES

[1]   Childs, D.W., 1993, *Turbomachinery Rotordynamics*: *Phenomena*, *Modeling and Analysis*, John Wiley & Sons, New York.

[2]   San Andrés, L., 2010, "Static and Dynamic Forced Performance of Tilting Pad Bearings: Analysis Including Pivot Stiffness," Modern Lubrication Theory, Texas A&M University Digital Libraries, https://repository.tamu.edu/handle/1969.1/93197

[3]   Lund, J.W., 1964, "Spring and Damping Coefficients for the Tilting-Pad Journal Bearing," ASLE Trans., **7**, pp. 342-352.

[4]   Lund, J.W.,1987, "The Influence of Pad Flexibility on the Dynamic Coefficients of a Tilting Pad Journal Bearing," ASME J. Tribol., **109**, pp. 65-70.

[5]   Rouch, K. E., 1983, "Dynamics of Pivoted-Pad Journal Bearings, Including Pad Translation and Rotation Effects," STLE Tribol. Trans., **26**, pp. 222-227.

[6]   Chen, W. J., 1995, "Bearing Dynamic Coefficients of Flexible Journal Bearings," STLE Trans., **38**(2), pp. 253-260.

[7]   Wilkes, J. C., 2011, "Measured and Predicted Rotor-Pad Transfer Functions for a Rocker-Pivot Tilting-Pad Bearing," PhD. Thesis, Mechanical Engineering, Texas A&M University, College Station, TX.

[8]   Debordes, H., Fillon, M., Frene, J., and Chan Hew Wai, C., 1995, "The Effects of Three Dimensional Pad Deformations on Tilting Pad Journal Bearings under Dynamic Loading," ASME J. Trib. **117**, pp. 379-384.

[9]   Ettles, C.M., 1980, "The Analysis and Performance of Pivoted Pad Journal Bearings Considering Thermal and Elastic Effects," ASME Jour. Of Lur. Tech. **102**, pp. 182-192.

[10]   Bouard, L., Fillon, M., and Frene, J., 1996, "Thermohydrodynamic Analysis of Tilting-Pad Journal Bearings Operating in Turbulent Flow Regime," ASME J.

Trib. **118**(1), pp. 225-231.

[11] Dmochowski, W., 2007, "Dynamic Properties of Tilting-Pad Journal Bearings: Experimental and Theoretical Investigation of Frequency Effects due to Pivot Flexibility," ASME J. Eng. Gas Turbines Power, **129**, pp. 865-869.

[12] Carter, C., and Childs, D.W., 2009, "Measurements versus Predictions for the Rotordynamic Characteristics of a Five-Pad Rocker-Pivot Tilting-Pad Bearing in Load-Between-Pad Configuration," ASME, J. Eng. Gas Turbines Power, **131**, 012507 1-9.

[13] Childs, D.W., and Harris, H., 2009, "Static Performance Characteristics and Rotordynamic Coefficients for a Four-Pad Ball-in-Socket Tilting Pad Journal Bearing," ASME, J. Eng. Gas Turbines Power, **131**, 062502 1-11.

[14] Harris, H., 2008, "Static Characteristics and Rotordynamic coefficients of a Four-Pad Tilting-Pad Journal Bearing with Ball-in-Socket Pivots in Load-Between-Pad Configuration," Master Thesis, Mechanical Engineering, Texas A&M University, College Station, TX.

[15] Kim, J., Palazzolo, A., and Gadangi, R., 1995, "Dynamic Characteristics of TEHD Tilt Pad Journal Bearing Simulation Including Multiple Mode Pad Flexibility Model," ASME J. Vib. Acoust., **117**, pp. 123-135.

[16] Kirk, R.G., and Reedy, S. W., 1988, "Evaluation of Pivot Stiffness for Typical Tilting-Pad Journal Bearing Designs," J. Vib. Acoust. Stress. Reliab. Des., **110**(2), pp. 165-171.

[17] San Andrés, L., 1996, "Turbulent Flow, Flexure-Pivot Hybrid Bearings for Cryogenic Applications," ASME J. Trib., **118**(1), pp. 192-200.

[18] Ikeda, K., Hirano, T., Yamashita, T., Mikami, M., and Sakakida, H., 2006, "An Experimental Study of Static and Dynamic Characteristics of a 580 mm (22.8in.) Diameter Direct Lubrication Tilting Pad Journal Bearing," ASME J. Trib., **128**, pp.146-154.

[19] Nicholas, J. C., 2003, "Tilting Pad Journal Bearings with Spray-Bar Blockers and Bypass Cooling For High Speed, High Load Applications," *Proc. of the*

32nd Turbomachinery Symposium, Turbomachinery Laboratory, Texas A&M University, College Station.

[20] Dmochowski, W., Brockwell, K., DeCamillo, S., and Mikula, A., 1993, "A Study of the Thermal Characteristics of the Leading Edge Groove and Conventional Tilting Pad Journal Bearings," ASME J. Trib., **115**(2), pp. 219-226.

[21] San Andrés, L., 2010, "Thermal Analysis of Finite Length Journal Bearings Including Fluid Effects," Modern Lubrication Theory, Texas A&M University Digital Libraries, https://repository.tamu.edu/handle/1969.1/93197

[22] San Andrés, L., 2006, "Hybrid Flexure Pivot-Tilting Pad Gas Bearings: Analysis and Experimental Validation," ASME J. Trib., **128**(1), pp. 551-558.

[23] Kulhanek, C., Childs, D., 2012, "Measured Static and Rotordynamic Coefficient Results for a Rocker-Pivot, Tilting-Pad Bearing With 50 and 60% Offsets," ASME, J. Eng. Gas Turbines Power, **134**, 052505 1-11.

[24] Delgado, A., Ertas, B., Drexel M., Naldi, L., and Vannini, G., 2010, "Identification and Prediction of Force Coefficients in a Five-Pad and Four-Pad Tilting Pad Bearing for Load-on-Pad and Load-Between-Pad Configurations," *Proceedings of ASME Turbo Expo 2010*, Paper GT2010-23802, June 14-18, Glasgow, UK.

[25] Delgado, A., Libraschi, M., and Vannini, G., 2012, "Dynamic Characteristics of Tilting Pad Journal Bearings from Component and System Level Testing," *Proceedings of ASME Turbo Expo 2012,* Paper GT2012-69851, June 11-15, Copenhagen, Denmark.

[26] Wilkes, J., DeCamillo, S., Kuzdzal, M., and Mordell, J., 2000, " Evaluation of a High Speed, Light Load Phenomenon in Tilting-Pad Thrust Bearings," *Proc. of the 29nd Turbomachinery Symposium*, Turbomachinery Laboratory, Texas A&M University, College Station.

[27] Kulhanek, C., 2010, "Dynamic and Static Characteristics of a Rocker-Pivot, Tilting-Pad Bearing With 50 and 60% Offsets," Master Thesis, Mechanical

Engineering, Texas A&M University, College Station, TX.

[28] Delgado, A., Ertas, B., Drexel M., Naldi, L., and Vannini, G., 2010, "A component level test rig for dynamic characterization of oil lubricated bearings using different input excitations," *Proceedings of ISROMAC Thirteenth International Symposium on Transport Phenomena and Dynamics of Rotating Machinery*, Hawai, April.

APPENDIX A- PIVOT DEFLECTION AND PIVOT STIFFNESS FOR TYPICAL

PAD-PIVOT CONTACT STRUCTURES

Various pivot types in TPJBs, such as rocker-back pivot and ball-in-socket pivot, have different pad pivot contact geometries. The pad and pivot materials and the geometry of the contact structure influence the pad pivot stiffness and pivot deflections when a static load acts on the pivot. The typical geometries applied in the pad pivot contact structure are (1) sphere on a sphere, (2) cylinder on a cylinder, and (3) sphere on a cylinder. For the kth pad, equations are given in Ref. [16] to obtain the pivot radial deflection (ξ_{piv}^k) and pivot stiffness (K_{piv}^k).

(1) Sphere on a sphere

For this contact geometry, the pivot radial deflection is estimated by,

$$\xi_{piv}^k = 1.04 \sqrt[3]{\left(F_{piv}^k\right)^2 \left(\frac{1-\upsilon_P^2}{E_P} + \frac{1-\upsilon_H^2}{E_H}\right)^2 \frac{D_H - D_P}{D_P D_H}} \tag{A.1}$$

Here, F_{piv} is the static load acting on the pivot. E_P, E_H are the pivot and housing elastic moduli while υ_P and υ_H denote the pivot and housing Poisson's ratios. D_P and D_H correspond to the diameters of the pivot and housing curvatures, respectively.

(2) Cylinder on a cylinder

The pivot radial deflection for this contact geometry is,

$$\xi_{piv}^k = \frac{2F_{piv}^k(1-\upsilon^2)}{\pi LE}\left(\frac{2}{3} + \ln\frac{4LED_P D_H(D_H - D_P)}{2.15^2 F_{piv}^k}\right) \tag{A.2}$$

where L is the contact length between the pad and pivot.

(3) Sphere on a cylinder

The estimated pivot radial deflection of this contact geometry is,

$$\xi_{piv}^k = 0.52 \left(1 + \sqrt[3]{\frac{D_H - D_P}{D_H}} \right) \sqrt[3]{\frac{\left(F_{piv}^k\right)^2}{D_P} \left(\frac{1-\upsilon_P^2}{E_P} + \frac{1-\upsilon_H^2}{E_H}\right)^2} \tag{A.3}$$

Equations.(A.1-A.3) give the nonlinear deflection-versus-load functions, as shown in Eq.(32), for each pad pivot contact structure. Reference [16] demonstrates that the pivot stiffness of the kth pad for all three structures can be estimated by,

$$\frac{1}{K_{piv}^k} = \frac{\partial \xi_{piv}^k}{\partial F_{piv}^k} = \frac{\partial f}{\partial F_{piv}^k} \tag{A.4}$$

Equation (A.4) shows that the slope of the deflection-versus-load curve gives the pivot flexibility.

(4) Load-deflection function

In certain instances, a polynomial (fifth-order) pivot load-deflection function is known emprically for a pad-pivot contact structure geometry, i.e.,

$$F_{piv}^k = a_0 + a_1 \xi_{piv}^k + a_2 \left(\xi_{piv}^k\right)^2 + a_3 \left(\xi_{piv}^k\right)^3 + a_4 \left(\xi_{piv}^k\right)^4 + a_5 \left(\xi_{piv}^k\right)^5 \tag{A.5}$$

Here, a_i, i=0,1,…5 are known parameters.

Equation (A.5) gives a load-versus-deflection function for the pad pivot structure, i.e., $F_{piv} = g(\xi_{piv})$. For this type of pivot, a simple Newton-Raphson iterative procedure is employed to estimate the pivot radial deflection (ξ_{piv}) in Eq.(32),

$$\left[\xi_{piv}^k\right]_{n+1} = \left[\xi_{piv}^k\right]_n - \delta F_{piv}^k \big/ K_{piv}^k \tag{A.6}$$

Here, the pivot stiffness equals to the slope of the load versus deflection curve, i.e.,

$$K_{piv}^k = \frac{\partial F_{piv}^k}{\partial \xi_{piv}^k} = a_1 + 2a_2 \xi_{piv}^k + 3a_3 \left(\xi_{piv}^k\right)^2 + 4a_4 \left(\xi_{piv}^k\right)^3 \tag{A.7}$$

APPENDIX B-EFFECT OF PIVOT FLEXIBILITY ON THE STATIC AND

DYNAMIC FORCED PERFORMANCES FOR A BALL-IN-SOCKET TPJB [13]

In this section, the pivot stiffness for the test bearing in Ref. [13] is assumed to vary from 10% of the fluid film stiffness to 100 times larger than the fluid film stiffness. The predicted static characteristics and dynamic force coefficients for the bearing with various pivot stiffnesses shows the effect of the pivot stiffness on the bearing stiffness coefficients. Figure 9 shows a schematic view of the test bearing. Table 2 lists the bearing geometry parameters, lubricant properties and operating conditions.
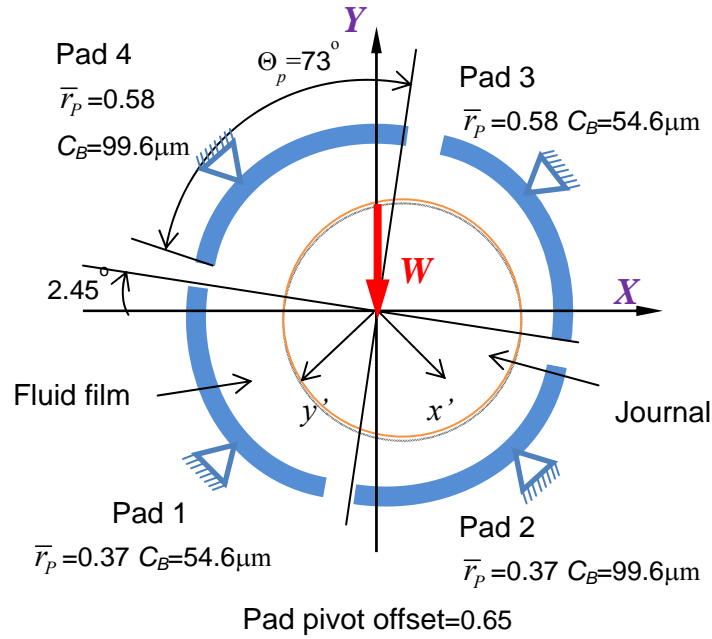

Fig. 9 Load configuration and pad arrangements of a test four-pad tilting pad journal bearing in Ref. [13]. Nominal bearing clearance C_B=95.3 μm, nominal pad preload $\overline{r}_P$ =0.37 (loaded pads) and 0.58 (unloaded pads).

Table 2 Parameters of the test ball-in-socket TPJB in Ref. [13].

Number of pads, N_{pad}	4
Configuration	LBP
Rotor diameter, D	101.6 mm
Pad axial length, L	101.6 mm
Pad arc angle, Θ_P	73°
Pivot offset	65%
Dimensionless preload of loaded pads, $\bar{r}_P$	Pad#1, #2 : 0.37
Dimensionless preload of unloaded pads,	Pad#3, #4 : 0.58
Nominal bearing clearance, C_B	95.3 μm
Measured bearing clearance, C_B	54.6 μm, 99.6 μm
Pad clearance, C_P	86.7μm, 158.1μm, 130μm, 237.1μm
Pad mass, m_P	1.2 kg
Pad moment of inertia, I_P	7.91×10^{-4} kg.m^2
Pivot type	Ball-in-Socket
Pivot material	Ball: Steel, Socket: Bronze
Measured pivot radial stiffness, K_{piv}	350 MN/m
Estimated pivot radial stiffness, $\bar{K}_{piv}$	443 MN/m (6 krpm), 548 MN/m (10 krpm)
Oil inlet temperature	~40 ^{o}C
Lubricant type	ISO VG32, DTE 797
Lubrication method	Spray bar blocker, by pass cooling
Lubricant density	856.2 kg/m^3
Oil supply viscosity at 40 ^{o}C, μ_0	0.0275 Pa.s
Oil viscosity at 60 ^{o}C, 67 ^{o}C	0.0151 Pa.s, 0.0125 Pa.s
Temperature viscosity coefficient, α	0.029 1/K
Specific load, W/LD	0 kPa-1,896 kPa
Journal speed, Ω	4,000 rpm-12,000 rpm

Table B.1 lists the direct static stiffness (ω=0), damping and virtual mass coefficients of the TPJB modeled with rigid pivots and for operation under different static loads and at a rotor speed of 6 krpm. Note that these bearing force coefficients can also be

considered as the fluid film stiffness, damping and virtual mass coefficients since the pad pivots are rigid.

Table B. 1 Force coefficients of a LBP TPJB with rigid pivots for operation at a rotor speed of 6 krpm.

Specific load	Stiffness coefficient (MN/m)		Damping coefficient (kN.s/m)		Virtual mass coefficient (kg)	
kPa	K_{XX}	K_{YY}	C_{XX}	C_{YY}	M_{XX}	M_{YY}
0	1,159	1,159	1,450	1,450	6.1	6.1
689	1,188	1,188	1,492	1,492	4.5	4.5
1,376	1,269	1,269	1,585	1,585	4.0	4.0
1,905	1,363	1,363	1,685	1,685	4.2	4.2

Table B.1 depicts that the TPJB direct stiffness, damping and virtual mass coefficients are the same along the loaded direction and unloaded direction ($K_{XX} = K_{YY}$, $C_{XX} = C_{YY}$, $M_{XX} = M_{YY}$).

Journal eccentricity Figure B.1 shows the effect of pivot stiffness on the journal center displacement along the load direction (Y) of a four-pad LBP bearing operating at a rotor speed of 6 krpm with specific loads equaling 0 kPa and 1,376 kPa. At the zero load condition, the journal experiences a small displacement which does not vary with pivot stiffness. When the specific load equals to 1,376 kPa, the journal displacement increases greatly as the pivot stiffness drops. The journal displacement along the Y direction (e_Y) exceeds the nominal bearing clearance for a bearing with a pivot stiffness less than 178 MN/m.
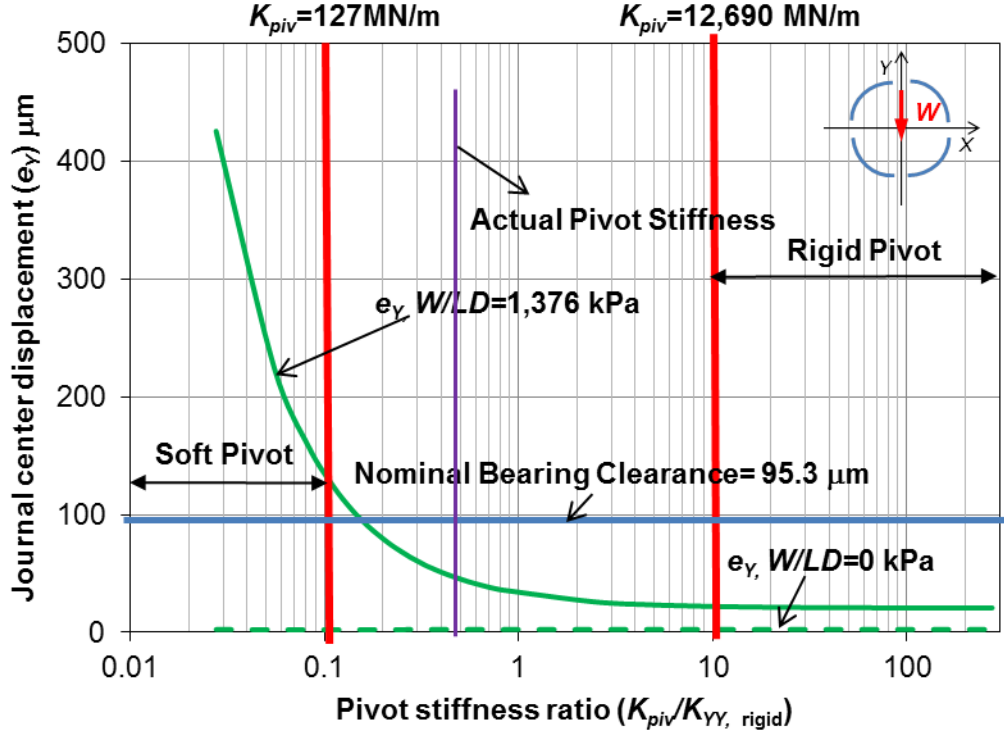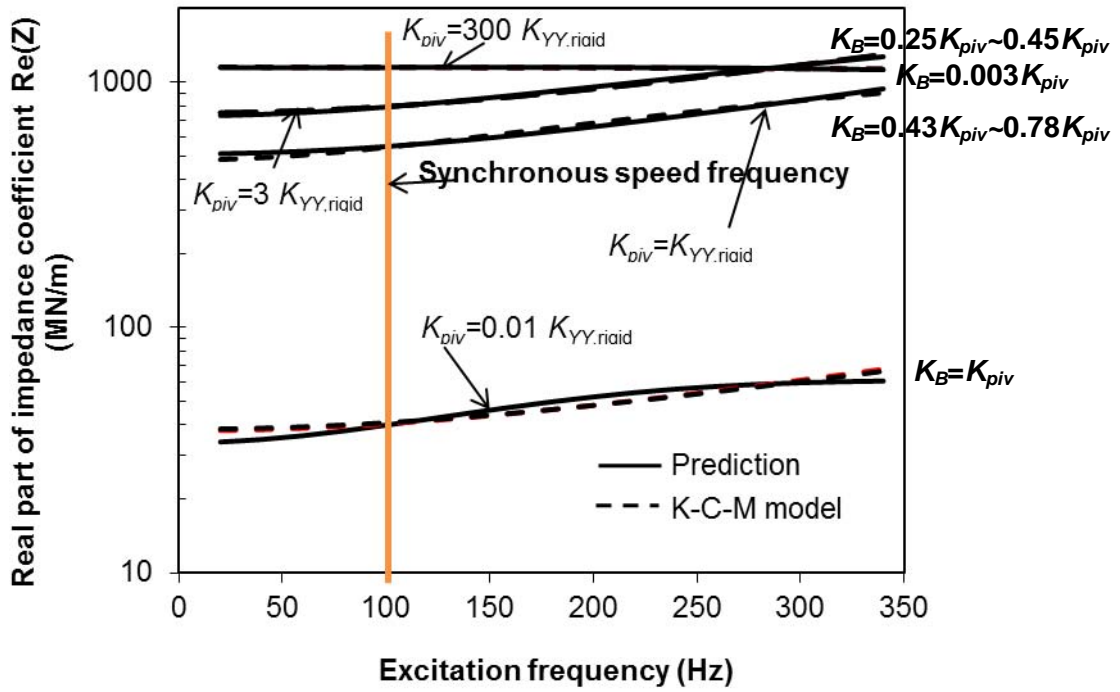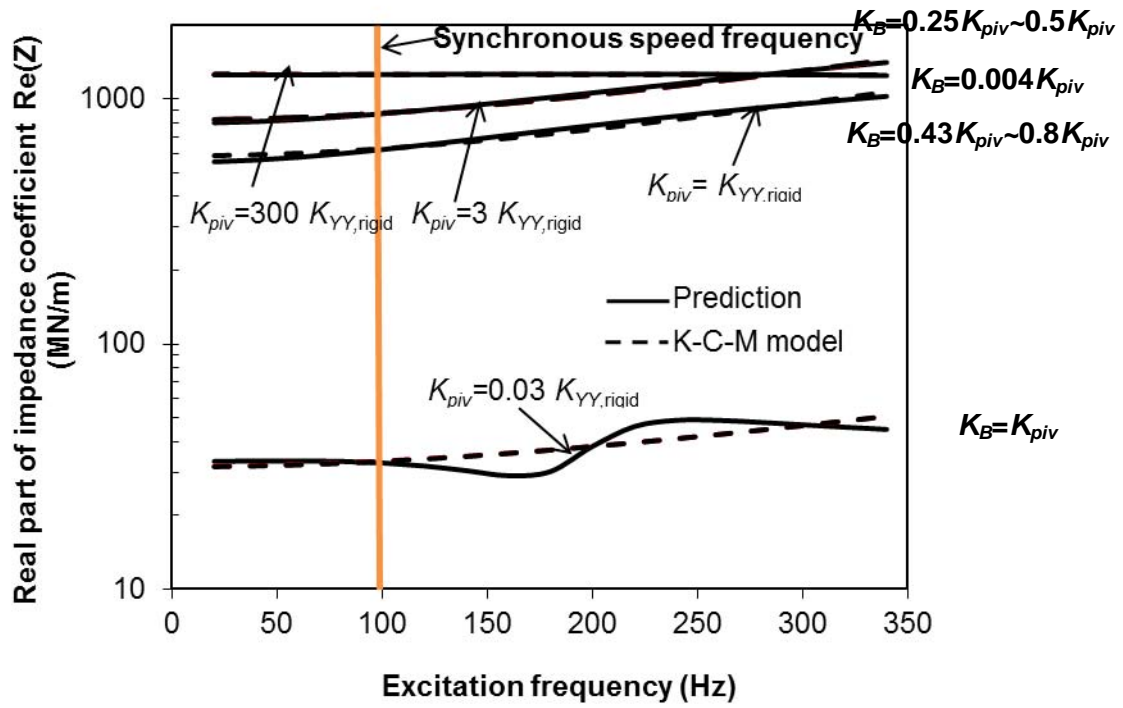
Fig. B. 1 Effect of pivot stiffness on the journal displacement along *Y* direction (e$_Y$) for operating at two specific loads. Rotor speed of Ω = 6 krpm. Bearing fluid film stiffness $K_{YY,rigid}$=1,269 MN/m.

Bearing real part of the impedance and damping coefficients Figure B.2 depicts the bearing real part of the impedance coefficients for the LBP bearings operating at rotor speed of 6 krpm with four pivot stiffnesses, 35 MN/m, 1,159 MN/m, 3,045 MN/m, and 350,000 MN/m, which are $0.03K_{YY,rigid}$, $K_{YY,rigid}$, $3K_{YY,rigid}$, and $300K_{YY,rigid}$. Note $K_{YY,rigid}$ is the stiffness coefficient of the bearing with rigid pivots (equals to fluid film stiffness) along the *Y* direction, as listed in Table B.1. For the bearings with pivot stiffnesses equaling $0.03K_{YY,rigid}$ and $300K_{YY,rigid}$, the impedance coefficients (real part) are frequency independent. However, the real part of impedance for the bearing with a pivot stiffness of $3K_{YY,rigid}$ increases dramatically with excitation frequency, yielding a negative virtual mass coefficient of large magnitude.

161

Figure B.3 displays the effect of pivot flexibility on the bearing damping coefficient at various excitation frequencies. For the bearing with almost rigid pivots (K_{piv}=300$K_{YY,\text{rigid}}$), the damping coefficient remains invariant with increasing frequency. As the pivot stiffness decreases, the damping coefficients are prone to be frequency dependent.
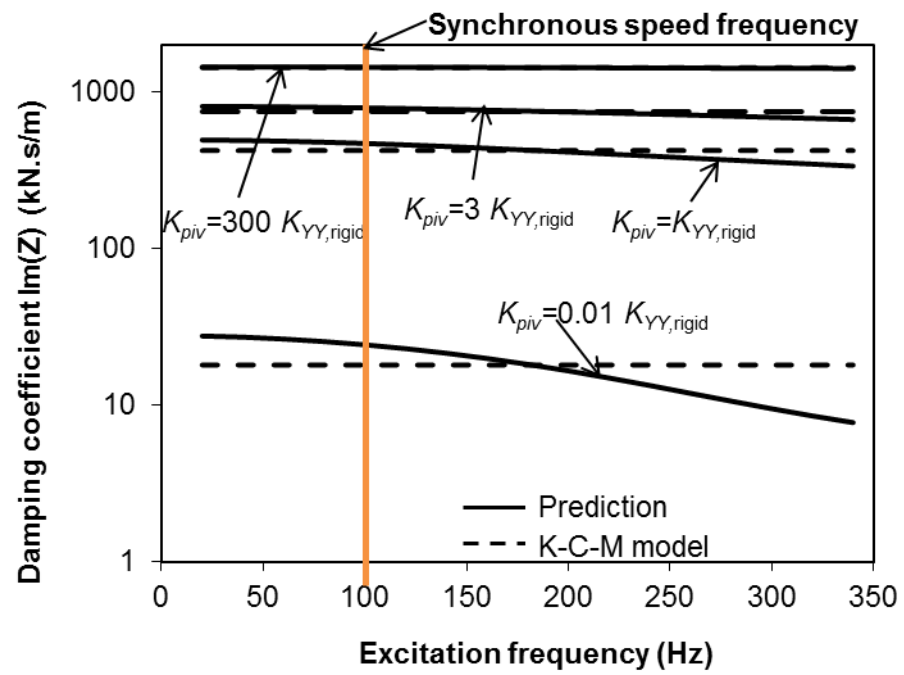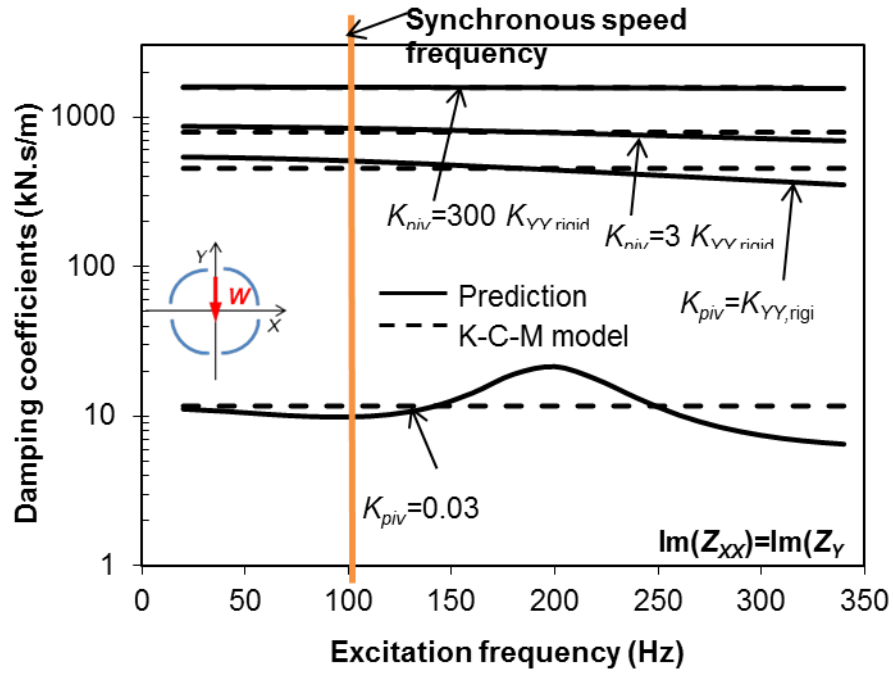

(a) Specific load *W/LD*=0 kPa

(b) Specific load *W/LD*=1,376 kPa

Fig. B. 2 Effect of pivot stiffness on the real part of impedances of a four-pad LBP bearing operating at a rotor speed of 6 krpm and two specific loads. K_{piv} = 300$K_{YY,rigid}$, 3$K_{YY,rigid}$, $K_{YY,rigid}$, and 0.03$K_{YY,rigid}$. Relationship between real part of the bearing impedances (K_B) and pivot stiffness (K_{piv}).

Synchronous speed frequency

$K_{piv}=300 \; K_{YY,rigid}$ $K_{piv}=3 \; K_{YY,rigid}$ $K_{piv}=K_{YY,rigid}$

$K_{piv}=0.01 \; K_{YY,rigid}$

Prediction
K-C-M model

(axis: Damping coefficient Im(Z) (kN.s/m) vs Excitation frequency (Hz))

(a) Specific load *W/LD*=0 kPa

(b) Specific load *W/LD*=1,376 kPa

Fig. B. 3 Effect of pivot stiffness on the imaginary part of impedances of a four-pad LBP bearing operating at a rotor speed of 6 krpm and two specific loads. K_{piv} = 300$K_{YY,rigid}$, 3$K_{YY,rigid}$, $K_{YY,rigid}$, and 0.03$K_{YY,rigid}$.

Table B.2 lists the correlation coefficient (r^2) of the curve fitted [*K-C-M*] force coefficients to the bearing impedances. For the bearing with a soft pivot stiffness (K_{piv}= 0.03$K_{YY,rigid}$), small correlation coefficients of the curve fitted damping coefficients indicate that the bearing damping coefficient is strongly frequency dependent. The [*K-C-M*] model does not capture adequately the bearing force coefficients for the bearing with either a too soft or a too rigid pivot, as shown in Table B.2.

Table B. 2 Correlation coefficients of curve fit parameter for the predicted impedances for a four-pad LBP bearing in Ref. [13] with different pivot stiffnesses. Rotor speed Ω= 6 krpm.

Specific load W/LD(kPa)	Pivot stiffness	$K_s-M_{XX}\omega^2$ $\rightarrow$Re (Z_{XX})	$K_s-M_{YY}\omega^2$ $\rightarrow$Re (Z_{YY})	$C_{XX}\omega$ $\rightarrow$Im(Z_{XX})	$C_{YY}\omega$ $\rightarrow$Im(Z_{YY})
0 kPa $K_{YY,\text{rigid}}$=1,159 MN/m	$0.03K_{YY,\text{rigid}}$	0.96	0.94	0.77	0.68
	$K_{YY,\text{rigid}}$	0.99	0.99	0.99	0.99
	$3K_{YY,\text{rigid}}$	1.00	1.00	1.00	1.00
	$300\ K_{YY,\text{rigid}}$	0.84	0.83	1.00	1.00
1,376 kPa $K_{YY,\text{rigid}}$=1,269	$0.03K_{YY,\text{rigid}}$	0.76	0.81	0.60	0.66
	$K_{YY,\text{rigid}}$	0.99	0.99	0.99	0.99
	$3K_{YY,\text{rigid}}$	1.00	1.00	1.00	1.00
	$300\ K_{YY,\text{rigid}}$	0.41	0.36	1.00	1.00

Bearing stiffness, damping and virtual mass coefficients Figures B.4-B.6 show the ratio of TPJB force coefficients along Y direction over the bearing stiffness with rigid pivots (fluid film stiffness $K_{YY,\text{rigid}}$) versus the pivot stiffness. Note $K_{YY,\text{rigid}}$ is the bearing fluid film stiffness along the Y direction at the specific load equaling 0 kPa and 1,376 kPa, i.e. $K_{YY,\text{rigid}}$=1,159 MN/m and $K_{YY,\text{rigid}}$=1,269 MN/m, respectively. Results show that at the zero load condition, as the pivot stiffness goes up to ten times higher than the fluid film stiffness ($K_{piv} \geq$ 11,590 MN/m), the bearing stiffness coefficient approaches the fluid film stiffness and remains constant with increasing pivot stiffness. The bearing stiffness equals to the pivot stiffness when the pivot stiffness is less than 10% of the fluid film stiffness.

Figure B.4 showcases the rigid pivot and soft pivot regions, in which the bearing stiffness is determined by the fluid film stiffness and pivot stiffness, respectively. Recall that the journal eccentricity increases as the pivot becomes softer. At the zero load condition, when the pivot stiffness locates between these two regions (116 MN/m~ 11,590 MN/m), the pivot stiffness and fluid film stiffness both determine the bearing static stiffness coefficient through a simple equation, i.e., $1/K_{YY} = 1/K_{YY,rigid} + 1/K_{piv}$. A

166

similar change of the bearing stiffness with pivot stiffness is associated with a high specific load condition (W/LD = 1,376 kPa). Hence, the bearing static stiffness coefficients identified at zero frequency can be estimated based on the simple equations shown in Fig. B.4. Note that the estimated pivot stiffness for the test bearing in Ref. [13] is located within the transition area ($K_{YY,\text{rigid}}/10 < K_{piv} < 100K_{YY,\text{rigid}}$) for operation at specific loads of 0 kPa and 1,376 kPa, as displayed in Fig. B.4.
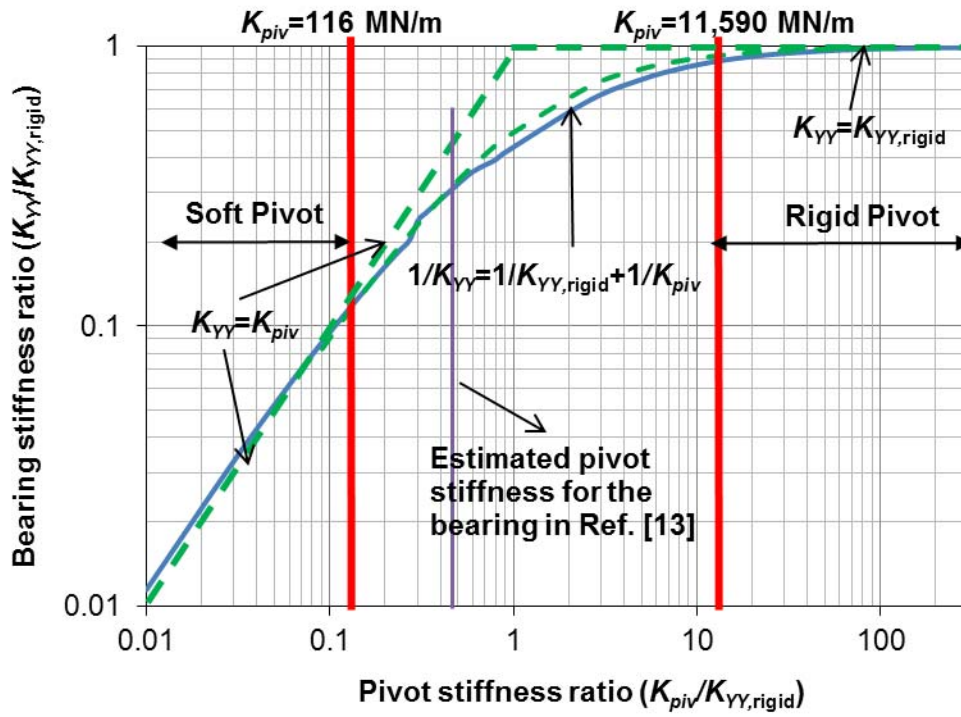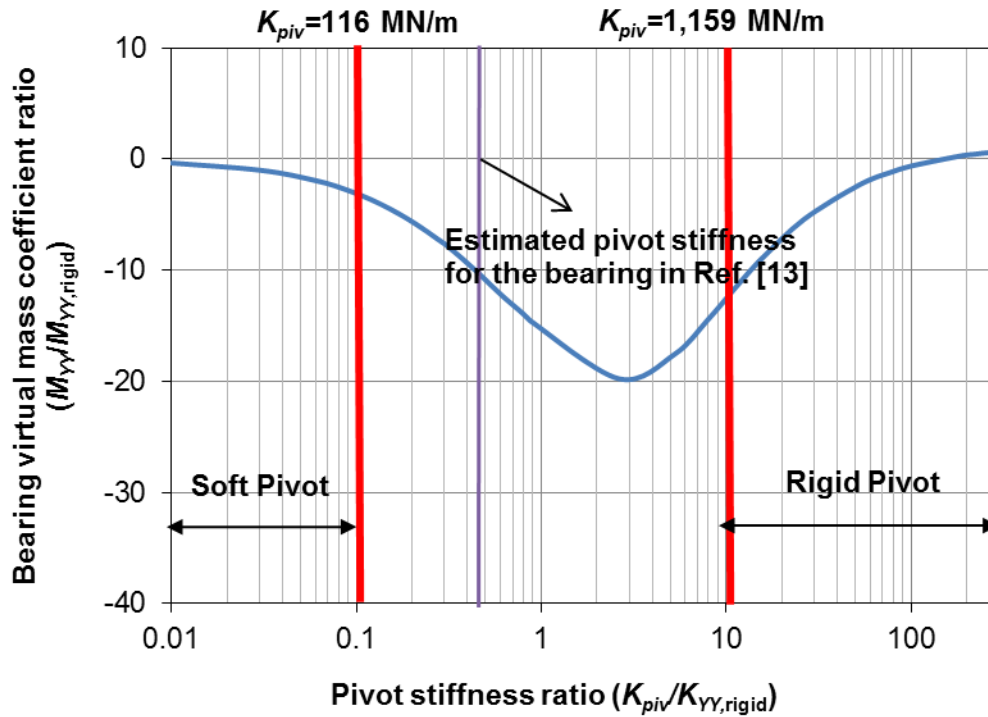

(a) Specific load *W/LD*=0 kPa
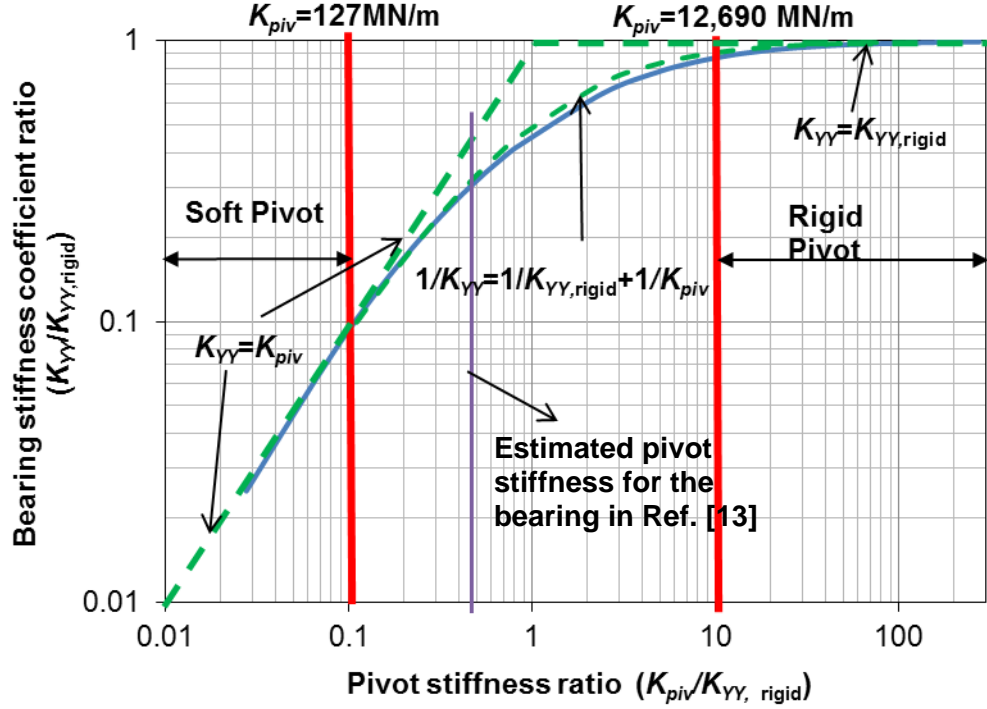
(b) Specific load *W/LD*=1,376 kPa

Fig. B. 4 Effect of pivot stiffness on the stiffness coefficients of a four-pad LBP bearing operating at a rotor speed of 6 krpm and two specific loads. Bearing fluid film stiffness $K_{YY,rigid}$=1,159 MN/m and 1,269 MN/m.

Figure B.5 shows the effect of pivot stiffness on the bearing damping coefficients along the load direction (*Y*) for operations at two specific loads and with a rotor speed of 6 krpm. The bearing damping coefficients are obtained from curve fitting the imaginary part of the bearing impedances using the [*K-C-M*] model, i.e. Im(*Z*)=*Cω*. Results show that as a pad pivot stiffness decreases, the bearing damping coefficients decrease greatly. At the zero load condition, a bearing with K_{piv}=0.1$K_{YY,rigid}$ shows, when compared to the coefficients of a rigid bearing (K_{piv}=10$K_{YY,rigid}$), just 10% of the stiffness and a mere 4% of damping coefficients. Thus, pivot flexibility has a more pronounced effect on reducing damping coefficients than the stiffnesses. In the region where a pivot is very stiff (K_{piv}>$K_{YY,rigid}$=1,159 MN/m), the bearing damping is that of the fluid film alone. On

168

the other hand, for soft pivots ($K_{piv}<0.1K_{YY,\text{rigid}} =11.6$ MN/m), the damping coefficient C_{YY} is proportional to K_{piv}.
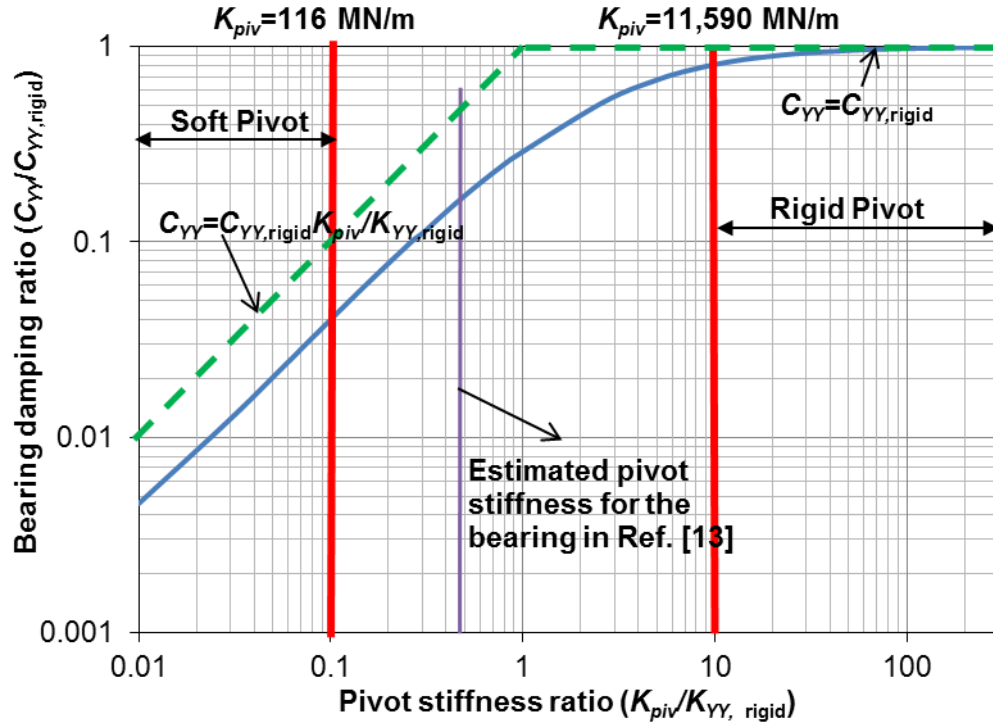
(a) Specific load *W/LD*=0 kPa
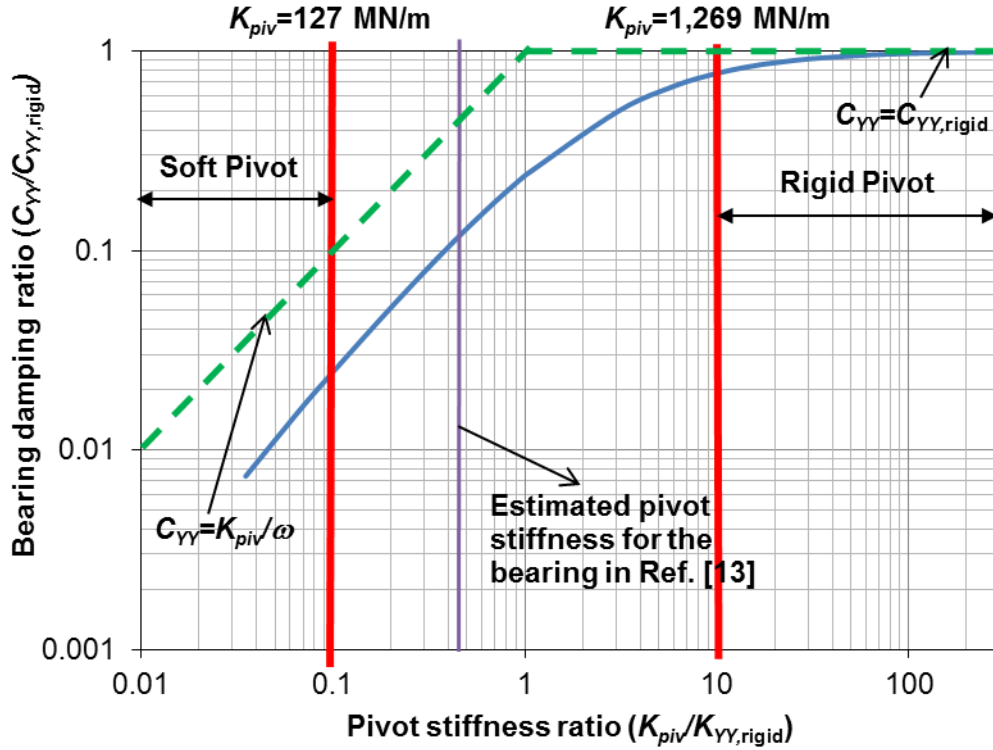
(b) Specific load _W/LD_=1,376 kPa

Fig. B. 5 Effect of pivot stiffness on the damping coefficients of a four-pad LBP bearing operating at a rotor speed of 6 krpm and two specific loads. Bearing fluid film damping $C_{YY,rigid}$=1,450 kN.s/m and 1,585 kN.s/m.

Figure B.6 depicts the effect of the pivot stiffness on the bearing virtual mass coefficients for operation at a speed of 6 krpm and two specific loads. The magnitude of the virtual mass coefficients affects the bearing dynamic stiffness (real part of the mechanical impedance) over the frequency range (0-340 Hz). Note the maximum frequency 340 Hz is more than three times larger than the synchronous speed frequency (100 Hz). The direct virtual mass coefficient ($M_{XX}=M_{YY}$) of the bearing with rigid pivots at 0 kPa and 1,376 kPa is 6.1 kg and 4.0 kg, respectively, as shown in Table B.1. Thus,

the negative virtual mass coefficients in Fig. B.6 reveal a "stiffening" effect on the bearing dynamic stiffnesses at high excitation frequencies.

The virtual mass coefficients of the bearing with almost rigid pivots (K_{piv}= ~350,000 MN/m) are ~6 kg for operations at two specific loads, see Fig. B.6. Hence, the dynamic stiffness coefficients, Re(Z), are frequency independent or decrease slightly with whirl frequency for the bearing with rigid pivots. As the pivot stiffness decreases, the virtual mass coefficients become negative and the magnitude first increases and then decreases, illustrating that the "stiffening" effect in the bearing dynamic stiffness coefficients at high frequencies varies with the pivot stiffness. Note that when the pivot stiffness is twice larger than the bearing stiffness ($K_{YY,rigid}$), the bearing has a virtual coefficient in a maximum magnitude, -120 kg and -132 kg for operation at specific loads of 0 kPa and 1,376 kPa, respectively.

(a) Specific load *W/LD*=0 kPa
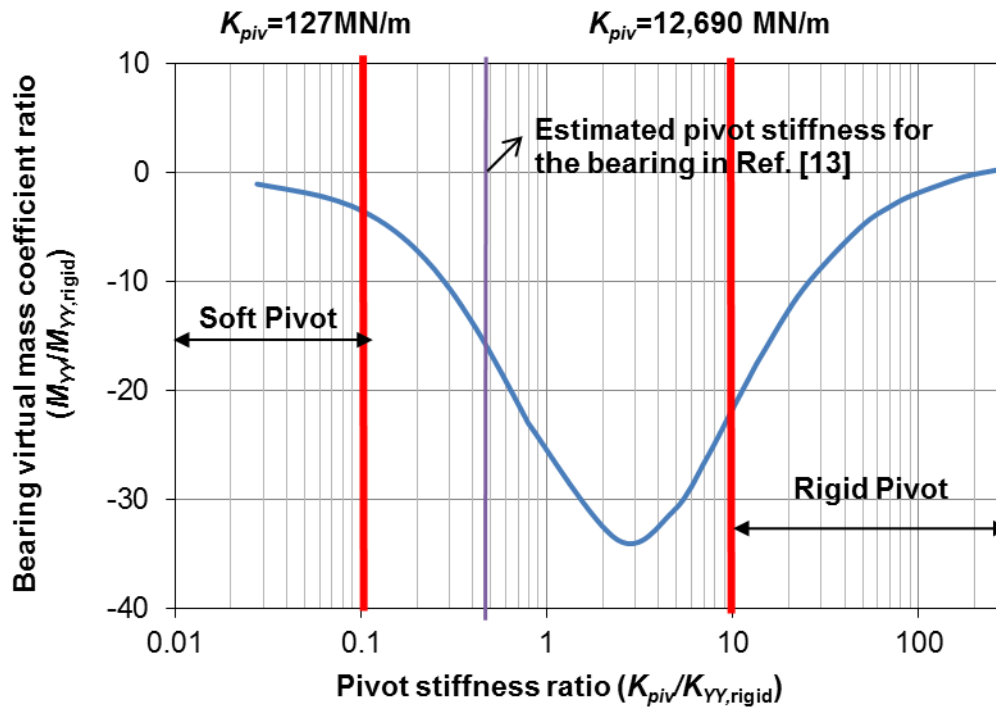
(b) Specific load *W/LD*=1,376 kPa

Fig. B. 6 Effect of pivot stiffness on the virtual mass coefficients of a four-pad LBP bearing operating at a rotor speed of 6 krpm Specific load W/LD=1,376 kPa. Bearing fluid film stiffness $K_{YY,rigid}$=1,159 MN/m and 1,269 MN/m.

APPENDIX C-EFFECT OF PIVOT FLEXIBILITY ON THE FORCED

PERFORMANCE FOR TPJBS WITH DIFFERENT GEOMETRICAL PARAMETERS

[23]

This section discusses the influence of pivot flexibility on the forced performance of TPJBs with various geometrical parameters. Table C.1 lists the geometry parameters of the bearing model and operating conditions, similar to those for a test TPJB in Ref. [23]. Table C.2 lists the operating conditions and geometrical parameters selected for the TPJB predictive model. The pivot stiffness of the bearings (LBP/LOP) with pad preloads equaling 0, 0.27 and 0.5 varies from 400 MN/m to infinite (rigid pivots).

Table C. 1 Parameters of a TPJB and operating conditions in Refs. [23,27].

Number of pads	5
Configuration	LBP
Pad arc angle	57.9^{o}
Rotor diameter, D	101.6 mm
Pad axial length, L	60.3 mm
Pivot offset	50%
Pad preload, $\bar{r}_P$	0.27
Cold bearing clearance, C_B	81.4 μm
Cold pad clearance, C_P	112 μm
Pad mass, m_P	0.44 kg
Pad inertia about pivot, I_P	2.49×10^{-4} kg.m^2
Pivot type	Rocker back
Estimated pivot radial stiffness, K_{piv}	641 MN/m
Lubricant type	ISO VG32
Oil supply temperature	43.6 ^{o}C
Oil density, ρ	856.2 kg/m^3
Oil viscosity at 43.6 ^{o}C	0.027 Pa.s

Table C.1 Continued

Temperature viscosity coefficient, α	0.029 1/K
Inlet thermal mixing coefficient, λ	0.90
Journal speed, Ω	16,000 rpm
Static specific load, W/LD	0-3,101 kPa
Excitation frequency range, ω	20-320 Hz

Table C. 2 Specific parameters for the model and operating conditions.

Static specific load, W/LD	0-3,101 kPa
Pad preload, $\bar{r}_P$	0, 0.27, 0.5
Load configuration	LBP, LOP
Pivot radial stiffness, K_{piv}	100 MN/m-1,000MN/m (rigid pivot)

The predictive model accounts for the thermal energy transport in the bearing. The bearing dimensionless stiffness, damping and virtual mass coefficients are defined as,

$$k = \frac{K \, C_P}{W}, \quad c = \frac{C \, \Omega \, C_P}{W}, \quad m = \frac{M \, \Omega^2 C_P}{W} \tag{C.1}$$

Note above, K, C and M are the bearing static stiffness, damping and virtual mass coefficients derived from the impedances using a [K-C-M] model. The bearing Sommerfeld number is defined as,

$$S = \frac{\mu_s NLD}{W}\left(\frac{R}{C_P}\right)^2 \tag{C.2}$$

where $N=\Omega/2\pi$ is the rotational speed in revolutions/s. C_P is the cold pad radial clearance and μ_s is the lubricant viscosity at supply temperature. Since the rotor speed equals to 16,000 rpm, a large static load yields a small Sommerfeld number.

Figures C.1 shows the journal eccentricity (e/C_B) of the LBP bearing with pad preloads equaling to 0 and 0.5 versus the Sommerfeld number (S). Predictions show that as the pivot stiffness decreases, the journal eccentricity increases significantly for the bearing with the 50% pad preload; however, this effect is not pronounced for the zero preload TPJB.

Figure C.2 depicts the modified drag friction coefficient ($f = \dfrac{T_{torque}}{C_B W}$) versus Sommerfeld number (S) for the LBP bearing with two pad preloads, 0 and 0.5. Note that the drag friction coefficient does not vary with the pivot stiffness, while it changes slightly with the pad preload.
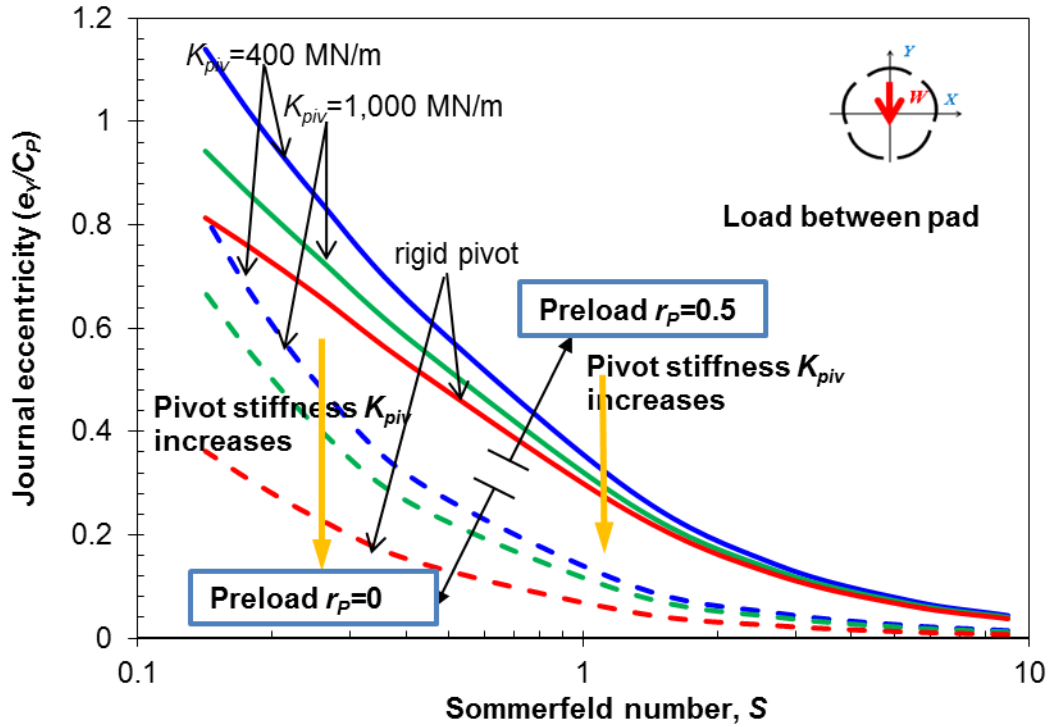
Fig. C. 1 Journal eccentricity for a TPJB. Pad preload $\bar{r}_p$ =0 and 0.5. LBP configuration. Rotor speed Ω=16 krpm. Pivot radial stiffness K_{piv} equals to 1,000 MN/m, 400 MN/m and infinite.
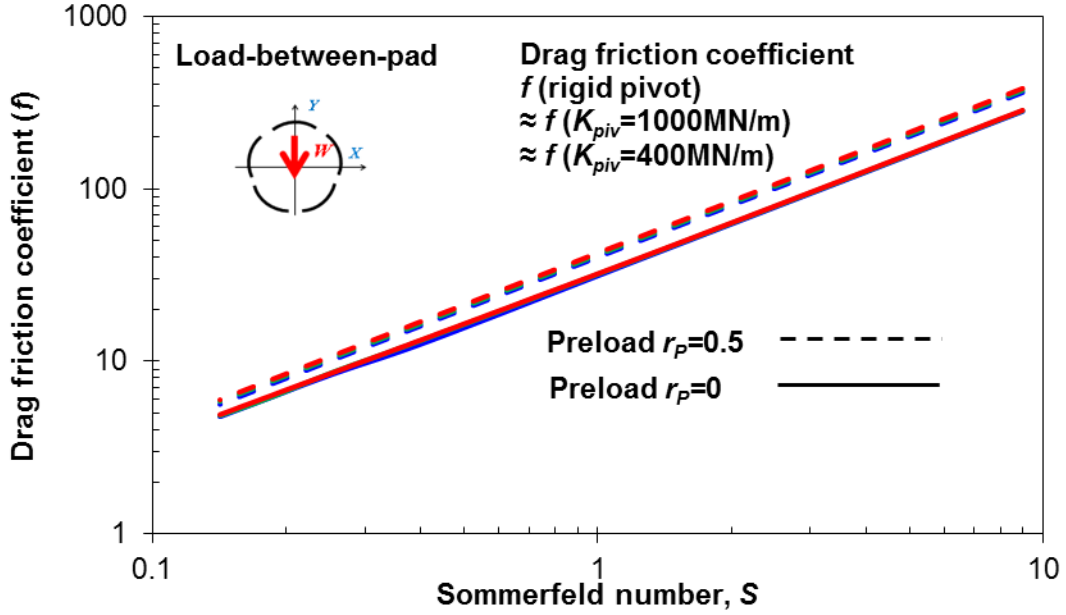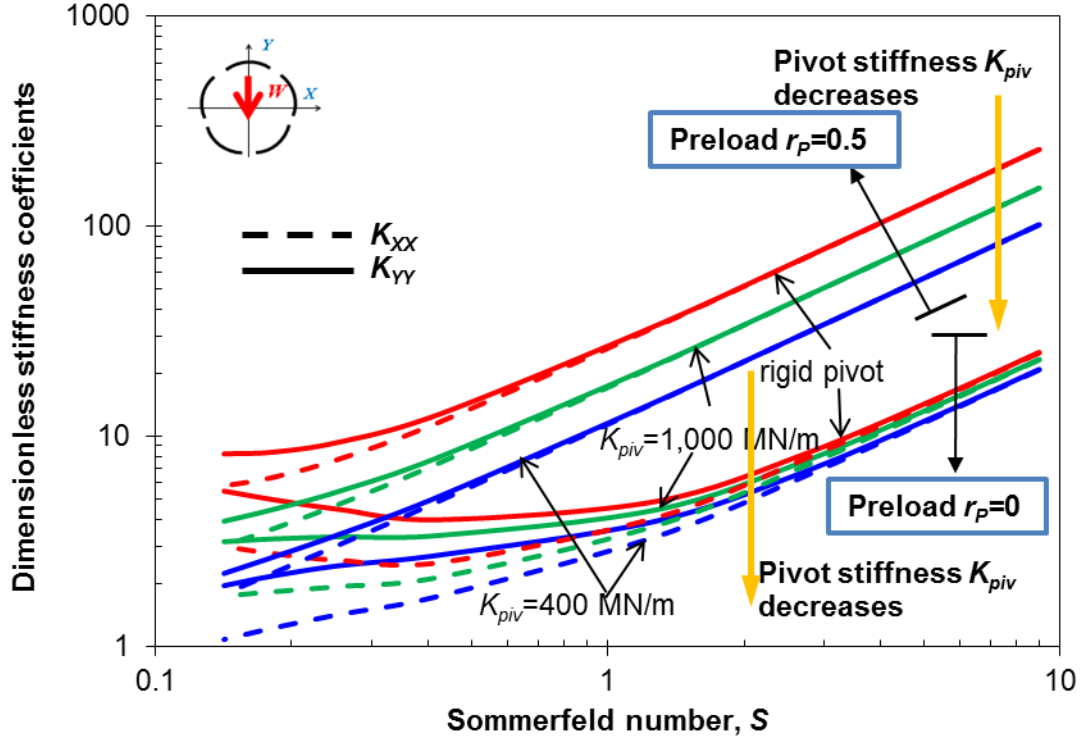
Fig. C. 2 Modified drag friction coefficient for a TPJB. Pad preload $\bar{r}_p$ =0 and 0.5. LBP configuration. Rotor speed Ω=16 krpm. Pivot radial stiffness K_{piv} equals to 1,000 MN/m, 400 MN/m and infinite.

Figures C.3 and C.4 show the dimensionless static stiffness and damping coefficients of the LBP bearings with two pad preloads versus Sommerfeld number (S). For a TPJB with the LBP configuration, an increase on pad preload from 0 to 0.5 increases dramatically the bearing stiffness and damping coefficients, in particular at a large Sommerfeld number (S>1). The TPJB stiffness and damping become orthotropic ($k_{XX} \neq k_{YY}$, $c_{XX} \neq c_{YY}$) at small Sommerfeld numbers (large static loads), as shown in Fig. C.3.

Figure C.3 illustrates that pivot flexibility decreases significantly the stiffness coefficients of the bearing with a 50% preload for operation with ($0 < W/LD < 3,101$ kPa). For a zero preload LBP bearing, pivot flexibility has a similar effect in reducing the bearing force coefficients only at large specific loads ($W/LD > 345$ kPa, S<1.3). For operation at a small load ($W/LD < 345$ kPa) and as the pivot stiffness decreases from 1,000 MN/m to 400 MN/m, the stiffness coefficients reduce by ~10% and ~50% for the LBP TPJBs with pad preload equaling 0 and 0.5, respectively. Note the stiffness

176

coefficient of the zero-preload TPJB decreases by about 60% at a maximum specific load of 3,101 kPa. Pad pivot flexibility has a more pronounced effect in reducing the bearing damping coefficients than the static stiffness coefficients, as shown in Figs. C.3 and C.4.
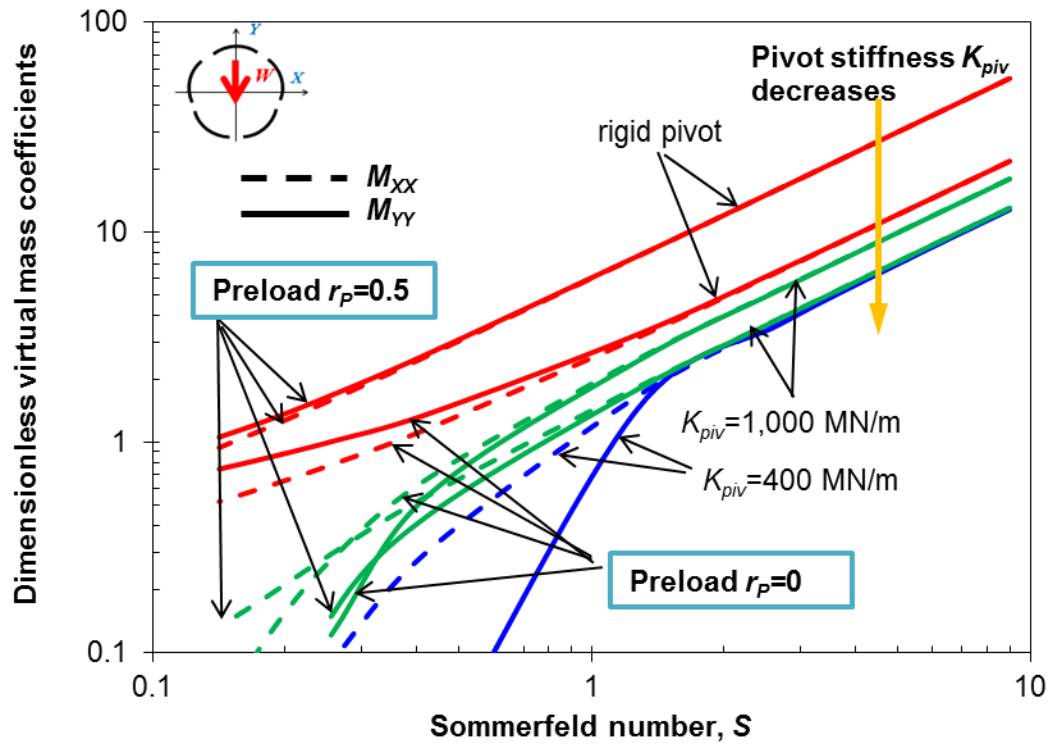

Fig. C. 3 Dimensionless stiffness coefficients for a TPJB. Pad preload $\bar{r}_p$ =0 and 0.5. LBP configuration. Rotor speed Ω=16 krpm. Pivot radial stiffness K_{piv} equals to 1,000 MN/m, 400 MN/m and infinite.
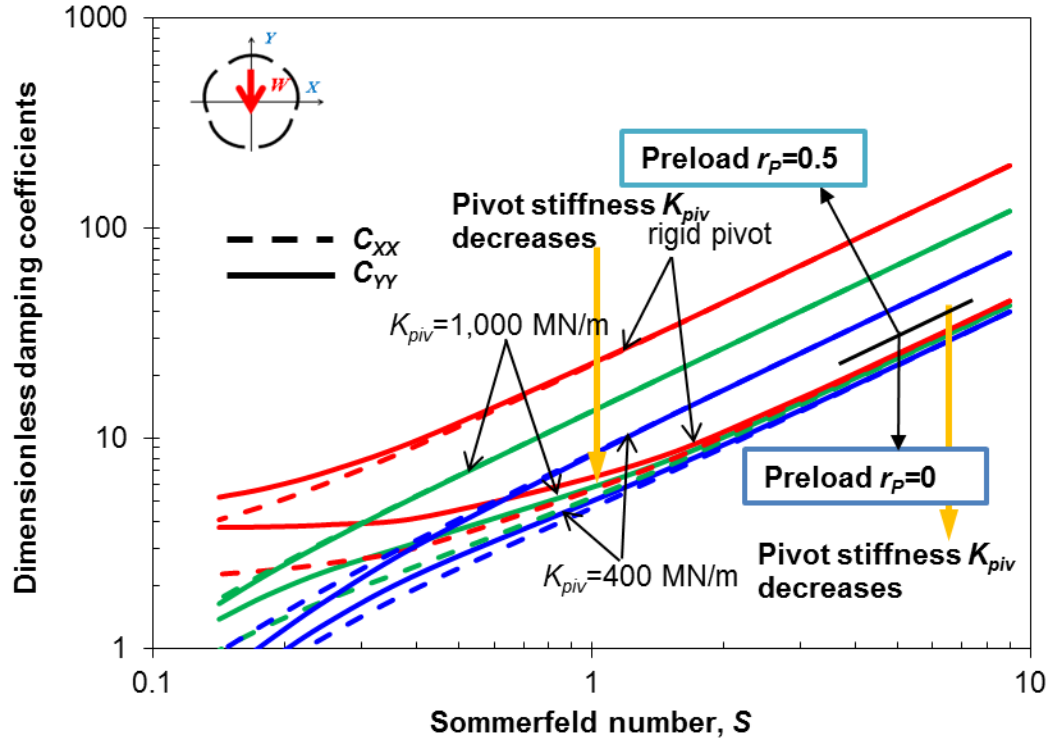
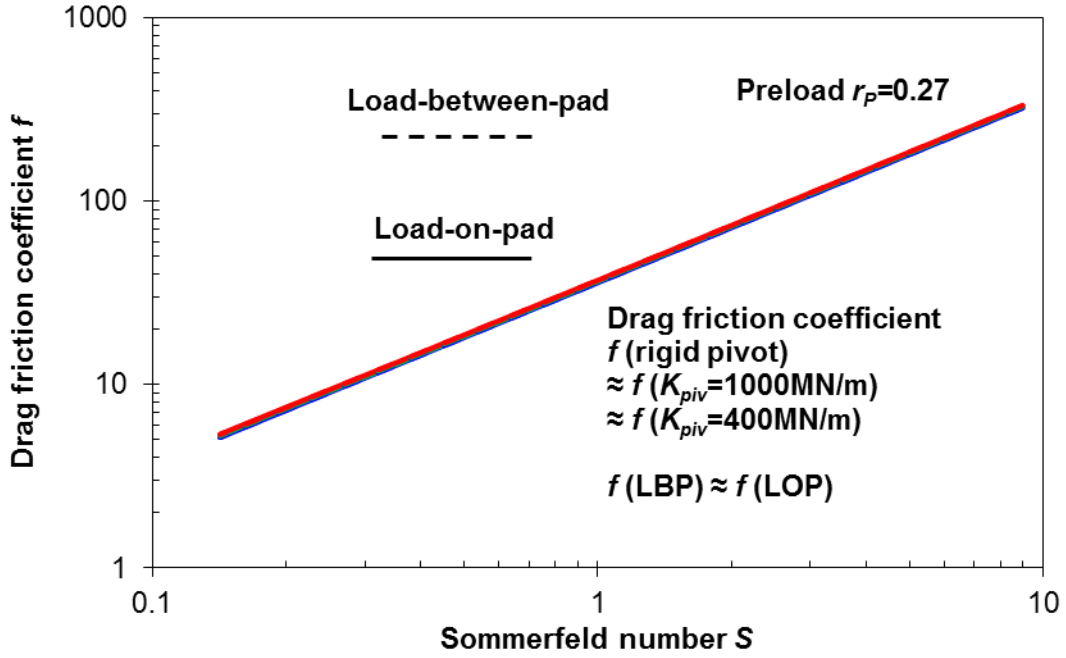**Fig. C. 4 Dimensionless damping coefficients for a TPJB. Pad preload $\bar{r}_p$ =0 and 0.5. LBP configuration. Rotor speed Ω=16 krpm. Pivot radial stiffness K_{piv} equals to 1,000 MN/m, 400 MN/m and infinite.**

Figure C.5 depicts the effect of pivot flexibility on the virtual mass coefficients of two five-pad LBP bearings with pad preloads equaling 0 and 0.5. The virtual mass coefficients are derived from the predicted real part of the impedances using a [*K-C-M*] model. Note Fig. C.5 does not show the virtual mass coefficients for the 0.5-preload LBP bearing with a pivot stiffness of 400 MN/m, since the virtual mass is negative, indicating that the bearing dynamic stiffness coefficients increase with whirl frequency. Results show that as the pivot stiffness decreases, the bearing virtual mass coefficients decrease and become negative. Thus pivot flexibility "stiffens" the bearing dynamic stiffness coefficients over a certain frequency range of analysis.

178

Fig. C. 5 Dimensionless virtual mass coefficients for a TPJB. Pad preload $\bar{r}_p$ =0 and 0.5. LBP configuration. Rotor speed Ω=16 krpm. Pivot radial stiffness K_{piv} equals to 1,000 MN/m, 400 MN/m and infinite.

Figure C.6 depicts the journal eccentricity of a LBP and LOP bearings with a pad preload of 0.27. Predictions show that the static journal eccentricity increases due to an increase in the pivot stiffness. There is no apparent difference between the journal eccentricity of a LBP and LOP bearings. Figure C.7 displays the drag friction coefficient of the LOP and LBP bearings with a pad preload of 0.27 versus Sommerfeld number (*S*). Note that the drag friction coefficients remain invariant with the pivot stiffness and load configuration (LBP or LOP).
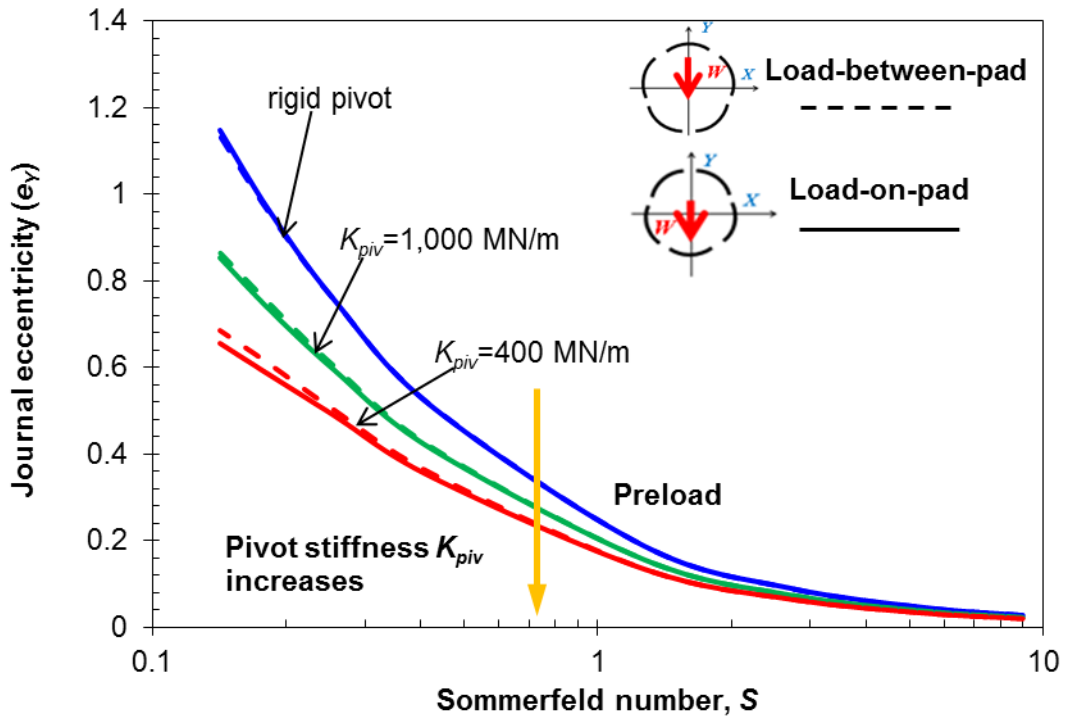
Fig. C. 6 Journal eccentricity for a TPJB. Pad preload $\bar{r}_p$ =0.27. LBP and LOP configurations. Rotor speed Ω=16 krpm. Pivot radial stiffness K_{piv} equals to 1,000 MN/m, 400 MN/m and infinite.
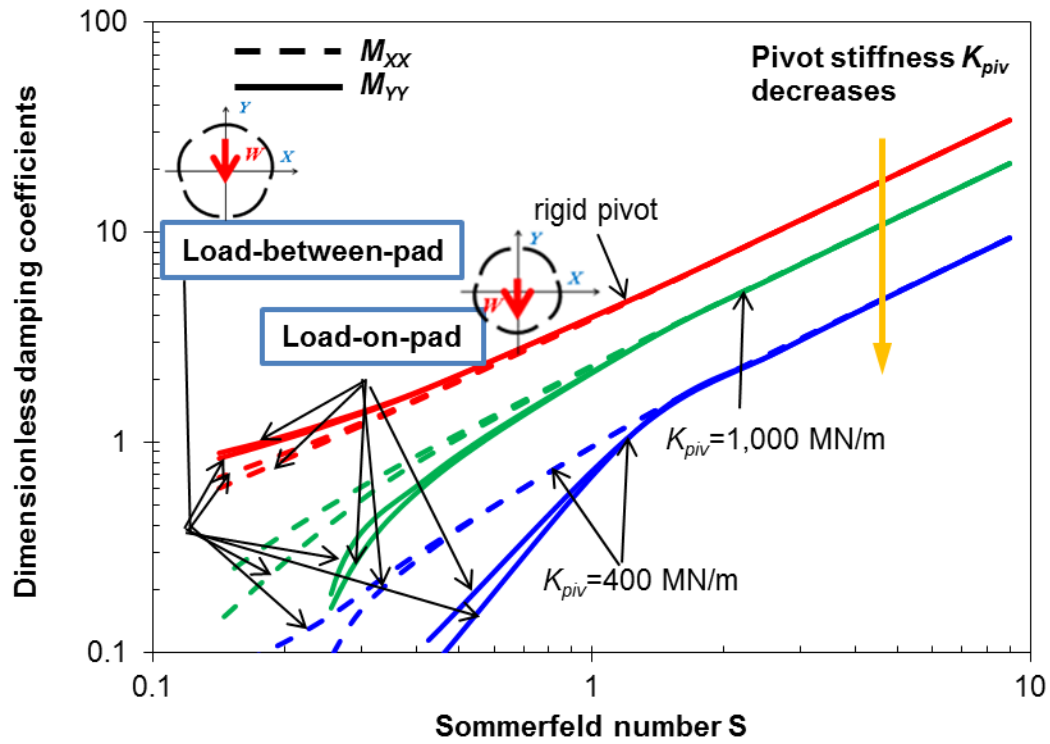
Fig. C. 7 Modified drag friction coefficient for a TPJB. Pad preload $\bar{r}_p$ =0 and 0.5. LBP configuration. Rotor speed Ω=16 krpm. Pivot radial stiffness K_{piv} equals to 1,000 MN/m, 400 MN/m and infinite.

Figures C.8-C.10 display the static stiffness, damping and virtual mass coefficients for LBP and LOP bearings with three pivot stiffnesses and at various static loads. Results show that for both LBP and a LOP bearings, the pivot stiffness reduces equally the bearing stiffness, damping and virtual mass coefficients, in particular at small loads ($S > 1$).
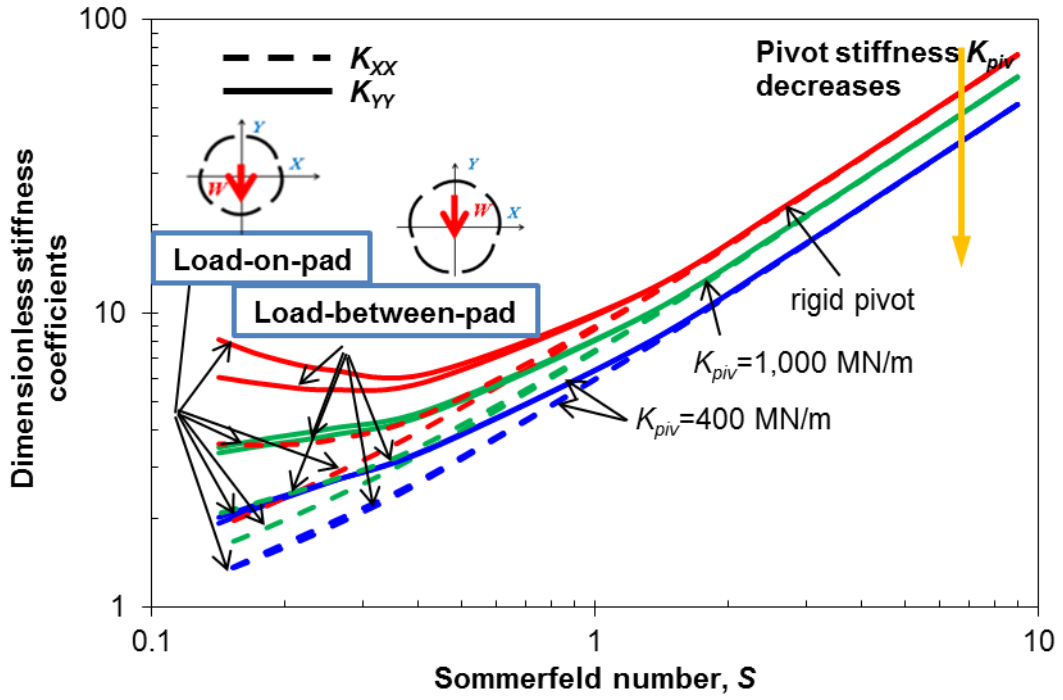
Fig. C. 8 Dimensionless stiffness coefficients for a TPJB. Pad preload $\bar{r}_p$ =0.27. LBP and LOP configurations. Rotor speed Ω=16 krpm. Pivot radial stiffness K_{piv} equals to 1,000 MN/m, 400 MN/m and infinite.
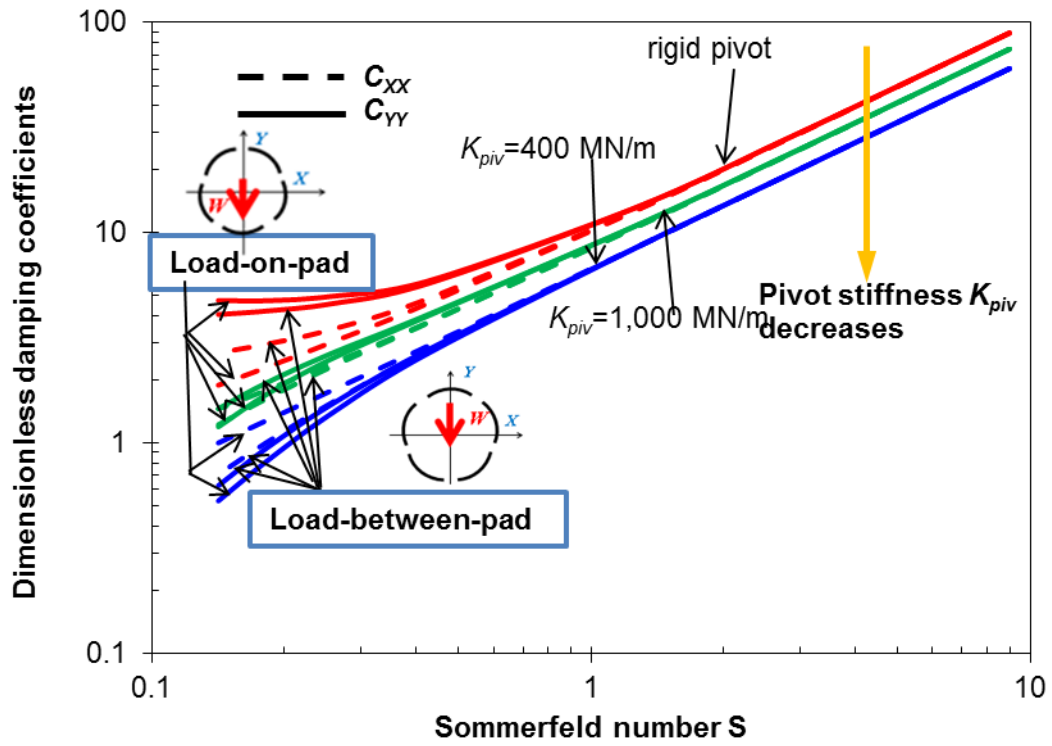
Fig. C. 9 Dimensionless damping coefficients for a TPJB. Pad preload $\bar{r}_p$ =0.27. LBP and LOP configurations. Rotor speed Ω=16 krpm. Pivot radial stiffness K_{piv} equals to 1,000 MN/m, 400 MN/m and infinite.

Fig. C. 10 Dimensionless virtual mass coefficients for a TPJB. Pad preload $\bar{r}_p$ **=0.27. LBP and LOP configurations. Rotor speed** Ω**=16 krpm. Pivot radial stiffness** K_{piv} **equals to 1,000 MN/m, 400 MN/m and infinite.**

APPENDIX D-EFFECTS OF TEMPORAL FLUID INERTIA, PAD MOMENT OF INERTIA, PAD MASS AND PIVOT FLEXIBILITY ON THE IMPEDANCE COEFFICIENTS FOR FOUR LOP AND LBP BEARINGS [24]

This section aims to investigate the effects of several important factors, such as temporal fluid inertia, pad mass and mass moment of inertia, and pivot stiffness, on the bearing impedance coefficients (real and imaginary) over a certain frequency range of analysis. Four LOP and LBP bearings with two pivot offsets to 0.5 and 0.6, in Ref. [24], are selected as examples.

Table D.1 gives the geometry parameters that the four test bearings share in Ref. [24] and the operating conditions. Table D.2 details the geometry for each bearing. An adiabatic thermal condition is selected for the predictive model.

Table D. 1 Test TPJBs geometry parameters and operating conditions in Refs. [24,28].

Pad arc angle	60°
Rotor diameter, D	110 mm
Pad axial length, L	44 mm
Pad mass, m_p	0.5 kg
Pad thickness, t	15.4 mm
Pad moment of inertia, I_P	$2.5 \times 10^{-4} \text{kg.m}^2$
Pivot type	Rocker back
Lubricant type	ISO VG32
Oil supply temperature, T_s	43.5 $^{\circ}$C
Oil density, ρ	856.2 kg/m^3
Oil viscosity at 43.5 $^{\circ}$C	0.027 Pa.s
Temperature viscosity coefficient, α	0.0291/K
Inlet thermal mixing coefficient, λ	0.85
Static specific load, W/LD	300 kPa

Journal speed, Ω	10 krpm

Table D. 2 Detailed geometry parameters of the TPJBs in Ref. [24].
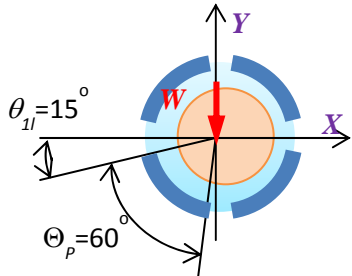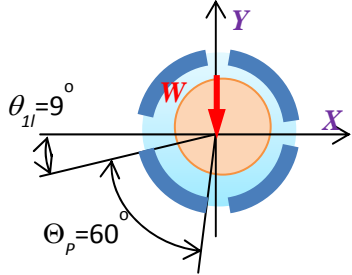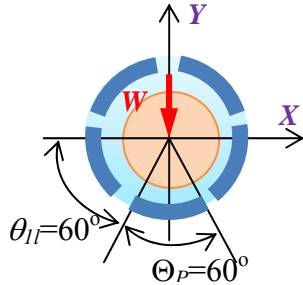
Bearing A		
Number of pads	4	
Load configuration	LBP	
Pivot offset	0.5	
Nominal pad preload	0.32	
Cold bearing radial clearance	99 µm	
Cold pad radial clearance	145.6 µm	
Bearing B		
Number of pads	4	
Load configuration	LBP	
Pivot offset	0.6	
Nominal pad preload	0.30	
Cold bearing radial clearance	102 µm	
Cold pad radial clearance	145.7 µm	
Bearing C		
Number of pads	5	
Load configuration	LOP	
Pivot offset	0.5	
Nominal pad preload	0.16	
Cold bearing radial clearance	101 µm	
Cold pad radial clearance	120 µm	

186
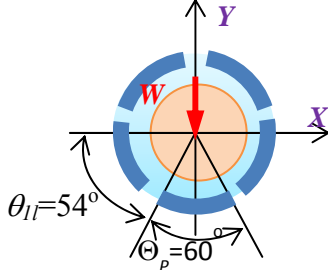
Bearing D	
Number of pads	5
Load configuration	LOP
Pivot offset	0.6
Nominal pad preload	0.16
Cold bearing radial clearance	101 μm
Cold pad radial clearance	120 μm

Table D.3 lists seven cases with different assumptions regarding the inclusion of the fluid inertia, pad moment of inertia and pad mass. Note that as the fluid inertia effect increases, i.e. the fluid density increases, the flow will become turbulent[15].

Table D. 3 Assumptions on fluid inertia, pad inertia and pad mass effects for each model.

Factors	Temporal fluid inertia	Pad moment of inertia	Pad mass
1	Neglect	Neglect	Neglect
2	Include (Fluid density = ρ)	Include (Pad inertia = I_P)	Include (Pad mass = m_P)
3	Neglect	Include (Pad inertia = I_P)	Include (Pad mass = m_P)
4	Include (Fluid density = ρ)	Neglect	Neglect
5	Include (Fluid density = 10ρ)	Neglect	Neglect
6	Neglect	Include (Pad inertia = I_P)	Include (Pad mass = $10m_P$)
7	Neglect	Include (Pad inertia = $10I_P$)	Include (Pad mass = m_P)
	Parameters: ρ=856.2 kg/m^3, I_P=2.5×10^{-4}kg.m^2, m_P=0.5 kg		

---

[15] The effect of turbulent flow is not accounted for in the predictive model.

Pad pivot stiffness also plays an important role in determining the bearing impedances, as well as the bearing static stiffness identified at zero whirl frequency. Thus, the predictive model employs three pivot stiffnesses: infinite (rigid pivot), ~1,800 MN/m and 200 MN/m. Note the test bearings in Ref. [24] have rocker-back pivots. Table D.4 lists the assumptions on the pad pivot contact type and structural stiffness.

Table D. 4 Pivot stiffness for each bearing model.

	Pivot type	Pad pivot contact curvature	Pivot stiffness
1	Rigid pivot	-	Infinite
2	Rocker back (almost rigid)	Cylinder on a cylinder	$\xi_{piv} = \dfrac{2F_{piv}(1-\upsilon^2)}{\pi LE}\left(\dfrac{2}{3} + \ln\dfrac{4LED_P D_H(D_H - D_P)}{2.15^2 F_{piv}}\right)$ $K_{piv} = F_{piv}/\xi_{piv}$ (1,630 MN/m~1,900 MN/m)
3	Rocker back	-	$K_{piv} = 200$ MN/m

Figures D.1 and D.2 show the predicted and experimental real parts of the bearing impedances for the five-pad LOP bearings with two pivot offsets, one with offset = 0.5 and the other with offset equaling 0.6. Figures D.1 and D.2 also display the effect of temporal fluid inertia, pad mass moment of inertia and pad mass on the impedance coefficients and the pivot stiffness of the bearing varies from 200 MN/m to infinite (rigid pivot). Note that the experimental impedances (real part) depend slightly on the excitation frequency [24]. However, the predicted bearing real part of impedance displays frequency dependency and relies on the inclusion of fluid and pad inertia effects. Results show that the temporal fluid inertia, pad moment of inertia and pad mass all decrease the bearing impedances, in particular at high excitation frequencies. The temporal fluid inertia effect (large fluid density) has a more pronounced effect than the

pad mass moment of inertia and pad mass do in reducing the bearing impedances (real part).

Note that decreasing pad pivot stiffness, although reduces the bearing stiffness coefficient identified at low frequencies (ω < 60 Hz), it increases the bearing dynamic stiffness coefficients at a high whirl frequency (ω > 60 Hz). For the 0.5-offset LOP bearing with almost rigid pivots ($K_{piv} \geq$ 1,630 MN/m), the predicted Re(Z) decreases with frequency. However, the Re(Z) of the bearing with soft pivots increase with frequency, in particular at high frequencies.

For the LOP bearing with the pivot offset equaling 0.6, the predicted real part of impedance is mildly frequency dependent, and an increased pivot flexibility causes a "stiffening" effect in the bearing real part of impedances, i.e., Re(Z) increases at high excitation frequencies, as shown in Fig.D.1(c) and Fig.D.2(c).
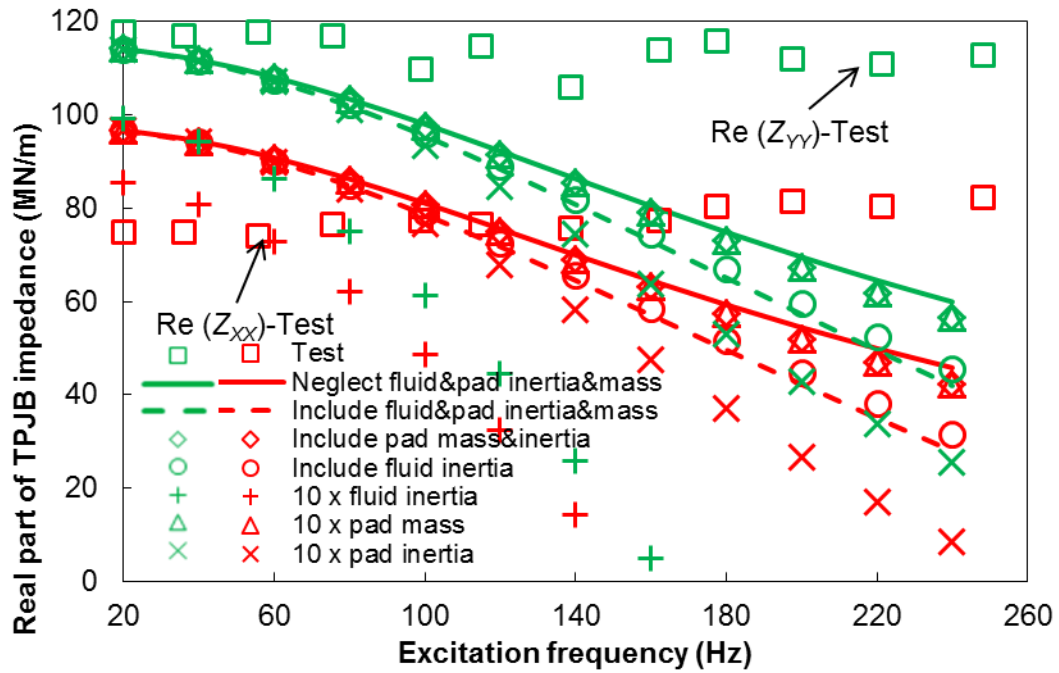
(a) Rigid pivot
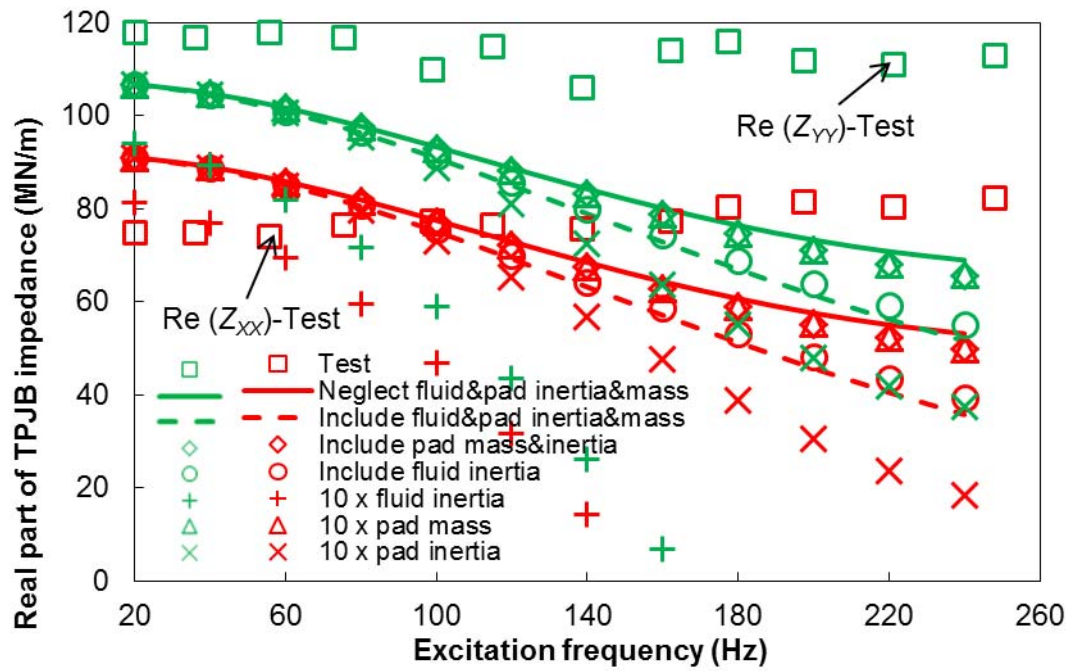
(b) Pivot stiffness = 1,630 MN/m~1,900 MN/m
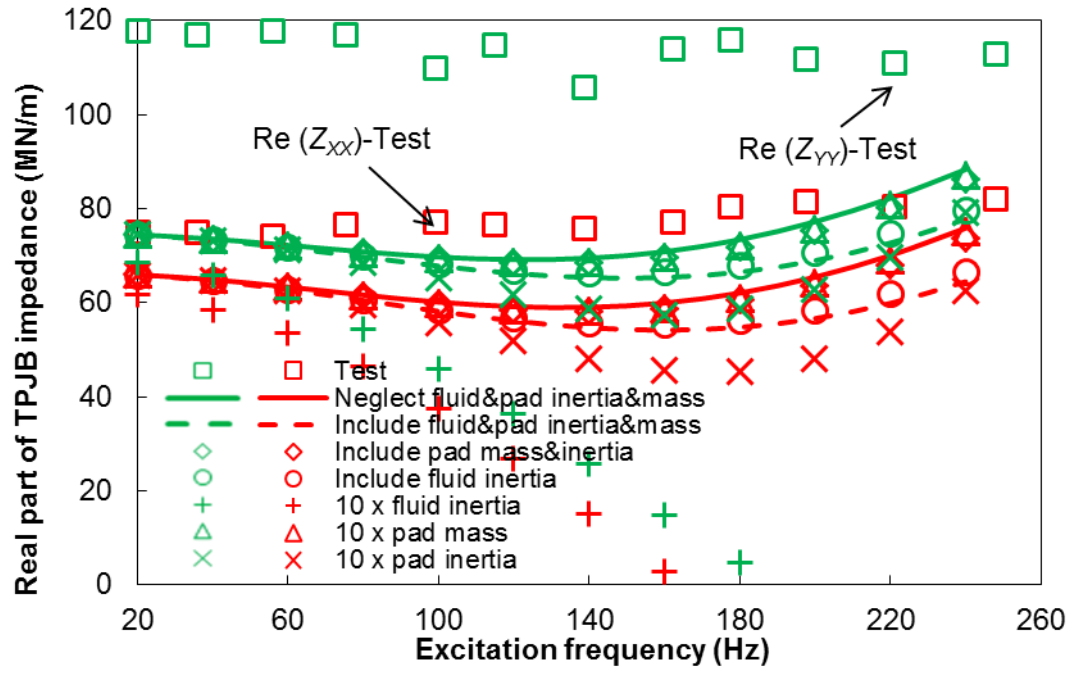
(c) Pivot stiffness = 200 MN/m

Fig. D. 1 Effect of temporal fluid inertia, pad moment of inertia, pad mass and pivot stiffness on the real part of impedance coefficients for a five-pad LOP bearing with three pivot stiffnesses. Pad pivot offset =0.5. Rotor speed Ω= 10 krpm. Current predictions and measurements in Ref. [24].
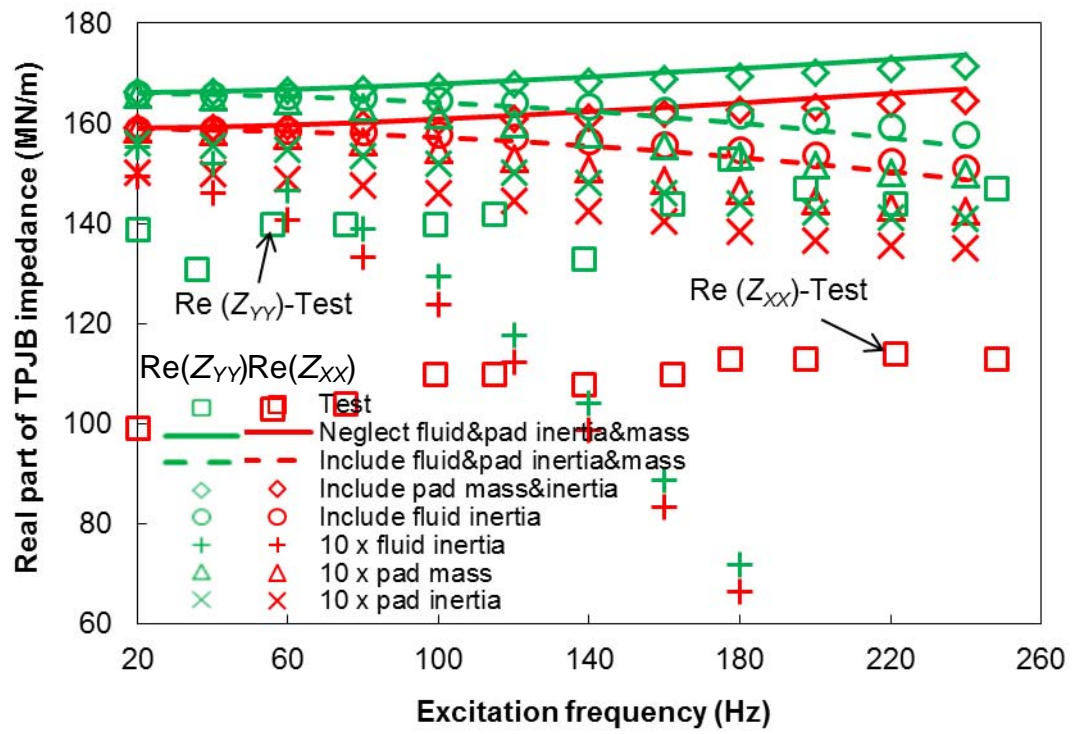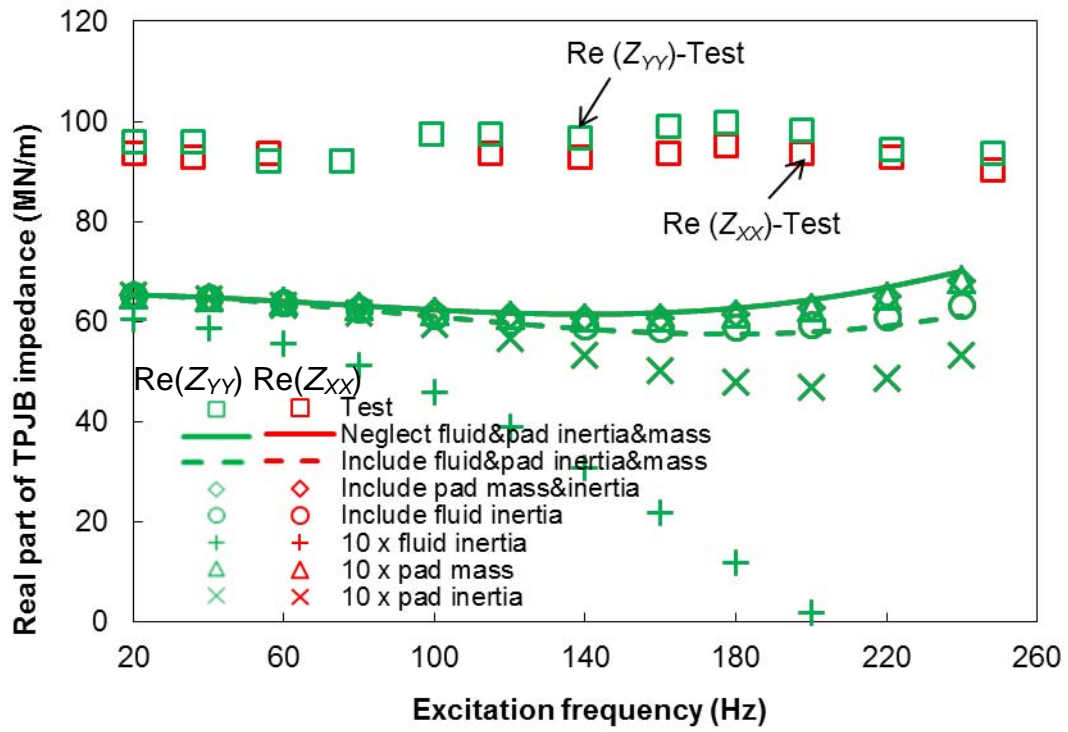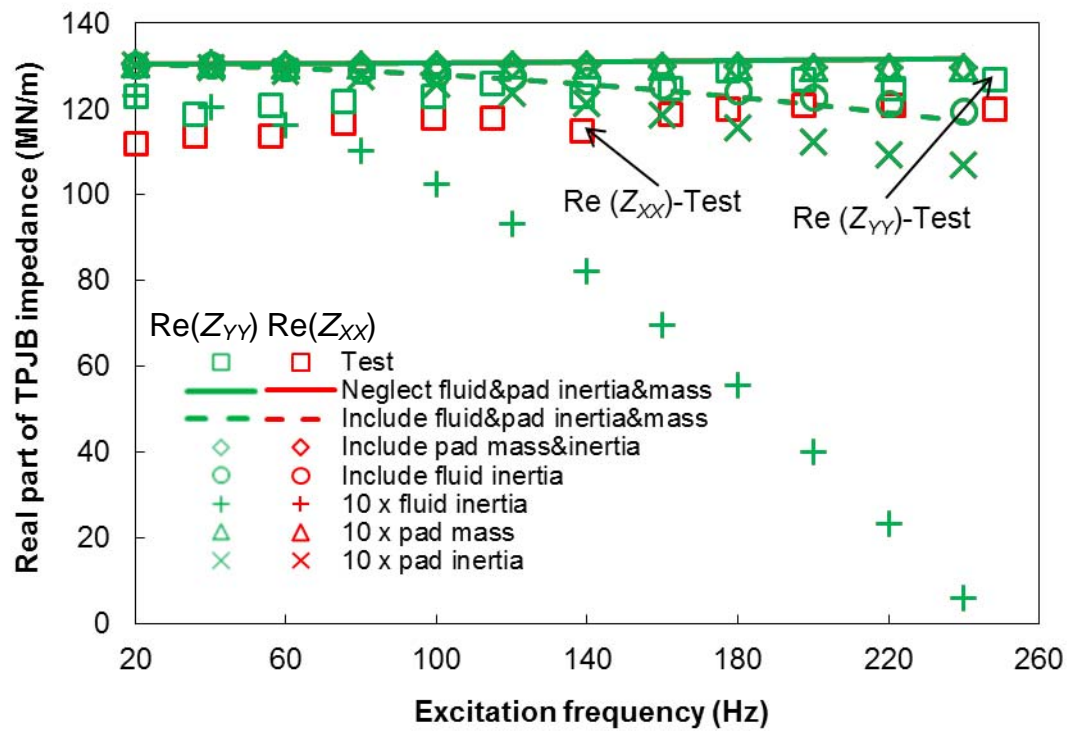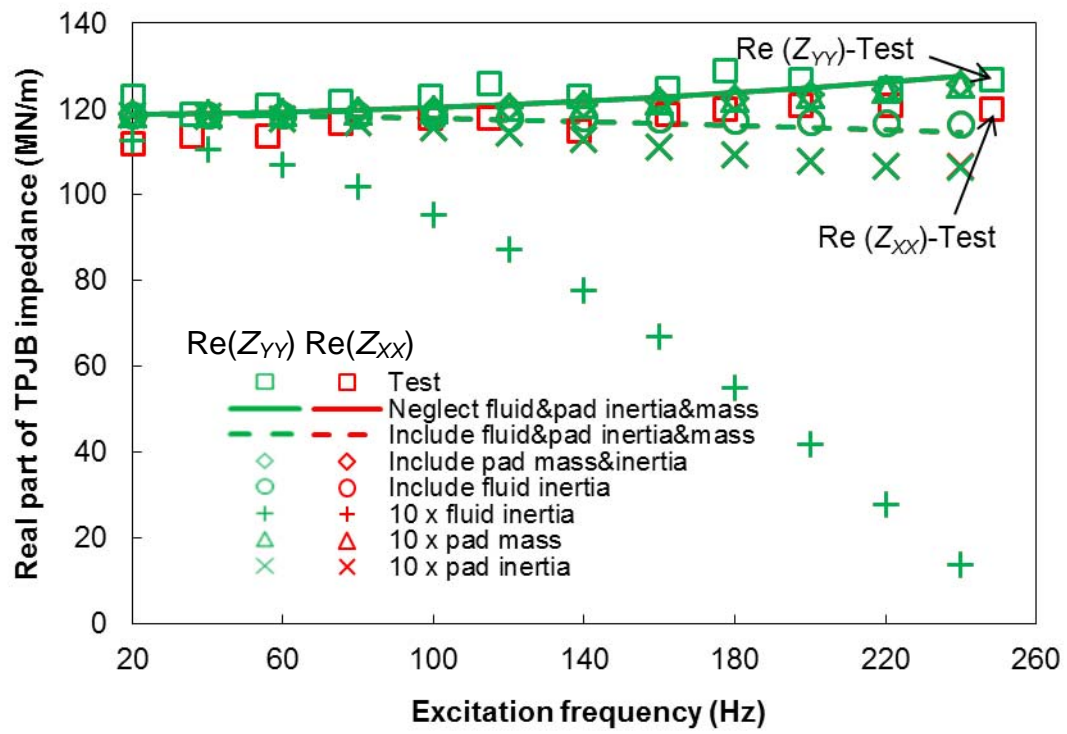
(a) Rigid pivot
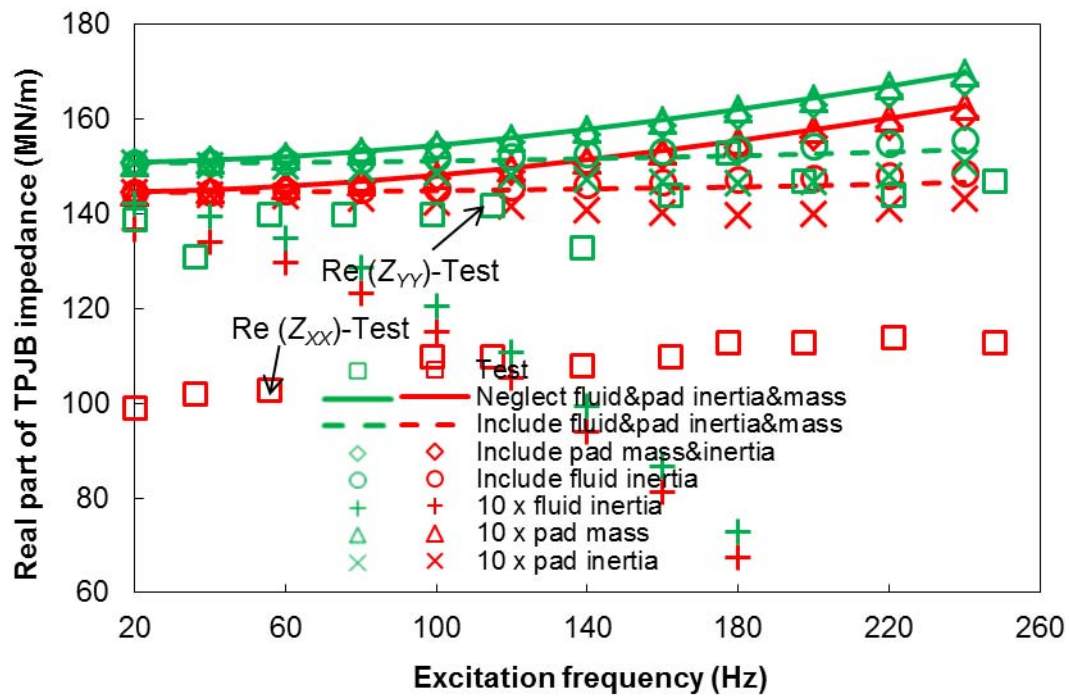
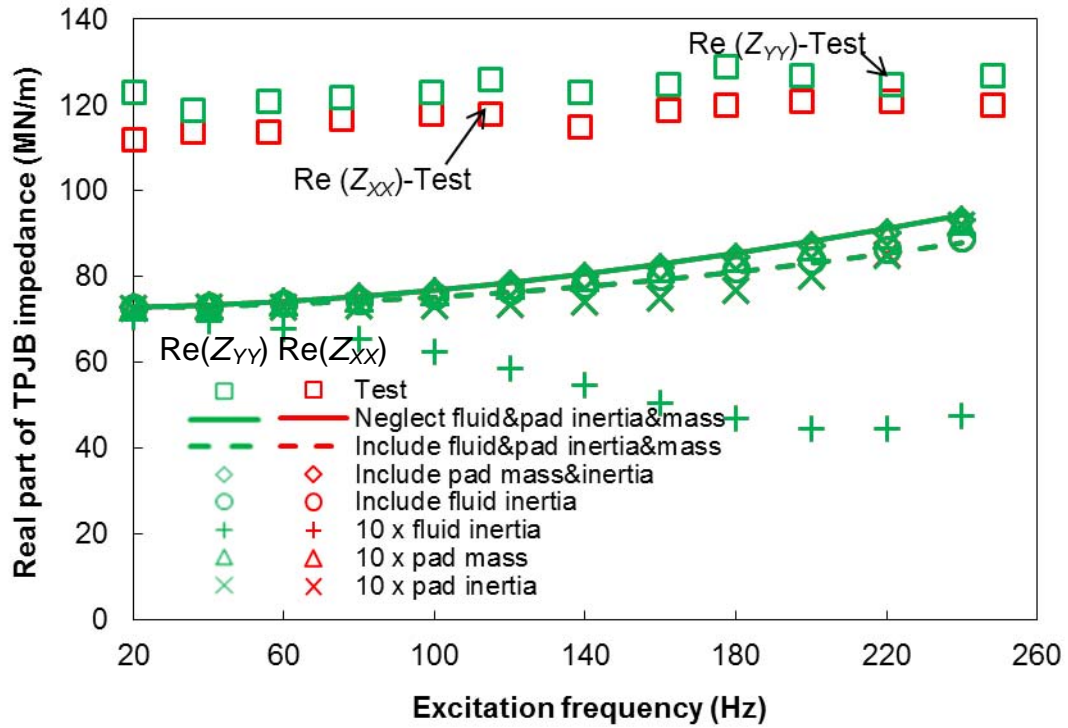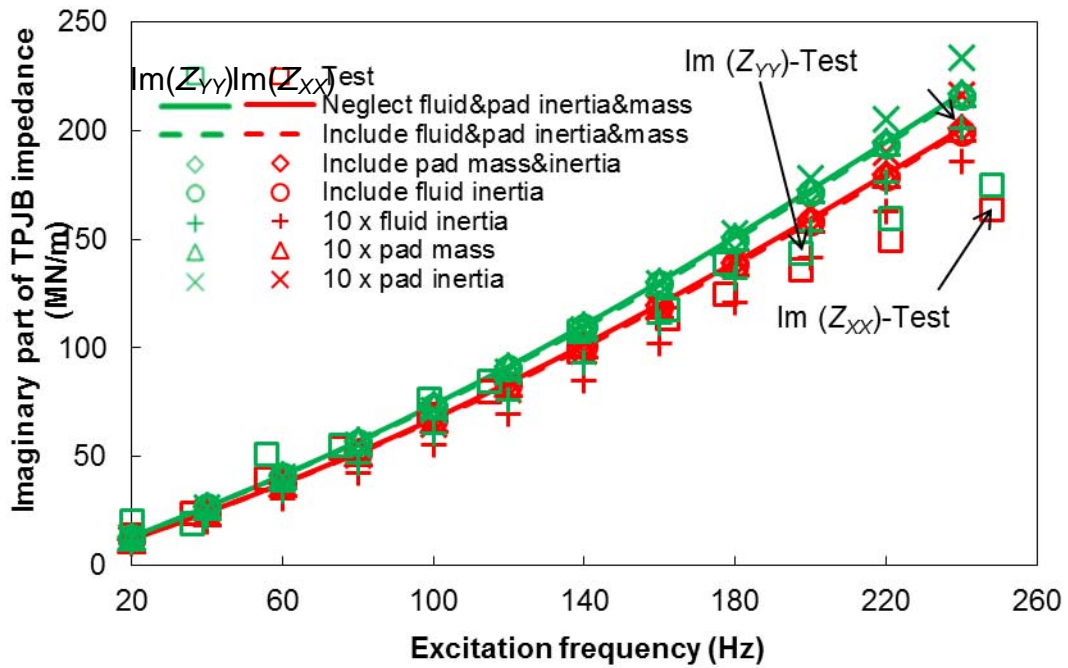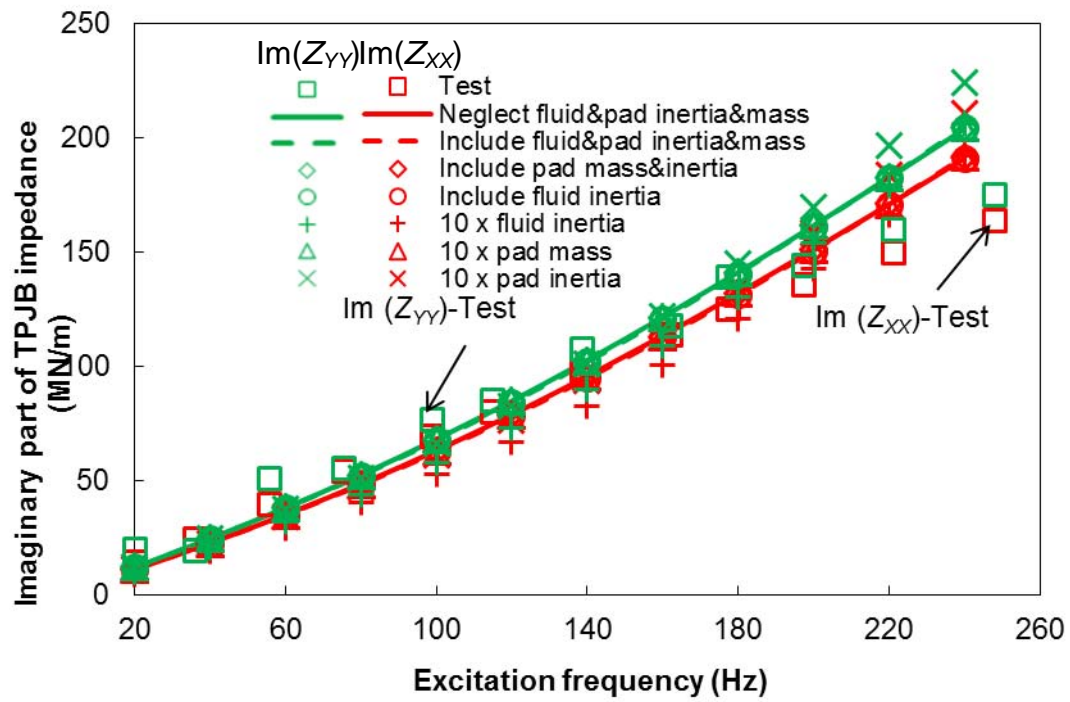**(b) Pivot stiffness = 1,630 MN/m~1,900 MN/m**
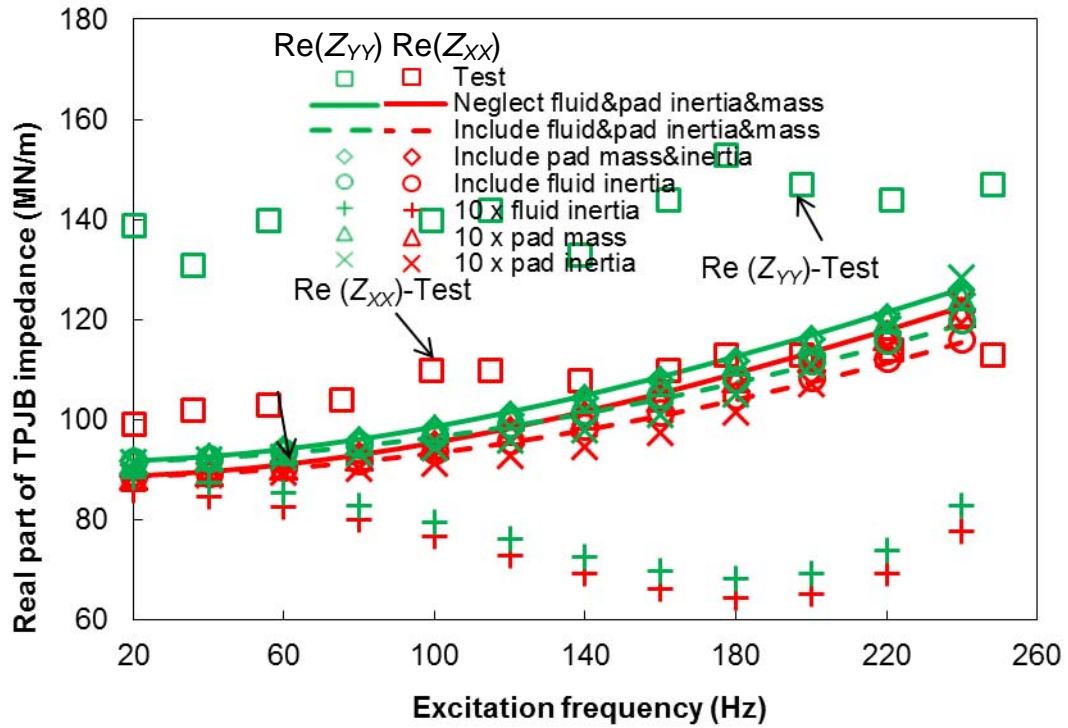
(c) Pivot stiffness = 200 MN/m

Fig. D. 2 Effect of temporal fluid inertia, pad moment of inertia, pad mass and pivot stiffness on the real part of impedance coefficients for a five-pad LOP bearing with three pivot stiffnesses. Pad pivot offset =0.6. Rotor speed Ω= 10 krpm. Current predictions and measurements in Ref. [24].

Figures D.3 and D.4 depict the comparison between the effects of fluid inertia, pad moment of inertia and pad mass on the impedance coefficients of four-pad LBP bearings with two pivot offsets, 0.5 and 0.6 and experimental results in Ref. [24]. Predictions show identical impedances at the X and Y direction, while experimental results show there is a small difference between the impedances $Re(Z_{XX})$ and $Re(Z_{YY})$. Results also show that the importance of those parameters on reducing the bearing real part of impedances at high frequencies (from high to low) is: fluid inertia > pad mass moment of inertia > pad mass.
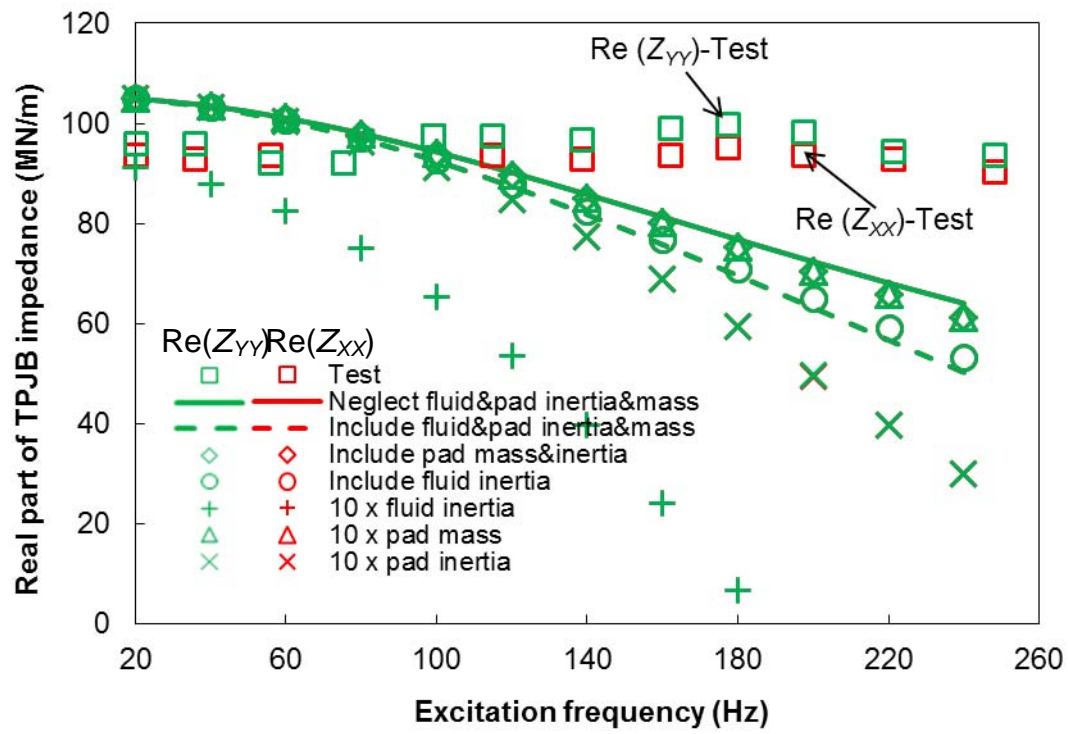
(a) Rigid pivot
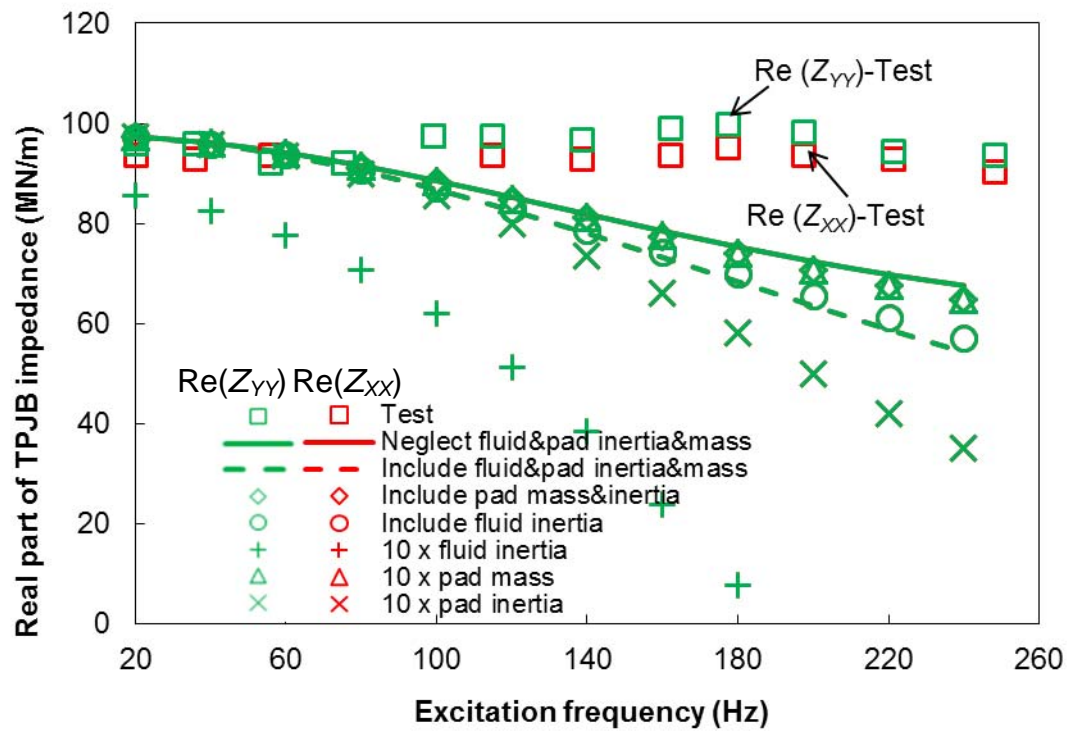
(b) Pivot stiffness = 1,630 MN/m~1,900 MN/m

(c) Pivot stiffness = 200 MN/m

Fig. D. 3 Effect of temporal fluid inertia, pad moment of inertia, pad mass and pivot stiffness on the real part of impedance coefficients for a four-pad LBP bearing with three pivot stiffnesses. Pad pivot offset =0.5. Rotor speed Ω= 10 krpm. Current predictions and measurements in Ref. [24].

(a) Rigid pivot

(b) Pivot stiffness = 1,630 MN/m~1,900 MN/m

(c) Pivot stiffness = 200 MN/m

Fig. D. 4 Effect of temporal fluid inertia, pad moment of inertia, pad mass and pivot stiffness on the real part of impedance coefficients for a four-pad LBP bearing with three pivot stiffnesses. Pad pivot offset =0.6. Rotor speed Ω= 10 krpm. Current predictions and measurements in Ref. [24].

Figures D.5 and D.6 display the predicted and experimental imaginary part of impedances for the LOP bearings with two pivot offsets, one with pivot offset=0.5 and the other with offset=0.6. Results show that the pad mass moment of inertia and pad mass increase the imaginary part of the bearing impedances, in particular at large excitation frequencies. The slope of the impedance reveals that the inclusion of the effects of pad mass and mass moment of inertia induces frequency dependent damping coefficients. An increase in the fluid density increases dramatically the bearing impedances (imaginary part) at a large whirl frequency (ω > 160 Hz) for the 0.6-offset

LOP bearings with three pivot stiffnesses. For the 0.5-offset LOP bearings with almost rigid pivots (K_{piv} = 1,630 MN/m~infinite), a significant increase in the fluid density decrease slightly the imaginary part of impedances. Figures D.7 and D.8 depict the effect of fluid inertia, pad mass moment of inertia, pad mass and pivot stiffness on the impedances (imaginary part) for two four-pad LBP bearings with the pivot offsets equaling 0.5 and 0.6.
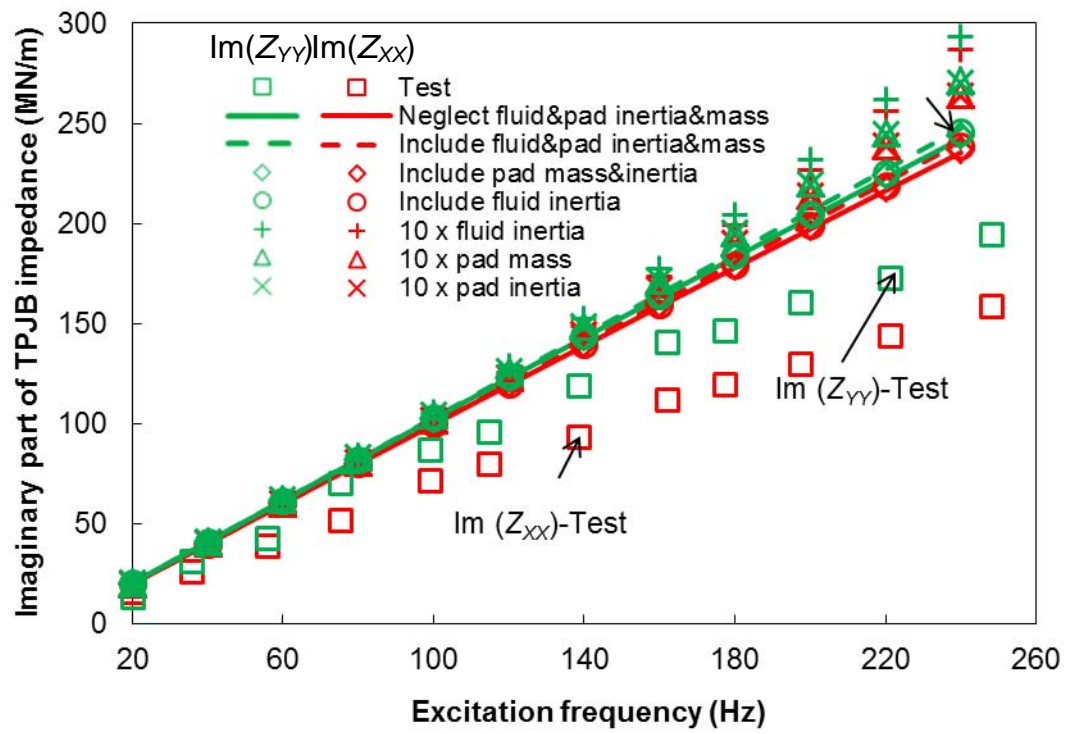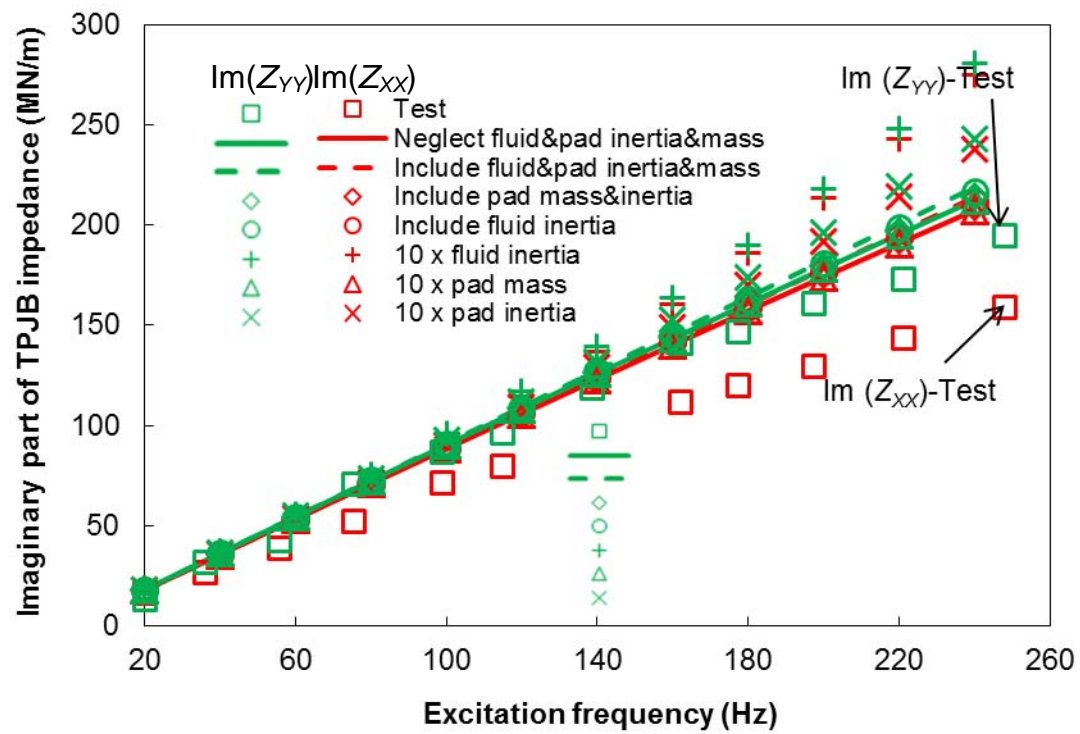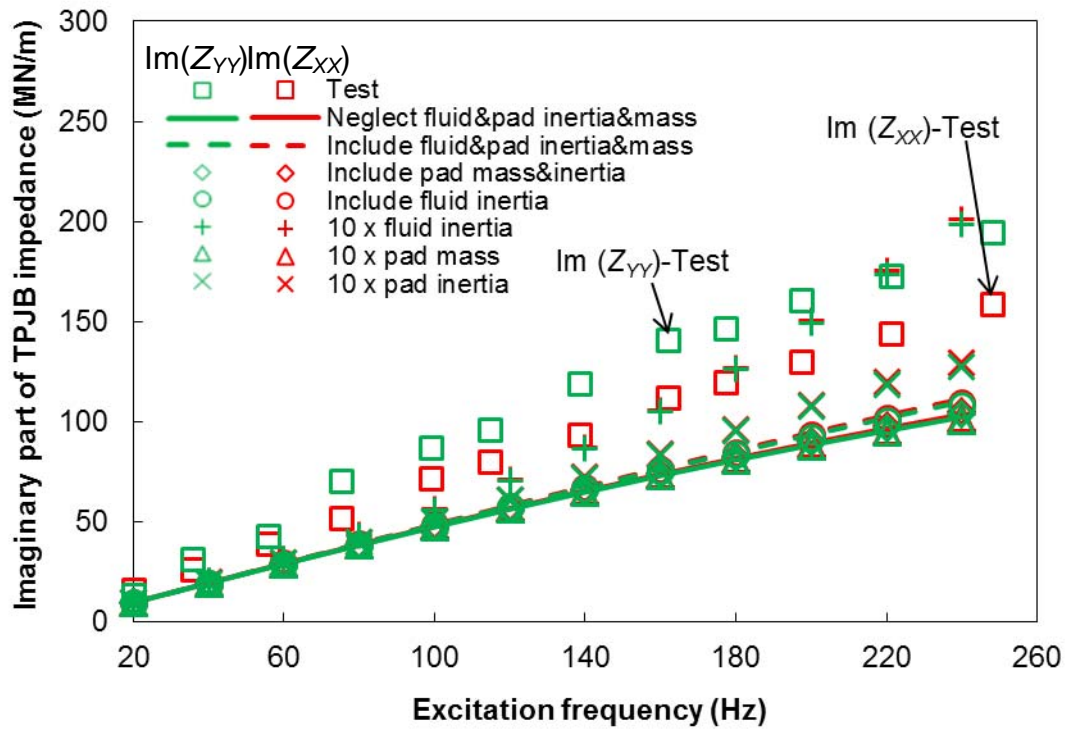

(a) Rigid pivot

(b) Pivot stiffness = 1,630 MN/m~1,900 MN/m
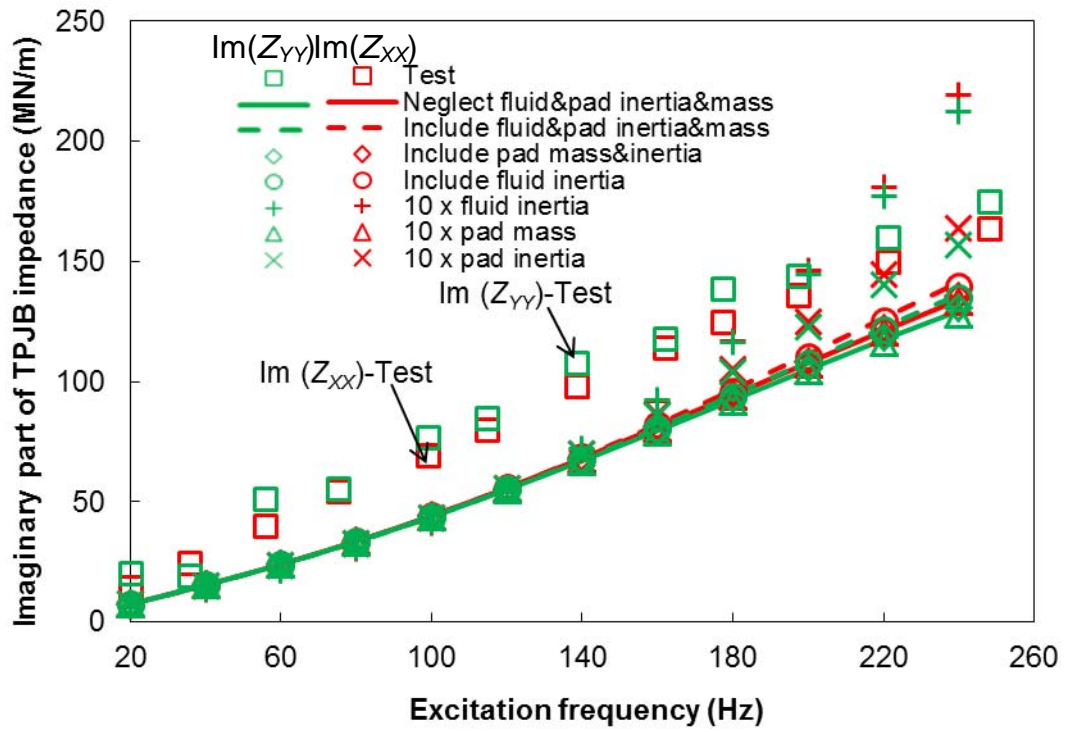
(c) Pivot stiffness = 200 MN/m

Fig. D. 5 Effect of temporal fluid inertia, pad moment of inertia, pad mass and pivot stiffness on the imaginary part of impedance coefficients for a five-pad LOP bearing with three pivot stiffnesses. Pad pivot offset =0.5. Rotor speed Ω= 10 krpm. Current predictions and measurements in Ref. [24].
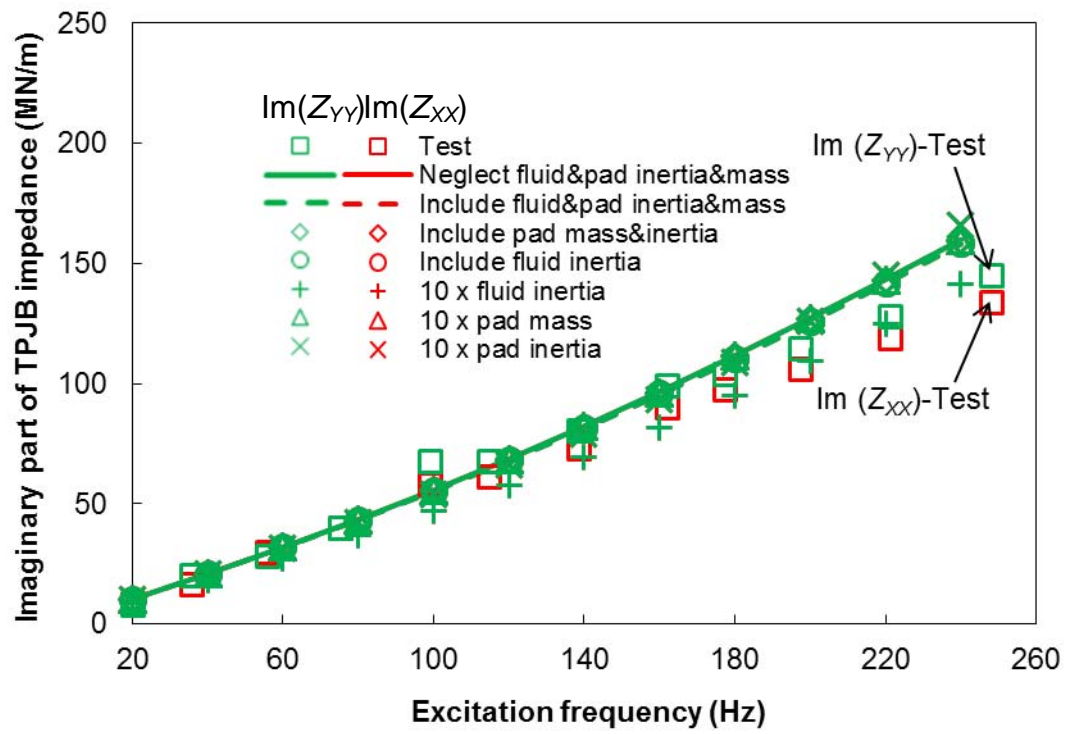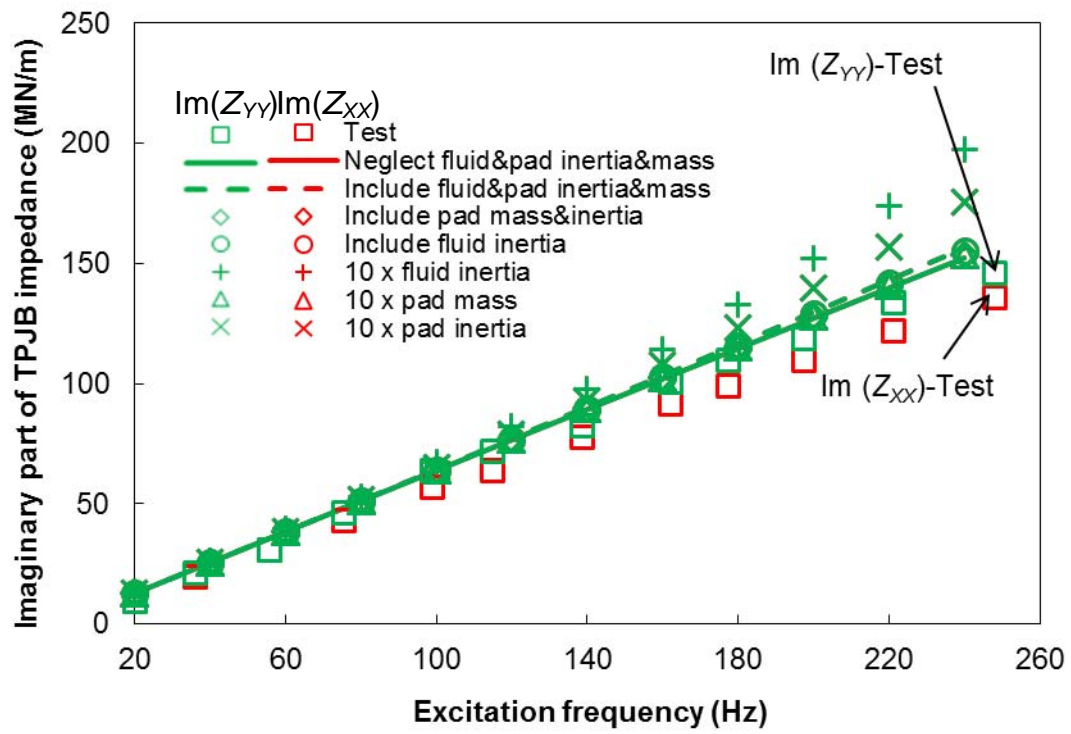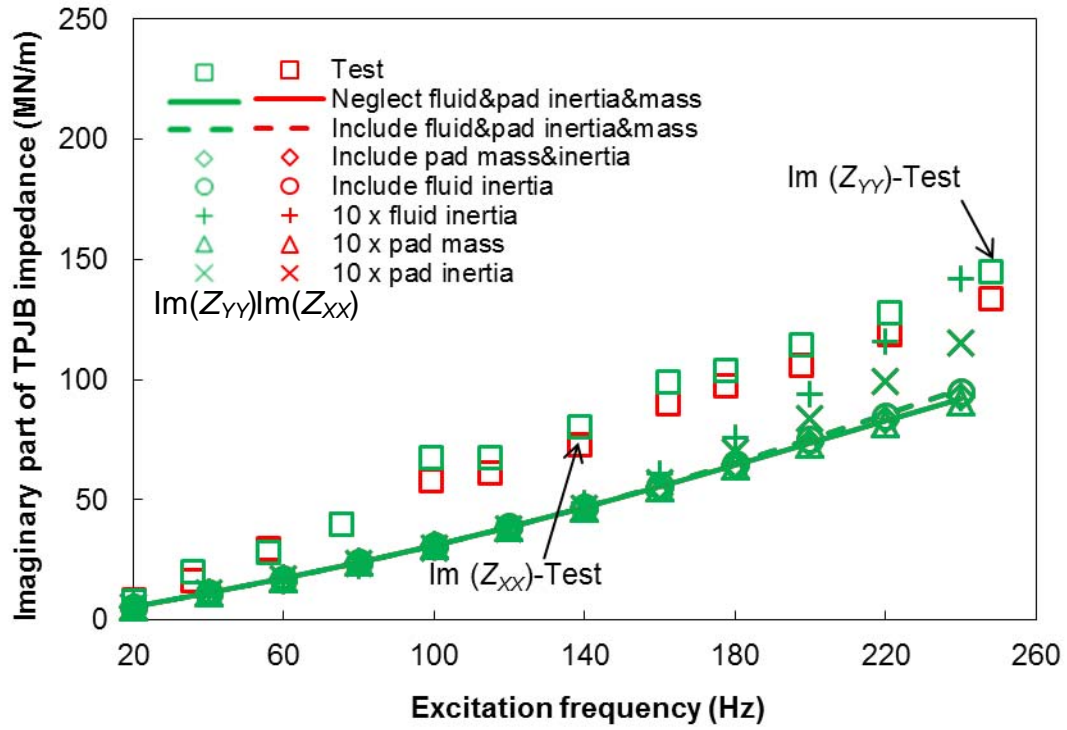
(a) Rigid pivot

(b) Pivot stiffness = 1,630 MN/m~1,900 MN/m

(c) Pivot stiffness = 200 MN/m

Fig. D. 6 Effect of temporal fluid inertia, pad moment of inertia, pad mass and pivot stiffness on the imaginary part of impedance coefficients for a five-pad LOP bearing with three pivot stiffnesses. Pad pivot offset =0.6. Rotor speed Ω= 10 krpm. Current predictions and measurements in Ref. [24].
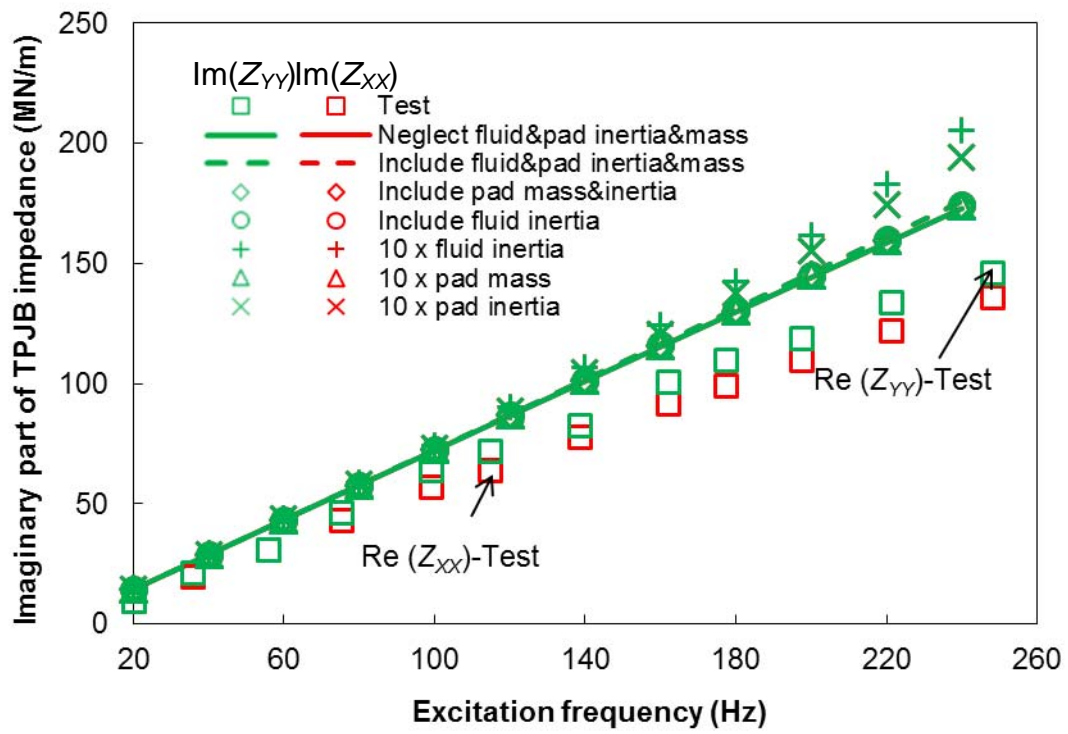
(a) Rigid pivot

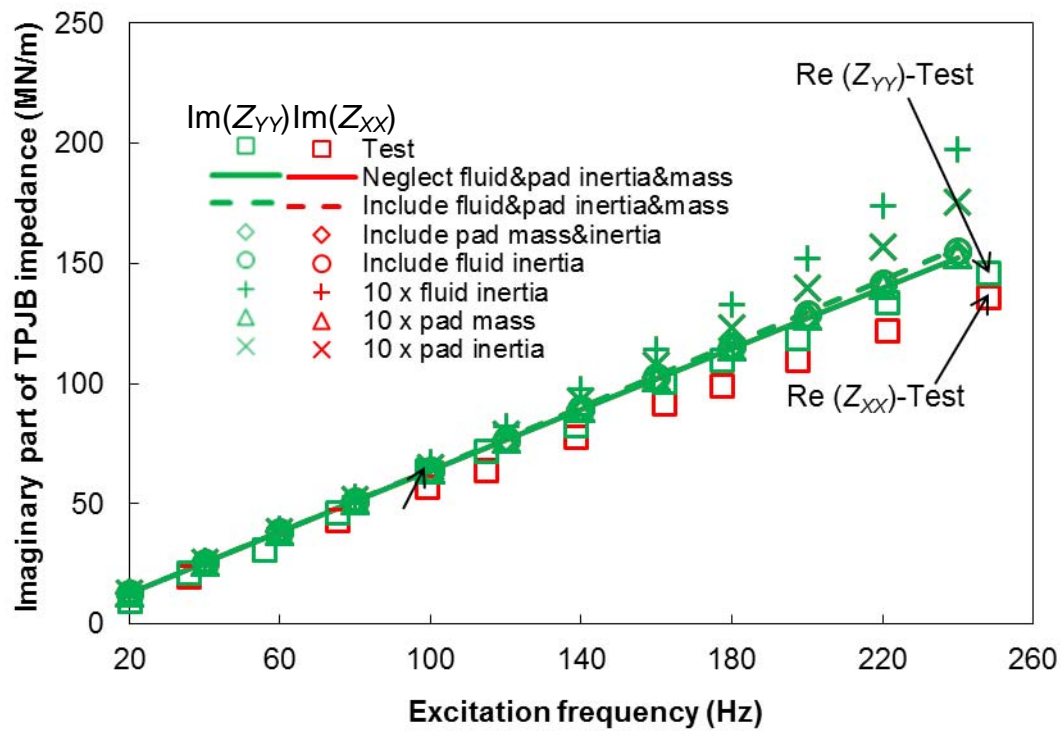**(b) Pivot stiffness = 1,630 MN/m~1,900 MN/m**
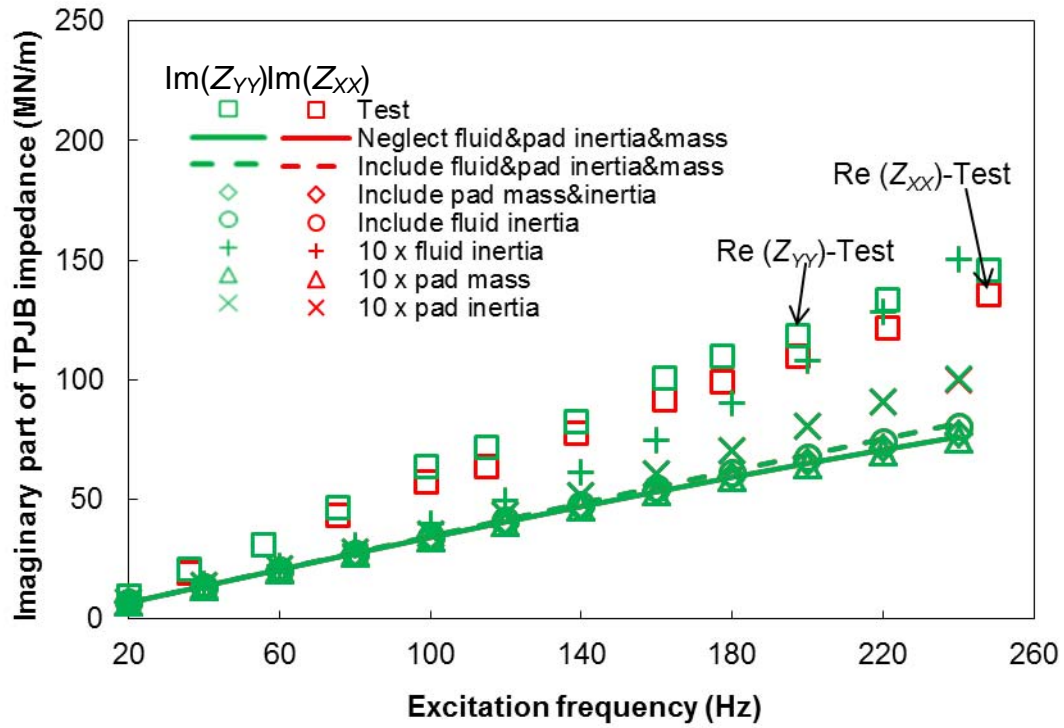
(c) Pivot stiffness = 200 MN/m

Fig. D. 7 Effect of temporal fluid inertia, pad moment of inertia, pad mass and pivot stiffness on the imaginary part of impedance coefficients for a four-pad LBP bearing with three pivot stiffnesses. Pad pivot offset =0.5. Rotor speed Ω= 10 krpm. Current predictions and measurements in Ref. [24].

(a) Rigid pivot

(b) Pivot stiffness = 1,630 MN/m~1,900 MN/m

(c) Pivot stiffness = 200 MN/m

Fig. D. 8 Effect of temporal fluid inertia, pad moment of inertia, pad mass and pivot stiffness on the imaginary part of impedance coefficients for a four-pad LBP bearing with three pivot stiffnesses. Pad pivot offset =0.6. Rotor speed Ω= 10 krpm. Current predictions and measurements in Ref. [24].